



HAL
open science

Deciphering competitive electrochemical routes at the nanoscale by operando optical imaging

Louis Godeffroy

► **To cite this version:**

Louis Godeffroy. Deciphering competitive electrochemical routes at the nanoscale by operando optical imaging. Chemical Physics [physics.chem-ph]. Université Paris Cité, 2023. English. NNT : 2023UNIP7066 . tel-04537635

HAL Id: tel-04537635

<https://theses.hal.science/tel-04537635>

Submitted on 8 Apr 2024

HAL is a multi-disciplinary open access archive for the deposit and dissemination of scientific research documents, whether they are published or not. The documents may come from teaching and research institutions in France or abroad, or from public or private research centers.

L'archive ouverte pluridisciplinaire **HAL**, est destinée au dépôt et à la diffusion de documents scientifiques de niveau recherche, publiés ou non, émanant des établissements d'enseignement et de recherche français ou étrangers, des laboratoires publics ou privés.

Université Paris Cité

École doctorale Chimie Physique et Chimie Analytique de Paris
Centre (ED 388)
*Laboratoire Interfaces, Traitements, Organisation et Dynamique
des Systèmes (UMR 7086)*

Deciphering competitive electrochemical routes at the nanoscale by *operando* optical imaging

Par **Louis GODEFFROY**

Thèse de doctorat de Chimie Physique

Dirigée par **Frédéric KANOUI**

Soutenue publiquement
le 6 octobre 2023

Devant un jury composé de :

Christel LABERTY-ROBERT

Professeure, Sorbonne Université

Rapportrice

Jon USTARROZ

Professeur associé, Université Libre de Bruxelles

Rapporteur

Mona TREGUER-DELAPIERRE

Professeure, Université de Bordeaux

Examinatrice

Fabien MIOMANDRE

Professeur, Ecole normale supérieure Paris-Saclay

Examineur

Frédéric KANOUI

Directeur de recherche CNRS, Université Paris Cité

Directeur de thèse

Jean-François LEMINEUR

Maître de conférences, Université Paris Cité

Co-encadrant

ABSTRACT

The deployment of renewable energy sources should pair with that of large-scale energy storage systems to balance their intermittent production. However, current technologies involving batteries or electrolyzers do not meet the price and safety requirements of such large-scale energy storage systems. Despite ongoing efforts to improve these aspects, the lack of standardized electrode preparation procedures hampers the reliable assessment and benchmarking of new materials.

This thesis introduces novel methodologies based on optical microscopy to evaluate the performance of individual catalyst and battery material particles, and improve the understanding of the underlying mechanisms. By correlating *in situ* optical microscopy with several other *ex situ* microscopies, with the help of machine vision and machine learning algorithms, data collection was significantly enhanced at individual particles. These new methodologies were tested on various energy storage and conversion systems, including Ni nanoparticles for electrochemical water splitting, MnO₂ thin films in aqueous Zn-MnO₂ batteries, and polycrystalline copper hexacyanoferrate microparticles as solid boosters in redox flow batteries.

KEYWORDS

Nanoelectrochemistry, optical microscopy, scanning electrochemical cell microscopy, nanopipettes, single nanoparticles, electrodeposition, electrocatalysis, hydrogen evolution reaction, Ni nanoparticles, aqueous batteries, Zn-MnO₂ batteries, redox flow batteries

RESUME

Le déploiement des énergies renouvelables devrait aller de pair avec celui des systèmes de stockage d'énergie à grande échelle pour équilibrer leur production intermittente. Cependant, les technologies actuelles impliquant des batteries ou des électrolyseurs ne répondent pas aux exigences de prix et de sécurité de ces systèmes de stockage d'énergie à grande échelle. Malgré les efforts continus fournis par les chercheurs pour améliorer ces points, l'absence de procédures standardisées pour la préparation des électrodes ralentit l'évaluation fiable ainsi que le criblage de nouveaux matériaux.

Cette thèse introduit de nouvelles méthodologies basées sur la microscopie optique pour évaluer les performances de particules individuelles de catalyseurs et de matériaux de batteries, et améliorer la compréhension des mécanismes sous-jacents. En corrélant la microscopie optique *in situ* avec plusieurs autres microscopies *ex situ*, avec l'aide d'algorithmes de vision artificielle et d'apprentissage machine, la collecte de données a été considérablement améliorée au niveau de particules individuelles. Ces nouvelles méthodologies ont été testées sur divers systèmes de stockage et de conversion d'énergie dont les nanoparticules de Ni pour la dissociation électrochimique de l'eau, les films minces de MnO_2 dans les batteries aqueuses Zn- MnO_2 , et les microparticules polycristallines d'hexacyanoferrate de cuivre comme *solid boosters* dans les batteries à flux redox.

MOTS-CLES

Nanoélectrochimie, microscopie optique, microscopie électrochimique à balayage, nanopipettes, nanoparticules individuelles, électrodéposition, électrocatalyse, réaction de dégagement d'hydrogène, nanoparticules de Ni, batteries aqueuses, batteries Zn- MnO_2 , batteries à flux redox

RESUME SUBSTANTIEL EN FRANÇAIS

Le dernier rapport du Groupe d'experts Intergouvernemental sur l'Evolution du Climat (GIEC), publié cette année, souligne une fois de plus l'urgence de réduire de manière significative nos émissions de gaz à effet de serre. Pour atteindre cet objectif, la majorité des gouvernements dans le monde ont décidé d'augmenter la part des énergies renouvelables dans le mix énergétique de leur pays. Cependant, la plupart des énergies renouvelables, telles que l'énergie éolienne et l'énergie solaire, sont intrinsèquement intermittentes, ce qui signifie que leur production ne correspond pas toujours à la demande. C'est pourquoi des efforts considérables sont actuellement déployés pour développer des stratégies de stockage de l'énergie à grande échelle et à long terme afin de permettre un ajustement efficace de la production. En particulier, les systèmes électrochimiques impliquant l'utilisation de batteries ou d'électrolyseurs suscitent un intérêt croissant. Toutefois, les technologies actuelles ne répondent pas encore aux exigences des systèmes de stockage à grande échelle, que ce soit pour des raisons de sécurité ou de prix. Alors que de nouveaux matériaux électroactifs capables de servir d'électrodes dans des batteries ou des électrolyseurs sont découverts chaque jour, l'absence de protocoles d'essai normalisés entrave considérablement l'identification d'alternatives prometteuses.

Pour évaluer les performances d'un nouveau matériau, il faut généralement le mélanger avec de la poudre de carbone et des liants. Bien qu'ils confèrent à l'électrode les propriétés physiques appropriées, ces additifs peuvent se dégrader dans les environnements agressifs nécessaires au fonctionnement des batteries et des électrolyseurs (fortement réducteurs/oxydants et/ou fortement alcalins/acides), ce qui affecte à la fois les performances intrinsèques du matériau et, par conséquent, les performances globales du dispositif. Au début de mon doctorat, deux stratégies principales avaient été envisagées dans la littérature pour résoudre ces problèmes. D'une part, certains chercheurs se sont concentrés sur le suivi de ces réactions secondaires, pendant le fonctionnement du dispositif ou *operando*, en utilisant des analyses chimiques ou physiques complémentaires *in situ* et en temps réel (le terme « *operando* » dans les études électrochimiques est apparu pour la première fois il y a une dizaine d'années et a pris beaucoup d'ampleur depuis). D'autre part, d'autres chercheurs ont proposé de réduire la complexité des électrodes pour éviter ces réactions secondaires et

ainsi révéler les performances intrinsèques du matériau, par exemple en examinant des particules isolées. Cela correspond à la *single entity electrochemistry* (que l'on peut traduire en français par « électrochimie sur entité unique ») telle que définie par Baker en 2018 dans une perspective séminale résumant les dix premières années de ce nouveau domaine de l'électroanalyse et suggérant des directions prometteuses.^[1]

Notre groupe de recherche a été actif sur les deux fronts en développant des méthodologies basées sur les microscopies électrochimiques à balayage (*scanning electrochemical probe microscopies*, SEPM, en anglais) et les microscopies optiques (MOs) pour suivre des processus électrochimiques *in situ*, en mettant l'accent sur l'électrochimie à l'échelle nanométrique, c'est-à-dire sur l'étude de la réactivité électrochimique de nanoparticules (NPs) individuelles. Au départ, les chercheurs se sont intéressés à des systèmes modèles tels que les NPs d'Ag, qui ont une électrochimie bien documentée et des propriétés plasmoniques bien connues facilitant leur détection par MO. Cela a permis de valider ces nouvelles méthodologies électroanalytiques dans différents groupes, dont le nôtre. Au moment où j'ai commencé mon doctorat, ces méthodologies étaient sur le point de se confronter à des processus plus complexes et à des matériaux d'intérêt pour des applications dans le stockage et la conversion de l'énergie.

L'objectif principal de mon doctorat était de participer à cette transition vers le suivi *operando* à l'échelle nanométrique de systèmes (électro)chimiques complexes tels que ceux rencontrés dans les batteries ou les électrolyseurs. Cette transition a nécessité de pousser le développement d'approches corrélatives multi-microscopiques afin d'améliorer la collecte de données sur des NPs uniques. Parallèlement, j'ai également contribué au développement de nouvelles stratégies de vision artificielle et d'apprentissage machine pour analyser ces vastes ensembles de données. Les principaux résultats de mon travail de doctorat peuvent être classés en deux catégories correspondant aux applications des matériaux étudiés : l'électrocatalyse (**Chapitres 2 à 4**) et les batteries (**Chapitres 5 et 6**). Dans les **Chapitres 2 à 4**, nous montrons comment les méthodologies existantes basées sur la MO peuvent être transposées et améliorées en utilisant des stratégies empruntées aux microscopies multi-corrélatives et à l'intelligence artificielle pour appréhender l'électrochimie complexe des NPs à base de Ni. Dans les **Chapitres 5 et 6**, en utilisant des méthodologies similaires, nous tentons d'élucider le mécanisme de stockage de charge de deux types de batteries aqueuses

pertinentes pour le stockage d'énergie à grande échelle, à savoir les batteries Zn-MnO₂ et les batteries à flux redox.

Globalement, cette thèse s'intéresse à l'imagerie optique des processus électrochimiques à l'échelle nanométrique, tant au niveau de NPs que de microparticules. Cette approche permet d'élucider des mécanismes complexes et de quantifier les performances de matériaux dans le contexte du stockage et de la conversion de l'énergie. Les sections suivantes décrivent plus en détail le contenu de chaque chapitre.

Le **Chapitre 1** présente le contexte socio-économique et scientifique de mon doctorat. Il passe également en revue les techniques employées pour étudier les matériaux de batteries et les électrocatalyseurs au niveau de la particule unique, en mettant l'accent sur les MOs.

Le **Chapitre 2** discute de l'intérêt de l'électrodéposition de nanocatalyseurs et étudie le mécanisme complexe de l'électrodéposition de NPs à base de Ni à partir de solutions aqueuses. Il présente le microscope à réflexion interférométrique (*interference reflection microscope*, IRM, en anglais) utilisé dans ce travail et démontre sa capacité à distinguer les NPs de Ni métallique des NPs de Ni(OH)₂ *in situ*, ainsi qu'à suivre leur croissance *in situ*. Ces résultats confirment le mécanisme de croissance « auto-terminée » (*self-terminated* en anglais) proposé pour les films minces de Ni métallique, même dans les cas où le pic de réduction caractéristique de l'électrodéposition de Ni est absent de la courbe électrochimique, et où les NPs croissent indirectement alors que la réduction de l'eau domine à l'électrode.

Le **Chapitre 3** vise à mieux comprendre ce pic de réduction, car des études antérieures ont indiqué sa corrélation non seulement avec la formation de Ni métallique, mais aussi avec une augmentation du pH résultant probablement de l'électrocatalyse de la réduction de l'eau. En réduisant la taille de la cellule électrochimique pour permettre d'imager toutes les NPs responsables du signal électrochimique, et avec l'aide d'algorithmes de vision artificielle et d'apprentissage machine pour analyser les données de la MO, le courant de croissance associé à toutes les NPs de Ni métallique a pu être évalué. En le soustrayant du courant total mesuré par le potentiostat, il a été possible d'estimer l'activité catalytique moyenne des NPs de Ni.

Le **Chapitre 4** étudie le processus d'électrodéposition au cours de plusieurs cycles consécutifs de voltampérométrie cyclique (*cyclic voltammetry, CV*, en anglais). Au lieu de former de nouvelles NPs de Ni à chaque cycle, un halo sombre se forme autour de toutes les NPs de Ni générées au cours du premier cycle. Ce halo, identifié comme étant composé de Ni(OH)_2 , s'accumule autour des NPs car elles ne sont pas complètement passivées au-delà du pic de réduction et continuent à catalyser la réduction de l'eau et donc à basifier leur voisinage. En comparant l'évolution expérimentale de la taille du halo à un modèle COMSOL, l'activité catalytique a pu être quantifiée au niveau de NPs uniques. En outre, cette méthodologie est étendue à d'autres chimies de NPs et de halos, révélant une amélioration spécifique de l'activité par Ni(OH)_2 .

Le **Chapitre 5** utilise une configuration de microscope différente pour étudier les processus de charge et de décharge se produisant dans les batteries aqueuses Zn- MnO_2 . L'électrodéposition/dissolution de MnO_2 s'avère être la principale voie de stockage de charge. Grâce à un modèle optique et à des caractérisations *ex situ* complémentaires de l'électrode de MnO_2 , la précipitation d'hydroxysulfate de zinc (*zinc hydroxide sulfate, ZHS*, en anglais) est détectée à un stade de décharge beaucoup plus précoce que dans les études antérieures. Le rôle crucial de ZHS en tant que tampon de pH local est également confirmé en charge, où des taux de dépôt de MnO_2 plus élevés sont observés autour des particules de ZHS.

Le **Chapitre 6** présente une approche combinant la microscopie électrochimique à balayage (*scanning electrochemical microscopy, SECM*, en anglais) et l'IRM pour étudier le transport des ions à l'intérieur de microparticules polycristallines d'hexacyanoferrate de cuivre utilisées comme *solid boosters* (que l'on peut traduire en français par « amplificateurs solides ») dans des batteries à flux redox. Dans ces systèmes, la conversion du matériau solide est réalisée par un médiateur redox. L'ultramicroélectrode (UME) du SECM est alors utilisée pour initier la conversion de particules individuelles en oxydant le médiateur dans leur voisinage. En outre, elle sert de miroir optique, réfléchissant la lumière à travers la particule vers l'objectif. Cela permet une évaluation simultanée et localisée de l'état de charge de la particule sur la base de son absorbance, bien que le microscope fonctionne en réflexion. Cette approche révèle l'importance du transport dans les pores des particules.

Outre les projets susmentionnés, j'ai également participé à d'autres projets au cours de mon doctorat, principalement dans le cadre de collaborations, qui ne seront que brièvement mentionnées ici. En collaboration avec le groupe de Jean-Marie Tarascon au Collège de France, nous avons étudié l'expansion et la contraction de microparticules d'oxyde de cobalt et de lithium pendant leur (dé)lithiation en utilisant de l'imagerie optique 3D.^[2] En outre, nous avons également étudié la dynamique de (dé)lithiation au sein de microparticules électrochromes de $\text{Li}_2\text{Ni}_2\text{W}_2\text{O}_9$.^[3] En collaboration avec le groupe de Damien Alloyeau à l'Université Paris Cité, nous avons tenté d'adapter la méthodologie présentée au **Chapitre 4** à la microscopie électronique à transmission (*transmission electron microscopy*, TEM, en anglais) *in situ*, car cette technique, bien qu'elle soit plus résolue spatialement, est tout aussi incapable de détecter les produits de réaction dissous et donc de quantifier directement l'activité catalytique. De plus, en collaboration avec le groupe de Julie McPherson à l'Université de Warwick, nous avons fait des progrès significatifs dans l'automatisation de l'analyse d'images TEM colocalisées pour quantifier la dégradation de catalyseurs lors de tests de stress accélérés.

Un autre projet sur lequel j'ai travaillé consistait à étudier l'électrochimie de NPs situées sur le bord extérieur de cellules-gouttelettes. Bien qu'elles ne semblassent pas être connectées à la cellule électrochimique, certaines de ces NPs présentaient des fluctuations d'intensité importantes corrélées au programme de potentiel appliqué. Nous avons découvert par la suite que des canaux d'électrolyte nanométriques reliaient ces NPs à la cellule électrochimique, les alimentant en eau et en ions pour maintenir l'équilibre des charges pendant qu'elles catalysaient la réduction de l'oxygène.

REMERCIEMENTS

Je tiens tout d'abord à remercier mon directeur de thèse, Frédéric Kanoufi, de m'avoir accordé sa confiance et accueilli dans son équipe. Ces trois années de thèse ont été très enrichissantes sur le plan intellectuel, mais aussi humainement. Grâce à toi et à toute l'équipe, j'ai eu la chance d'évoluer dans un cadre chaleureux et bienveillant, élément clé de la réussite de ma thèse. Peu nombreux sont ceux qui accordent autant d'attention au bien-être et à la réussite des étudiants qu'ils encadrent, et je t'admire beaucoup pour cela. J'essaierai d'en faire autant dans la suite de ma carrière.

Un grand merci donc aussi à Jean-François Lemineur, mon co-encadrant, à Jean-Marc Noël, Jérôme Médard, Viacheslav (Slava) Shkirskiy, Jean Pinson, Fetah Podvorica et Catherine Combellas, ainsi qu'à tous les étudiants de l'équipe que j'ai côtoyés : Chérif Adouama, Mathias Miranda Vieira, Paolo Ciocci, Nikolaos Kostopoulos, Théo Lasseur, Puvaneswari (Yashna) Teluchina-Appadu, Romain Gay, Aleksei Makogon, Marine Cheng, Enrico Daviddi et Silvia Voci. Merci pour votre gentillesse et votre bonne humeur, qui ont rendu les obstacles rencontrés pendant la thèse plus faciles à surmonter. Il me manquerait de l'espace pour écrire sur chacun d'entre vous, mais je voudrais néanmoins dire quelques mots sur certains.

Jean-François, j'ai pris énormément de plaisir à échanger avec toi sur les expériences et sur l'enseignement. Tu es un enseignant très dévoué et je t'admire beaucoup pour cela. Tes étudiants ont beaucoup de chance de t'avoir comme enseignant. Jérôme, un grand merci pour tous les efforts que tu fais pour nous aider dans nos recherches ; l'équipe a beaucoup de chance de t'avoir. Jean, ce fut un réel honneur d'être votre voisin de paillasse durant ces trois années. Votre enthousiasme et votre humilité forcent l'admiration.

Mes sincères remerciements également à tous les membres de l'ITODYS, en particulier à Sarra Gam Derouich pour la formation à la microscopie électronique à balayage, à Sophie Nowak pour la formation à la diffraction des rayons X, ainsi qu'à tous les étudiants pour avoir contribué à faire de cette thèse une très belle expérience humaine.

Je tiens aussi à témoigner toute ma reconnaissance aux membres de mon jury de soutenance, Fabien Miomandre, Christel Laberty-Robert, Jon Ustarroz et Mona Tréguer-Delapierre, pour avoir accepté d'évaluer mon travail et pour la discussion qui s'en est suivie.

Je voudrais également exprimer ma gratitude aux nombreux collaborateurs qui ont contribué à ce travail : Jean-Marie Tarascon, Ivette Aguilar, Simon Redor et Raj Pandya du Collège de France pour l'étude de divers matériaux de batterie ; Damien Alloyeau et Nathaly Ortiz-Peña du laboratoire MPQ d'Université Paris Cité pour les mesures de TEM *in situ* ; Julie Macpherson, Daniel Houghton et Pei Zhao de l'Université de Warwick pour l'analyse automatisée d'images TEM ; Sanli Faez et Zhu Zhang de l'Université d'Utrecht pour le développement d'un nouveau microscope ultra-performant ; ainsi que Pekka Peljo, Mahdi Moghaddam, Jerzy Jasielec et Mousumi Dey de l'Université de Turku pour l'étude de batteries redox flow de nouvelle génération.

Enfin, je tiens à remercier toute ma famille pour m'avoir soutenu dans les moments difficiles, et en particulier Ivette, avec qui j'ai la chance de partager ma vie depuis bientôt cinq ans. Ces dernières années ont été très intenses, et je suis très heureux et fier de les avoir surmontées à tes côtés.

TABLE OF CONTENTS

Abstract	iii
Résumé	iv
Résumé substantiel en français	v
Remerciements	xi
List of abbreviations	xvii
General introduction	1
Chapter 1 Socio-economic and scientific context	7
1.1 Socio-economic context	7
1.1.1 The duck curve	7
1.1.2 What kind of energy storage for grid-scale applications?	8
1.2 Scientific context: electrocatalysis goes nuts	10
1.3 Single-nanoparticle approaches	13
1.3.1 Separating the NPs in time: nano-impact electrochemistry	13
1.3.2 Separating the NPs in space	23
1.4 Optical microscopy approaches	41
1.4.1 Electrocatalysis	43
1.4.2 Batteries	47
1.5 Issues and opportunities related to optical microscopies in the context of single-entity electrochemistry and of my PhD	52
1.5.1 Issues	52
1.5.2 Opportunities	54
Chapter 2 Investigating the competing electrodeposition mechanisms of Ni-based nanoparticles	57
2.1 Introduction	57
2.2 Results and discussion	59

2.2.1	Low Ni ²⁺ concentration	62
2.2.2	High Ni ²⁺ concentration	68
2.3	Conclusion	72
Chapter 3 On the origin of the reduction peak in Ni electrodeposition		75
3.1	Introduction	75
3.2	Results and discussion	77
3.2.1	Electrodeposition of Ni NPs	77
3.2.2	Optical image analysis	80
3.2.3	Dimensions of the NPs	82
3.2.4	Chemical composition of the NPs	84
3.2.5	From local nanoscale descriptors to global electrochemistry	89
3.3	Conclusion	95
Chapter 4 Assessing the electrocatalytic activity of single nanoparticles by imaging nanoscale reaction footprints		97
4.1	Introduction	97
4.2	Results and discussion	101
4.2.1	Description of the phenomenon	101
4.2.2	Case of Ni NPs	103
4.2.3	COMSOL model	106
4.2.4	Activation and size effect	109
4.2.5	Versatility of the strategy	112
4.3	Conclusion	114
Chapter 5 Decoupling the dynamics of zinc hydroxide sulphate precipitation/dissolution in aqueous Zn–MnO₂ batteries		117
5.1	Introduction	117
5.2	Results and discussion	119

5.2.1	Operating principle	119
5.2.2	Cyclic voltammetry – qualitative analysis	121
5.2.3	Cyclic voltammetry – quantitative analysis in the ZHS-saturated electrolyte	127
5.2.4	Galvanostatic cycling	134
5.3	Conclusion	142
Chapter 6 Probing local charge storage pathways within single polycrystalline microparticles for redox flow batteries		147
6.1	Introduction	147
6.2	Results and discussion	149
6.2.1	Probing the charge/discharge of individual CuHCF microparticles by opto-electrochemistry	149
6.2.2	Charge/discharge dynamics at the single-microparticle level	153
6.2.3	Sub-particle imaging of the charge/discharge dynamics	164
6.3	Conclusion	168
General conclusion		171
Materials and methods		177
M.1	Materials	177
M.1.1	Chemicals	177
M.1.2	ZHS synthesis	177
M.1.3	CuHCF synthesis	177
M.1.4	Micropipette fabrication	178
M.1.5	ITO and Au cleaning	178
M.1.6	Pt NP electrodeposition on ITO	178
M.2	Opto-electrochemical experiments	180
M.2.1	Inverted microscope	180
M.2.2	Upright microscope	181

M.3 Other instruments	181
M.3.1 Scanning electron microscopy	182
M.3.2 Atomic force microscopy	182
M.3.3 Transmission electron microscopy	182
M.3.4 Galvanostatic cycling in Swagelok cell	182
M.3.5 Inductively coupled plasma-mass spectrometry	183
M.3.6 Fourier-transform infrared reflection-absorption spectroscopy	184
M.3.7 X-ray photoelectron spectroscopy	184
M.3.8 X-ray diffraction	184
M.4 Image processing (inverted microscope)	185
M.4.1 NP localization and optical intensity extraction (Chapters 2-4)	185
M.4.2 Modelling of NP growth (Chapter 3)	185
M.4.3 Extraction of hydroxide shell size (Chapter 4)	193
M.5 Influence of NP geometry on the flux	194
Appendix 1 Additional information about the COMSOL simulations	197
A1.1 Influence of the limit of detection of the halo	197
A1.2 Approximate analytical solution	197
A1.3 Relationship between kp and k°	199
A1.4 Dissolution of the $\text{Mg}(\text{OH})_2$ halos: determination of kp	200
A1.5 Influence of the nucleation delay	202
A1.6 Examples of Pt NPs cycled in Ni^{2+} and Mg^{2+}	203
Appendix 2 Optical models	207
A2.1 Single-component film	207
A2.2 Two-component film	208
References	211

LIST OF ABBREVIATIONS

AFM atomic force microscopy/microscope

ALD atomic layer deposition

CA

chronoamperometry/chronoamperogram

CE counter electrode

CNT carbon nanotube

CO₂RR CO₂ reduction reaction

CP chronopotentiometry

CuHCF copper hexacyanoferrate

CV cyclic voltammetry/voltammogram

DFM dark-field microscopy/microscope

DMC dimethyl carbonate

EC ethylene carbonate

ECL electrochemiluminescence

EQCM electrochemical quartz crystal
microbalance

ESM electrochemical strain
microscopy/microscope

EU European Union

FcMeOH ferrocenemethanol

FEC fluoroethylene carbonate

BEM boundary element method

BET Brunauer-Emmett-Teller

FIB focused ion beam

FSCV fast-scan cyclic
voltammetry/voltammogram

FT-IRRAS Fourier transform infrared
reflection-absorption spectroscopy

HCNS hollow carbon nitride nanosphere

HER hydrogen evolution reaction

HM high magnification

HOPG highly oriented pyrolytic graphite

HOR hydrogen oxidation reaction

ICP-MS inductively coupled plasma mass
spectrometry

IM intermediate magnification

IPCC Intergovernmental Panel on Climate
Change

IRM interference reflection
microscopy/microscope

iSCAT interferometric scattering
microscopy/microscope

ITO indium tin oxide

KPFM Kelvin probe force microscopy/microscope

LCO lithium cobalt oxide, Li_xCoO_2

LDH layered double hydroxide

LIB Li-ion battery

LM low magnification

LSV linear sweep voltammetry/voltammogram

MLG monolayer graphene

MOF metal-organic framework

NADH nicotinamide adenine dinucleotide

NB nanobubble

NC nanocube

NI nanoisland

NIE nano-impact electrochemistry

NMC lithium nickel manganese cobalt oxide, $\text{LiNi}_x\text{Mn}_y\text{Co}_{(1-x-y)}\text{O}_2$

NO₃RR nitrate reduction reaction

NP nanoparticle

NR nanorod

NS nanosphere

NWO niobium tungsten oxide, $\text{Nb}_{14}\text{W}_3\text{O}_{44}$

OER oxygen evolution reaction

OM optical microscopy/microscope

ORR oxygen reduction reaction

OTECCM optically targeted electrochemical cell microscopy

OTF optical transfer function

PB Prussian blue

PBA Prussian blue analogue

PC propylene carbonate

PQQ pyrroloquinoline quinone

PS polystyrene

PSF point spread function

PSIM plasmonic scattering interferometry microscopy/microscope

QRCE quasi-reference counter electrode

QRE quasi-reference electrode

RAC redox active colloid

RDE rotating disk electrode

RFB redox flow battery

ROI region of interest

SAM self-assembled monolayer

SB solid booster

SB-FB solid-boosted flow battery

SECCM scanning electrochemical cell microscopy/microscope

SECM scanning electrochemical microscopy/microscope

SEI solid electrolyte interphase

SEM scanning electron microscopy/microscope

SEPM scanning electrochemical probe microscopy/microscope

SG-TC substrate generation-tip collection (mode)

SICM scanning ion conductance microscopy/microscope

SI-SECM surface interrogation scanning electrochemical microscopy

SNPE single-nanoparticle electrode

SP-IRIS single particle interferometric reflectance imaging sensor

SPM scanning probe microscopy/microscope

SPR surface plasmon resonance

SPRM surface plasmon resonance microscopy/microscope

SS-LIB solid-state Li-ion battery

SSRM scanning spreading resistance microscopy/microscope

STEM scanning transmission electron microscopy

STM scanning tunnelling microscopy/microscope

STXM scanning transmission X-ray microscopy/microscope

TEM transmission electron microscopy/microscope

TEMPTMA N,N,N-2,2,6,6-heptamethyl piperidinyloxy-4-ammonium chloride

TIRDFM total internal reflection dark-field microscopy/microscope

TIRFM total internal reflection fluorescence microscopy/microscope

TIRM total internal reflection microscopy/microscope

TMD transition metal dichalcogenide

TMPD N,N,N',N'-tetramethyl *p*-phenylenediamine

TOF turnover frequency

UME ultramicroelectrode

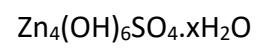
UN United Nations

WE working electrode

XPS X-ray photoelectron spectroscopy

XRD X-ray diffraction

ZHS zinc hydroxide sulfate,



GENERAL INTRODUCTION

The latest report from the Intergovernmental Panel on Climate Change (IPCC), published this year, once again emphasizes the urgent need to significantly reduce greenhouse gas emissions. To achieve this goal, governments worldwide have chosen to increase the proportion of renewable energy sources in their energy mix. However, most renewables, such as wind and solar power, are inherently intermittent, which means their production may not always align with demand. Therefore, substantial efforts are currently underway to develop strategies for large-scale and long-term energy storage to enable effective production adjustment. In particular, electrochemical systems involving the utilization of either batteries or electrolyzers are attracting increasing interest. However, current technologies do not meet the requirements for large-scale storage systems, either due to safety or pricing concerns. While new electroactive materials capable of serving as electrodes in batteries or electrolyzers are being discovered every day, the lack of standardized testing protocols significantly impedes the identification of promising alternatives.

Assessing the performance of a new material typically involves processing it with carbon powder and binders. While they grant the electrode the appropriate physical properties, these additives may degrade in the harsh environments required to drive batteries and electrolyzers (strongly reducing/oxidizing and/or strongly alkaline/acidic), affecting both the material's intrinsic performance and therefore the device's overall performance. At the start of my PhD, two main strategies had been considered in the literature to tackle these issues. On the one hand, some researchers focused on monitoring these side reactions, under operation or *operando*, by using complementary *in situ* and real-time chemical or physical analyses (the term "*operando*" in electrochemical studies first appeared around ten years ago and has grown ever since). On the other hand, other researchers suggested reducing the complexity of the electrodes to avoid these side reactions and reveal the material's intrinsic performance e.g., by examining isolated particles. This corresponds to "single entity electrochemistry" as defined by Baker in 2018 in a seminal perspective summarizing the first ten years of this new field of electroanalysis and suggesting promising directions.^[1]

Our research group has been active on both sides by developing methodologies based on scanning electrochemical probe microscopies (SEPMs) and optical microscopies (OMs) to monitor electrochemical processes *operando*, with a focus on nanoscale electrochemistry i.e., on the investigation of the electrochemical reactivity of individual nanoparticles (NPs). Initially, the focus primarily revolved around model systems like Ag NPs, which have a well-documented electrochemistry and well-known plasmonic properties facilitating detection through OM. This has enabled these novel electroanalytical methodologies to be validated in various groups, including our own. At the time my PhD began, these methodologies were about to move on to more complex processes and materials of interest for energy storage and conversion applications.

The primary objective of my PhD was to participate in this transition towards the *operando* nanoscale monitoring of complex (electro)chemical systems such as those encountered in batteries or electrolyzers. This transition required to push the development of correlative multi-microscopy approaches to enhance data collection at single NPs. Concurrently, I also contributed to the development of new machine vision and machine learning strategies for analysing these extensive datasets. The main findings of my PhD work can be categorized into two areas corresponding to the applications of the studied materials: electrocatalysis (**Chapters 2-4**) and batteries (**Chapters 5 and 6**). In **Chapters 2-4**, we show how the existing OM-based methodology could be transposed and improved using strategies borrowed from multi-correlative microscopies and artificial intelligence to apprehend the complex electrochemistry of Ni-based NPs. In **Chapters 5 and 6**, using similar methodologies, we focus on two aqueous battery technologies relevant for large-scale energy storage, namely aqueous Zn-MnO₂ and redox flow batteries.

Overall, this thesis delves into the optical imaging of electrochemical processes at the nanoscale, both at NPs and within microparticles. This approach helps unravel complex mechanisms and quantify the performance of materials within the context of energy storage and conversion. The following sections outline the content of the thesis in more detail.

Chapter 1 provides an elaboration of the socio-economic and scientific context of my PhD. It also reviews the techniques employed to study battery materials and electrocatalysts at the single particle level, with a specific emphasis on OMs.

Chapter 2 delves into the interest of electrodepositing nanocatalysts and investigates the intricate electrodeposition mechanism of Ni-based NPs from aqueous solutions. It introduces the interference reflection microscope (IRM) used in this work and demonstrates its capability to distinguish metallic Ni and Ni(OH)₂ NPs *in situ*, as well as to monitor their growth *operando*. These results confirm the self-terminating growth mechanism proposed for metallic Ni thin films, even in cases where the characteristic reduction peak associated with Ni electrodeposition is absent from the electrochemical trace, and the NPs grow indirectly while water reduction dominates at the electrode.

Chapter 3 aims to gain further insight into this reduction peak, as previous studies have indicated its correlation not only with the formation of metallic Ni, but also with a pH increase resulting from water reduction electrocatalysis. By reducing the size of the electrochemical cell to enable comprehensive imaging of all NPs responsible for the electrochemical signal, and with the assistance of machine vision and machine learning algorithms to analyse the OM data, the growth current associated to all metallic Ni NPs could be evaluated. Subtracting it from the total current measured by the potentiostat allowed to estimate the average catalytic activity of the Ni NPs.

Chapter 4 investigates the electrodeposition process over several consecutive cyclic voltammetry (CV) cycles. Instead of forming new Ni NPs in each cycle, a dark halo forms around all Ni NPs generated during the first cycle. This halo, which is identified as Ni(OH)₂, accumulates around the NPs as they are not fully passivated beyond the reduction peak and continue to catalyse water reduction. By comparing the experimental evolution of the halo's size to a COMSOL model, the catalytic activity could be quantified at the single NP level. Furthermore, this methodology is extended to other NP and halo chemistries, revealing the specific enhancement of activity by Ni(OH)₂.

Chapter 5 utilizes a different microscope configuration to investigate the charge and discharge processes occurring in aqueous Zn-MnO₂ batteries. The electrodeposition/dissolution of MnO₂ is shown to serve as the primary pathway for charge storage. Through an optical model and complementary *ex situ* characterizations of the MnO₂ electrode, the precipitation of zinc hydroxide sulfate (ZHS) is detected at a much earlier stage of discharge than in previous

reports. The crucial role of ZHS as a local pH buffer is further confirmed on charge, as higher deposition rates are observed around ZHS particles.

In **Chapter 6**, a combined scanning electrochemical microscopy (SECM) and IRM approach is introduced to investigate ion transport within polycrystalline copper hexacyanoferrate microparticles utilized as solid boosters in redox flow batteries. In these systems, the conversion of the solid material is achieved through a redox mediator. The ultramicroelectrode (UME) of the SECM is then employed to initiate the conversion of individual particles by oxidizing the mediator in their vicinity. Additionally, it serves as an optical mirror, reflecting light back through the particle towards the objective. This enables simultaneous and localized assessment of the particle's state-of-charge based on its absorbance, despite operating in reflection mode. This approach reveals the importance of transport within the pores of the particles.

Apart from the aforementioned projects, I have also participated in other projects during my PhD, mainly in the framework of collaborations, which will only be briefly mentioned herein. In collaboration with the group of Jean-Marie Tarascon at Collège de France, we have investigated the expansion and contraction of lithium cobalt oxide microparticles during (de)lithiation using 3D optical imaging.^[2] Additionally, we also studied the (de)lithiation dynamics within electrochromic $\text{Li}_2\text{Ni}_2\text{W}_2\text{O}_9$ microparticles.^[3] In collaboration with the group of Damien Alloyeau at Université Paris Cité, we attempted to adapt the methodology presented in **Chapter 4** to *in situ* transmission electron microscopy (TEM), as this technique is equally unable to detect dissolved gaseous reaction products. Furthermore, in collaboration with the group of Julie McPherson at Warwick University, we made significant progress in automating the analysis of identical-location TEM images to quantify catalyst degradation during accelerated stress tests.

Another project I worked on involved studying the electrochemistry of NPs located at the outer edge of droplet cells. Despite not appearing to be connected to the electrochemical cell, some of these NPs exhibited intensity fluctuations in correspondence to the applied potential program. It was later discovered that nanometric electrolyte channels connected these NPs to the electrochemical cell, feeding them with water and ions to maintain the charge balance while they catalysed oxygen reduction.

Chapter 1 SOCIO-ECONOMIC AND SCIENTIFIC

CONTEXT

In this chapter, the socio-economic and scientific context of my PhD will be presented in more detail. The latter will emphasize the importance of developing single nanoparticle approaches for the electrochemical characterization of electrocatalysts and battery materials, which is the ultimate goal of my PhD. Afterwards, the main findings of this field of research will be reviewed.

1.1 SOCIO-ECONOMIC CONTEXT

1.1.1 THE DUCK CURVE

The sixth assessment report published in 2022 by the International Panel for Climate Change (IPCC), the United Nations (UN) body for assessing the science related to climate change, again emphasized the adverse impacts of anthropogenic greenhouse gas emissions on ecosystems and people.^[4] Following the publication of this report, the European Union (EU) decided to make reaching its goal of reducing emissions by at least 55% by 2030 a legal obligation.^[5] Among other political levers like toughening CO₂ emission standards for cars, the so-called “Fit for 55” package also contains plans to boost renewable energy and deploy infrastructure for alternative fuels (e.g., recharging points and refuelling points for hydrogen and liquified methane).

However, increasing the share of renewable energy is not without problems. Wind and solar power, which are the most common renewables, happen to be intermittent, meaning that they only produce (convert) energy during specific/limited periods of time. A solar panel, for example, only produces electricity when the sun is shining (and not always with the same efficiency depending on the panel’s orientation and the season). This is problematic as electricity production must always match electricity demand, while demand peaks at around 7 pm in France (in winter),^[6] precisely when no/less sun is shining. Hence, increasing the share of renewable energy in the total energy mix requires significant energy storage capacities in

order to store energy when it is produced in excess, and restore it when the production curve falls below the demand curve. In the case of solar power, the difference between these two curves is known as the “duck curve” because of its shape resembling a duck. An example of such curve is given in Figure 1-1, illustrating the mismatch between solar power production and electricity demand in California. Otherwise, one could also rely on dispatchable energy sources, which can be programmed on demand, to compensate for this mismatch. However, apart from hydroelectric and geothermal energy which cannot be deployed everywhere, there are no renewable and dispatchable options. In this respect, nuclear energy experiences a renewed interest as low-carbon – yet not renewable – and dispatchable energy source.^[7]

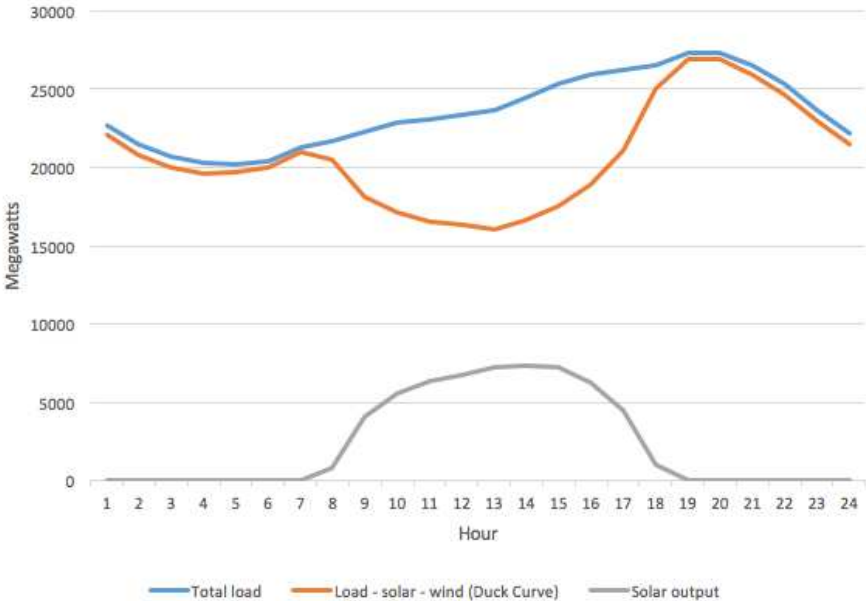


Figure 1-1. Graph of California’s hourly electric load (blue) vs load less solar and wind (duck curve, orange) along with solar power output (grey). Data is from <http://www.caiso.com/market/Pages/ReportsBulletins/DailyRenewablesWatch.aspx> and is for October 22, 2016, a day when the wind output was low and steady throughout the day. Reprinted from https://en.wikipedia.org/wiki/Duck_curve under the terms of the CC BY-SA 4.0 licence.

1.1.2 WHAT KIND OF ENERGY STORAGE FOR GRID-SCALE APPLICATIONS?

Energy can be stored in many different ways. It can for example be stored as potential energy in dams or gravity batteries,^[8] but most energy is stored in chemical batteries (e.g., Li-ion batteries, LIBs) or chemical fuels (e.g., hydrogen). Given the maturity of the Li-ion technology,

it was naturally the first one to be considered for grid-scale applications. However, LIBs have three main disadvantages in this context:

- Scarcity: With the electrification of the automobile industry (the EU banned the sale of new petrol and diesel cars from 2035),^[9] Li demand is expected to sextuple by 2030.^[10] Li production would then probably not be enough to satisfy both the needs of the automobile industry and of the energy suppliers, not to mention those of the portable electronics industry. In addition, this competition would make the price of Li increase even more.
- Geopolitics: As shown in Figure 1-2, only a few countries in the world possess Li deposits, making most European countries dependent on China and Australia.
- Hazard: Being composed of organic electrolytes, LIBs are susceptible to fire, as demonstrated by the great number of battery fires reported every day. While cell phone or car batteries might not cause severe damages, large-scale storage systems could potentially be very dangerous. In 2021, a 300 MW Tesla plant caught on fire in Australia and caused the lock-down of the entire neighbourhood because of the toxic fumes emanating from the fire.^[11]

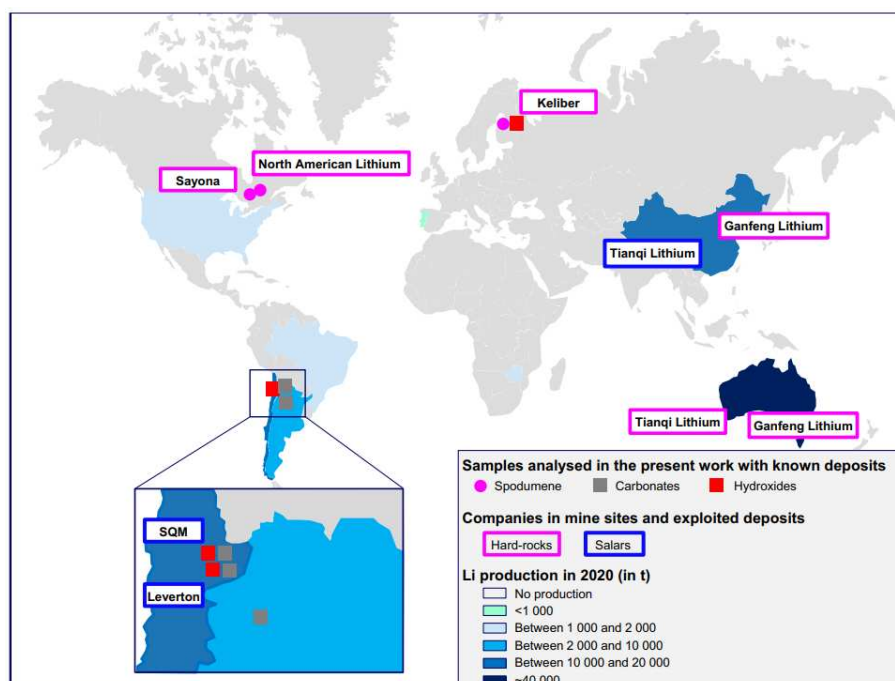


Figure 1-2. Map of world Li production in 2020 and location of the major Li mining and refining companies. Reprinted from ref. ^[12] under the terms of the CC BY 4.0 licence.

For these three reasons, aqueous battery technologies using other host cations than Li^+ are starting to emerge. While they could never compete with LIBs in portable electronic devices because of their much lower gravimetric capacity, some of them are still interesting candidates for grid-scale applications due to their inherent safety and higher stability (long-term storage). Mass or volume are not as critical when building large-scale storage systems compared to cell phone batteries, for example. Among these emerging technologies, the most promising ones are probably the aqueous rechargeable Zn-MnO₂ battery (which will be discussed in detail in **Chapter 5**) and the metal-air battery (e.g., Zn-air or Fe-air battery).

Storing energy in chemical fuels could also be a viable alternative to LIBs. Hydrogen, for example, which is obtained by the electrolysis of water, is an interesting candidate. Even though its production (electrolyser) and back-conversion into electricity (fuel cell) are not very efficient and generate high power losses, hydrogen has the unique advantage of offering the possibility to be used directly as a fuel in transportation, for example. This amount of energy would then not be subtracted from the grid, lowering electricity demand and hence also flattening the duck curve.

1.2 SCIENTIFIC CONTEXT: ELECTROCATALYSIS GOES NUTS

To convert energy (e.g., electricity, light or thermal energy) into chemical fuels and vice versa, catalysts are often required. Broadly speaking, a catalyst is a substance that enables a chemical reaction to proceed at a faster rate. Some reactions might not occur at all without the help of a catalyst. If the catalyst and the molecule of interest (substrate) are in the same phase, we talk about homogeneous catalysis. Otherwise, we talk about heterogeneous catalysis and the reaction occurs only at the surface of the (usually solid) catalyst. For most industrial processes, heterogeneous catalysis is preferred because of the higher stability of the catalysts and the easier separation of the products. However, the reaction rate is then strongly dependent on the surface area of the catalyst. In order to achieve high surface areas, nanoparticles (NPs) or nanostructured surfaces are increasingly used because of their inherently high surface-to-volume ratio. This is particularly interesting in the case of water splitting as the best performing catalysts (e.g., Pt and IrO₂) are very scarce and expensive; in addition to providing larger surface areas and enhanced mass transport, optimizing the volume of catalyst also

significantly drops costs. To drop costs even more, intensive research efforts have recently been devoted to the discovery of new precious metal-free catalyst nanomaterials. Over the years, increasingly complex materials have been proposed, challenging our ways of studying them.

Although several studies have claimed to obtain better performances than Pt for the hydrogen evolution reaction (HER), it is interesting to note that companies have not yet shifted from classical Ni plates or carbon-supported Pt NPs. This has to do with:

- The cost of these new materials. Multi-step syntheses of complex (e.g., core-shell) nanostructures are usually very expensive (even if the raw materials not necessarily are, they require a lot of manpower) and difficult to scale up (developing a new industrial synthesis process can take several years).
- How performance is defined and evaluated.

Indeed, many studies rely on the overpotential measured by linear sweep voltammetry (LSV) to demonstrate the superiority of their catalyst. However, as recently shown for a random example catalyst, this parameter has little meaning by itself since the cell voltage can increase dramatically over time under constant current operation.^[13] Through this experiment presented in Figure 1-3, the author wanted to emphasize the necessity to evaluate the long-term stability of a catalyst in realistic conditions to make research relevant for industry. For a catalyst to be cost-effective, it should operate for at least thousands of hours, while lab-scale experiments are usually carried out over the course of a few hours only.

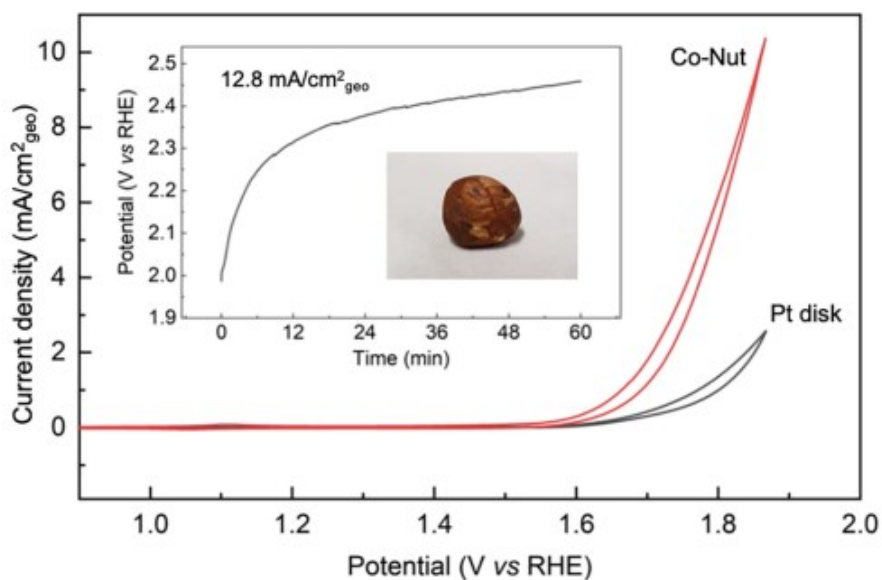


Figure 1-3. Cyclic voltammetry (CV) and chronopotentiometry (CP, inset) of a Co-“impregnated” hazelnut-derived electrode measured with a rotating disk electrode (RDE). The response of the bare Pt RDE is shown for comparison. Reprinted with permission from ref. ^[13]. Copyright 2022 American Chemical Society.

Another issue arises from the way electrodes are prepared in the first place. To test the activity of a newly synthesized nanocatalyst, it is usually mixed with carbon powder and polymers, and pasted on a current collector (ideally inert for the reaction of interest or at least much less active than the catalyst). The whole forms the electrode that is subjected to electrochemical testing. The carbon powder ensures a good electronic conductivity throughout the catalytic film and the polymer a good adhesion of the latter to the current collector. This is especially important when the reaction of interest is a gas evolution reaction like the HER or the oxygen evolution reaction (OER). The high mechanical stress induced by the formation of gas bubbles within the film could lead to partial or complete detachment from the current collector. Despite being useful at the device level, these additives make it difficult to unravel the intrinsic activity of the nanocatalyst and thus to compare it to others. This is because of the enormous diversity of active sites, nonuniform electrical conductivity, and the poorly defined mass transport within the film. This would not be such a major issue if researchers and industry had agreed on standardized testing protocols. But unlike in the field of batteries, where such testing protocols have been introduced early on to accelerate knowledge transfer, researchers

are still reluctant to change their habits. This applies both to the preparation of the electrodes and to their characterization.

For Akbashev, the field's current situation has to do with the high reward given to publications lacking scientific rigour. To increase the scientific meaningfulness of the reported data, journals should ask for precise metrics when new materials are proposed for publication. Nature Research (formerly Nature Publishing Group) has already started to implement this in the field of photovoltaics, for example, but not yet in the field of electrocatalysis.

1.3 SINGLE-NANOPARTICLE APPROACHES

Another way to avoid these heterogeneities is to minimize the complexity of the electrode to the point of isolating individual NPs. Even if the field of batteries is more standardized and less subjected to the issues presented above, investigating single particles in battery electrodes is still interesting from a fundamental point of view since microscopic behaviours can have an influence on macroscale performance.^[2,14] Over the past twenty years, several approaches have been proposed to probe the electrochemical behaviour of single NPs. To be probed individually, the NPs need to be separated. This can be done either in time or in space, thus defining two categories of techniques. In the following, each technique will be briefly presented and major findings in the context of energy storage and conversion will be reviewed. Optical microscopy (OM) approaches, which are central to this thesis, will be treated at the end in a separate section.

1.3.1 SEPARATING THE NPs IN TIME: NANO-IMPACT ELECTROCHEMISTRY

This category only counts one member: nano-impact electrochemistry (NIE). First proposed by Bard in 2007^[15] and further popularized by Compton,^[16] this technique is based on the stochastic collision of suspended NPs at a polarized ultramicroelectrode (UME). As schematized in Figure 1-4, depending on the nature of the NPs, the electrolyte and the applied potential, the NPs will either perturb the diffusion layer of the UME (blocking impacts, A), catalyse a reaction at their surface (electrocatalytic amplification, B), or be transformed upon

contacting the UME (transformative impacts, C). Each of these processes will produce a distinctive current spike on the measured chronoamperogram (CA) from which the size of the NP and the charge transfer/diffusion kinetics of the process can be extracted.^[17,18]

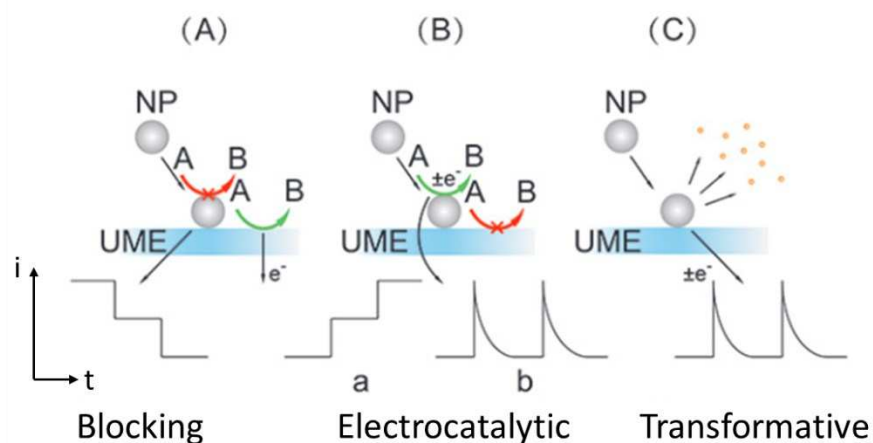


Figure 1-4. Typical nano-impact types: (A) blocking impact, (B) electrocatalytic amplification, and (C) transformative impact. Adapted with permission from ref. ^[17]. Copyright 2017 Wiley-VCH Verlag GmbH & Co. KGaA, Weinheim.

1.3.1.1 BLOCKING IMPACTS

Blocking impacts are measured when insulating NPs hit the UME while a soluble redox probe is being converted at the UME. Once at the surface of the UME, the insulating NPs block part of its electrochemically active surface area, leading to a current drop which is proportional to the size of the NPs. Using blocking impacts, Dick *et al.*^[19] could for example size single biomacromolecules (antibodies, enzymes, and DNA) down to 2 nm. However, given that only insulating materials can be probed in this way, blocking impacts were not applied in the context of energy storage and conversion.

1.3.1.2 ELECTROCATALYTIC AMPLIFICATION

As mentioned before, electrocatalytic amplification was the first kind of nano-impact to be reported by Bard in 2007.^[15] The idea was to use a reporter reaction (H^+ or H_2O_2 reduction) to detect the collision of single 4-nm sized Pt NPs on an inert detector electrode (C UME). Once at the surface of the UME, the Pt NPs would catalyse the reporter reaction and produce a

current step (or rectangle depending on whether the NP sticks or bounces off, as in the case of blocking impacts) on the measured CA (Figure 1-5A,B). More than just allowing to detect a NP, this current step is indicative of its size, its residence time on the electrode surface and hence of the nature of the NP-electrode surface interaction. As demonstrated for the oxidation of N_2H_4 on Pt NPs, the NP concentration and diffusion coefficient can also be estimated from the frequency of impacts.^[20]

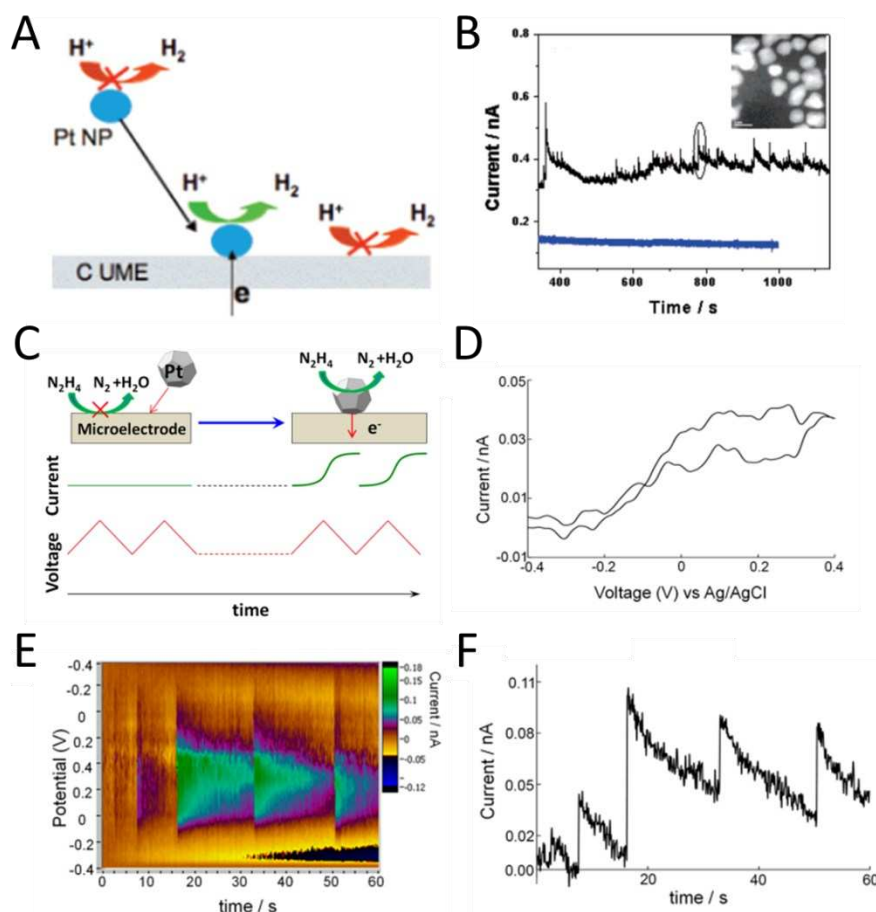


Figure 1-5. (A) Schematic of a single Pt NP collision event: the NP diffuses to the electrode, collides, and catalyses H^+ reduction during its residence time. (B) Current spikes measured at a C fibre UME in 50 mM sodium dihydrogen citrate solution in the absence (blue) and presence (black) of 4 nm Pt NPs (≈ 25 pM). Inset: TEM image of the Pt NPs (scale bar: 5 nm). Adapted with permission from ref. ^[15]. Copyright 2007 American Chemical Society. (C) Schematic of the detection of single NP collision events by fast-scan cyclic voltammetry (FSCV). (D) Background-subtracted CV showing the faradaic response of a 4 nm Pt NP for N_2H_4 oxidation. (E) FSCV recording at $v = 400$ $V s^{-1}$ showing the detection of 5 Pt NPs on a $5 \mu m$ C UME in 15 mM N_2H_4 . (F) Current–time trace taken from E at +0.1 V vs Ag/AgCl

showing the progressive deactivation of the NPs once they land on the UME. Adapted with permission from ref. ^[21]. Copyright 2014 American Chemical Society.

The first reports on electrocatalytic amplification were mostly focused on the analysis of the NPs themselves and their interaction with the electrode surface. Using the same system, Bard later investigated the influence of self-assembled monolayers (SAMs) both on the Au UME and the Pt NPs on the measured current steps.^[22] In the first scenario, the current was shown to decrease as the length of the alkyl chain increased due to the exponential decay of electron transport across the SAM. In the second scenario, the current was shown to decrease as the SAM concentration increased (constant alkyl chain length) due to the blockage of the catalytic surface sites. For IrO_x NPs catalysing water oxidation, the current steps were also shown to be very sensitive to the surface state of the Pt UME used in this case. To obtain reproducible results, the Pt UME had to be treated with NaBH₄ prior to the experiment.^[23]

To further broaden the range of accessible materials, the detection of 14-nm sized Au NPs was also carried out using NaBH₄ oxidation as reporter reaction.^[24] More recently, individual graphene sheets could be detected by labelling them with Fe and Fe/Pt NPs which initiated oxygen reduction (ORR) when they hit the electrode.^[25] Using the same principle, Pd-coated carbon nanotubes (CNTs) could also be detected using hydrogen oxidation (HOR) as reporter reaction. But more than just detecting individual objects, the steady-state current (measured at high overpotentials) associated to single CNTs was here used to determine their length.^[26] N₂H₄ oxidation was also used to probe the aggregation of Pt NPs induced either by increasing the ionic strength of the solution^[27] or simply by the reaction itself.^[28] Aggregation is highlighted by higher current steps and a lower landing frequency as it reduces the effective NP concentration. In the latter case, aggregation was confirmed by electron microscopy, and although the exact origin of this phenomenon remains elusive, it indeed seems to be caused by the reaction since no aggregation was observed in the absence of N₂H₄ or H₂.

It is only starting from 2012 that researchers tried to get more insight into the catalytic reaction. That year, Compton^[29] described an experimental protocol to determine the electron transfer kinetics at single NPs which consists in measuring impacts at different potentials (multi-step CA or CV at low scan rate)^[26] and reconstructing a CV from the mean current values. Comparing this CV to simulations as usual then gives access to the electron

transfer rate constant. This method was demonstrated for the reduction of H^+ at single Au and Ag NPs of radii 7-15 nm, highlighting a kinetic acceleration at smaller sizes (or “nano effect”) for Ag NPs but not for Au NPs. It also allowed to determine the adsorption rate constant of H_2 on Pt NPs, which turned out to be different from that measured for drop-casted NPs using classical CV.^[30] Probably because of aggregation on the surface, this study shows that such parameters can only be assessed correctly by measuring individual NPs.

Later, Zhang^[21,31] proposed a method based on fast-scan CV (FSCV) to capture the transient voltametric response of single Pt NPs for N_2H_4 oxidation as they collide with the electrode (Figure 1-5C,D). One advantage of this method is that by measuring several consecutive cycles on the same NP, its deactivation (decrease in peak current and increase in overpotential) upon cycling can also be probed as shown in Figure 1-5E,F. Given that the residence time of a NP on the electrode surface is in the order of 10 ms, scan rates in the order of 100 V s^{-1} have to be used for such experiments. While this is until now the only purely nano-impact-based approach that allows to determine the electron transfer rate constant truly at the single-NP level, the high scan rates required make it difficult to implement. Another way to assess the CV of a single NP is to use a pipette to deliver and then address a single NP on a surface.^[32] The advantage of this approach is that any kind of electrode material can be used (not all can be built as UMEs) and that the electrochemical experiments can therefore readily be combined for example with transmission electron microscopy (TEM) since they can be performed directly on a TEM grid. This approach was demonstrated for Au NPs catalysing N_2H_4 oxidation. Pipette-based approaches to single-NP electrochemistry will be discussed in more detail below in *Scanning electrochemical probe microscopies*, section 1.3.2.1.

More recently, Tschulik obtained interesting results on OER catalysts.^[33–35] In the case of Co_3O_4 nanocubes (NCs), they showed that using Pt UMEs instead of C UMEs promoted the formation of a highly active phase on the NCs’ surface.^[35] By investigating different NP morphologies (NC and nanosphere, NS) exhibiting different crystal facets ((001) and mostly (111), respectively), they also rationalized the facet-dependent activity of this material.^[34] In the case of 4-nm sized $CoFe_2O_4$ spinel NPs, the authors determined that the reaction was not limited by the diffusion of the reactant (HO^-) towards the NPs as it is usually the case, but by the diffusion of the product (O_2) away from them. Moreover, single-NP turnover frequencies (TOFs) determined from the current steps turned out orders of magnitude larger than TOFs reported for state-of-

the-art OER catalysts as supported NP films.^[33] The same observation was made by Long in the case of Au NP-based enzyme mimetics^[36] and Pd NPs catalysing H⁺ reduction.^[37] They also found high TOFs for the oxidation of nicotinamide adenine dinucleotide (NADH) at catechol modified Au NPs^[38] and for the oxidation of N₂H₄ at pyrroloquinoline quinone (PQQ)-modified multi-walled CNTs,^[39] demonstrating at the same time the applicability of NIE to molecular electrocatalytic systems.

Long also investigated the size-dependent catalytic activity of Au NPs for the reduction of polysulfide electrolyte,^[40] which is a key reaction in Li-S batteries.

1.3.1.3 TRANSFORMATIVE IMPACTS

Transformative impacts are measured when the NPs undergo an electrochemical conversion (e.g., dissolution) at the microelectrode. As shown in Figure 1-4C, their current trace is characterized by an exponential decay whose time constant is indicative of the charge transfer/diffusion kinetics. Transformative impacts were extensively used to study the oxidation of Ag NPs,^[41] but much less in the fields of batteries^[14] and electrocatalysis. In 2017, Zampardi *et al.*^[42] demonstrated for the first time that battery materials (in this case, 200-nm sized LiMn₂O₄ NPs) could be studied by NIE. Their study revealed that the rate-determining step of the delithiation reaction at high overpotentials was the ion transfer across the particle-electrolyte interface, setting a theoretical upper limit for the discharge rate of batteries using LiMn₂O₄ in an aqueous environment. By comparing classical CV experiments on composite electrodes to NIE in the case of K⁺ deinsertion from Prussian blue (PB) NPs, they later showed that the intrinsic behaviour of the PB NPs significantly differed from that of the composite electrode, again stressing the importance of developing single-NP approaches.^[43] In aqueous media, NIE was also successfully applied to LiCoO₂^[44] and LiFePO₄ NPs.^[45] In all cases, the rate-determining step of the delithiation reaction was determined to be ion diffusion inside the particle. Interestingly, Löffler *et al.*^[46] demonstrated that in a nonaqueous LIB electrolyte, the intrinsic lithiation rate of individual TiO₂ particles was not determined by the ion transfer kinetics or bulk diffusivity, but rather by solid-solid electron transfer. In nonaqueous media, NIE was also successfully applied to Na-ion battery materials. Xu *et al.*^[47] demonstrated that

contrary to what had been reported for the bulk materials, the internal Na⁺ diffusion within single particles of layered metal oxides depended on their crystal phase.

More recently, nano-impacts were also used to generate nanocatalysts from the content of micelles. Precursors can indeed be encapsulated in water nanodroplets dispersed in an organic phase and reduced upon impacting an electrode to form a metallic NP. Evers *et al.*^[48] utilized this strategy to deposit Au NPs on a C fibre which showed excellent ORR activity for a minimal Au loading. In the same way, Glasscott *et al.*^[49] generated tailored high entropy alloy NPs by loading micelles with several different precursors.

1.3.1.4 COMBINATIONS

Although the electrocatalytic counterparts of the reactivity of individual NPs seem more relevant to study, transformative impacts provide interesting insights into the initial transformation step of electrocatalysts which are still poorly understood.^[50] By carefully analysing the oxidative current spikes associated to the collision of single Ni(OH)₂ NPs on a C UME, Miranda Vieira *et al.*^[51] managed to deconvolute the contributions of Ni(OH)₂-to-NiOOH conversion (H⁺ deinsertion) and OER catalysis at the single-NP level (Figure 1-6A,B). This allowed to establish the size-activity relationship of these NPs at high throughput (Figure 1-6C), but also improved the understanding of this initial transformation step by providing a solid-state diffusion coefficient of H⁺ inside Ni(OH)₂. A similar approach had been proposed by Compton in the case of HOR and HER on mesoporous Pt NPs.^[52-54] Only for these peculiar Pt NPs sold by the company Nanocompositix, a current peak attributed to H adsorption or desorption was detected before the catalytic current plateau,^[52] which revealed a higher electrochemically active surface area than expected for spherical NPs.^[53,55] By studying different NP sizes, they confirmed that the internal surface also contributed to the catalytic activity as the electron transfer rate constant scaled with NP size to the power of 2.6-2.9 > 2.^[54] However, since this peak was also observed at higher potentials where H adsorption should not occur, it was later argued that it might have a capacitive contribution.^[56]

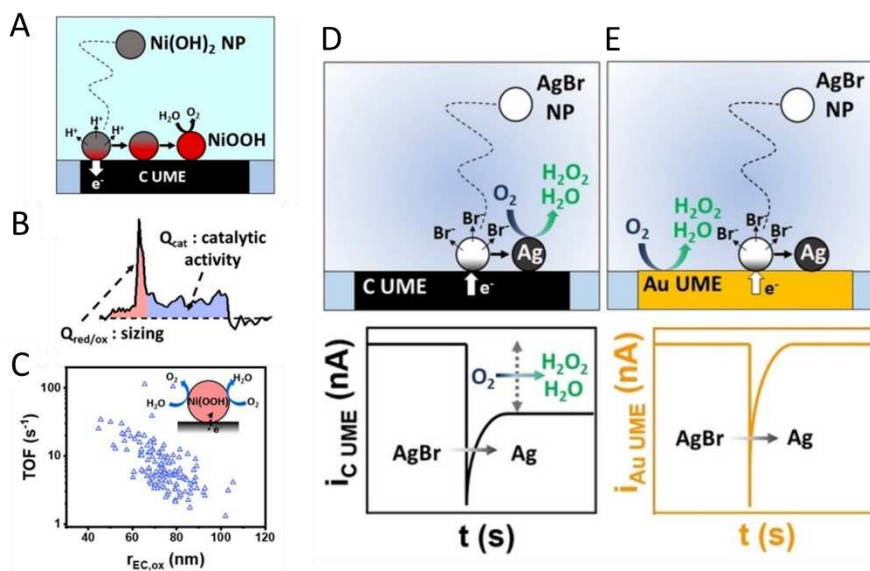


Figure 1-6. (A) Mechanism proposed for the oxidative impacts of Ni(OH)₂ NPs: conversion to NiOOH followed by ORR. (B) Analysis of an individual current spike. (C) TOF of individual Ni(OH)₂ NPs as a function of their electrochemical radius $r_{EC,ox}$. Adapted with permission from ref. [51]. Copyright 2022 American Chemical Society. Mechanism occurring during the reductive impacts of AgBr NPs at (D) a C UME and E an Au UME. Reprinted with permission from ref. [57]. Copyright 2022 Wiley-VCH GmbH.

To achieve the deconvolution of transformation and electrocatalysis (this time, statistically), one can also change the electrode material or simply probe the NPs at different potentials. The first approach was proposed by Kostopoulos *et al.* [57] to investigate the reduction of AgCl NPs to Ag NPs followed by the ORR on the freshly formed Ag NPs. As shown in Figure 1-6D, if the electrode is inert to the electrocatalytic reaction, the initial transformative current spike will be followed by an electrocatalytic current plateau like in the previous cases. But if the electrode is also active as in Figure 1-6E, it will deplete the reactant so that when the NP hits the electrode, only a transformative current spike will be measured. The second approach was proposed by Pumera for transition metal dichalcogenide (TMD) NPs. Oxidative spikes – which were attributed to the conversion of the NPs ($M^{4+} \rightarrow M^{6+}$) – were used to size the NPs, and reductive spikes – which were attributed to the HER – were used to evaluate their catalytic activity. Since the impact frequency was the same in both scenarios, the authors could conclude that all NPs which were oxidizable were also catalysing the HER. [58]

1.3.1.5 DISCUSSION

One could wonder why there are so few examples of applications in the field of batteries although interesting results could be obtained, the required instruments are relatively accessible, and the experimental setup is relatively straightforward and easily adaptable to air- and/or moisture-free environments.^[59] This is probably because nano-impact experiments can only be performed in stable dispersions, whereas most commercial battery materials are composed of microparticles (10s of microns, because they are much easier to handle), which are almost impossible to stabilize in suspension. This limits de facto the applicability of NIE to battery materials. For now, LiFePO₄ is the only material which is commercially used in the form of NPs due to its poor electronic conductivity.^[60] Another reason is the relatively slow conversion of battery materials, which flattens the current spike and makes it more challenging to distinguish from the noise.

The stability of the dispersion is also an issue for electrocatalysts: in regular nano-impact experiments, the electrolyte concentration can rarely exceed 10 mM, which is far below standard concentrations for device testing (≈ 1 M). Above a certain concentration, the repulsive coulombic interactions which stabilize the NPs get screened by the counter ions of the electrolyte and the NPs start to aggregate.^[27] While aggregation can tell us a lot about the surface chemistry of NPs,^[61] it hinders the proper characterization of the NPs themselves. To broaden the range of accessible concentrations, Defnet *et al.*^[62] designed a microjet collision system which consists of a micropipette filled with the NPs facing a C fibre UME (10 μm spacing, Figure 1-7A). Using a microinjector, the NPs are ejected from the micropipette towards the microelectrode through the concentrated electrolyte. Thanks to convection, the NPs are not in contact with the concentrated electrolyte long enough to aggregate (Figure 1-7B,C). This method was demonstrated for Pt NPs reducing H⁺ in HClO₄ solutions up to 750 mM.

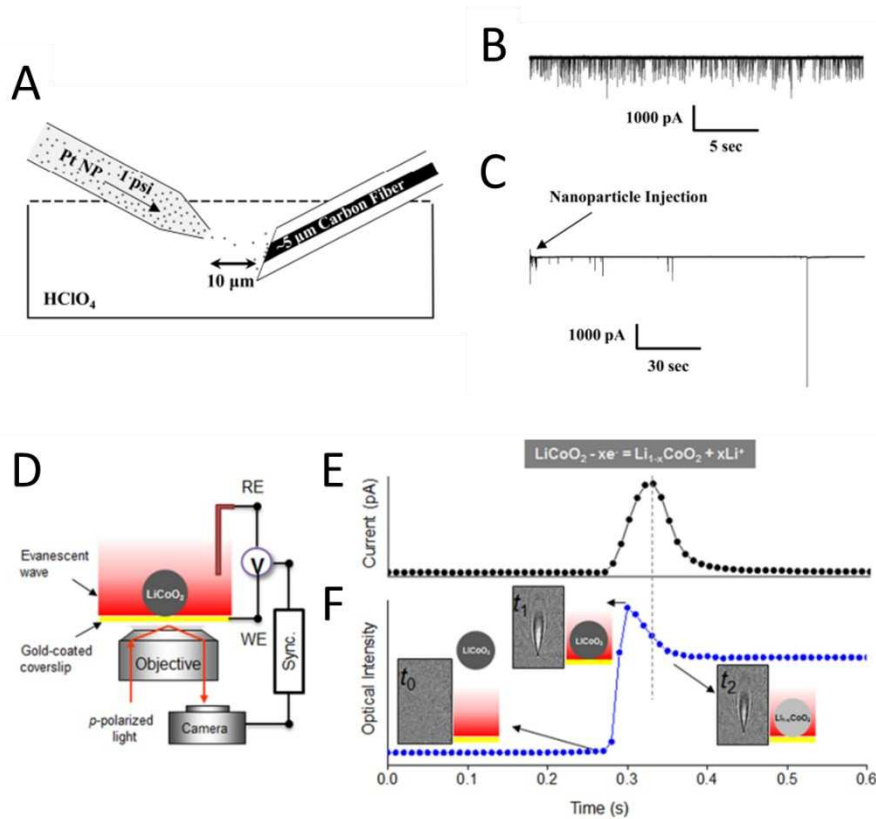


Figure 1-7. (A) Schematic of the microjet collision system. 30 nm Pt NPs are dispensed under 1 PSI pressure through a HClO_4 solution ranging from 5 mM to 3 M and onto a 5 μm C fibre UME. Due to the displacement of the acid, the effective concentration at the electrode surface ranges from 1.25 to 750 mM. (B, C) NP collisions recorded at -400 mV vs Ag/AgCl with and without the microjet system, respectively, in 25 mM HClO_4 (effective concentration). Adapted with permission from ref. [62]. Copyright 2019 American Chemical Society. (D) Schematic of the correlative surface plasmon resonance microscopy (SPRM) imaging and electrochemical recording of single LiCoO_2 NP collision events. (E) Current spike and (F) plasmonic image intensity associated with the extraction of Li^+ ions during the oxidation of a LiCoO_2 NP on an Au UME. Reprinted with permission from ref. [63]. Copyright 2017 American Chemical Society.

Another issue is the residence time of the NP at the electrode surface which limits the accuracy of the current's reading. To improve the collision duration, Long introduced near-wall hindered diffusion by confining the UME and the NPs in a microchannel. This was demonstrated on Pd NPs catalysing the HER.[64] Furthermore, nano-impacts also lack structural information to establish structure-activity relationships. Combining NIE with an OM technique, surface plasmon resonance microscopy (SPRM), as shown in Figure 1-7D, Sun *et al.*[63] could easily attribute individual current spikes to specific collisions and further

characterize the corresponding NPs *in situ* by SPRM or *ex situ* by scanning electron microscopy (SEM), providing a further separation in space of the NPs' electrochemistry (Figure 1-7E,F).

1.3.2 SEPARATING THE NPS IN SPACE

To separate NPs in space, they are usually deposited on surfaces and probed by means of microscopy. Among all microscopy methods that have been employed to investigate the energy storage and electrocatalytic properties of NPs, we can cite scanning electrochemical probe microscopies (SEPMs), *in situ* atomic force microscopy (AFM), scanning tunnelling microscopy (STM), transmission electron microscopy (TEM), scanning transmission X-ray microscopy (STXM), and optical microscopies (OMs) which will be discussed in a separated section.

1.3.2.1 SCANNING ELECTROCHEMICAL PROBE MICROSCOPIES

Scanning electrochemical probe microscopies (SEPMs) are a family of scanning probe microscopies (SPMs, like AFM and STM) that use an electrochemical current (signal) as feedback for topography measurements (constant-current mode) or directly as "height" for activity mappings of flat surfaces (constant-height mode). The most common SEPMs are scanning electrochemical microscopy (SECM), scanning electrochemical cell microscopy (SECCM), and scanning ion conductance microscopy (SICM). While AFM and STM can also be operated in electrochemical conditions, they use other feedback mechanisms. As such, they will be discussed in a separate section.

In SECM, the probe is an UME. It can be operated in different modes, the most common ones being the feedback mode (Figure 1-8A) and the substrate generation-tip collection (SG-TC) mode (Figure 1-8B). In the feedback mode, a redox mediator is continuously converted at the surface of the UME. If the latter is close enough to the substrate so that the diffusion layer interacts with the substrate, the electrical properties of the substrate can be probed as an increase (positive feedback, conductive) or decrease (negative feedback, insulating) of the steady-state current. In the SG-TC mode, the products generated at the substrate are collected at the UME at a larger distance so that no feedback occurs. This mode is particularly relevant

in the context of energy conversion and storage as the local activity can be quantified *operando* from the current measured at the UME.

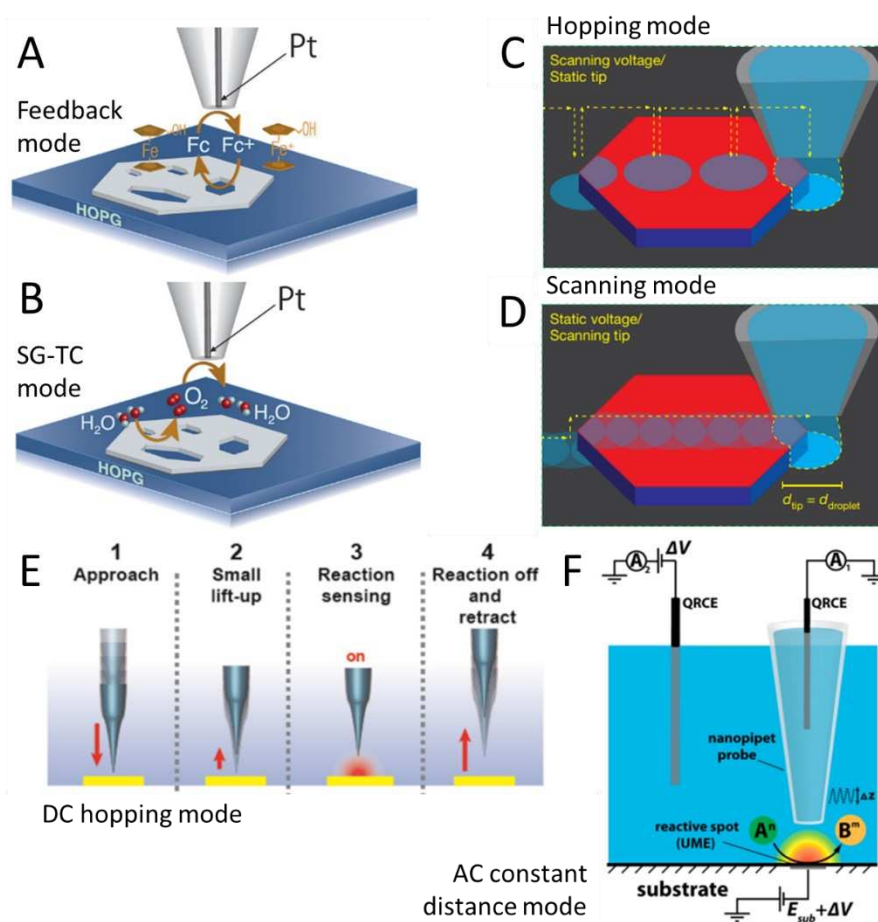


Figure 1-8. SECM Schematic representation of (A) positive feedback produced by the oxidation/reduction of ferrocenemethanol (Fc here) and (B) SG-TC of O_2 generated at a NiO nanosheet. Adapted from ref. [65]. **SECCM** Schematic representation of (C) the scanning mode performed at constant voltage and height, and (D) the hopping mode, in which a CV can be obtained at each point. Adapted with permission from ref. [66]. Copyright 2021 The Author(s), under exclusive licence to Springer Nature Limited. **SICM** (E) Schematics of the main steps of the DC hopping mode imaging procedure. Adapted from ref. [67] under the terms of the CC BY 4.0 licence. (F) Schematic representation of the AC constant distance mode which uses the AC tip current induced by the tip's oscillation as feedback to adjust the tip's height. Adapted with permission from ref. [68]. Copyright 2016 American Chemical Society.

In SECCM, the probe is a pipette containing the electrolyte and the reference/counter electrode. In contrast to SECM, it is generally scanned across a dry surface in a hopping mode

as schematized in Figure 1-8C. Here, the feedback current is the current measured at the substrate when the pipette wets it and closes the electrochemical cell. As each pixel of the mapping corresponds to a unique electrochemical cell, all classical electrochemical methods can be employed in hopping mode SECCM. SECCM can also be operated in the scanning mode at a constant height as shown in Figure 1-8D, but only constant potential experiments can be performed in this configuration like in SECM.

In SICM, the probe is the same as in SECCM. The difference is that the pipette and substrate are immersed in the electrolyte like in SECM. In this configuration, ionic currents flowing through the pipette tip are probed. As depicted in Figure 1-8E,F, it can either be operated in a DC hopping mode or in an AC constant distance mode using the AC tip current induced by the tip's oscillation as feedback.

BATTERIES

SECM has been widely used to study local heterogeneities in battery electrodes, but the lateral resolution in most cases was not high enough to investigate single particles.^[69–72] As for traditional SPMs, the lateral resolution of SEPMs is dictated by the probe's size, and UMEs smaller than a few micrometres are challenging to fabricate. It is only recently that researchers have found ways to reproducibly fabricate nanoelectrodes (NEs, see *Particle-on-a-stick*, section 1.3.2.2). Using 300 nm Pt NEs, Rodriguez-Lopez investigated solid electrolyte interphase (SEI) formation on few-layer graphene by combining feedback images with Li⁺-sensitive images based on Li amalgamation into Hg-modified electrodes.^[73] The feedback images (Figure 1-9A) revealed local changes in conductivity while the Li⁺-sensitive images (Figure 1-9B) revealed the importance of ionic channels in enabling Li⁺ intercalation through the SEI.^[74,75] The Li⁺-sensitive images are obtained by integrating the Li(Hg) stripping peak of CVs performed at each position of the UME.

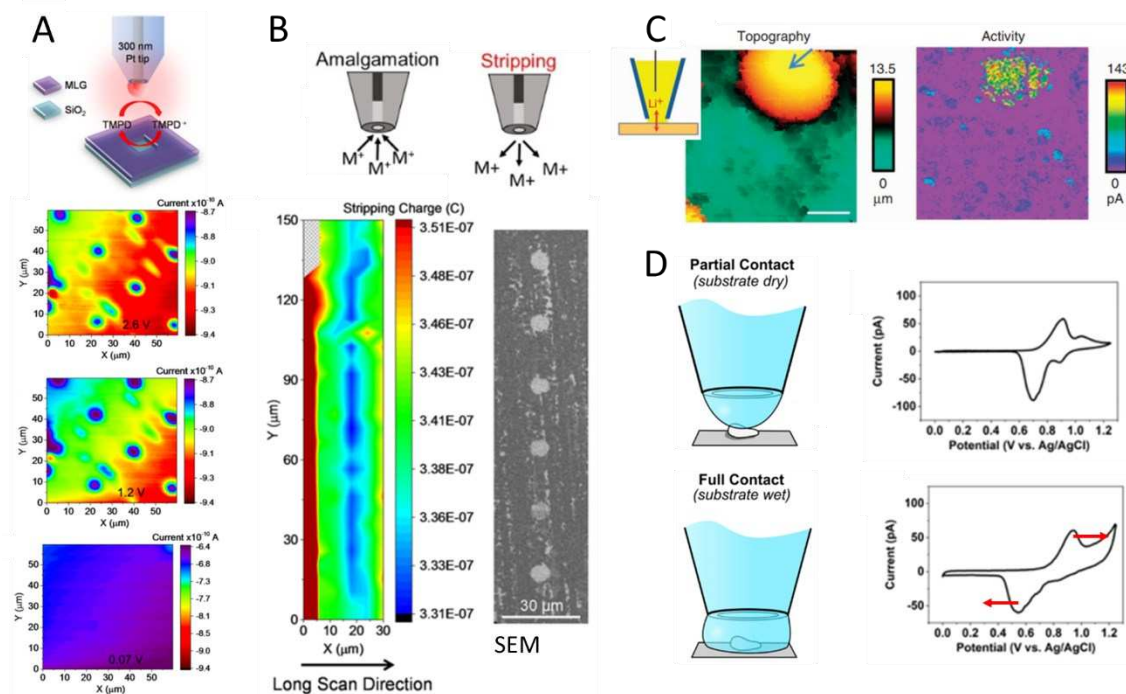


Figure 1-9. (A) Series of SECM feedback images at various substrate potentials of a patterned monolayer graphene (MLG) substrate using N,N,N',N'-tetramethyl *p*-phenylenediamine (TMPD) as redox mediator. The current changes reflect changes in substrate kinetics following SEI formation. (B) CV-SECM image of the sample after SEI formation (left). The substrate is biased at 0.07 V to intercalate Li^+ and CVs are taken at each position at 25 V/s to measure the local Li^+ concentration from the Li stripping charge. The blue areas represent areas of lower Li^+ concentration i.e., of larger Li^+ flux towards the substrate. Their location matches with the patterned ionic channels designed for improving Li^+ insertion (right). Adapted with permission from refs. [74,75]. Copyright 2016 American Chemical Society and 2022 Wiley-VCH GmbH. (C) Simultaneous SECCM topography (left) and current (right) images associated to Li^+ deintercalation from a LiFePO_4 electrode at 0.65 V vs Ag/AgCl in aqueous 3 M LiCl (scale bar: 5 μm). Adapted from ref. [76]. Copyright 2014, Nature Publishing Group. (D) CVs from representative single LiMn_2O_4 NPs supported on glassy carbon (GC) with different extents of meniscus contact ($v = 1$ V/s, $d_{\text{tip}} = 2$ μm , electrolyte: aqueous 1 M LiCl). Adapted from ref. [77] under the terms of the CC BY 4.0 licence.

Despite NEs getting more readily available, reducing the probe's size raises another issue: the smaller the UME, the closer to the surface it needs to be in order to "feel" it. This is an issue because SECM mappings are usually performed at a constant height, while real battery electrodes have rough surfaces. To circumvent this issue, AFM-SECM setups operating in the intermittent contact mode have recently been introduced.[78] Using a Pt NE mounted on an

AFM cantilever, Mahankali *et al.*^[79,80] investigated the chemistry of Li₂S particles during operation of a Li-S battery. The nanoscale lateral resolution they achieved with this setup revealed two distinct behaviours within the same particle upon oxidation: the conductive part of the particle underwent dissolution, while the insulating part chemically reacted with the generated intermediate polysulfide species.

SECCM was also successfully applied in battery research. Nanoscale lateral resolutions can more readily be achieved in this configuration as pipettes are much easier to miniaturize than UMEs, and the hopping mode of SECCM de facto avoids any issues related to surface roughness (it even allows to record the topography simultaneously, which is not possible in classical SECM). Moreover, an SECCM setup was recently installed in an Ar-filled glovebox, allowing for the investigation of LIB electrodes in industrially relevant nonaqueous electrolytes.^[81]

Takahashi *et al.*^[76] were the first ones to investigate the local redox activity of composite battery electrodes (in this case, LiFePO₄ electrodes) at the nanoscale using SECCM (Figure 1-9C). Their investigation revealed variations in reaction rate depending on the local composition of the electrode, but most importantly showed that the reaction was mostly limited to the region enclosed by the pipette, thereby demonstrating the relevance of SECCM measurements in this context. After this pioneering work, researchers focused more on isolated NPs to access their intrinsic properties which might otherwise be obscured by matrix effects. On the same material, Schougaard and Mauzeroll studied the heterogeneity between groups of isolated NPs as a shift in the oxidation and reduction potentials.^[82,83] At the same time, they extended the possibilities of SECCM by introducing organic solvents and ionic liquids, which allow investigating high-energy cathode materials. Using smaller pipettes, Unwin went one step further and probed the redox activity of individual LiMn₂O₄ NPs and correlated the results to SEM.^[84] Surprisingly, morphologically similar NPs exhibited a wide range of activities. They later demonstrated that this could partly be rooted in the heterogeneous contacts between the substrate and the meniscus cell.^[77] As depicted in Figure 1-9D, a finer control over the meniscus cell position allowed to tune the particle/substrate electrolyte wetting, which was found to have a great impact on the peak separation. Nevertheless, the NPs were only partially converted in each case because of the high cycling rates ($\approx 200\text{C}$).

SECCM was also used to study thin-film electrodes at the nanoscale. By correlating the morphology and electrochemical properties of ZrO_2 -coated LiCoO_2 , Inomata *et al.*^[85] showed that the inhomogeneous island-like current responses they obtained corresponded to areas with different coating thicknesses. As a proof of concept for the SECCM setup placed in an Ar-filled glovebox, Takahashi *et al.*^[81] investigated the facet-dependent diffusion coefficient of $\text{Li}_4\text{Ti}_5\text{O}_{12}$ on a thin-film electrode.

SICM is also a powerful technique to study both the topography and electrochemistry of battery electrodes at the nanoscale. On Sn electrodes, it provided a nanoscale picture of the electrolyte's catalytic decomposition to form a SEI.^[86] Later, like in the work of Inomata *et al.*,^[85] the impact of atomic layer deposition (ALD)-deposited Al_2O_3 films on SEI formation on MnO electrodes was investigated.^[87] It was shown that a minimum Al_2O_3 thickness is needed to prevent thick SEI formation.

ELECTROCATALYSIS

SECM is the most explored SPEM for the investigation of complex electrocatalytic mechanisms (detection of intermediate species) and local electrocatalytic activity.^[88–90] However, as discussed above in the case of batteries, nanoscale lateral resolution could only be reached recently with the improvement of NE fabrication methods. In 2014, Sun *et al.*^[91] mapped the HER activity of single Au NPs (10 to 20 nm) using extremely small NEs (≥ 3 nm), significantly improving the lateral resolution compared to previously reported electrochemical images. Later, the HOR activity of individual Pt NPs was investigated in the same way by Kim *et al.*^[92] In both cases, two different redox mediators were used to differentiate between the topography (in the feedback mode, Figure 1-10A-C) and the catalytic activity (in the SG-TC mode, Figure 1-10D-F) of the NPs: an outer-sphere redox mediator (ferrocene derivative) was used to determine the topography, and an inner-sphere redox mediator (H^+/H_2) was used to determine the catalytic activity (a larger tip was also used in this case to improve the collection efficiency as shown in Figure 1-10D).

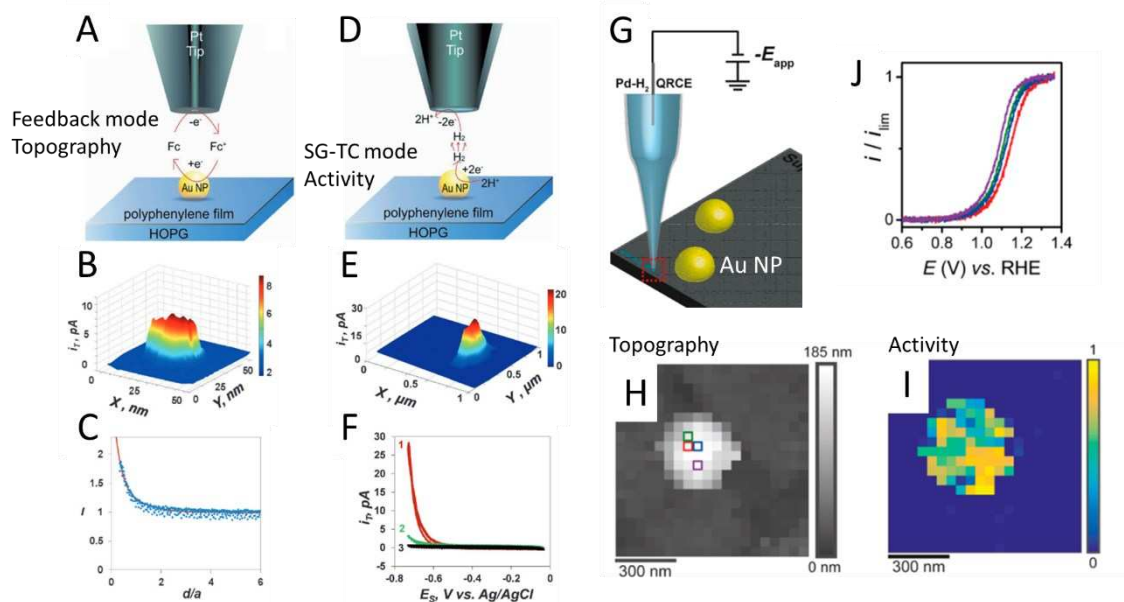


Figure 1-10. (A) Schematic of the feedback mode used to probe the topography of single Au NPs. (B) Feedback image of a 20 nm Au NP deposited on a highly oriented pyrolytic graphite (HOPG)/polyphenylene substrate obtained with a 14 nm-radius Pt tip. (C) Current–distance curve of the tip approaching the Au NP. The solution contained 1 mM ferrocenemethanol (FcMeOH) and 0.1 M KCl. $E_T = 400$ mV vs Ag/AgCl, unbiased substrate. (D) Schematic of the SG-TC mode used to probe the HER activity of single Au NPs. (E) SG-TC image of the HER at a 20 nm Au NP obtained with a 15 nm-radius Pt tip. $E_T = 500$ mV, $E_S = -750$ mV. (F) Tip/substrate CVs obtained with a 60 nm-radius Pt tip by scanning E_S at different E_T : 500 (1), 400 (2), and 100 mV (3). The solution contained 10 mM HClO₄ and 0.1 M NaClO₄ and the potential sweep rate was 100 mV/s. Adapted with permission from ref. ^[91]. Copyright 2014 WILEY-VCH Verlag GmbH & Co. KGaA, Weinheim. (G) Schematic of the voltametric hopping mode of SECCM used to probe the electrocatalytic activity of single Au NPs. (H) Topographical and (I) normalized current map (for $E_{app} = 1.15$ V vs RHE) associated to the electrocatalytic oxidation of N₂H₅⁺ on a single Au NP. The nanopipette probe ($d_{tip} \approx 30$ nm) contained 12.3 mM (N₂H₅)HSO₄ and 100 mM HClO₄. (J) Normalized LSVs collected at the individual pixels labelled in H ($v = 1$ V/s). Adapted from ref. ^[93] under the terms of the CC BY 4.0 licence.

The same principle was then applied to investigate edges and defects in 2D nanomaterials (Figure 1-8A,B). Sun *et al.*^[65] mapped the OER activity of semi-2D NiO nanosheets with 15 nm spatial resolution and showed that the less coordinated edges of the nanosheets were ≈ 200 times more active than the fully coordinated basal planes. The same observation was made for 2H-MoS₂ nanosheets, whereas 1T-MoS₂ nanosheets and NiFe layered double hydroxide (LDH) particles were found to be highly active overall.^[94,95] Interestingly, the two MoS₂ phases

showed very different reactivities towards ferrocenemethanol (FcMeOH), allowing to locate 1T and 2H regions in mixed-phase samples. More recently, Gu *et al.*^[96] investigated the electrocatalytic activity of S vacancies in the basal planes of MoS₂ and confirmed their role in improving the overall HER activity of MoS₂. Quantitative kinetic data (Tafel plot, onset potential) could be extracted for individual vacancies. More than studying a single material, SECM was also employed to study the interaction between two materials, specifically between a MXene support (Ti₃C₂T_x) and Au NPs (20 nm), at the nanoscale.^[97] The charge distribution on the basal plane was shown to be significantly enhanced around Au NPs, leading to improved HER activity (comparable to that of Au).

MoS₂ was also employed as a benchmark catalyst to demonstrate the relevance of SECCM measurements in this context. The advantage of this technique (and SICM) compared to SECM is that the topography and activity can be mapped in a single run, without having to change the electrolyte's composition. Hence, the height- or shape-dependent activity enhancement of multi-layer step edges or defects could be evaluated directly.^[93,98–100] For single-crystalline {111}-oriented 2D Au nanocrystals, on the other hand, the catalytic activity was shown to be uniform over the whole nanocrystal.^[101]

To investigate the facet-dependent activity of Au, two other strategies were proposed. The first one consisted in scanning across a flat polycrystalline electrode. Using this strategy, Mariano *et al.*^[102] showed that the grain boundaries were more active than the grain surfaces for CO₂ reduction (CO₂RR) to CO, but not for the competing HER, consistent with a higher strain field. The second strategy consisted in probing individual well-defined NPs expressing specific facets. Using this strategy, Choi *et al.*^[103] demonstrated that Au NCs (predominantly expressing {100} facets) had a superior HER activity to that of Au nano-octahedra (predominantly expressing {111} facets). However, this strategy has its limits since relatively broad current distributions were measured for each geometry.

Another advantage of SECCM compared to SECM is that it is not affected by diffusional broadening since the electrolyte is confined to a limited area. Hence, provided that the pipette is small enough, the catalytic activity can be quantitatively mapped even at the sub-nanoentity

¹ Interestingly, Takahashi *et al.*^[99] proposed to use SECCM not only as an analytical tool, but also as a synthetic tool to locally generate defects on the basal planes.

level. This was demonstrated by Bentley *et al.* for N_2H_5^+ oxidation on 300 nm Au NPs using 30 nm pipettes (Figure 1-10G-J).^[93] The authors showed that the reaction rates varied significantly across the surface of individual Au NPs, which can therefore not be considered as uniformly active.

Carbon-based catalysts, which are promising alternatives to expensive noble metal-based catalysts, were also investigated by SECCM. In 2014, Byers *et al.*^[104] demonstrated that single-walled CNTs had an intrinsic ORR activity close to that of standard Au catalysts. The activity was further shown to be greatly enhanced at kinked and oxidized sites. Using slightly larger pipettes, Tarnev *et al.*^[105] investigated zeolitic imidazolate framework (ZIF-67)-derived Co@N-doped C composite particles with respect to the OER. They observed activity differences relative to the number of particles in the wetted area but always obtained consistent TOFs (between 0.25 and 1.5 s^{-1}), demonstrating the absence of NP-NP interactions.

As already discussed above, SICM also has the advantage of providing topography and activity mappings simultaneously contrary to SECM. This feature was exploited to investigate N_2H_4 oxidation and H^+ reduction on a 600 nm Pt NE,^[68] and BH_4^- oxidation on single Au NPs.^[67] In all cases, the reaction produces a change in the local ionic composition which can be detected at the tip.

However, with the introduction of AFM-SECM as discussed above, the topographical gap is slowly closing between SECCM/SICM and SECM. In the field of electrocatalysis, AFM-SECM was introduced by Kolagatla *et al.* to investigate the ORR at Fe,N-modified HOPG^[106] and individual Pt NPs.^[107] In addition to mapping topography and H_2O_2 production in the SG-TC mode with a 16 nm lateral resolution, they also mapped the ORR current by using the substrate as working electrode (WE) and the Pt NE as counter electrode (CE). To improve the collection efficiency of H_2O_2 and be able to map the ORR current and H_2O_2 production simultaneously, they later introduced Au-coated Pt NEs where the Au serves as second WE for H_2O_2 collection and the Pt NE only as CE to measure the ORR current.^[108]

1.3.2.2 PARTICLE-ON-A-STICK

Both aforementioned separation methods for probing the electrochemistry of individual objects carry some limitations. On the one hand, the local electrochemical measurements using confined electrochemical cells are often blind to the objects probed. They require multiple attempts (multiple pipette landings) to find a desired location or confrontation to *post-mortem* substrate imaging. In any case, they require control over the dispersion of the objects on the substrate. On the other hand, NIE requires electrolytic conditions enabling stable colloidal dispersions and the use of a miniaturized detector to catch the NPs on the fly, often without knowing the real structure of the captured NPs. Combining both approaches can minimize their drawbacks. “Particle-on-a-stick” measurements consist in isolating single NPs at the tip of NEs to probe their electrochemical response. This can be achieved either by letting NPs spontaneously adsorb on the NE from a suspension, by growing them directly on the NE, or by using a micromanipulator to pick and place them on the NE. From there, unlike in nano-impact experiments, all traditional electrochemical techniques can be applied to a single NP. This approach became very popular with the optimization and automatization of C NE fabrication.^[109]

The first approach seems the most straightforward but as discussed above, NPs do not always stick to the electrode surface. To immobilise an Au NP on a Pt NE, Li *et al.*^[110] modified the Pt surface with an amine-terminated silane (Figure 1-11A,B). The ORR activity of the NP in 0.1 M KOH could then be evaluated as shown in Figure 1-11C. Yu *et al.*^[111] still managed to immobilize single Au NPs on bare C NE. This allowed them to show that the catalytic activity towards HER of electrostatically adsorbed Au NPs was better than when a polyphenylene film was used to anchor them.

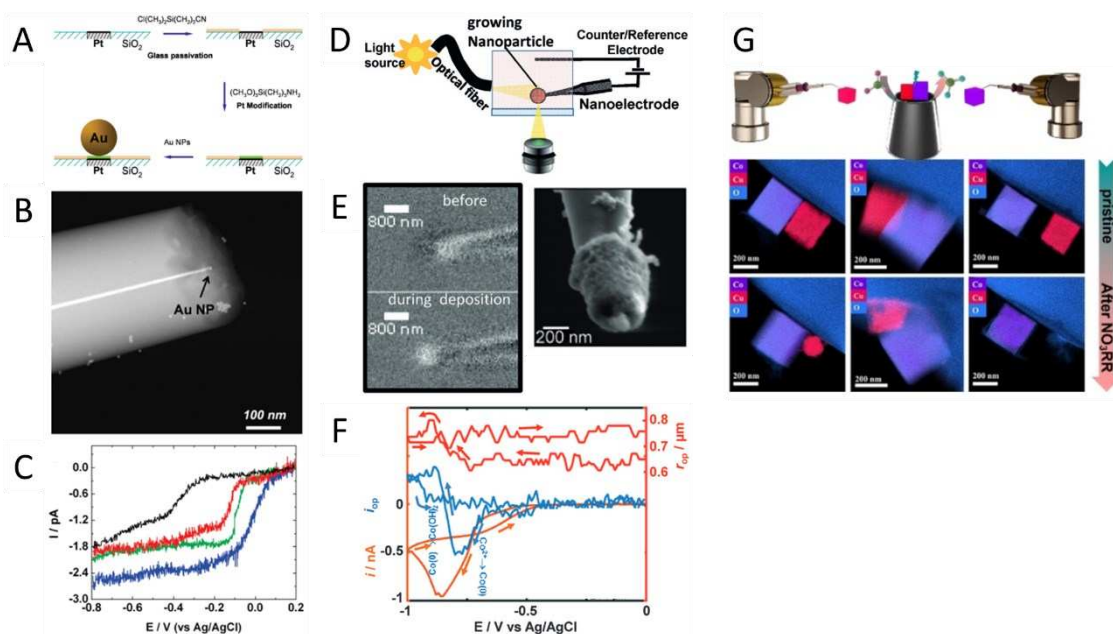


Figure 1-11. (A) Procedure for the preparation of Au single-NP electrodes (SNPEs). (B) TEM image of a single Au NP immobilized on a Pt NE. (C) LSVs of an O_2 -saturated 0.1 M KOH solution using a bare 7 nm-diameter Pt NE (black), a 14-nm Au SNPE (red), a 18-nm Au SNPE (green), and a 24-nm Au SNPE (blue). The scan rate was 10 mV s^{-1} . Adapted with permission from ref. ^[110]. Copyright 2010 American Chemical Society. (D) Dark-field optical microscopy setup used to monitor the deposition of single Co NPs on C NEs. (E) Background-subtracted optical images of a NP deposited by CA whose radius is below the diffraction limit (left), and representative SEM image (right). (F) Simultaneous monitoring of the electrochemical current (orange), the optical current (blue), and the particle radius (estimated from the super-localization of the edges) during Co deposition on a pre-existing $\text{Co}(\text{OH})_2$ NP. Adapted from ref. ^[112]. Copyright 2017 Wiley-VCH Verlag GmbH & Co. KGaA, Weinheim. (G) Schematic of the fabrication process of two-particle NE assemblies (top) and energy dispersive X-ray spectroscopy (EDX) mapping of three $\text{Cu}_2\text{O}+\text{Co}_3\text{O}_4$ assemblies with different interparticle distances before and after 5 CV cycles (bottom). Reprinted from ref. ^[113] under the terms of the CC BY-NC-ND 4.0 licence.

To avoid the issues (time cost, low success rate, additional surface functionalization step, poor electrical contact) related to the immobilization of suspended NPs, several researchers turned to electrodeposition to grow NPs directly on the NE. Clausmeyer *et al.*^[114] electrodeposited $\text{Ni}(\text{OH})_2$ NPs on C NEs to investigate their energy storage and catalytic properties. From the evolution of the peak current with the scan rate like in traditional electrochemistry, they showed that the NPs' charging was limited by the diffusion of H^+ inside the NP. By looking at

the Tafel slope of different NPs, they also showed that the OER activity was independent of size. Brasiliense *et al.* investigated the anodic^[112] and cathodic^[115] electrodeposition of Co-based NPs on C NEs. By following the process using dark-field microscopy (DFM, Figure 1-11D,E), they could probe the volumetric expansion of Co-oxide NPs upon electrochemistry. Comparing the scattered light intensity to the electrochemical current as shown in Figure 1-11F gave insights into the concurrent catalytic processes (ORR during reduction or OER during oxidation). Using pulsed CA, Huang *et al.* managed to electrodeposit single faceted Pt NPs on C NEs and probe their shape-dependent activity for formic acid oxidation.^[116,117] A templating strategy was also proposed by Aiyappa *et al.*^[118] to grow single metal organic frameworks (MOFs) on C NEs. After pyrolysis, they were then left with single Co/N-doped composite NPs which exhibited very high catalytic activity towards the OER. Post-catalysis observation of the NPs by TEM revealed the agglomeration of the Co centers. Combined with TEM, single-particle-on-a-nanoelectrode measurements then constitute a powerful approach to perform accelerated stress tests of electrocatalysts.

Another immobilization strategy consists in picking NPs and placing them on the NEs using micromanipulators (Figure 1-11G). This strategy was developed by Schuhmann^[119] and successfully applied to the investigation of the structural transformation of Co_3O_4 NPs at high current densities.^[120] More recently, single Co_3O_4 and Cu_2O NPs were both immobilized on the same C NE at a precise distance from each other to unveil distance-dependent structural changes during tandem nitrate reduction (NO_3RR) electrocatalysis as shown in Figure 1-11G.^[113] Instead of picking and then placing the NP on the NE in a two-step process, Rodriguez-Lopez proposed to “pick” the NP directly with the NE by approaching it to the NP in a SECM configuration until an ohmic contact is created. They used this strategy to elucidate the intraparticle diffusion coefficient and redox active concentration of viologen-redox active colloids (RACs) in the context of redox flow batteries.^[121] Similarly, Mirkin proposed to approach the NE so close to the NP (< 3 nm) that they become coupled by a tunneling current. They named this approach the “tunneling mode” of SECM and used it to evaluate the HER and HOR rate at single Au NPs in the absence of ohmic contact between the Pt NE and the Au NP.^[122,123]

If the NE becomes very small, it can be seen as a single NP by itself. This observation was exploited by White to study the nucleation of H_2 , N_2 and O_2 nanobubbles (NBs, from H^+

reduction, N₂H₄ oxidation and H₂O₂ oxidation, respectively) at Pt NPs using Pt nanodisk electrodes ranging from 4 to 200 nm. In all cases, the critical concentration of dissolved gas required for NB nucleation was found to be significantly larger than the saturation concentration at room temperature and pressure.^[124–131]

1.3.2.3 EC-STM, AFM, TEM, AND STXM

Apart from purely electrochemical techniques, other imaging techniques have also been operated in electrochemical conditions to provide new insights into structural/compositional changes at the nanoscale and into the location of active sites. In the following, recent results obtained by EC-STM, AFM, TEM and STXM will be reviewed. The objective of this section is not to give a comprehensive picture but rather to give an overview of the capabilities of each technique in the context of energy storage and conversion.

EC-STM

In the context of electrocatalysis, EC-STM was both used to locate the active sites on electrocatalytic surfaces and to probe their reconstruction under operation.^[88–90] Although STM is considered a topographical tool, Bandarenka showed in 2017 that the active sites of electrocatalytic surfaces could also be detected by STM as regions of higher tunnelling current noise (Figure 1-12A,B).^[132] Based on this principle, they showed that the most active sites of Pt(111)-based surfaces for the ORR in acidic media were the step edges, while the most active sites in alkaline media were the Pt(111) terraces.^[133] More than just detecting the active sites, they later showed that quantitative information about the local catalytic activity can be extracted from the tunnelling current noise. A linear relationship between the tunnelling current noise and the TOF was found.^[134] Using the same method, Kosmala *et al.*^[135] demonstrated that Fe films covered with monolayer graphene outperform Pt for the HER. This outstanding activity was attributed to single Fe atoms trapped within C vacancies and curved graphene areas on step edges.

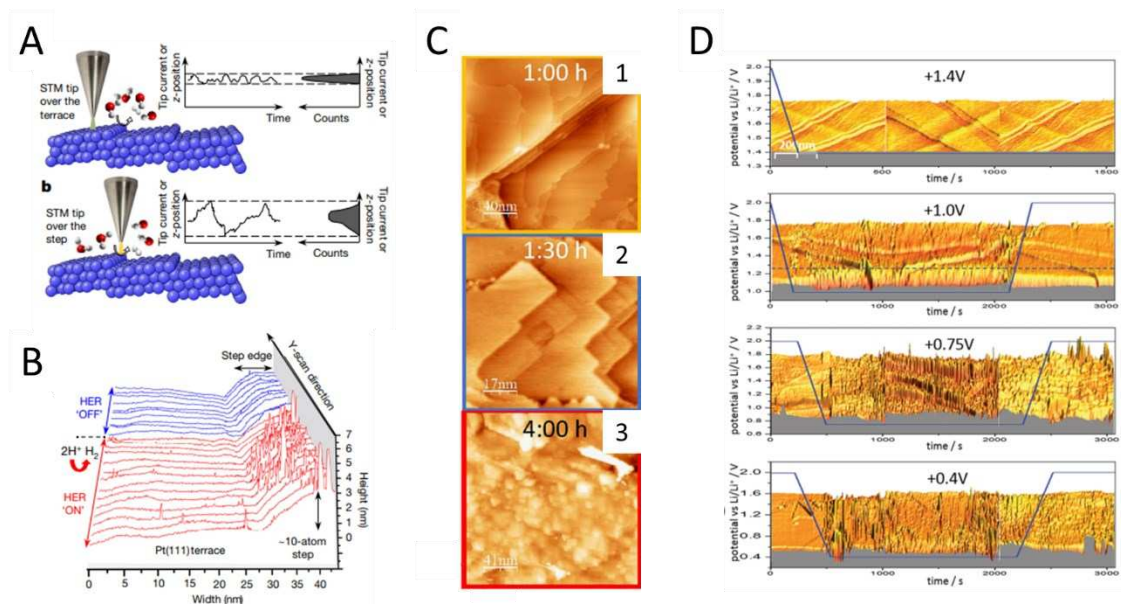


Figure 1-12. (A) Scheme explaining the concept of noise-EC-STM for the direct identification of catalytically active surface sites. When the local environment between the STM tip and the sample changes, the tunnelling barrier also changes. Hence, increased tunnelling current noise is likely to be measured when the tip is over a step edge, which is more active than a terrace. If the STM is operated in constant-current mode, then the noise is revealed in the measured z-position. (B) STM line scans (constant-current mode) obtained over a Pt(111) surface in 0.1 M HClO₄, when the potential is either sufficiently negative or too positive to initiate the HER ('ON' or 'OFF'). Adapted from ref. [132]. Copyright 2017, Macmillan Publishers Limited, part of Springer Nature. (C) Series of EC-STM images showing the morphological evolution of a graphene-covered polycrystalline Cu surface during CO₂RR in 0.1 M CO₂-saturated KHCO₃: from polycrystalline Cu (1) to Cu(100) facets (2) and finally to nanocuboids (3). Adapted from ref. [136]. (D) Real time EC-STM images of HOPG in 1 M LiPF₆ in EC/DCM (1:1) during a pulse CA at different potentials. Reprinted from ref. [137] under the terms of the CC BY 4.0 licence.

In a more traditional manner, Hai Phan *et al.* [136] used EC-STM to investigate the reconstruction of polycrystalline Cu surfaces under CO₂RR conditions. The surfaces were shown to reconstruct into nanocuboids (Figure 1-12C) whose size depends on the applied potential and the duration of the electrolysis. The authors also showed that smaller features with enhanced activity can be prepared if the Cu surface is initially covered with monolayer graphene. Similarly, Stumm *et al.* [138] probed the structural dynamics of cobalt oxide nanoislands (NIs) supported on Au(111) under OER conditions. While some agglomeration was observed, the NIs mostly retained their morphology. At potentials below the OCP, however, the NIs were

shown to dissolve, double bilayer NIs being slightly more resistant to dissolution than bilayer NIs.

There are very few reports on the use of EC-STM in the field of batteries.^[72] Since most battery materials come in the form of microparticles, AFM was often preferred to STM (see below). Still, interesting insights into the formation of the SEI at graphitic (here HOPG) LIB anodes were obtained by Seidl *et al.* using EC-STM.^[137] More than just following steady-state topographical changes (graphite exfoliation, SEI precipitation on the basal planes) at different applied potentials like Hai Phan *et al.*, they also acquired real time images of SEI precipitation on the basal planes (Figure 1-12D). This allowed them to conclude that SEI precipitation becomes irreversible when the cell is cycled below 1.0 V vs Li⁺/Li.

EC-AFM

Due to the nature of the interaction between the AFM tip and the substrate, EC-AFM was mostly used to probe morphological changes of electrocatalysts and battery materials.^{2[71,72,90,139,140]}

In 2017, Boettcher investigated the structural dynamics of single-layered Ni(OH)₂ nanosheets as electrocatalysts for the OER. They showed that due to the insertion of ions from the electrolyte, the nanosheets expanded in volume by 56% under OER conditions.^[141] They also evidenced the absorption of Fe cations into the nanosheets which further increased their apparent volume.³ Later, they showed that substituting Ni with Co resulted in higher porosity of the nanosheets, reducing mechanical stress during redox cycling and therefore enhancing their stability.^[142] Similarly, Mefford *et al.*^[66] studied the volumetric expansion of β-Co(OH)₂

² Although the active sites of electrocatalytic surfaces cannot be detected directly like in STM, they could still be detected indirectly via the nucleation of NBs. In 2009, Lohse showed that H₂ and O₂ NBs produced by the electrolysis of water on HOPG could be imaged by AFM.^[455] At the time, the authors were interested in the NBs themselves, but these could also serve to map the active sites as commonly done in OM studies (see *Optical microscopy approaches*, section 1.4). This still needs to be verified on surfaces with well-defined active sites such as Pt(111)-based surfaces. Noteworthy, like in the case of White's NEs, the current dropped at a nonzero value after the NBs had formed and covered the electrode surface. According to White,^[124] the NBs do not block the entire surface because a residual current is required to balance the diffusional outflux of gas and stabilize them.

³ KOH is the standard supporting electrolyte for OER studies of metal oxides and (oxy)hydroxides. However, most KOH sources contain Fe impurities which have recently been shown to absorb into Ni(OH)₂, enhancing its catalytic activity.^[456] This phenomenon makes it more challenging to evaluate the intrinsic activity and stability of metal (oxy)hydroxides.

nanoplates upon oxidation into β -CoOOH (Figure 1-13A). In theory, a contraction is expected, but as for the Ni(OH)₂ nanosheets, HO⁻ ions first intercalate into β -Co(OH)₂ to form an intermediate expanded α -CoO₂H_{1.5}·0.5H₂O structure (Figure 1-13B).

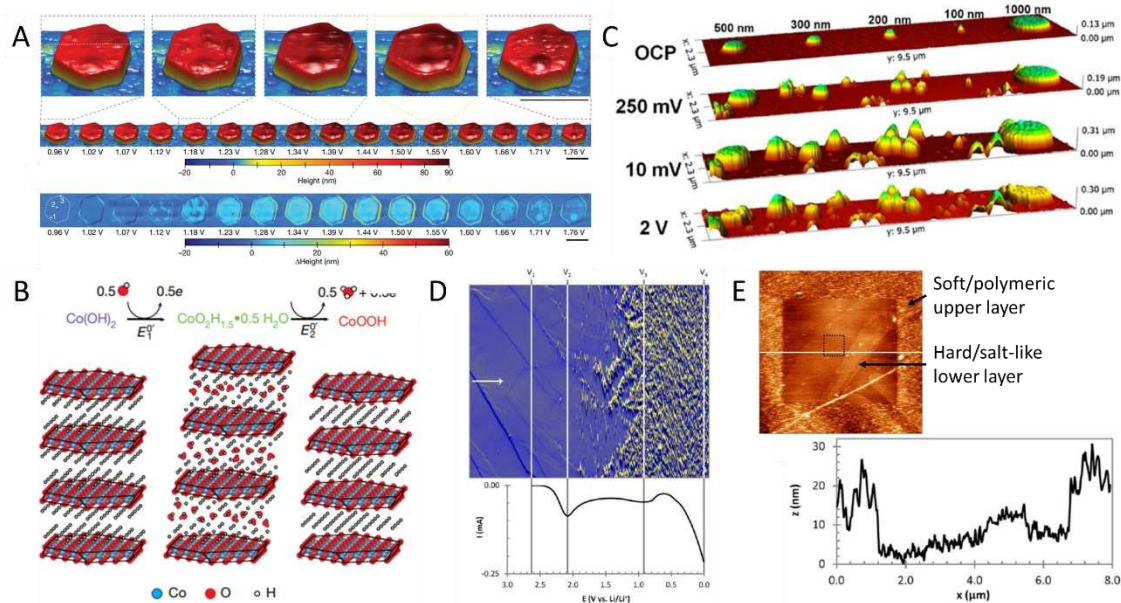


Figure 1-13. (A) Topography of a β -Co(OH)₂ particle in 0.1 M KOH at different applied voltages (top) and differential height compared to the particle morphology at the open-circuit voltage (0.96 V, bottom). Scale bars: 500 nm. (B) Mechanism responsible for the expansion and contraction of the particle. Adapted with permission from ref. [66]. Copyright 2021 The Author(s), under exclusive licence to Springer Nature Limited. (C) *In situ* 3D AFM images during lithiation and delithiation of a-Si nanopillars taken at several potentials during the first cycle. Reprinted with permission from ref. [143]. Copyright 2013 American Chemical Society. (D) SEI live formation on HOPG in 1.5 M LiTFSI dissolved in ethylene carbonate (EC) imaged (top) during an LSV (bottom) from the OCV (V_1) to 0 V (V_4) performed at a scan rate of 5 mV s⁻¹. (E) Topographic AFM image acquired at 0 V after repeated scanning of the inner region to mechanically remove the soft upper SEI layer (top) and line profile illustrating the thickness of this layer (bottom). Adapted with permission from ref. [144]. Copyright 2014 American Chemical Society.

As explained above, AFM was often preferred to STM for investigating battery electrodes because it more easily adapts to their rough surfaces. In addition to morphological changes, EC-AFM was also used to examine the mechanical properties of battery materials as well as their interfacial chemistry.

As discussed above, ion (de)intercalation can induce dramatic volume changes. In some cases, this can compromise the material's structural integrity, ultimately leading to capacity loss. This process was investigated by Park *et al.* on focused ion beam (FIB) micro-machined Li_xCoO_2 cylinders,^[145] which experienced a volume increase of 1.3% upon delithiation, in good agreement with previous X-ray diffraction (XRD) studies. The authors chose to work on such samples because volumetric changes of regular shaped objects are much easier to track and model. Applying the same concept to an anode material, Becker *et al.*^[143] investigated the morphology evolution of a-Si nanopillars (100 nm in height and 100-1000 nm in diameter) produced by e-beam lithography upon cycling. During the first cycle, the nanopillars permanently expanded as shown in Figure 1-13C. Then, from cycle to cycle, they became rougher until they eventually fractured. Since the nanopillars were eroded under the AFM tip even for small contact forces, the authors also suggested a degradation of the nanopillar's mechanical properties upon cycling, which they later confirmed by performing *in situ* nanoindentation measurements.^[146] In the case of MoS_2 , another promising anode material for LIBs, lithiation was shown to induce irreversible wrinkling due to a phase transition.^[147] Apart from the structural degradation of the anode material itself, Li dendrite growth is also a key issue affecting the performance and safety of LIBs. Li deposition on graphite anodes was studied by Shen *et al.* in ethylene carbonate (EC)- and fluoroethylene carbonate (FEC)-based electrolytes.^[148] They showed that only the harder LiF-rich SEI which forms in FEC-based electrolytes efficiently suppresses Li dendrite growth.

This difference in behaviour depending on the electrolyte's composition shows the importance of SEI formation and more broadly of interfacial chemistry on battery operation. Due to its trace presence, reactivity, and inhomogeneity, *in situ* EC-AFM (and STM) is particularly relevant to investigate the formation mechanism, morphology and mechanical properties of the SEI. Like Seidl *et al.*,^[137] Cresce *et al.* investigated SEI formation on HOPG in real time (Figure 1-13D).^[144] In contrast to STM, AFM was able to detect that the SEI consists of two distinct layers: a 20 nm thick soft/polymeric upper layer which can be mechanically removed by the tip upon scanning, and a hard/salt-like lower layer (Figure 1-13E). SEI formation on Si was investigated in the same way by Chen *et al.*^[149] A SEI can also form on cathode materials such as $\text{LiNi}_{0.5}\text{Mn}_{1.5}\text{O}_4$ particles. In this case, a stable 4-5 nm thick film was

shown to form at about 4.78 V on (111) facets upon charging, whereas no film was detected on (100) facets.^[150]

The interfacial chemistry of other battery chemistries was also studied by EC-AFM. In the context of redox flow batteries, Watkins *et al.*^[151] highlighted the formation of interfacial films on graphitic electrodes upon cycling. They showed that these films – which were softer than the underlying graphitic surface – formed exclusively on the basal planes and during the reduction of the radical cation. The combination of AFM and SECM measurements revealed that these films significantly slowed down the electron transfer, which is detrimental to the battery. Li-O₂ and Li-S batteries also have a rich interfacial chemistry whose dynamics is not yet fully understood. During ORR at a HOPG electrode, Wen *et al.*^[152] showed that nanoplates rapidly grow from the step edges, eventually forming a homogeneous Li₂O₂ film. While this reaction is perfectly reversible during the first cycle, byproducts such as LiCO₃ and LiOAc with irregular shapes accumulate on the electrode after several cycles. Similarly, Lang *et al.*^[153] showed that partially reduced Li₂S₂ NPs accumulate in Li-S batteries upon cycling, leading to capacity loss.

In addition to measuring the morphology and mechanical properties of materials, AFM can also be used to probe their electrical (conductive (c)-AFM, scanning spreading resistance microscopy, SSRM) and diffusional properties (electrochemical strain microscopy, ESM). However, these techniques generally cannot be implemented *in situ* as the AFM tip needs to be biased and can therefore react with the electrolyte, unless the electrolyte is solid like in solid-state LIBs (SS-LIBs). Masuda *et al.*^[154] demonstrated the possibility to use *in situ* Kelvin probe force microscopy (KPFM) to directly visualize the internal electrical potential distribution in a composite SS-LIB cathode. Upon charging, the potential increased over the entire electrode, suggesting that Li⁺ ions are depleted even in the solid electrolyte, micrometres away from the interface.

EC-TEM AND STXM

EC-TEM and STXM are getting increasingly popular to study catalysts and battery materials.^[66,155–157] They provide the highest spatial resolution and an additional spectroscopic

information, but with the cost of expensive equipment and non-negligible beam damage (see below).

1.4 OPTICAL MICROSCOPY APPROACHES

Optical microscopies (OMs) are particularly suited for probing single-entity electrochemistry. On the one hand, thanks to the recent advances in camera technology, they provide a high temporal resolution, which is crucial for the investigation of nucleation and growth processes as well as solid-state diffusion processes. On the other hand, more than simply providing a high temporal resolution, they do so at high throughput as hundreds of different objects can be imaged at once, giving them a clear advantage over SPMs. Moreover, scanning a tip over an object can potentially damage it^[143] or disrupt its diffusion layer. EC-TEM and STXM are also quite invasive. The electron and X-ray beams can alter the object either directly or indirectly by interacting with the electrolyte and generating free radicals (radiolysis). Although detrimental photochemical reactions can also occur in optical microscopes when lasers are used as light source, less powerful LEDs operating in the visible range are used in most cases. Moreover, OMs do not require thin layer cells like EC-TEM and EC-TXM, which might disrupt the NPs' diffusion layer.

Despite the numerous advantages of OMs, they have one major drawback: the optical diffraction limit. Two objects closer than $\frac{\lambda}{2NA} \approx 300 \text{ nm}$, with λ the wavelength of the incident light and NA the numerical aperture of the objective, cannot be resolved. This also means that the shape of objects smaller than 300 nm cannot be resolved. Whereas the spatial resolution of SPMs can always be tuned by changing the probe's size, the optical diffraction limit is a hard limit that cannot be overcome. TEM and STXM are also subjected to the diffraction limit, but since the wavelength of electrons and X-rays is much smaller, it lies below the nanometre. Nevertheless, this does not mean that NPs cannot be detected on an optical microscope. They still interact with (scatter) the incident light, producing diffraction spots that can be detected on a camera. However, to be able to detect the diffraction spot of a NP, specific illumination and collection geometries need to be used to increase the signal-to-noise

ratio. The most frequent ones are schematized in Figure 1-14A along with their respective advantages and disadvantages.

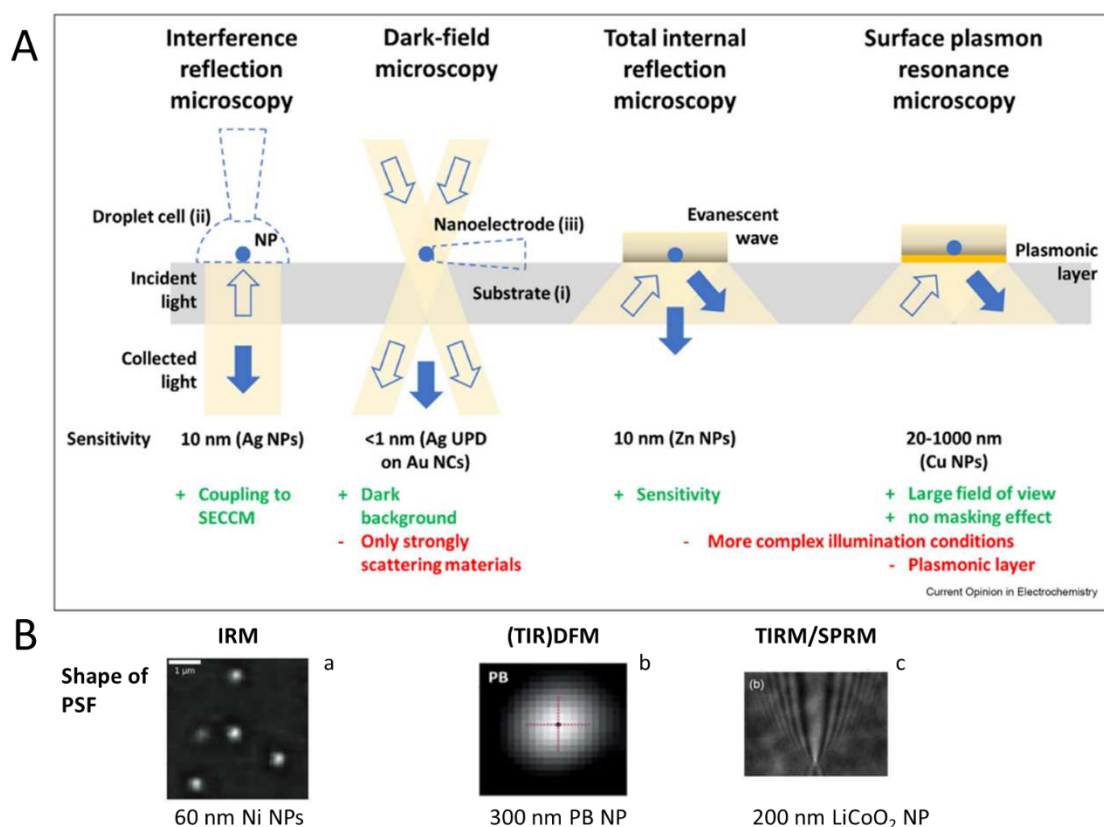


Figure 1-14. (A) Most represented configurations when coupling OM and electrochemistry. Individual NPs can be probed either at a macroscale electrode (i), within micro- or nanoscale droplets (ii), or at the tip of a NE (iii). Reprinted with permission from ref. ^[158]. Copyright 2022 Elsevier B.V. (B) Shape of the point spread function (PSF) in each configuration. ^aAdapted with permission from ref. ^[159]. Copyright 2022 Wiley-VCH GmbH. ^bAdapted from ref. ^[160] under the terms of the CC BY-NC 3.0 licence. ^cAdapted with permission from ref. ^[161]. Copyright 2017 American Chemical Society.

Even if detecting NPs on an optical microscope is already a great achievement, it is not enough to be able to probe their electrochemistry. Luckily, changes in the NP's composition and local environment (i.e., changes in the local refractive index) translate into changes in the intensity of the diffraction spot, which can be followed dynamically. The NP's motion can also be tracked with sub-pixel accuracy by fitting the diffraction spot with an adequate function (super-localization). Indeed, depending on the illumination and collection geometry, the

diffraction spot (also known as point spread function, PSF) can have different shapes and needs to be treated differently (see examples in Figure 1-14B).

In the following, we will see how these concepts were applied for investigating the electrochemical behaviour of single NPs in the context of energy storage and conversion.

1.4.1 ELECTROCATALYSIS

Tracking morphological changes seems the most obvious thing to do when using a microscopy technique. However, as discussed above, OM techniques are not very well suited to tracking morphological changes at the nanoscale due to the optical diffraction limit. Still, small volume changes of microparticles can be measured with sub-pixel accuracy by applying super-localization concepts to their edges. This was done by Brasiliense *et al.* to investigate the breathing of cobalt oxide particles deposited on C NEs under ORR and OER conditions (see *Particle-on-a-stick*, section 1.3.2.2).^[112,115]

Apart from structural changes of microparticles, OMs have mostly been used to investigate the formation of surface NBs during electrocatalytic reactions. Surface NBs are easily detected as they have a very different refractive index compared to that of the electrolyte. Moreover, the high temporal resolution of optical microscopes makes them particularly suited for the investigation of relatively fast NB nucleation and growth processes.

Tao was the first one to use electrogenerated H₂ as a measure of the catalytic activity of single Pt NPs towards the HER.^[162] Thanks to the proportionality between the plasmonic signal and the electrochemical current in surface plasmon resonance microscopy (SPRM),^[163] the authors could determine the CVs of single Pt NPs by monitoring the evolution of their plasmonic signal upon generating H₂ (Figure 1-15A,B). Zhang and Kanoufi later questioned the fact that NBs are good reporters for the catalytic activity of single NPs by evidencing hydrogen spillover from one NP to a neighbouring NP^[164] (Figure 1-15C-E) or to a neighbouring nucleation site on the support (Figure 1-15F,G).^[165] Indeed, Kanoufi showed by interference reflection microscopy (IRM) that the H₂ NBs which form on top of Pt NPs steadily grow although they rapidly cover the Pt NP on which they formed (Figure 1-15D), disconnecting it from the electrochemical cell. As schematized in Figure 1-15E, these H₂ NBs are suggested to be fed by neighbouring Pt NPs

devoid of H₂ NB. Nevertheless, interesting insights into electrocatalytic reactions could still be obtained by monitoring the formation of NBs.

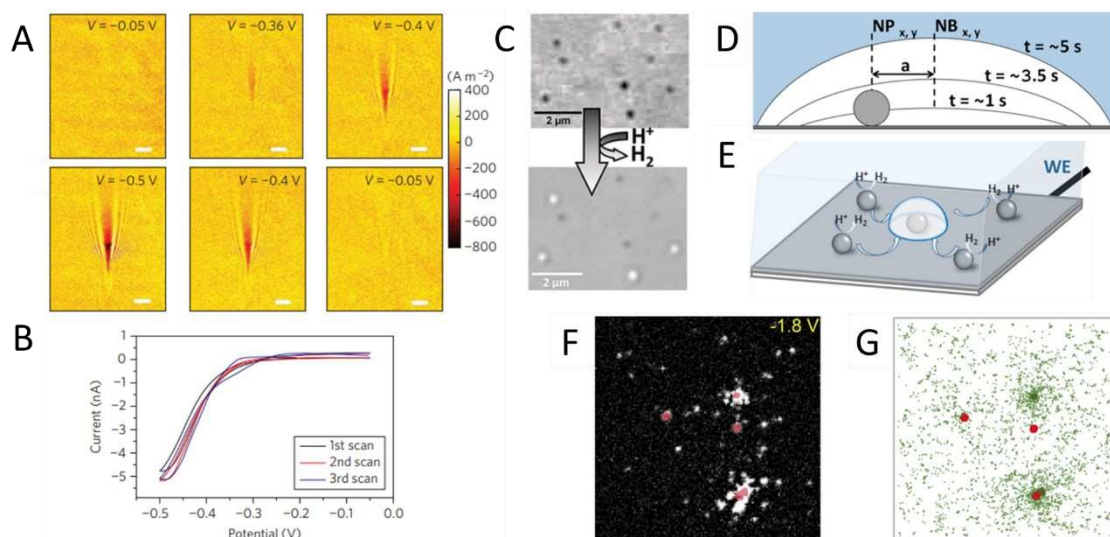


Figure 1-15. (A) Plasmonic current density image of a single Pt NP at different potentials during a CV. Scale bar: 3 μm. (B) CV of the Pt NP obtained by integrating the current density over the scattering pattern, including the tail. Adapted with permission from ref. ^[162]. Copyright 2012, Nature Publishing Group. (C) Optical images taken before and after CA at -1 V vs Pt in 5 mM H₂SO₄ for 50 s. Adapted with permission from ref. ^[164]. Copyright 2021 American Chemical Society. (D, E) Two schematics (side and perspective view, respectively) of a H₂ NB disconnecting a Pt NP during HER and being fed by neighbouring Pt NPs. (F) Total internal reflection fluorescence microscopy (TIRFM) image (22.8×22.8 μm²) showing H₂ NBs on an Au nanoplatform-modified indium tin oxide (ITO) electrode in 25 mM H₂SO₄ + 1 M Na₂SO₄ + 5 nM rhodamine 6G at -1.8 V vs Pt during a CV. (G) Scatter plot showing the accumulated spatial distribution of H₂ NBs between -1.5 V and -1.8 V. Each coloured dot represents one detected NB. In (F) and (G), the Au nanoplates are highlighted with false colour based on a same-location SEM image (not shown). Adapted from ref. ^[165].

By adding a fluorophore to the solution, which would adsorb at the NB|solution interface, Zhang showed by total internal reflection fluorescence microscopy (TIRFM) that H₂ NBs formed at a very early stage on indium tin oxide (ITO), ca. 500 mV before the thermodynamic reduction potential of H⁺ into H₂.^[165] On ITO covered with a thin film of Au/Pd alloy (30 nm), however, their nucleation required a significant overpotential, while O₂ NBs formed at an early stage during the OER.^[166] When they changed the fluorophore from a rhodamine derivative to the more hydrophobic Nile red, they observed brighter and longer nucleation events,

suggesting that the H₂ NB/electrolyte interface is hydrophobic.^[167] The fact that longer events were detected also confirmed the high stability of NBs on surfaces.^[168] The main drawback of single-molecule fluorescence microscopy is that one needs to accumulate a significant number of images, so that it becomes difficult to catch fast dynamics.

By super-localizing a large number of surface NBs, the active sites of electrocatalytic surfaces could also be mapped with a high spatial resolution.^[169] Thanks to the unique ability of IRM to distinguish between H₂ NBs and In⁰ NPs, Ciocci *et al.*^[170] unveiled a partition of the electrode in potential (Figure 1-16A) and space (Figure 1-16B) between the formation of H₂ NBs and In⁰ NPs during the HER on ITO, which was attributed to local variations in charge transfer kinetics (related to local film conductivity as measured by SECM). Although the diffraction spots are wider along the beam's direction in SPRM and therefore more challenging to fit, Cheng *et al.*^[171] could still show from the detection of O₂ NBs that the catalytic sites of graphene sheets for oxygen evolution at negative potentials were primarily located on the edges (Figure 1-16C,D). The evolution of oxygen at negative potentials is due to the disproportionation of the superoxide anion formed during the ORR, suggesting that graphene acts as a superoxide dismutase (SOD) mimic. To map the active sites of Au for the HER with a sub-diffraction limit spatial resolution using SPRM, Wang *et al.*^[172] introduced a second perpendicular beam which reduced the uncertainty on the NB's position along the direction of the first beam as shown in Figure 1-16E.

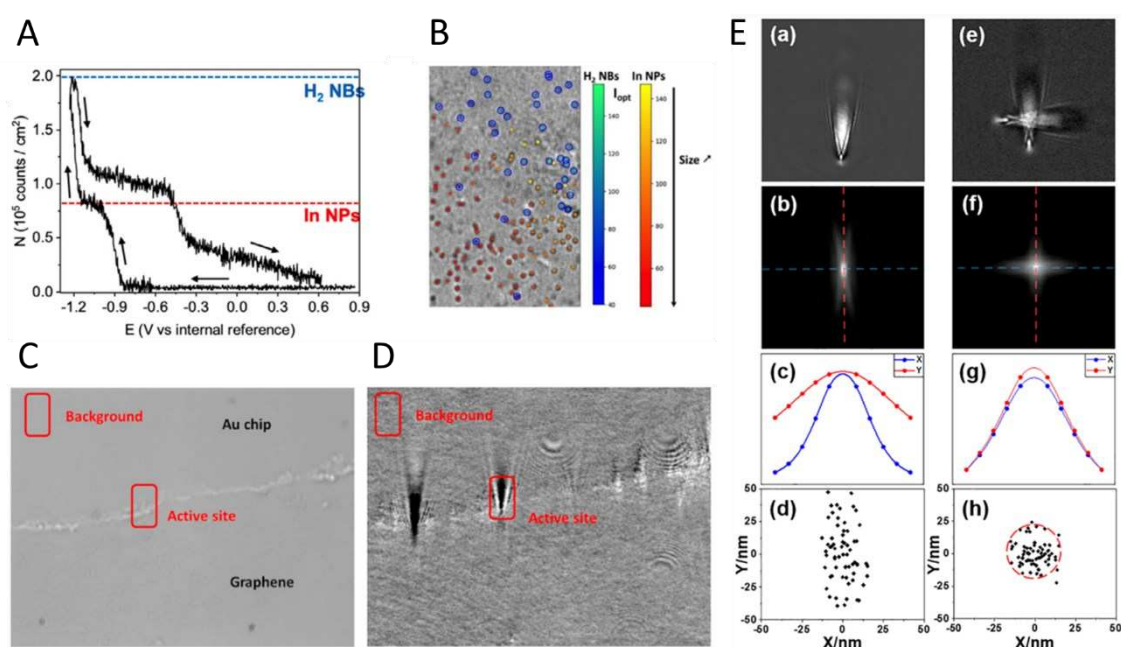


Figure 1-16. (A) Number, N , of features detected on the image with respect to the electrode potential. Two potential regions are identified and associated to the reduction of ITO into In^0 and the formation of H_2 NBs. (B) Reconstructed image showing how each population grows selectively in a different region of the ITO electrode. Adapted with permission from ref. ^[170]. Copyright 2021 Elsevier Ltd. (C) Bright-field image of a graphene sheet transferred onto an Au chip. (D) Corresponding SPRM image during oxygen evolution. Adapted with permission from ref. ^[171]. Copyright 2022 Elsevier Ltd. (E) Original SPR image (a, e) and its spatial correlation image (b, f) of the conventional single-beam (a–d) and dual-beam configuration (e–h). (c, g) Gaussian fits of the line profiles along x (blue) and y (red) highlighted in (b, f). The localization accuracy along the y direction is significantly improved in the dual-beam configuration (h) compared to the conventional single-beam configuration (d). Reprinted with permission from ref. ^[172]. Copyright 2021 American Chemical Society.

Even if it is difficult to probe the catalytic activity of individual NPs using NBs as reporters, single NB nucleation events could still be used in a statistical way to screen the activity of catalysts. Using dark-field microscopy (DFM), Xu *et al.*^[173] screened the HER activity of Au@Pt NPs with different shell thicknesses. The formation of H_2 NBs on top of the NPs was shown to induce a significant increase of the scattering signal, which scaled with the amount of Pt on the NPs (Figure 1-17A,B). Benefiting from the depth-sensitivity of total internal reflection dark-field microscopy (TIRDFM), Wang *et al.*^[174] proposed another approach based on the z -displacement (“hopping”) of the NP when an O_2 NB forms between the Cu substrate and the NP during OER as illustrated in Figure 1-17C. This indicator, which has the advantage of limiting interferences coming from morphological changes of the NP during OER, could be accurately correlated to the activity (TOF) of a broad range of materials ($\text{Ca}_3\text{Co}_{3.2}\text{Fe}_{0.8}\text{O}_9$, $\text{Ca}_3\text{Co}_4\text{O}_9$, Co_3O_4 , Pt-g- C_3N_4 , and IrO_2 , Figure 1-17D). Ma *et al.*^[175] used the electrochemiluminescence (ECL) blinking technique to quantify the HER activity of hollow carbon nitride NSs (HCNSs). The NP is initially in its ON state, turns OFF when a H_2 NB grows on top of it, and then turns ON again when the NB collapses (Figure 1-17E). The authors found that the durations of the ON and OFF states were distributed according to a power law (Figure 1-17F), meaning that there are multiple catalytic sites with stochastic activities on each HCNS. The coefficient of the power law, which was shown to increase with improved HER activity from modified HCNSs, could be

used as an activity indicator as well (Figure 1-17G). However, to generate ECL, the conditions in which the electrocatalytic reaction is performed are quite different.

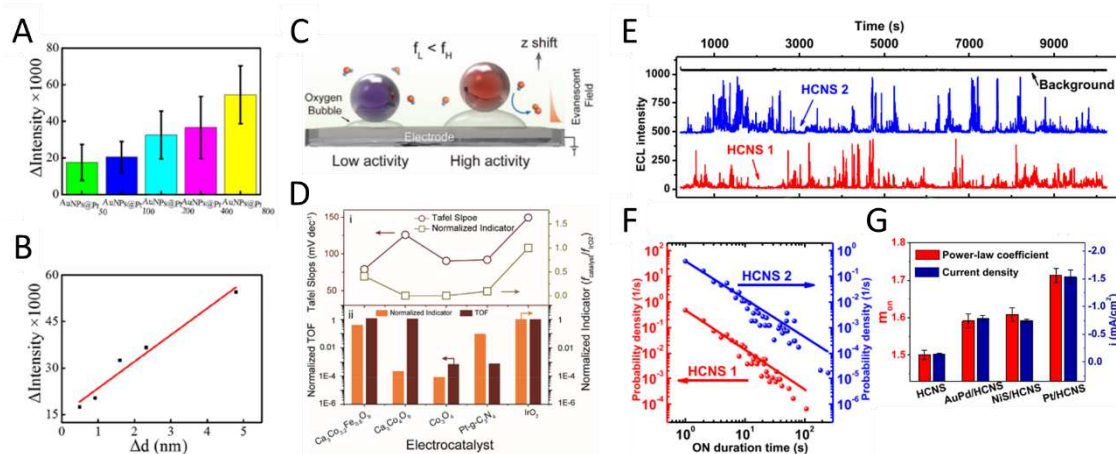


Figure 1-17. (A) Average scattering intensity during H₂ NB generation over single Au@Pt NPs with different Pt shell thicknesses. (B) Relationship between the scattering intensity when the NB is formed and the Pt shell thickness. Adapted with permission from ref. [173]. Copyright 202 American Chemical Society. (C) Schematic of the electrochemically generated gas bubble-induced vertical motion or “hopping” of electrocatalysts. The hopping is recorded through the attenuated scattered light intensity in the evanescent field and is quantitated by the diffusion coefficient obtained from a mean square displacement analysis. (D) Normalized indicator compared with Tafel slopes (top panel) and normalized TOFs of various catalysts (bottom panel). Adapted with permission from ref. [174]. Copyright 2022 American Chemical Society. (E) ECL trajectories of two single HCNSs and the background during a CA at -1.5 V. Electrolyte: 100 mM K₂SO₄ + 100 mM K₂S₂O₈ (co-reactant). (F) Probability density of the ON state duration for the two HCNSs. The dots represent the probability densities of different durations. The lines represent the fits by a power law distribution. (G) Comparison between the power law coefficient m_{on} and the current density for four modified HCNSs at -1.5 V (N = 3). Adapted with permission from ref. [175]. Copyright 2020 American Chemical Society.

1.4.2 BATTERIES

In the field of batteries, mostly cathode materials were investigated using OMs. Jiang *et al.* [161] were the first ones to do that at the single-NP level. Employing SPRM, they investigated the diffusion kinetics of Li⁺ within single LiCoO₂ NPs in aqueous 1 M LiNO₃. Jiang *et al.* are disciples of Tao who is at the origin of most technological advances related to SPRM. But contrary to Tao’s pioneering work on Pt NPs evolving H₂, [162] here the SPR intensity relates to changes in

the refractive index of the NP itself as it is being converted, and not of its surroundings (H₂ NB). Hence, there is no doubt about the optical signal arising from the NPs themselves (see discussion on hydrogen spillover above), and further SEM characterization of the same NPs enabled to establish an accurate structure-activity relationship. They later applied the same methodology to PB NPs intercalating K⁺ ions from aqueous 1 M KNO₃.^[176] They observed a classical thin film behaviour, with intraparticle K⁺ diffusion affecting the electrochemical response only above 60 mV/s (Figure 1-18A,B). To determine if the K⁺ ions diffuse vertically or horizontally through the NPs, they employed another microscopy technique based on total internal reflection microscopy (TIRM) which simultaneously introduces different angle-dependent illumination depths (Figure 1-18C left).^[177] As demonstrated on Brownian NPs in Figure 1-18C right, this allows to track the vertical displacement of the NPs, which is otherwise inaccessible. Since the NPs have a cubic shape, only the vertical displacement of the optical centre of mass can hint towards one mechanism or the other (Figure 1-18D,E). Since they detected no vertical displacement of the optical centre of mass (Figure 1-18F), K⁺ diffusion is likely to occur outside-in and not bottom-up as commonly thought. Using DFM, they still observed a slight horizontal displacement of the optical centres of mass on some NPs, suggesting the presence of inactive zones in these NPs.^[160] They used DFM in this case because they needed to super-localize the diffraction spots with a higher spatial resolution (see shape of PSF under TIR illumination in Figure 1-14B). When coupled to a spectrometer, DFM also allows to measure the visible scattering spectrum of single NPs. More recently, with the aim of improving the understanding of the charge storage mechanism, they measured the optical impedance spectrum of single PB NPs.^[178] As already demonstrated on Au nanorods (NRs),^[179] the scattering intensity varies sinusoidally when a sinusoidal potential is applied (Figure 1-18G), allowing for a scattering intensity-potential transfer function to be defined (optical transfer function, OTF). The PB NPs showed a typical pseudocapacitive behaviour depending on the modulation frequency f . As shown in Figure 1-18H, in the low frequency range, the amplitude $|OTF| \propto f^{-0.5}$ (pointing to a diffusion limited process), while in the high frequency range, $|OTF| \propto f^{-1}$ (pointing to a surface limited process). Thanks to the well-defined geometry of the PB NPs, the depth of surface charging – ca. 2 unit cells – could also be determined.

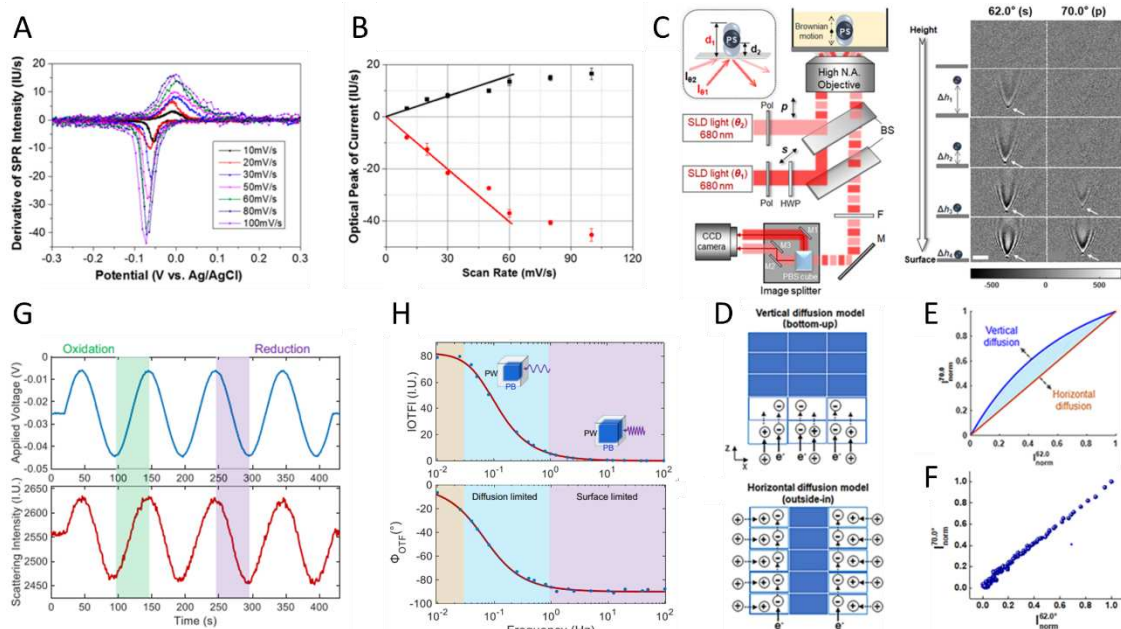


Figure 1-18. (A) Time derivative of the SPR intensity of a single PB NP at different scan rates. (B) Oxidation (black) and reduction (red) peak currents as a function of the scan rate. Adapted with permission from ref. [176]. Copyright 2017 American Chemical Society. (C) Schematic of the dual angle (da)-TIRM setup (left) and da-TIRM image flow of a polystyrene (PS) nanosphere diffusing towards the substrate (right, scale bar: 5 μm). (D) Vertical (top) and horizontal (bottom) diffusion models. (E) Theoretical $I_{norm}^{70.0^\circ}$ vs $I_{norm}^{62.0^\circ}$ curves corresponding to vertical (blue) and horizontal diffusion (orange). (F) Experimental curve obtained upon oxidizing a PB NP, hinting at horizontal diffusion. Adapted with permission from ref. [177]. Copyright 2021 American Chemical Society. (G) Scattering intensity of a single PB NP as a function of the sinusoidal potential modulation (frequency: 0.01 Hz, amplitude: 20 mV, offset: -25 mV). (H) Bode plots of the OTF's amplitude (top) and phase (Φ_{OTF} , bottom). The purple, blue and orange areas represent the high-frequency region, low-frequency region, and depletion region, respectively. Adapted from ref. [178] under the terms of the CC BY 4.0 licence.

Using a regular transmission microscope, Evans *et al.* [180,181] investigated the electrochromic conversion of hexagonal WO_3 NRs upon lithiation in 1 M LiClO_4 in propylene carbonate (PC). They observed variable conversion dynamics among single particles but most interestingly, that particle-particle interactions significantly impacted the conversion dynamics. Single particles were converted 4 times faster than homogeneous thin films prepared from the same particles. Like the PB NPs, the WO_3 NRs exhibit a hybrid charge storage mechanism, which was investigated here by performing CAs at different potentials. [182] Longer NRs were shown to store more pseudocapacitive charge than shorter ones, either due to a larger amount of step

edges on the sides which expose more hexagonal binding sites, or to a higher structural water content. By comparing the amount of pseudocapacitive charge and the number of surface W atoms, they determined a similar depth of surface charging to that of the PB NPs.

As already discussed in the section dedicated to nano-impacts (section 1.3.1), battery materials are rarely used as NPs, and usually incorporated in a matrix composed of carbon powder and binders. Moreover, in contrast to most of the examples presented above, they are most often cycled in organic electrolytes and in the absence of oxygen. To investigate battery materials under realistic conditions, specifically designed electrochemical cells have been developed in recent years, particularly by the company EL-CELL (Figure 1-19A). Reasonably tight, these cells allow for the battery to be operated in the absence of oxygen (and thus with metallic Li as CE) without needing to transfer the whole optical setup inside a glovebox (see *Scanning electrochemical probe microscopies*, section 1.3.2.1).^[69,81] Merryweather *et al.*^[183] adapted this cell to an interferometric scattering (iSCAT) microscope to investigate the phase transitions and Li⁺ diffusion dynamics in commercial Li_xCoO₂ microparticles within a matrix, in 1 M LiPF₆ in a 50:50 mixture of EC and dimethyl carbonate (DMC). In addition to directly visualizing phase transitions and determining Li⁺ diffusion rates at the single particle level, they also visualized the formation of domain boundaries between different crystal orientations associated with the monoclinic lattice distortion at the Li_{0.5}CoO₂ composition (Figure 1-19B). Similarly, they also investigated single-crystal LiNi_xMn_yCo_(1-x-y)O₂ (NMC) particles, challenging the fact that (de)lithiation occurs uniformly within individual particles.^[184] Later, they investigated the structural dynamics of rod-like Nb₁₄W₃O₄₄ (NWO) microparticles during high-rate cycling.^[185] In this case, they observed non-equilibrium phase separations (Figure 1-19C) that lead to particle cracking (Figure 1-19D), some parts of the particle then becoming electrically disconnected and eventually leading to capacity loss.

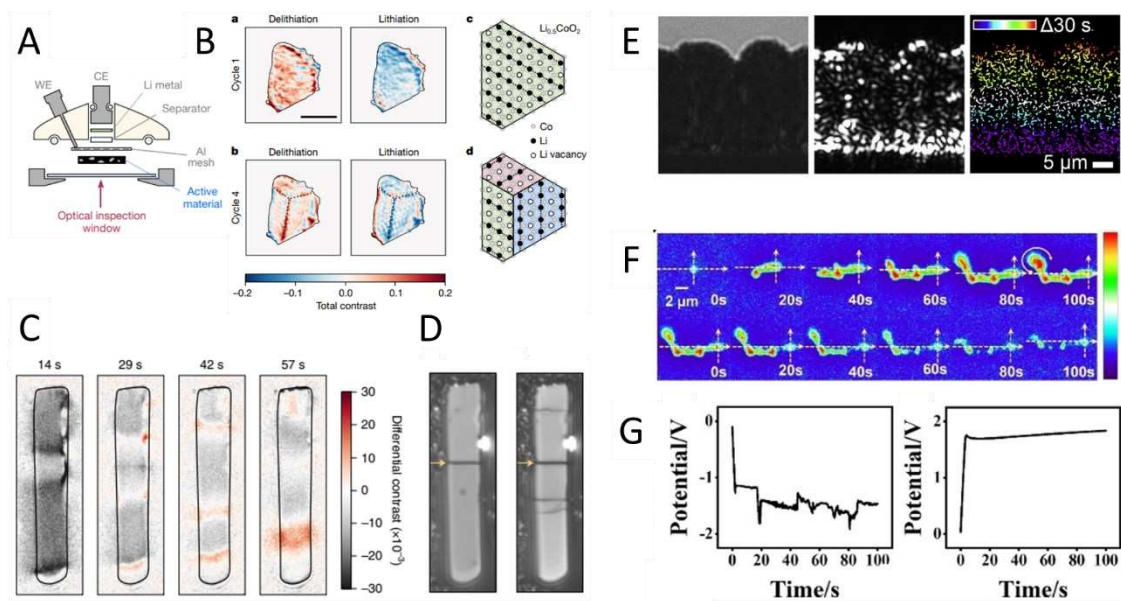


Figure 1-19. (A) Geometry of the OM half-cell. (B) (a, b) Images showing the total contrast resulting from Li ordering in cycle 1 (a) and cycle 4 (b), for delithiation (left) and lithiation (right). Scale bar: 5 μm . For cycle 4 (b), the formation of the ordered state produces domain-like features, with three regions separated by bright lines at approximately 120° (highlighted with black dotted lines). (c, d) Schematics of a $\text{Li}_{0.5}\text{CoO}_2$ particle with Li^+ ions ordered into rows. The cases of a single monoclinic domain (c) and of three monoclinic domains (d, with orientations of the rows differing by 120°) are shown. Adapted with permission from ref. ^[183]. Copyright 2021, The Author(s), under exclusive licence to Springer Nature Limited. (C) Differential images of a NWO particle during 20C delithiation. (D) Raw scattering image of the same particle after the 20C delithiation (left) and after nine additional cycles covering a range of cycling protocols (right). Adapted with permission from ref. ^[185]. Copyright 2022, The Author(s), under exclusive licence to Springer Nature Limited. (E) Bright-field (left), dark-field (centre), and temporal colour-coded super-resolution trace image (right) of the Zn dendrite growth process at a current density of 79.16 mA/cm^2 . The experiment was carried out in 1 M ZnSO_4 over 30 s, at a frame rate of 500 fps. Reprinted from ref. ^[186] under the terms of the CC BY-NC-ND 4.0 licence. (F) Plating (top) and stripping (bottom) of a single Zn dendrite on a Pt reflective nanopore electrode in 1 M ZnSO_4 at 1 nA (scale bars: 2 μm). (G) Corresponding evolution of the potential (CE: ITO). Adapted from ref. ^[187]. Copyright 2022 Wiley-VCH GmbH.

On the anode side, the formation of dendrites was extensively investigated.^[188,189] At the nanoscale, however, mostly Zn dendrites were studied by Rao. Using TIRDFM, they showed that the growth traces of Zn dendrites could be precisely reconstructed (Figure 1-19E).^[186] This allowed them to evaluate the role of current density and Zn salt nature and concentration on

dendrite growth. They also confirmed that the depletion of Zn^{2+} promotes vertical growth, which is even worse under fast charging conditions.^[190] By using reflective Pt nanopores as electrodes, they went one step further and probed the electrochemistry (Figure 1-19G) of single dendrites at the same time as visualizing their morphology changes by OM (Figure 1-19F). Correlating both pieces of information revealed a competition between growth and passivation.^[187] More recently, IRM was also used to probe the formation of a SEI on Cu during lithiation.^[191] In this case, as the objective faced the electroactive surface, the cell could not be tight, and the setup therefore needed to be placed inside a glovebox. The insights obtained by this technique were very similar to those obtained by AFM on graphite electrodes.^[144]

1.5 ISSUES AND OPPORTUNITIES RELATED TO OPTICAL MICROSCOPIES IN THE CONTEXT OF SINGLE-ENTITY ELECTROCHEMISTRY AND OF MY PHD

1.5.1 ISSUES

Even if OMs are very relevant and powerful techniques for investigating the electrochemistry of single NPs in the context of energy storage and conversion, they face several issues which might lead to wrong interpretations.

For instance, when the NPs are simply drop-casted on the electrode and not incorporated into a conductive matrix, their behaviour might be controlled by the heterogeneous electrical contacts with the electrode and not at all reflect their intrinsic properties. When they studied PB NPs, Jiang *et al.*^[176] observed very heterogeneous behaviors among single NPs, which they could not rationalize based on their morphology determined by SEM. They later found that this was likely due to the heterogeneous electrical contacts with the electrode by depositing a thin Pt layer on top of the NPs and electrode (Figure 1-20A).^[192] Once they were properly connected to the electrode through the Pt layer, most NPs recovered activity, showing they had not been probed at their full potential before. Although this is an effective strategy, it is not applicable to commercial electrodes as it requires expensive high-vacuum equipment. An increasingly popular alternative to avoid any issues related to heterogeneous electrical

contacts with the electrode is the direct electrodeposition of NPs on the electrode.^[193] However, beyond noble metals, electrodeposition mechanisms are very complex and have not yet been fully unravelled.

One objective of my PhD is to try to unravel the complex electrodeposition mechanisms of transition metal and transition metal oxide NPs. In **Chapter 2**, we will investigate the electrodeposition mechanism of Ni-based NPs from aqueous electrolytes. In **Chapter 5**, we will demonstrate that the electrodeposition of MnO₂ is the main charge storage pathway in aqueous Zn-MnO₂ batteries, and how it is affected by the presence of zinc hydroxides.

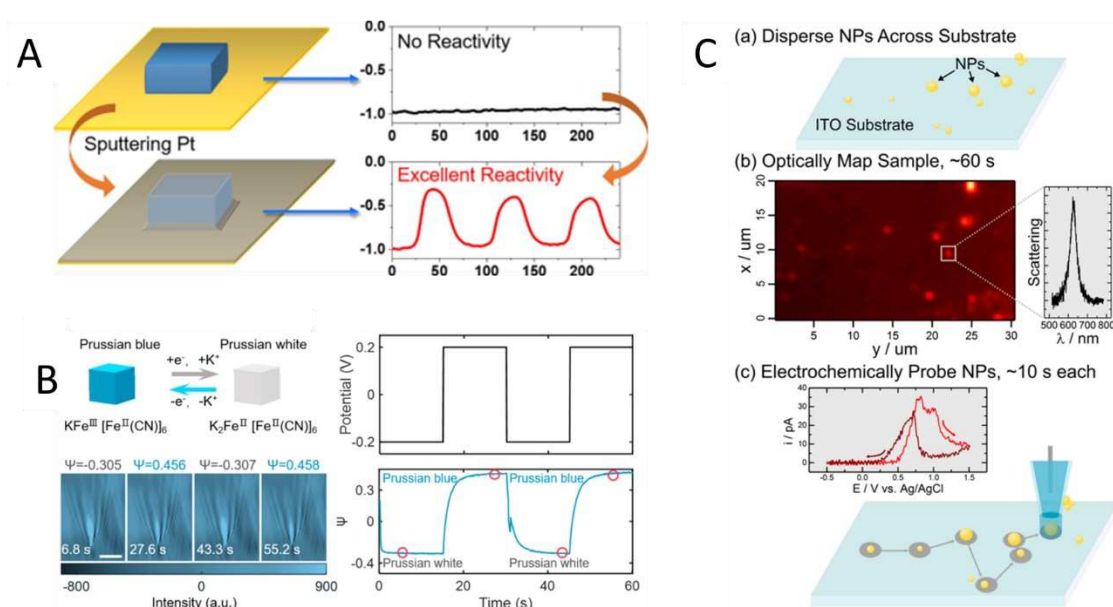


Figure 1-20. (A) Schematic illustration of the Pt sputtering treatment's influence on the electrochemical behaviour of single PB NPs. Reprinted with permission from ref. ^[192]. Copyright 2020 American Chemical Society. (B) Schematic and plasmonic images showing the reduction/oxidation of a single PB NP (left, scale bar: 8 μ m) and ψ profile of the NP when applying consecutive potential steps between -0.2 and 0.2 V (right). Adapted with permission from ref. ^[194]. Copyright 2022 American Chemical Society. (C) Procedure for probing individual NPs via optically targeted electrochemical cell microscopy (OTECCM). The sample is prepared by dispersing the NPs of interest onto a noncatalytic substrate electrode at low coverages (a). The resulting sample is first characterized optically using a hyperspectral imaging protocol (b). This data is used to locate individual NPs and compare their optical signatures to that expected for individual NPs. Targeted electrochemical measurements are then made via SECCM on the identified NPs (c). Reprinted with permission from ref. ^[195]. Copyright 2018 American Chemical Society.

Compared to other techniques, OMs also provide rather poor chemical information. To gain chemical information, Wu *et al.*^[194] recently introduced a quantitative phase extraction method in SPRM (termed plasmonic scattering interferometry microscopy, PSIM). While this method can precisely follow the compositional evolution of many different nanomaterials and potentially even identify unknown reaction products based on their refractive index as shown in Figure 1-20B, it requires a rather complex optical setup. Another way is to correlate the optical images with *ex situ* spectroscopic mappings (Raman, energy dispersive X-ray (EDX)) like it is already routinely done with SEM images.

Another objective of my PhD work is to automatize and accelerate this process. In **Chapter 3**, we will implement machine vision algorithms to automatically correlate various microscopy images and spectroscopic mappings to gain morphological and chemical information on electrodeposited Ni-based NPs. Such algorithms were also useful for studying corroding Al surfaces,^[196] but this will not be discussed in this thesis.

As already discussed above, OMs are sensitive to local variations in refractive index. However, they are usually not sensitive enough to probe dissolved species in the vicinity of the NPs.^[197,198] This is why only gas NBs were used as reporters for the electrocatalytic activity of NPs although we have seen before that they might not always reflect the intrinsic properties of the NP on which they grow. Moreover, using NBs as reporters restricts the number of reactions that can be studied (ORR, for example, does not produce gas). However, what most electrocatalytic reactions such as HER, HOR, ORR, OER, CO₂RR, NO₃RR, etc. produce in common, are pH changes.

In **Chapter 4**, we propose a new optical method to evaluate the catalytic activity of single NPs based on the generated pH gradient.

1.5.2 OPPORTUNITIES

Despite the issues presented above, OMs can readily be combined with other techniques to improve their throughput and precision, and vice versa.

OMs have for example been used to improve the throughput of SECCM by localizing NPs of interest. Their position can then be transmitted to the SECCM software, and they can be

probed directly without needing to map the entire surface. This is especially interesting when the NP surface density is low. This approach was proposed both by Hill^[195] and Schuhmann.^[199] More than simply localizing the NPs, Hill also probed the visible scattering spectrum of each NP (Au NRs) and correlated it to its catalytic activity (Figure 1-20C). We used a similar approach to position a pipette above a precise location of a complex sample, an *in situ* TEM chip from Protochips, to locally electrodeposit Pt NPs on it. However, this project will not be discussed in this thesis.

Similarly, we also used the optical monitoring to position a Pt UME above an isolated copper hexacyanoferrate (CuHCF) particle to address its redox mediated conversion electrochemically and optically at the same time. This will be the object of **Chapter 6**. Electrochemical ion intercalation was also probed in a controlled environment in the case of electrochromic $\text{Li}_2\text{Ni}_2\text{W}_2\text{O}_9$ particles,^[3] but this will not be discussed in this thesis.

Recently, we have also shown that the current measured in SECCM might not solely reflect the contribution of the NPs inside the meniscus, but also that of the NPs right outside of it. We evaluated this on Pt NPs subjected to a negative potential scan in 10 mM KCl. Although they did not seem connected to the electrochemical cell, NPs located outside the meniscus still experienced changes in optical intensity in correspondence of the potential scan. This can be explained by the presence of a nanometric electrolyte layer connecting peripheral Pt NPs to the meniscus, which can then reduce O_2 and/or water. These reactions produce a HO^- gradient which is compensated by a flow of water from the meniscus to the NPs, generating a detectable decrease in optical intensity and eventually increase in size. This phenomenon was described in detail in ref. ^[200] and will not be further discussed in this thesis. Nevertheless, this study shows once again that OM can improve our understanding of the electrochemical responses measured in SECCM and SECM.

Chapter 2 INVESTIGATING THE COMPETING ELECTRODEPOSITION MECHANISMS OF NI-BASED NANOPARTICLES

This chapter was adapted with permission from ref. ^[158,201]. Copyright 2021 Wiley-VCH GmbH and 2022 Elsevier B.V. All rights reserved.

2.1 INTRODUCTION

As mentioned in **Chapter 1**, a parasitic contact resistance can be introduced when NPs are simply drop-casted on the electrode, preventing them from reacting at their full capacity. While incorporating the NPs into a conductive matrix is an effective strategy to solve this issue in the case of battery materials, it raises other issues in the case of electrocatalysts: electrocatalytic reactions are strongly dependent on the catalyst's surface state, which might be altered within a matrix. An increasingly popular alternative to avoid any issues related to heterogeneous electrical contacts with the electrode is the direct electrodeposition of NPs on the electrode.^[202] In addition to lowering the contact resistance, the strong anchoring provided by electrodeposition also prevents detachment of the NPs under operation. Moreover, electrodeposition allows to optimize material use as NPs will only be deposited where the electrode is also accessible to the electrocatalytic reaction.

It is also a rather versatile synthetic route: in the case of noble metals such as Au, different sizes, shapes, and surface densities can be obtained by changing the nature of the plating bath, the applied current/potential, or the deposition time.^[203] The output can even be predicted from the electrochemical trace. However, beyond noble metals, electrodeposition mechanisms are more complex so that the output is much more difficult to predict. In this chapter, we will use OM to gain more insight into the electrodeposition mechanism of Ni-based NPs from aqueous electrolytes in the context of their HER activity. This follows recent investigations of our group on the electrodeposition of Ag NPs^[204] and will allow to explore

the potentialities of OM for investigating the electrodeposition mechanism of different metals and oxides.

Ni-based NPs afford promising electroactivity in energy conversion and storage systems.^[205,206] They are indeed good electrocatalysts for water splitting and oxygen reduction,^[207,208] and can even outperform Pt in borohydride fuel cells.^[209] Typically, the electrodeposition of Ni-based materials yields a variety of electrochemical responses, depending on the electrolyte composition (pH, buffer strength,...) and electrode (nature and preparation). Owing to its competition with water reduction, the signature of Ni²⁺ reduction may be absent from the electrochemical curve.^[210–214] Such competition, by changing the local pH, produces either metallic Ni or Ni hydroxide, and the diversity of electrochemical responses makes the composition and electroactivity of the deposited material quite challenging to anticipate.^[214] Moreover, this competition does not only occur on the electrode, but also on the Ni NPs themselves, which start catalysing water reduction as soon as they nucleate. This leads to a self-terminating growth as the local pH increase caused by water reduction triggers the precipitation of a passivating Ni(OH)₂ layer on top of the NPs.^[211,212,214]

To apprehend the contributions of such competing chemical pathways, a complementary *in situ* signature is needed.^[215–220] For instance, coupling electrochemistry to high-resolution label-free OM^[218–220] has proved to be an effective strategy to monitor the electrodeposition of single NPs with high temporal resolution and sensitivity,^[204,221–224] as well as to differentiate metallic NPs from dielectric NPs^[225–228] or gas NBs.^[229,230] OMs have actually been proposed a long time ago as a means to depict *in situ* the growth of objects during electro-crystallization processes.^[231,232] These methods were mostly constrained to counting low population densities of objects >10 μm in size so as not to cope with the resolution and detection limits of optical systems. As discussed in **Chapter 1**, the last two decades have witnessed tremendous technical and fundamental advances in optics, so that OMs are now able to detect objects whose size, density or characteristic formation time is improved by several orders of magnitude (about 3). Compared to other imaging techniques such as SPMs (AFM or STM) or TEM, OMs often enable faster acquisition rates and higher throughput without disturbing the NPs or their diffusion layer. However, care must be taken to the illumination conditions as high power irradiation may induce solution heating, convection, or even trigger photochemical reactions, which may distort the visualization. OMs also allow versatility in the

experimental configurations, as individual NPs can be probed on macroscale electrodes,^[201,233,234] within micro- and nanoscale droplet cells as shown in **Chapters 2-4**,^[235–237] or at the tip-end of a NE.^[238] All this makes a significant improvement to the *operando* monitoring of electrochemical processes,^[239–242] and particularly of electrodeposition processes.

In this chapter, we then propose to monitor the electrodeposition of Ni-based NPs by OM. The OM used in this work is named interference reflection microscopy, IRM. It is a label-free OM, operated in reflection mode (i.e., epi-illumination), which relies on the detection of local changes in light scattering. These changes are then both related to local shape or size variations and, in terms of chemical analysis, to local changes in refractive index.^[243,244] The objective of this chapter is to show how such label-free OM can be used to gain insight into the electrodeposition mechanism of Ni-based NPs from the complementary *operando* recording of optical signatures. Particularly, this chapter develops the methodologies that can be employed to elucidate the formation of different types of NPs (in terms of shape, composition, or size), and therefore how IRM can be used to unravel the competition between different mechanistic paths.

2.2 RESULTS AND DISCUSSION

Herein, the cathodic nucleation and growth of individual Ni-based NPs on ITO, used as optical sensor and electrode, was scrutinized by IRM. The experimental configuration is depicted in Figure 2-1 (experimental details can be found in **Materials and methods**, section M.2.1). To capture the reported diversity in electrochemical signatures, we leverage the capability of SECCM to screen, at high throughput, multiple areas of the electrode. The experiments consist in confining a droplet of a 1 to 5 mM NiCl₂ + 0.1 M KCl electrolyte on the ITO with the tip-end of a micropipette. This allows constructing a microelectrochemical cell onto the ITO surface, which can be operated as a microelectrode whose size is controlled by the size of the pipette. As the ITO is transparent, it is also possible to image dynamically this microelectrochemical cell during electrochemical experiments in reflection mode, by IRM.

The optical imaging strategy consists in collecting, through a microscope objective and a camera, the full field image of the ITO surface (the focus is made on the ITO|electrolyte interface). Using a high magnification and high numerical aperture (oil immersion, x63, NA = 1.4) objective, one can image a ca. 50x50 μm^2 region of the ITO surface with a spatial resolution given by the camera's pixel size, ca. 55 nm in this case. Each pixel of the image (there are several millions in one image) collects the light reflected by a given localized region of the interface and then explores the physical and chemical processes occurring in this region. The local optical signal collected by each pixel, or averaged over a certain number of pixels, is hereafter denoted I_{opt} . As images are acquired continuously e.g., with a frequency of 20 frames per second (fps), it is then possible to capture, on each pixel, dynamic variations of I_{opt} during an experiment. As the images are made of millions of pixels each, such *operando* monitoring requires analysing millions of local variations of I_{opt} i.e., billions of data points.

In the IRM configuration, I_{opt} accounts for the interference between the plane wave reflected by the ITO|electrolyte interface (E_{refl}) and the spherical wave backscattered by the objects (in this case, NPs) sitting at that interface (E_{scat}) according to:

$$I_{opt} = |E_{refl} + E_{scat}|^2 = |E_{scat}|^2 + |E_{refl}|^2 + |E_{scat}| |E_{refl}| \cos \theta, \quad (2-1)$$

where θ is the phase lag between both waves. This enables their *operando* individual optical visualization inside the microelectrochemical cell. While the scattering term $|E_{scat}|^2$ may scale, for NPs, as d_{NP}^6 according to Mie theory, the interference term $|E_{scat}| |E_{refl}| \cos \theta$ is expected to scale as d_{NP}^3 , allowing for the detection of smaller NPs than what can usually be achieved by dark-field microscopy (DFM) for example. Moreover, the interference term also shows that dielectric NPs, which are more prone to electromagnetic field transmission (refraction) than (reflective) metallic ones i.e., which produce a larger phase lag θ between E_{refl} and E_{scat} , tend to be visualized with negative I_{opt} values (dark-contrasted features) while metallic ones are rather visualized with positive I_{opt} values (bright-contrasted features).

Hence, this tool should be able to distinguish between the two expected types of NPs. As a reminder of the literature survey presented in the introduction, it is presumed that depending on the experimental conditions, Ni or Ni(OH)₂ NPs will be formed under cathodic polarization. The methodology used to distinguish the features associated to these two types of NPs and to

analyse them is schematized in Figure 2-1c1-c3. To increase the identification sensitivity, a colour (RGB) camera is used, multiplying by three the optical information collected by each pixel as the images are recorded (and can be split) along three spectral ranges, respectively in the red (R, ≈ 615 nm), green (G, ≈ 540 nm), and blue (B, ≈ 450 nm). For analysis, each RGB image is split along these three colour channels as shown in Figure 2-1c3. The less sensitive G channel detects the most scattering NPs as bright-contrasted features. The G channel is then most likely sensitive to metallic NPs, such as the Ni NPs. Then, this population is subtracted from the more sensitive B channel, highlighting a new population of NPs detected as dark-contrasted features and assigned to Ni(OH)_2 NPs.

Apart from the location on the ITO surface, the role of Ni^{2+} concentration is also investigated. The results obtained at 1 and 5 mM Ni^{2+} are compared in the following sections.

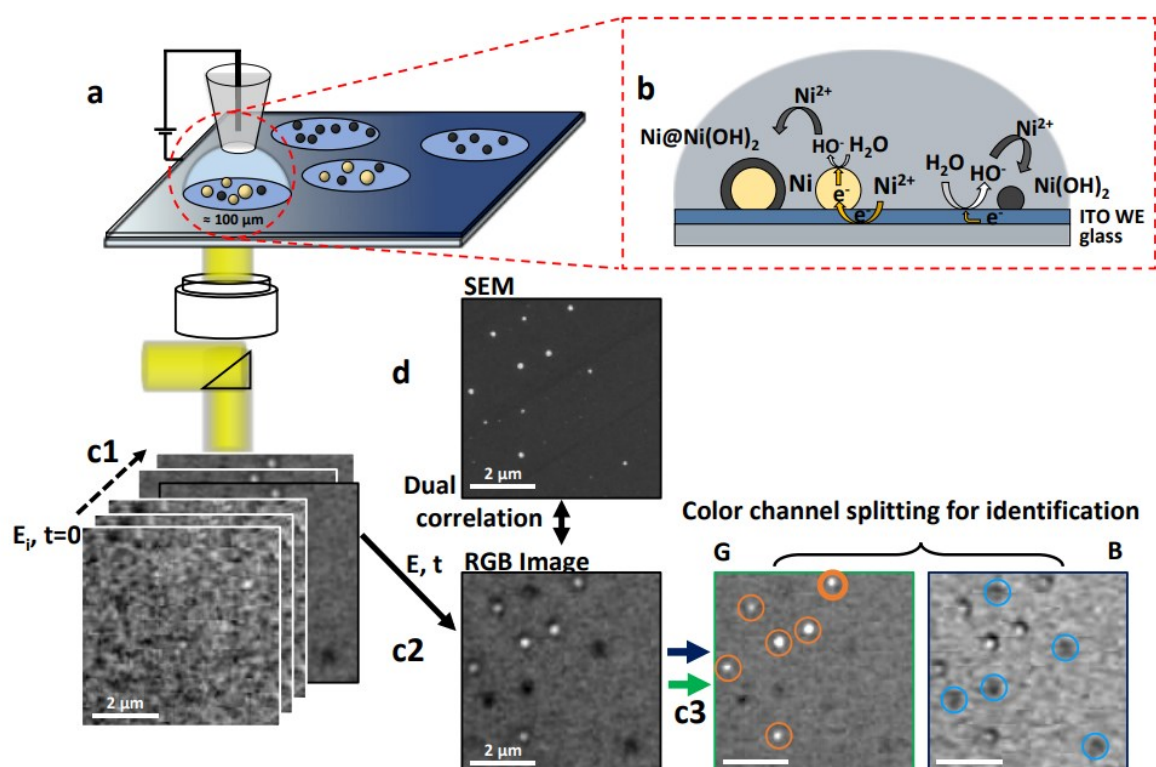


Figure 2-1. Experimental setup (a) used for probing inside individual microelectrochemical cells (dashed circle) the variability in Ni electrodeposition mechanisms (b) by *operando* OM (c1) and identical-location *ex situ* SEM (d). Scheme of the differentiation of NP populations by splitting the colour channels (c3) of each raw RGB image (c2) extracted from movies (c1) recorded over a $55 \times 39 \mu\text{m}^2$ region of each droplet submitted to a LSV.

2.2.1 LOW Ni^{2+} CONCENTRATION

Figure 2-2a1 and b1 show two representative LSV experiments performed 1 mM Ni^{2+} from microdroplets landed on different areas of the ITO. During these LSVs, the potential of the confined ITO microelectrode was swept from 0 to -1.6 V vs the Pt wire inserted into the pipette and serving as both counter and reference electrode. Meanwhile, the confined ITO microelectrode is monitored optically. Along with the corresponding electrochemical trace, Figure 2-2a2 and b2 present the ensemble-averaged I_{opt} variations for the two populations of optical features detected in the images (respectively Figure 2-1c2 and 2-2c1). In these plots, the I_{opt} values of all bright-contrasted features ($I_{opt} > 0$) detected in the G channel of a given image are averaged, giving rise to the orange curve in Figure 2-2a2. Similarly, after removal of these bright-contrasted features, the I_{opt} values of all novel dark-contrasted features ($I_{opt} < 0$) detected in the B channel are also averaged, giving rise to the blue curves in Figure 2-2a2 and b2. These I_{opt} curves then reflect the average behaviour of each NP population, the metallic Ni NPs as the orange curve and the $\text{Ni}(\text{OH})_2$ NPs as the blue curve.

From the electrochemical point of view, these experiments differ, respectively, from the presence or absence of a sharp reduction peak at -1.45 V vs Pt. From the optical point of view, they both show that nanosized features are formed. Indeed, from the optical images given in Figure 2-1c2 or 2-2c1, diffraction-limited features (i.e., of dimensions of the order of the wavelength, ca. 300 nm) appear on the images, suggesting NPs are formed during the electrodeposition process. However, they differ from the formation of either the two populations of bright- and dark-contrasted features or of only one population of dark-contrasted features as shown in Figure 2-2a2 and b2. This difference of behaviour is most likely rooted in the heterogeneities of the ITO surface that affect its electroactivity. Indeed, while investigating the HER on ITO by IRM, Ciocci *et al.*^[245] have shown that the formation of H_2 NBs competes with the formation of In NPs in spatially distinct regions. Similarly, Molina *et al.*^[246] have shown by DFM that the oxidation of Au NPs only occurs in specific regions of the ITO surface. Highly heterogeneous behaviours have also been observed for outer sphere electron transfer reactions at ITO electrodes by SECCM.^[247]

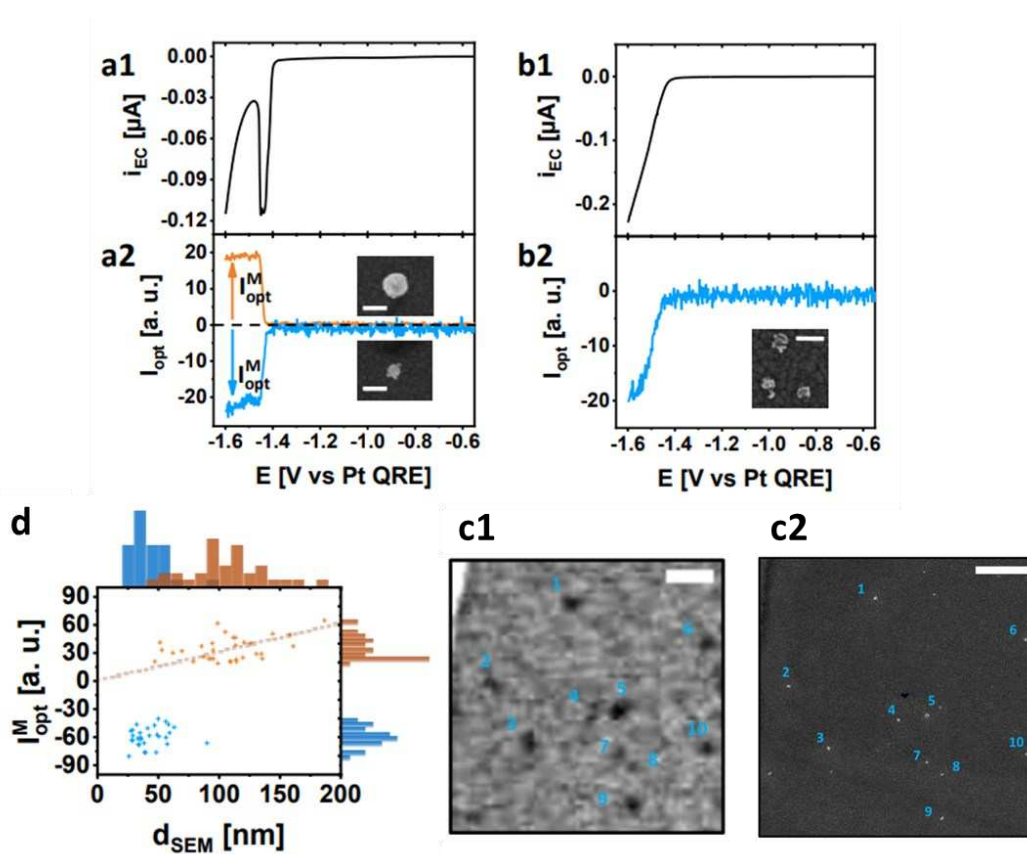


Figure 2-2. Examples of (a1, b1) LSVs of 1 mM NiCl₂ + 0.1 M KCl (scan rate: 50 mV s⁻¹, vs a Pt quasi-reference electrode, QRE) and (a2, b2) ensemble-averaged I_{opt} transients of the two different NP populations (orange: bright-contrasted NPs, N = 170 in (a2); light blue: dark-contrasted NPs, N = 31 in (a2) and 430 in (b2)). Insets: representative SEM images (scale bars: 100 nm). Optical image (grayscale) (c1) and identical-location SEM image (c2) recorded at the end of LSV (b1) (scale bars: 1 μm). (d) Identical-location IRM-SEM: I_{opt}^M , defined in (a2), vs size for bright-contrasted (a) and dark-contrasted NPs (b); dashed line provides a linear regression ($I_{opt}^M = \alpha d_{SEM}$, $r^2 = 0.88$) for the bright-contrasted NPs.

In the following, we first describe and analyse the observed electrochemical behaviours, then we discuss the optical data with a particular attention to complement the optical images with identical-location SEM images which allow a structural identification of the bright- and dark-contrasted features.

According to Moffat *et al.*,^[211,212] the reduction peak in Figure 2-2a1 ($\approx 70\%$ incidence from 20 LSVs) is related to Ni²⁺ reduction and the deposition of a Ni film. However, it is also concomitant to water reduction, resulting in the precipitation of a Ni(OH)₂ layer, which was

shown to enhance the catalytic activity of Ni for water reduction,^[248,249] until it completely blocks further charge transfer (if this is true for Ni NPs beyond the reduction peak as confirmed in **Chapter 4**, we will see in **Chapter 3** that this is not the case *during* the reduction peak). The sharp current decay then supports an overall self-terminating deposition mechanism encountered in Ni and other metal electrodepositions.^[212,250] If Moffat *et al.* generated Ni films, here the optical images (Figure 2-1c2 and 2-2c1) suggest the formation of NPs. Nevertheless, the ensemble-average I_{opt} transients in Figure 2-2a2 for each NP population show that on average, they evolve in a very narrow potential range until a limit value I_{opt}^M is reached. If I_{opt}^M evolves as an increasing function of particle size (as predicted from Mie theory for example), then the pace at which the limit is reached still advocates for a fast-terminated growth. Moreover, the potential at which the limit is reached is also correlated to the electrochemical peak, in line with a self-terminated growth mechanism.

To gain more insight into the mechanism, the same experiment was also conducted in a pH \approx 6 phosphate buffer (Figure 2-3). In this case, a slower basification and hence a later termination of the NPs' growth is expected. Indeed, in the timescale of the experiment, no peak was detected on the CV (Figure 2-3a, upper panel) and a continuous increase in I_{opt} was measured (Figure 2-3a, lower panel) as the NPs continuously grew and merged into a homogeneous film (Figure 2-3b,c).

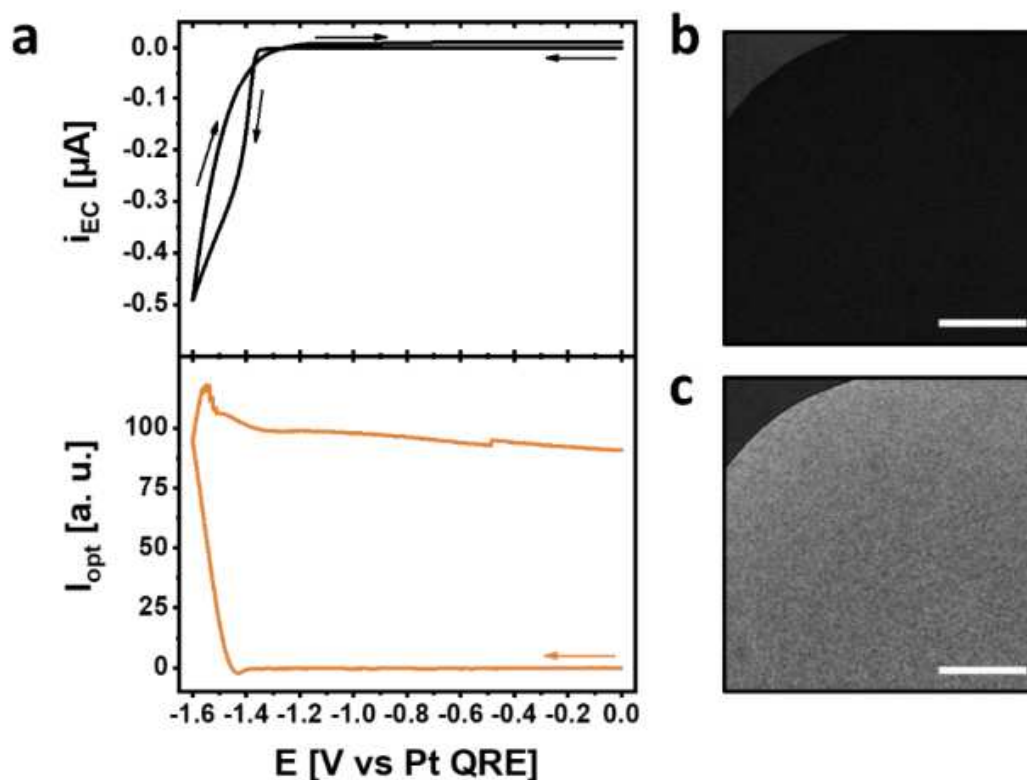


Figure 2-3. (a) CV of 1 mM NiCl_2 + 0.1 M phosphate buffer (top, $\text{pH} \approx 6$, scan rate: 50 mV s^{-1}) and average I_{opt} over a $20 \times 20 \mu\text{m}^2$ region of the wetted ITO electrode i.e., the dark region in (b) (bottom, from grayscale movie). (b) Optical image recorded before the CV. The dark region corresponds to the region where the electrolyte droplet wets the ITO, which is only partially imaged (grayscale, scale bar: $10 \mu\text{m}$). (c) Optical image recorded at the end of the CV showing that the whole wetted area of the ITO is uniformly transformed (grayscale, scale bar: $10 \mu\text{m}$).

In order to identify the objects formed during this reduction peak, and more generally during electrochemical experiments, we rely on *post-mortem* analysis of the samples. Identical-location SEM imaging of the ITO electrode was performed at the end of the LSVs. Figure 2-1d shows the SEM image of the ITO surface in the same location as the optical image presented in Figure 2-1c2. Identical-location SEM imaging is rather important, as it will probe, with higher spatial resolution, the structure and size of the objects detected optically. It might in turn allow to quantify the dynamic optical measurement by correlating I_{opt} to the actual size of the NPs.

From the SEM analysis, the bright-contrasted features are spherical NPs (Figure 2-2a2, top) with a $110 \pm 50 \text{ nm}$ size distribution (Figure 2-2d). As for each SEM-imaged NPs we also have

the limit value of the optical intensity at the end of its growth, I_{opt}^M , the distribution presented in Figure 2-2d provides ground for size- I_{opt}^M correlation. It shows that NP size roughly increases with I_{opt}^M . It further suggests that during NP growth, the I_{opt} value is also an instantaneous estimate of NP size, which might be relevant for understanding the dynamics of NP growth from the optical imaging (this will be discussed in **Chapter 3**). It further allows estimating the limit of detection, lod, of IRM. The lod is typically estimated based on the linear regression of the size- I_{opt}^M correlation, such as in Figure 2-2d, and the noise level of the I_{opt} transients (examples in Figure 2-2a2 and b2). It corresponds to the size at which the regression is equal to three times the noise level. For the bright-contrasted features, one estimates a lod of the order of 20 nm. From both their regular spherical shape and boundary element method (BEM) simulations of the optical response of Ni and Ni(OH)₂ NPs (Figure 2-4a), these bright-contrasted NPs are most likely composed of metallic Ni. According to Moffat *et al.*, Ni should be covered by a passivating Ni(OH)₂ layer by the end of the LSV. If this cannot be ascertained during the fast NP growth step (I_{opt} rise) nor by SEM, a slight I_{opt} decrease is observed after this growth step, which can be attributed to the formation of a Ni(OH)₂ layer according to BEM simulations (Figure 2-4b,c).

The BEM simulation of interferometric microscopy images was first proposed by Ünlü's group in the Single Particle Interferometric Reflectance Imaging Sensor (SP-IRIS) configuration.^[251–253] In this configuration, the NP is immobilized on a flat semi-infinite reflective substrate (Si) covered with a thin dielectric layer (SiO₂), and is imaged from the top, in reflection mode. This model was straightforwardly adapted by us to the IRM configuration, where the NP is imaged from the backside through the glass coverslip and the ITO, which serves as reflective surface.^[227,230]

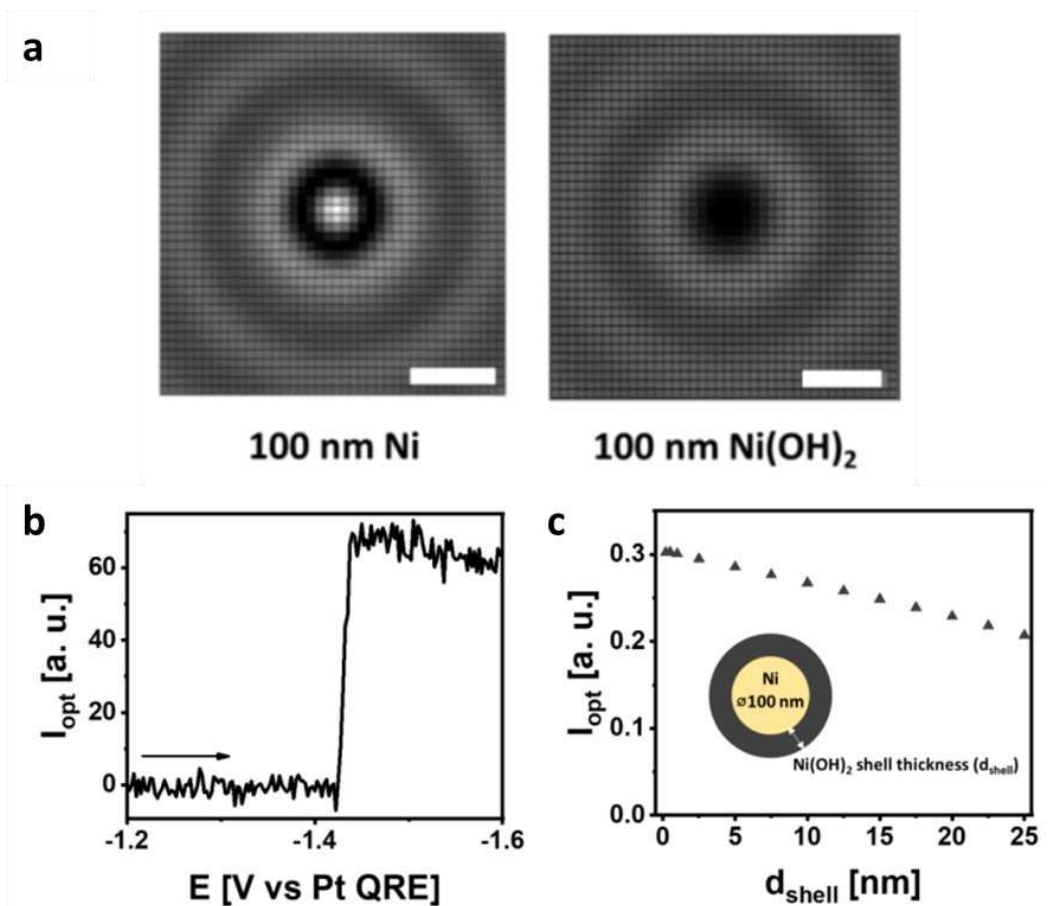


Figure 2-4. (a) BEM simulations of the optical image of 100 nm-sized NPs of Ni and Ni(OH)₂, respectively, demonstrating the discrimination potential of IRM (incident wavelength: 490 nm, scale bars: 500 nm). (b) Experimental I_{opt} transient showing the formation of a single bright-contrasted NP (final size from I_{opt}^M -size correlation: 230 nm) which exhibits a noticeable decrease in I_{opt} following its appearance (green channel). (c) Simulations of the optical response of a Ni sphere (diameter: 100 nm) embedded in a growing shell of Ni(OH)₂. These simulations were performed for an incident wavelength of 540 nm corresponding to the maximum sensitivity of the green channel of the camera, the channel which was used for the analysis of the bright-contrasted features. The refractive indices of ITO (1.93 at 540 nm) and Ni (1.90 + 3.55i at 540 nm) were obtained from an online database^[254] and interpolated to the desired wavelength. The refractive index of Ni(OH)₂ (1.50 at 540 nm) was obtained from ref. ^[255]. The ambient medium was assumed to have the same refractive index as pure water (i.e., 1.33).

The identification of the dark-contrasted NPs is a bit more challenging. Indeed, the dimmer bright-contrasted NPs and many dark-contrasted ones were lost or moved during the surface rinsing process necessary to perform the SEM analysis. The dark-contrasted features that

could be co-localized by SEM after the LSVs resemble the objects imaged either in Figure 2-2a1 or b1. They present smaller diameters (40 ± 15 nm) than their bright-contrasted counterparts and have a more fractal shape (Figure 2-2a2 bottom, b2, and c2) similar to those obtained by cathodic electrosynthesis of $\text{Ni}(\text{OH})_2$ NPs.^[213,256] The absence of the Ni^{2+} reduction signature in the second type of LSV (Figure 2-2b1) and the concomitant appearance of NPs with the water reduction wave (Figure 2-2b2) suggest that they result from the precipitation of $\text{Ni}(\text{OH})_2$. The size distribution of the $\text{Ni}(\text{OH})_2$ NPs is depicted in Figure 2-2d as a function of their individual I_{opt}^M value. There is no clear size- I_{opt}^M correlation in this case, but a lod can still be estimated from the noise level of the optical signal, which is again <25 nm.

We summarize this section presenting the methodology used to track the electrodeposition of Ni-based NPs by IRM. Using micropipettes to confine a micrometric droplet of electrolyte on an ITO surface, it was possible to drive the reduction of a low concentration Ni^{2+} solution at micrometric ITO electrodes. Electrochemically, two characteristic behaviours are observed, showing either a sharp reduction peak associated to the formation of metallic Ni or, at more negative potentials, a wave likely due to water reduction. The dynamic optical monitoring of these processes suggests the formation of NPs, and particularly two types of NPs. During the sharp reduction peak, spherical Ni NPs are formed (attested by their positive contrast, identical-location SEM imaging, and BEM simulations). In the absence of this peak, fractal $\text{Ni}(\text{OH})_2$ NPs are formed (attested by their negative contrast, identical-location SEM imaging, and BEM simulations). These $\text{Ni}(\text{OH})_2$ NPs are produced owing to water reduction, which induces a local basification of the solution near the electrode. The optical monitoring is used to get different mechanistic insights. First, the dynamics of NP growth can be obtained from individual I_{opt} transients. Identical-location SEM analysis provides a correlation between the size of the Ni NPs and their optical signature. It shows that the growth of Ni NPs is a self-limiting process, most likely owing to the interference with water reduction. Indeed, $\text{Ni}(\text{OH})_2$ is also formed during the sharp reduction peak of Ni electrodeposition, suggesting that Ni^{2+} reduction is concomitant to water reduction, and might prevent the Ni NPs from growing further as previously suggested in the literature.^[211,212,214]

2.2.2 HIGH Ni^{2+} CONCENTRATION

Thanks to this mechanistic platform, we then continue our mechanistic analysis of Ni electrodeposition at higher Ni^{2+} concentration. When the Ni^{2+} concentration was increased to 5 mM, the same variability in electrochemical responses was observed, showing either the Ni^{2+} reduction peak (37% occurrence from 54 LSVs), or only water reduction. An example of the latter case is presented in Figure 2-5a1. Some chosen optical images associated to this LSV experiment are presented in Figure 2-5b. They show that the process starts with the appearance of dark-contrasted $\text{Ni}(\text{OH})_2$ NPs shortly after the onset of water reduction, like for the analogous LSV at 1 mM in Figure 2-2b1. However, bright-contrasted Ni NPs also appear, but now at more negative potentials. The same dynamic analysis of individual features is undertaken. Figure 2-5a2 shows, as Figure 2-2, the ensemble-average behaviour for the Ni and $\text{Ni}(\text{OH})_2$ NPs (as the orange and blue curves, respectively). These curves attest from the nucleation and growth dynamics of the ensemble. In contrast to what was observed at 1 mM, a gradual increase of the ensemble-averaged I_{opt} is observed for both the dark-contrasted $\text{Ni}(\text{OH})_2$ and the bright-contrasted Ni NPs (Figure 2-5a2).

It is particularly different for the Ni NPs and might call for a different electrodeposition mechanism. It is possible that this slower dynamic is because Ni NP growth is not self-limiting anymore and a slower growth of each individual Ni NP is detected. To explain this behaviour, one could invoke that the earlier water reduction accompanied with the nucleation and growth of $\text{Ni}(\text{OH})_2$ NPs lowers the local pH, preventing the formation of a passivating $\text{Ni}(\text{OH})_2$ shell around the Ni NPs, whose growth would then not be completely stopped.

It could also be that instead of the slow growth of each individual NP, their progressive nucleation on the electrode surface is rather probed. One way to rationalize this is to look at single NPs, and to draw the I_{opt} traces for each individual NP. Some of them are presented in Figure 2-5a3. Interestingly, at the single-NP level, the I_{opt} transients still present a sharp rise, suggesting again the self-terminating growth of individual NPs. As pointed out for galvanic replacement at single Ag NPs,^[220,222] such individual behaviour is totally obscured in the ensemble response, which then reflects the difference in the onset (nucleation) potential of each NP.

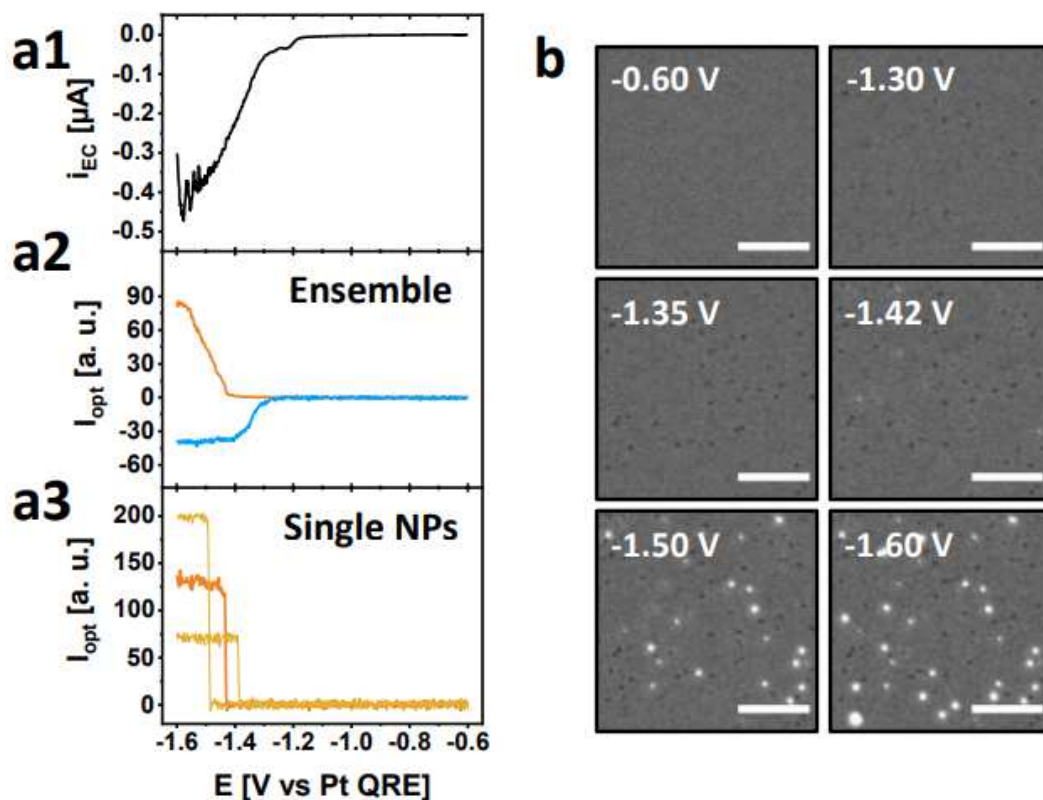


Figure 2-5. (a1) LSV of 5 mM NiCl₂ + 0.1 M KCl (scan rate: 50 mV s⁻¹), (a2) ensemble-averaged I_{opt} transient of both NP populations (orange: bright-contrasted NPs, N = 354; blue: dark-contrasted NPs, N = 427), (a3) single-NP I_{opt} transients of the median, first and third quartile of the Ni NP population. (b) Optical images acquired during LSV (scale bars: 5 μm).

These observations are consistent with literature data. Unlike in Figure 2-2, even if water reduction is easier than Ni²⁺ reduction in the probed area, Ni NPs are still able to nucleate without showing the Ni²⁺ reduction signature. This agrees with Penner *et al.*^[210] who demonstrated, by *post-mortem* SEM analysis, the indirect electrodeposition of pure Ni NPs on carbon electrodes even though water reduction was predominant. The same indirect Ni NP growth is demonstrated here with a wider diversity of phenomena observed thanks to the *in situ* complementary optical monitoring.

This dynamic *in situ* analysis allows a richer description of the mechanisms involved in Ni NP electrodeposition. The onset potential distribution of individual Ni NPs is presented in Figure 2-6, along with their I_{opt}^M value (equivalent to their final size), for both Ni²⁺ concentrations. For 1 mM Ni²⁺ (Figure 2-6a), the onset potential distribution presents a narrow peak, mimicking the sharp self-terminating Ni²⁺ reduction peak in the LSV (Figure 2-2a1). The sudden drop in

nucleation events highlights the increased predominance of water reduction at potentials below -1.5 V. Moreover, the final NP size decreases as its onset potential becomes more negative: the earlier a NP nucleates, the larger it will be by the end of the LSV, as it will have had more time to grow. This situation is generally encountered in progressive electrochemical nucleation processes such as NP electrodeposition^[204] or gas NB generation.^[230] If it is also detected during the self-limited growth of Ni NPs, it is likely because the pH increases homogeneously over the entire electrode upon water reduction. Overall, water reduction limits Ni²⁺ reduction not only by limiting the growth of already nucleated Ni NPs, but also by limiting the formation of new nuclei.

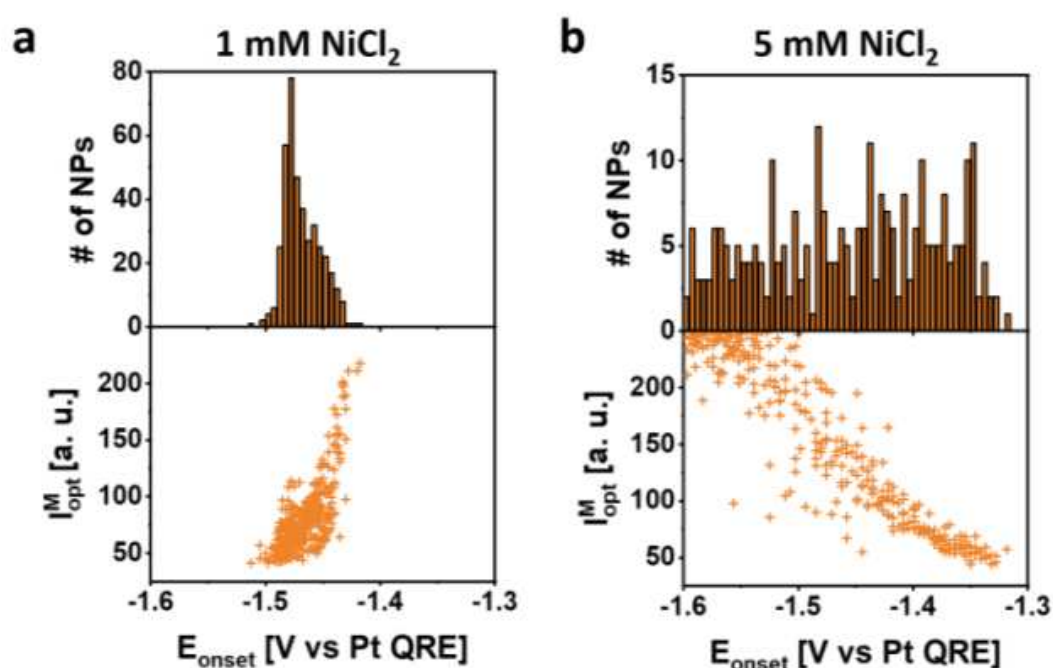


Figure 2-6. Onset potential distribution of the Ni NPs and corresponding I_{opt}^M values for 1 mM (a, N = 170) and 5 mM Ni²⁺ (b, N = 334).

Contrarily, for 5 mM Ni²⁺ (Figure 2-6b), the nucleation frequency of new Ni NPs is rather constant over the explored potential range. As mentioned above, the growth of individual NPs is still self-terminating (Figure 2-5a3). The sum of all the sharp (<0.3 s) individual events of NP nucleation and growth, at a constant frequency, then rationalizes the observed ensemble-averaged slowly increasing optical response of Figure 2-5a2. The latter is then rather indicative of an accumulation of newly nucleating Ni NPs. Meanwhile, unlike for 1 mM Ni²⁺, the final size of the NPs increases as their onset potential becomes more negative. This seemingly

counterintuitive behaviour shows the influence of the electrode potential on the competition between water and Ni^{2+} reduction. If the initial formation of $\text{Ni}(\text{OH})_2$ NPs suggests water reduction dominates, the competition turns in favour of Ni^{2+} reduction at more negative potentials, the growth rate of Ni NPs increasing with overpotential. Interestingly, during the first 100 mV of the overall indirect deposition (Figure 2-6b), NPs with a rather narrow size (I_{opt}^M) distribution are produced, at least much narrower than upon direct deposition (Figure 2-6a). In agreement with Penner *et al.*, it suggests that in this electrodeposition regime, one can control finely the size (and dispersion) of the electrodeposited NPs.

2.3 CONCLUSION

In conclusion, high-resolution OM coupled to electrochemistry and complemented with correlative SEM helps elucidating the complex mechanisms associated to the electrodeposition of Ni-based NPs. The growth of metallic Ni and/or $\text{Ni}(\text{OH})_2$ NPs is identified based on *in situ* optical differentiation with sub-25 nm lod. The preferential direct formation of both materials is usually rationalized based on the identification of the signature of either Ni^{2+} or water reduction in the electrochemical trace. *In situ* OM shows this is generally more complex. In particular, metallic Ni NPs can still nucleate and grow, indirectly, below the water reduction wave, although the Ni^{2+} reduction signature is invisible. Investigating these direct and indirect mechanisms at the single entity level highlights that individual NPs always experience a fast self-terminating growth, in agreement with the shape of the direct Ni^{2+} reduction signature. Contrarily, the indirect mechanism is characterized, from an ensemble-averaged examination, by a gradual growth. This difference reflects the change in nucleation dynamics, which is related to the competition between Ni^{2+} and water reduction. Overall, the proposed methodology allows probing, and in turn predicting *in situ* and in real time the size and surface density of Ni NPs. The methodology can be extended to the electrodeposition of the many NPs whose electrochemical signature lacks reproducibility or is difficult to identify. Particularly, the visualization of hydroxides should apply to electro-crystallization processes.

Chapter 3 ON THE ORIGIN OF THE REDUCTION PEAK IN Ni ELECTRODEPOSITION

In **Chapter 2**, we have shown how OM can be used to detect NPs of different compositions and to monitor their growth semi-quantitatively. Comparing the behaviour of single NPs to that of the ensemble revealed different routes for Ni electrodeposition, leading either to the formation of both Ni and Ni(OH)₂ NPs, or only of Ni(OH)₂ NPs. The objective of this chapter is to provide quantitative insights into the underlying mechanisms by using OM to assess the electrochemistry of individual NPs.

This chapter was adapted with permission from ref. ^[159]. Copyright 2022 Wiley-VCH GmbH.

3.1 INTRODUCTION

If it is now possible to predict more precisely the composition of the electrodeposited NPs based on the electrochemical trace, it remains challenging to quantify the exact amount of Ni (and Ni(OH)₂) NPs that was deposited on the electrode (loading), which is crucial for correctly assessing its catalytic activity. Even if we have clearly established a correlation between the formation of Ni NPs and the reduction peak, Moffat *et al.*^[257] have shown by SECM that it is also correlated to a pH increase, meaning that it also contains a significant contribution from water reduction. This is not surprising since water reduction is the reason why a passivating Ni(OH)₂ layer forms on top of the Ni NPs and limits their growth. The objective of this chapter is to evaluate the contributions of growth and catalysis to the reduction peak. To achieve this, we use smaller pipettes so that all the NPs responsible for the electrochemical signature are visualized all at once by OM.^[258–260] Such methodology provides both the global electrochemical response of the ensemble of NPs (growth + catalysis) and the optical response of all individual NPs (growth). By bridging the gap between microscopic and macroscopic measurements,^[261] it should provide a unique and complete (local to global,^[262] or single to ensemble)^[263] identification and quantification^[263] of electrocatalytic phenomena at the nanoscale.

To obtain an even more precise picture, as schematized in Figure 3-1, electrochemistry in a micro-sized droplet is coupled to different correlative microscopies with different resolutions, revealing electrochemistry at different scales, from the micrometre to the nanometre scale. First, an *operando* high-temporal-resolution OM is employed, which is then complemented by different *post-mortem* identical-location high-spatial-resolution microscopies (SEM, EDX, and AFM). The objective is to adapt the resolution of each technique so that by combining them all, we reconstruct an image containing all the information from each of these techniques with the highest possible resolution (spatial, temporal, and structural/chemical). The *operando* microscopy used here is the same label-free refractive index-based OM, IRM,^[8] as presented in **Chapter 2**.

However, the methodology presented here applies to any other (optical) microscopy available to image electrochemistry *operando*.^[241,242,261,264–267] This methodology is made possible through the intensive assistance of machine vision concepts such as border following, centroid finding, template matching, and unsupervised machine learning algorithms. The latter are of particular interest since they deal with unlabelled samples to reveal internal data structure and reduce data dimensionality, ruling out the possible human bias during data processing.^[268–270] Recent reviews in the fields of microscopy,^[271,272] atomic-scale simulation,^[269,273] biology,^[268] etc. highlighted the power of unsupervised machine learning algorithms for clustering particle distributions, biological tissues, and atomic structures. However, it is still poorly exploited in electrochemistry.^[267,270,274–277] In this chapter, we show how such automatized data treatment can be constructed and used to provide various local descriptors for each (and all) NP(s) imaged, which can be used to reconstruct the global electrochemical response and in turn unveil the nanoscale contributions contained in the electrode response.

In the case of the electrodeposition of Ni NPs, the interest of an *operando* imaging is that seeing it from the local (individual NP) and global perspectives, one can reveal more than just the sum of the individuals^[263] and quantify the intrinsic electrocatalytic activity of Ni NPs for water reduction, or HER, while they are produced. Owing to the high reactivity of metallic Ni, this is a challenging measurement task. To the best of our knowledge, it was precisely addressed only through the surface interrogation mode of SECM (SI-SECM).^[278] This technique uses a UME to deliver a reactant close to a surface, which will titrate a specific surface species.

In this case, the oxidized form of FcMeOH was used to titrate the hydrogen intermediates formed on the surface of Ni during the HER, which allowed quantifying the catalytic activity of metallic Ni while it was only very slightly oxidized.

3.2 RESULTS AND DISCUSSION

3.2.1 ELECTRODEPOSITION OF Ni NPs

As illustrated in Figure 3-1a and like in **Chapter 2**, the experimental setup is a combination of a pipette-confined droplet electrochemical cell and a wide-field OM (IRM) in which an ITO-coated glass coverslip acts both as optical sensor and as working electrode for the electrodeposition of Ni NPs. The pipette was filled with a Ni²⁺-containing solution, a Pt wire (acting as quasi-reference counter electrode, QRCE) was placed inside of it from the top, and then it was approached to the ITO surface until a droplet cell of approximately 25 μm in radius was formed. The whole area of the ITO surface wetted by the electrolyte droplet can then be monitored optically by illuminating from the backside through a 63x oil immersion optical objective, and collecting the light reflected by the droplet|ITO interface after passing back through the same objective onto a CMOS camera (details in **Materials and methods**, section M.2.1). A typical optical image of the ITO surface recorded under such reflecting condition is provided in Figure 3-1b and shows as the darkest oval region the droplet|ITO interface.

A LSV is performed at the working ITO microelectrode confined by a droplet cell containing 1 mM Ni²⁺ + 10 mM KCl. Figure 3-1c represents the LSV obtained during a reductive potential scan engaging the electrodeposition of Ni at the ITO surface. At ca. -0.6 V, the current starts decreasing (region denoted as 1 in Figure 3-1c). This can be presumably related to the onset of the ORR (Equation 3-1) on the ITO surface.^[259]



Further decreasing the potential (region 2 in Figure 3-1c) leads to a peak at ca. -1.3 V related to Ni²⁺ reduction (Equation 3-2).^[257,279]



This process is monitored optically at a frequency of 20 images per second and such *operando* optical observation confirms, as discussed in **Chapter 2**, the electrodeposition of Ni NPs. Indeed, within the droplet region, detected as the dark oval region in Figure 3-1b, bright-contrasted features start to appear as soon as the electrode potential is more negative than ca. -1.1 V. Some examples of such bright-contrasted features are provided in the zoom of Figure 3-1b.

After sweeping the potential beyond the peak at ca -1.35 V, the current is finally decreasing again because of the solvent break-down, most likely catalysed by the deposited Ni NPs. This current step is denoted as region 3 in Figure 3-1c. The exact origin of the peak at ca. -1.3 V (region 2 in Figure 3-1c) is still not clear in the literature.^[280] We have shown in **Chapter 2** that it is related to the two-electron reduction of Ni²⁺ into metallic Ni at the origin of the NPs' formation. However, this reaction competes with the ORR (Equation 3-1) and the HER (Equation 3-3), which both locally increase the pH (as evidenced by Moffat *et al.*)^[257] and thus favour the precipitation of Ni(OH)₂ (Equation 3-4).



Therefore, the rise in reduction current detected in region 2 in Figure 3-1c might also probe the onset of autocatalytic water reduction at the Ni NPs or Ni(OH)₂-coated Ni NPs, Ni(OH)₂ being known to enhance the catalytic activity of various metals.^[281,282] However, further Ni(OH)₂ precipitation might be quickly inhibited as the Ni(OH)₂ layer eventually blocks charge transfer, explaining why the reduction current rapidly drops.

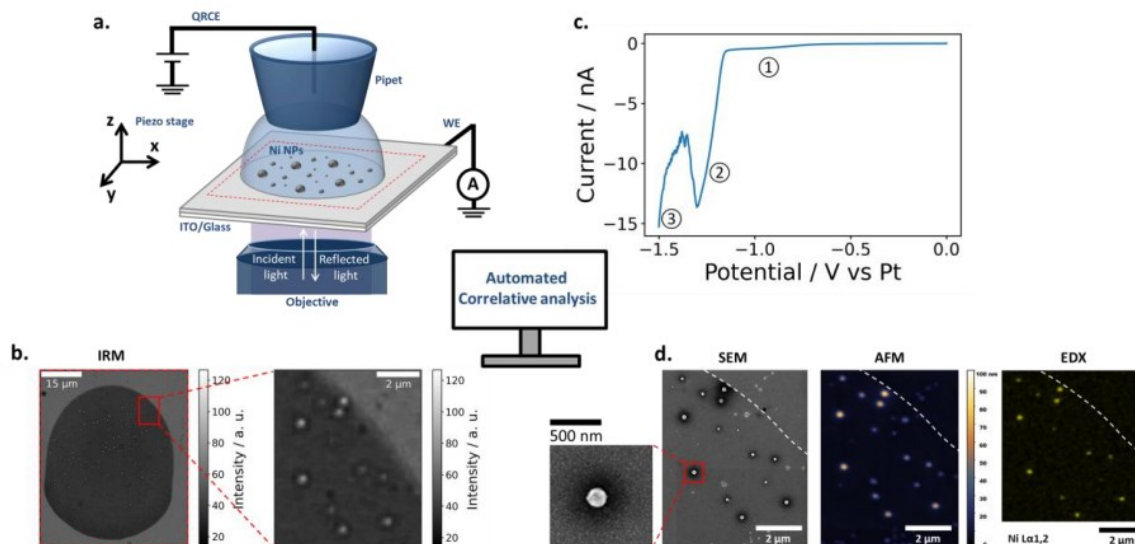


Figure 3-1. Correlative *operando/post-mortem* multi-microscopy approach for probing the electrochemistry of Ni NPs. (a) Schematic representation of the experimental setup used for probing the electrodeposition and electrocatalytic properties of Ni NPs from a 1 mM NiCl₂ + 0.1 M KCl electrolyte droplet confined onto an ITO electrode by a micropipette (ca. 25 μm in diameter). (b, c) *Operando* optical monitoring with (b) examples (here at -1.5 V vs Pt) of optical images (large field-of-view and region of interest, ROI, at the droplet's border) recorded during (c) a LSV from 0 to -1.5 V vs Pt at 100 mV/s. (d) *Ex situ* SEM (with enlarged view of a single NP), AFM and EDX maps of identical surface locations recorded *post-mortem* after the opto-electrochemical experiment.

The objective of this chapter is to decipher the contribution of the competing reactions contained in the electrochemical signature from the optical images. To do so, the *operando* optical images recorded during the LSV are extensively analysed. The positions of all the NPs in the optical images are localized and the evolution of their optical intensity is recorded during the whole experiment and at the single NP level. This procedure is named hereafter collecting single “optical transients”, which act as real-time reporters of the NP’s activity. Using optical modelling, it was possible to quantify, from such optical transients, the dynamic growth and electrocatalytic activity of the NPs.^[283,284]

Herein, the optical data collected for each NP are complemented with correlative identical-location *post-mortem* SEM, EDX and AFM analyses, as illustrated in Figure 3-1d in a small region of interest (ROI). We will show how the structural data collected by such complementary images allow to fully unravel the NPs’ geometry and composition, and can be

used, if properly correlated, as calibration procedure for the optical measurement, making optical transients quantitative.^[283]

3.2.2 OPTICAL IMAGE ANALYSIS

Colour optical images were acquired during the LSV at a 20 Hz frequency and were synchronized with the potential ramp. The very first image is considered as the background and is subtracted from all following images. Each colour image is then split along its three colour channels and the red one is selected for data treatment as it presents the best signal-to-noise ratio for the Ni NPs. The Ni(OH)₂ NPs, which should not contribute to the electrochemical response, are also practically invisible in the red channel. The last frame of the optical monitoring, recorded at -1.5 V, is shown in Figure 3-2a. It highlights the presence of Ni NPs appearing as bright-contrasted features.

The first descriptor to be evaluated from the optical images was the position of all newly formed NPs. Their exact locations in the droplet cell were extracted (Figure 3-2b) by an automatized procedure inspired from the Crocker and Grier centroid finding algorithm^[285] and further refined to reach sub-pixel resolution (usually of ca. 1/10 pixel i.e., 5 nm here). The contour of the droplet cell was also retrieved using a border following algorithm^[286] to sort optical features and systematically remove them if located outside of the droplet boundary. It is worth noting that the contour analysis run on all images in the sequence indicates there is no or negligible droplet expansion in the course of the experiment. The contours of the first and last image overlay perfectly in Figure 3-2b.

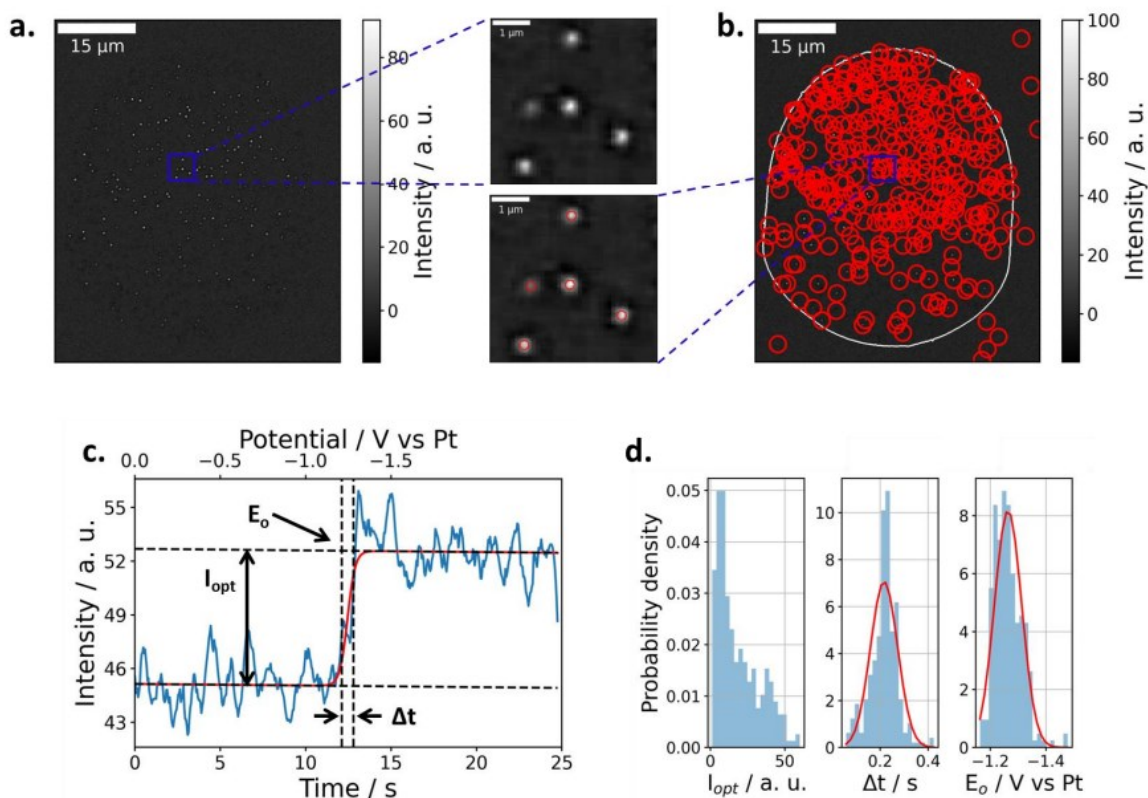


Figure 3-2. Automated NP detection procedures used to extract individual NP descriptors from *operando* optical images. (a) Background-subtracted image of the ITO electrode (large field-of-view and ROI) when polarized at -1.5 V during the LSV (raw image in Figure 3-1b). (b) Optical image (large field-of-view and ROI) illustrating the droplet border localization and the detection of NPs using the centroid finding algorithm, where each red circle refers to a localized optical mass and in which the droplet cell contour has been retrieved by a border following algorithm. (c) Example of optical transient from which three descriptors are extracted. It was obtained by evaluating the change in pixel intensity in a 4x4 pixel ROI around the detected NP location. (d) Dispersion graphs of the NPs' final background-subtracted optical intensity (I_{opt}), growth time (Δt) and onset potential (E_0) obtained from the temporal analysis described in (c) with best normal distribution fit (red curve).

From the last image depicted in Figure 3-2b, the positions of 340 NPs were found, stored and further used as the anchor points in the next sections. At first sight, the NPs seem randomly deposited at the electrode surface with a rather homogeneous radial distribution.

A dynamic analysis is also conducted for each NP, as illustrated in Figure 3-2c. The local optical intensity fluctuations (i.e., optical transients) in each NP region (defined as a 4x4 pixel region centred on the stored NP coordinates) are collected, filtered and analysed individually to

finally extract three other essential NP descriptors: the NP final optical intensity (I_{opt})⁴, the NP growth time (Δt) and the NP onset potential (E_o). The latter are illustrated in the transient example of Figure 3-2c and summarized in the distributions of Figure 3-2d. I_{opt} corresponds to the maximum variation of the optical intensity from the moment when a single NP is detected on the image, emerging from the background, to the moment when its intensity reaches a steady value. The duration of this variation is noted Δt , while the moment the NP is first detected is named the onset time, t_o , which is converted into an onset potential, E_o . I_{opt} is theoretically related to the final NP volume, V , from Equation 2-1 in **Chapter 2**. Similarly, Δt corresponds to the duration of the NP's growth, and is then also related, as I_{opt} , to the final NP volume. The E_o distribution follows a normal distribution, with a mean value of $\mu_{E_o} = -1.27 V$, close to the peak potential detected in the LSV in Figure 3-1c (-1.30 V). Actually, like in **Chapter 2**, the E_o distribution mimics the peak pattern in the LSV in Figure 3-1c, indicating that the onset of NP formation is indeed related to the onset of the reduction current.

3.2.3 DIMENSIONS OF THE NPS

The final NP size is evaluated by SEM. The characterization of the NPs' structure is usually achieved by *post-mortem* electron microscopy analysis in a very small ROI and by considering the results representative of the whole population. However, in order to correlate the final NP size with its optical descriptors (Δt and I_{opt}) and later evaluate the electrochemical current associated to NP growth or structure-activity relationships at the single-NP level, it is crucial to carry out a full correlative comparison between the optical and electron microscopy images. The method used is described below (details in **Materials and methods**, section M.4.2).

⁴ Equivalent to I_{opt}^M in **Chapter 2**.

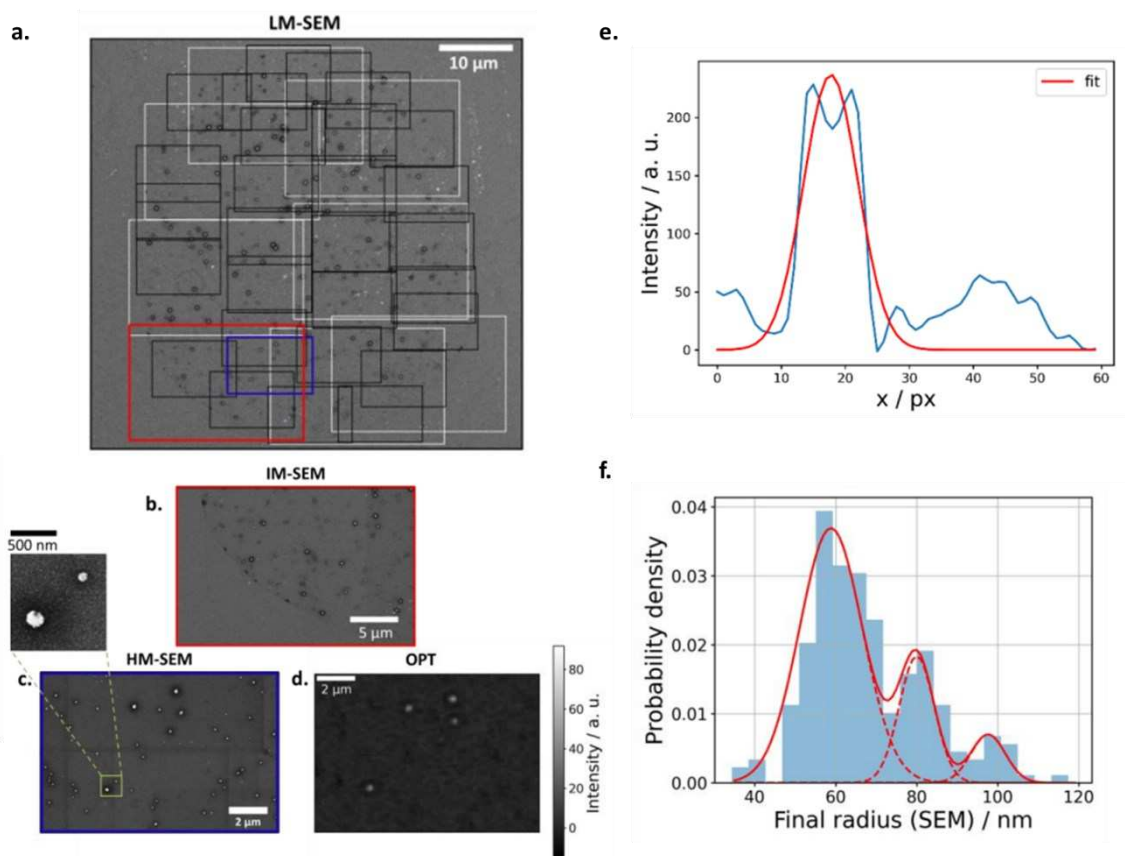


Figure 3-3. Automated feature-based image alignment in OM and SEM for accurate co-localization (recognition) and sizing of individual NPs. (a) Low-magnification (LM) SEM image of the droplet cell with the contours of intermediate- (IM, white) and high-magnification (HM, black) images overlaid after template matching. The collection of the IM and HM images constitute the image database used for NP sizing. (b) Example of IM SEM image, (c) HM SEM image (with enlarged view of two NPs), and (d) corresponding optical image. (b) and (c) can be located in (a) by using the colour code. (e) Example of SEM intensity profile used to size the NPs and Gaussian fit (red line). (f) Size dispersion graph of the NPs detected optically but sized from the SEM images.

Herein, SEM at low magnification (LM) allows localizing the micrometric footprint of the droplet cell and the electrodeposited NPs in a relatively straightforward way. However, sizing the NPs by SEM requires acquiring high-magnification (HM) images, limiting the SEM field-of-view or the image size, and therefore greatly complicates the correlative approach. We then resorted to a template matching algorithm to localize and assess the size of all the NPs produced on the electrode.

Briefly, a database of higher-resolution SEM images is constructed by acquiring intermediate- (IM) and high-magnification (HM) SEM images within the droplet footprint to fully cover its surface area. Then, the template matching algorithm was employed to overlay all HM and IM SEM images on the LM image (Figure 3-3a) and to prioritize them. In this way, a single NP selected on the LM image can be identified both in the IM image (Figure 3-3b) and in the most appropriate HM image (Figure 3-3c) from the image database. Once identified, its lateral size is extracted automatically with high accuracy based on a Gaussian fit (Figure 3-3e). Finally, the optical and LM SEM images were correlated using reference NPs (positions known on both images), enabling to identify at a high resolution the final lateral size of each optically detected NP. The automated comparison of the optical and electron microscopy images confirms that SEM reveals many more NPs than the bright-contrasted features observed optically in the red colour channel of the optical images. Actually, SEM detected exactly 919 NPs vs 340 NPs detected optically. The size dispersion graph of the NPs detected optically and sized by SEM is shown in Figure 3-3f.

3.2.4 CHEMICAL COMPOSITION OF THE NPs

In **Chapter 2**, we have shown that the detection of NPs in the different colour channels of the images as well as the optical contrast could significantly vary depending on NP composition and size, offering an elegant way to distinguish NP compositional differences and to modulate the sensitivity of the optical method.^[280] During the LSV, in addition to reducing Ni^{2+} to Ni, biasing the electrode negatively also causes local pH fluctuations that lead to the precipitation of $\text{Ni}(\text{OH})_2$ NPs which are detected rather as dark-contrasted features in IRM, as illustrated in Figure 3-4a. This is the reason why more NPs were detected by SEM than by IRM. In the red channel, IRM is selective of the Ni NPs. The $\text{Ni}(\text{OH})_2$ NPs are mostly detected in the blue channel as dark-contrasted features, as discussed above and in **Chapter 2**. If we add the number of dark-contrasted $\text{Ni}(\text{OH})_2$ NPs detected in the blue channel to the number of bright-contrasted Ni NPs detected in the red channel, the total number of NPs detected optically (882, 96%) is close to that detected by SEM (919). In addition, the ITO layer turned out to be very inhomogeneous, revealing nanoscale inclusions that can also be detected optically.

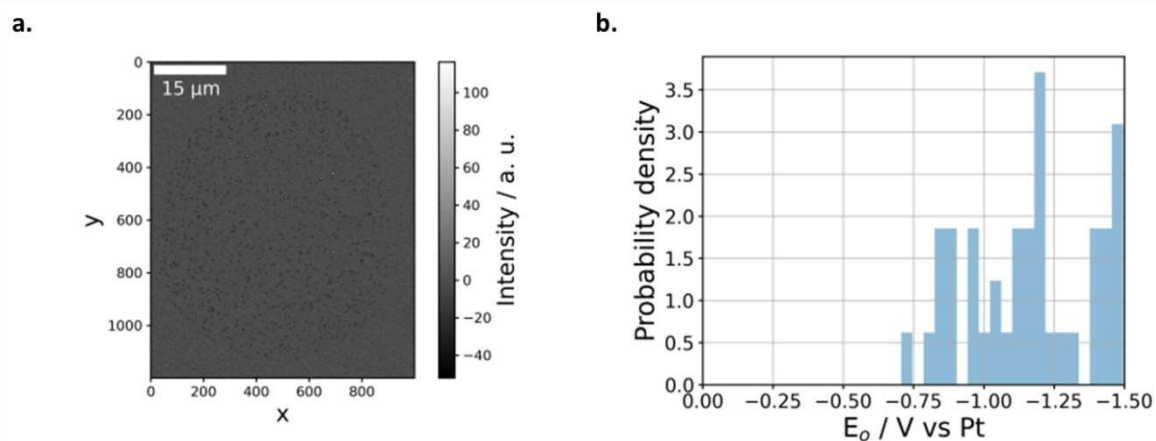


Figure 3-4. (a) Optical image of the droplet cell in the blue channel showing many more dark-contrasted features that are related to the presence of $\text{Ni}(\text{OH})_2$ NPs at the ITO surface. (b) Detection of $\text{Ni}(\text{OH})_2$ NPs at the ITO surface during the potential sweep. Nucleation events are detected at less cathodic potentials and particularly during the ORR wave (region 1) in the LSV of Figure 3-1c, indicating that part of the $\text{Ni}(\text{OH})_2$ is associated to ORR.

Herein, the objective is to use SEM imaging, together with EDX analysis, to categorize all detected entities based on their chemical identity. A careful observation of the SEM images permits to highlight differences in NP contrast and morphology. Even if it is often subjective, the human eye can here separate the NPs into three distinct categories: i) bright and smooth NPs, ii) fractal NPs and iii) less contrasted NPs. Representative example images of each category constitute Figure 3-5a. Starting from these observations, we then performed a classification of the NPs based on their appearance in SEM images by means of an agglomerative clustering algorithm belonging to the family of unsupervised machine learning algorithms (the methodology is schematized in Figure 3-5b and explained in more details **Materials and methods**, section M.4.2). It results in the identification of 4 distinct groups that are revealed from the principal component analysis visualized in the plot of Figure 3-5b. The belonging of each NP to one of the groups is indicated in the full-view LM and a zoomed HM SEM image by a colour code presented respectively in Figure 3-5c and d. In each of the 4 groups, all NP possessed identical chemical composition, identified by an independent EDX analysis of a limited ($N = 20$) but statistically representative population of each category. Two representative EDX spectra are given in Figure 3-5e. This strategy allowed us to avoid destructive and time-consuming EDX analysis of all NPs. It also permitted a further sub-classification of the NPs based on their size.

One example of this correlative machine learning-SEM-EDX analysis is shown in Figure 3-5d. A closer look at the EDX spectra and especially at the Ni/O ratio also allows the identification of 3 types of NPs with distinct compositions lying on the electrode surface. First (i), two populations of metallic Ni NPs with radii of 72 ± 14 nm (noted as large) and 54 ± 7 nm (noted as small) are found. It is important to note that the EDX spectra still revealed a small amount of O at these NPs' location (Figure 3-5e, O/Ni ratio is ca. 0.1) coming either from the ITO substrate or from the coating of the Ni NP by a Ni(OH)_2 shell. The two other categories are made respectively of (ii) Ni(OH)_2 NPs with a O/Ni ratio greater than 0.5, and (iii) ITO nano-heterogeneities for which no Ni is detected.

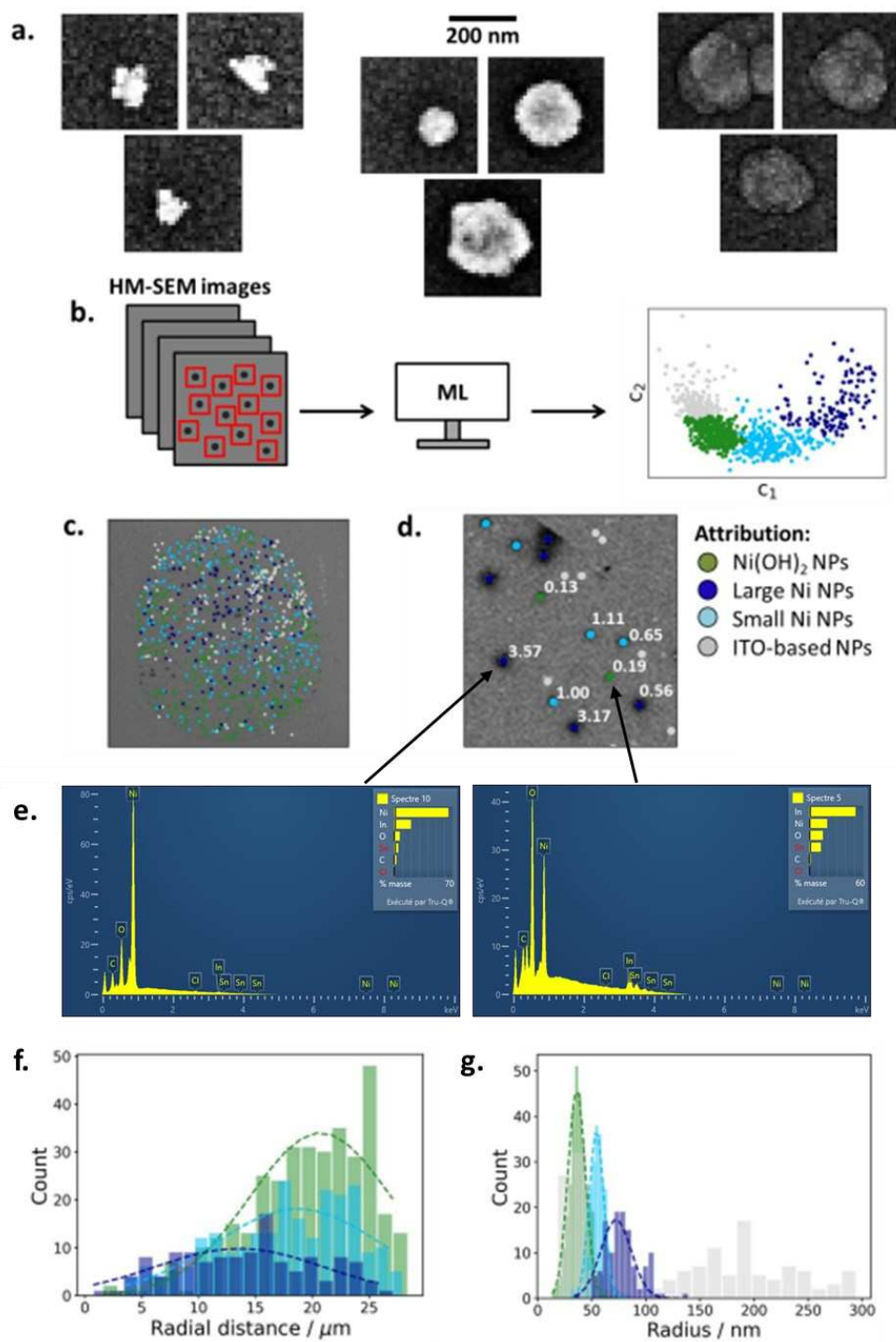


Figure 3-5. Agglomerative clustering by size and chemical composition of the electrodeposited NPs from SEM-EDX analysis. (a) Examples of the three types of NPs that can be distinguished from the database of *post-mortem* SEM images defined in Figure 3-3. (b) Schematic representation of the agglomerative clustering procedure used for the NPs' classification. Individual NP crops are flattened, and the two first principal components are computed before being processed by Ward's algorithm. (c, d) Chemical attribution to each NP detected in the SEM images based on the results given by the agglomerative clustering. (c) LM SEM image illustrating the spatial arrangement of the

classified NPs. Yellow, purple, green and blue correspond to Ni(OH)₂ NPs, large Ni NPs, small Ni NPs, and ITO inhomogeneities, respectively. (d) HM SEM image with chemical attribution and Ni/O ratio obtained by EDX analysis. (e) EDX spectra of the NPs highlighted in (d). (f) Radial distributions for the Ni-based NPs. (f) Size dispersion graphs for each NP group based on SEM images.

The light and dark blue dots corresponding to small and large metallic Ni NPs, respectively, account for 40% of all the NPs i.e., 364 NPs. This number is in fairly good agreement with the number of Ni NPs detected optically as bright-contrasted features (N = 340, 93%). It indicates that OM detected most of the electrodeposited Ni NPs, and definitely all the largest ones that should contribute the most to the Ni reduction current.

The green dots population is the second most represented one (N = 349 NPs) and corresponds to Ni(OH)₂ NPs formed upon precipitation of Ni²⁺ ions associated to competing water or O₂ reduction. It is interesting to note that these green dots seem spatially separated from the large Ni NPs (i.e., the dark blue population). One of the reasons for such segregation could be that Ni electrodeposition competes with water or O₂ reduction on the ITO electrode. Therefore, when these parasitic reduction reactions are predominant, only small metallic Ni NPs nucleate, while larger Ni NPs are present in regions where O₂/water reduction is inhibited. Ni(OH)₂ NPs are also located closer to the border of the droplet cell, where O₂ diffusion is believed to be accelerated. This preferred localization of the Ni(OH)₂ and small Ni NPs near the droplet edge is more clearly visible in Figure 3-5f that represents the radial distribution of the different NP populations. If the distribution of large Ni NPs is rather homogeneous over the whole droplet, small Ni and Ni(OH)₂ NPs are more massively found 20-25 μm from the droplet centre. It suggests that the ORR is most likely the main contribution to the pH fluctuations near the edges, yielding local Ni(OH)₂ NP precipitation. This conclusion about the importance of ORR at ITO is in line with the visualization of the electrochemically triggered crystallization of CaCO₃^[259] and is further optically confirmed by the appearance of Ni(OH)₂ NPs during the ORR wave (region 1 in Figure 3-1c) along the LSV (see onset time distribution in Figure 3-4b).

One can also notice that ITO heterogeneities are also separated from the Ni(OH)₂ NPs. This competition between parasitic reduction reactions is ruled by the electrode composition and its ability to trigger one of the reactions or the other. A similar behaviour has been recently

evidenced for the competition between ITO reduction and H₂ NB nucleation at the very same ITO electrodes,^[287] or from the nanoscale imaging of the heterogeneous electrochemical activity of ITO surfaces.^[288,289]

3.2.5 FROM LOCAL NANOSCALE DESCRIPTORS TO GLOBAL ELECTROCHEMISTRY

From the descriptors extracted from the temporal analysis provided by the optical image sequence, the NPs' size can be inferred. Owing to the low density of metallic Ni NPs on the electrode surface, the growth of each NP can be considered independent, or isolated, from its neighbours.^[290-292] The electrochemical growth of each NP is then expected to occur by steady-state hemispherical diffusion of Ni²⁺ ions to a 3D nanoscale collector (the NP). It is thus possible to derive the dynamic evolution of the NP's size during its growth from the expression of the diffusive flux to a 3D collector.^[293,294]

The final size r_{max} of each NP can then be inferred from its characteristic growth time Δt :

$$r_{max} = (2fCV_m D)^{0.5}(\Delta t + \Delta t_{LOD})^{0.5}, \quad (3-5)$$

where, C and D are respectively the bulk concentration and diffusion coefficient of Ni²⁺, and V_m the molar volume of metallic Ni. f and Δt_{LOD} are correction factors. Δt_{LOD} describes the limit of detection of the optical microscope. It corresponds to the time difference between the nucleation of the NP and the initial detection of its optical footprint. According to the BEM simulations presented in Figure 3-6, Ni NPs are detected as bright-contrasted features in the red channel starting from 30 nm in radius, which corresponds to $\Delta t_{LOD} = 0.04$ s (less than one frame). On the other hand, f accounts for the influence of the 3D geometry of the NP on its diffusional flux and its expression can be computed by finite elements simulations or found in the literature (details in **Materials and methods**, section M.5).^[295,296]

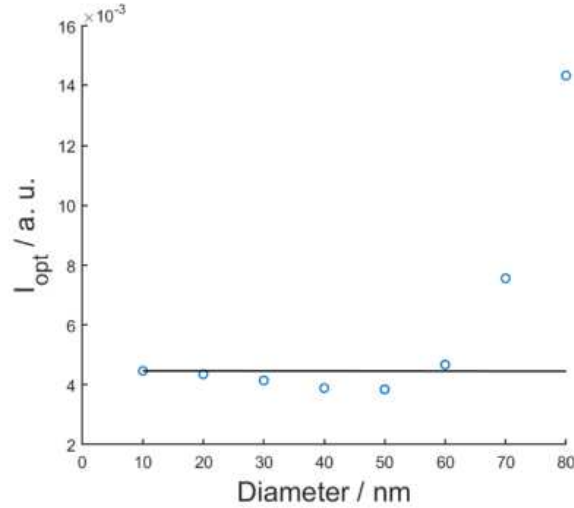


Figure 3-6. Simulated intensity of a growing Ni hemisphere compared to the background intensity (straight black line). Details about the BEM simulations can be found in **Chapter 2**.

Estimating the f pre-factor requires a precise knowledge of the NPs' geometry. Unfortunately, the SEM-inferred NP radius, r , is not fully sufficient to characterize the 3D geometry of a NP, as electrodeposition processes often result in spherical caps with a height, h , different from their projected diameter (determined by SEM). Herein, the precise evaluation of NP height is obtained by identical-location AFM images (as in Figure 3-1d). A full 3D geometrical description of several ($N = 15$) NPs is then obtained by correlative SEM-AFM analysis (Figure 3-7a and b, see also Figure 3-1d for a second example of correlative analysis), where SEM provided the projected diameter of the NPs and AFM their height. Note that the automatized alignment for identical-location analysis of the AFM image with the SEM (or/and optical) image can be made by implementing the same image recognition procedure described in Figure 3-3. The results of the r vs h correlation are shown in Figure 3-7b for the same individuals. For all NPs, the height imaged by AFM varies linearly with the projected radius r , indicating that all NPs have the same aspect ratio, h/r , and therefore produce the same contact angle with the electrode surface. The height h is smaller than the corresponding projected radius r , indicating, as schematized in Figure 3-7c, that the contact angle, θ , is lower than 90° . For $\theta < 90^\circ$, or equivalently $h < r$, the contact angle can be estimated from the slope in Figure 3-7b by using Equation 3-6.

$$\theta = 2 \operatorname{atan} \left(\frac{h}{r} \right) \quad (3-6)$$

An average value of the NP contact angle of ca. 75° is obtained. Then, f is calculated and amounts for 1.25 based on the data published in the literature (Figure M-8 in **Materials and methods**).^[296] The size dispersion graph resulting from the NP growth model calculated by means of the optical growth time Δt is presented in Figure 3-7d. The optically inferred mean NP size is in excellent agreement with the one directly measured by SEM analysis. However, the SEM size distribution (Figure 3-3f) is broader and reveals the presence of ($N = 60$ i.e., 16.5%) larger NPs with $r > 80$ nm. If one considers that such larger NPs could not be explained from the above diffusion-controlled growth model, they should most likely be produced from the merging of multiple NPs growing from different neighbouring nucleation sites.

Such NP merging was demonstrated from *ex situ* identical-location electron microscopy dynamic monitoring of electrodeposition processes.^[297,298] A clustering comparison of the final NP volume estimated from SEM and from the diffusion model shows in Figure 3-7e that the larger NPs revealed by SEM correspond to the merging of 2 or 3 NPs, suggesting their formation through 2 or 3 nucleation sites. Optical methods do not have the spatial resolution to resolve such phenomena *in situ*. However, neither the *post-mortem* SEM analysis could evidence it as the resulting NPs looked almost spherical. Noteworthy, its occurrence is supported by the multi-correlative approach proposed here.

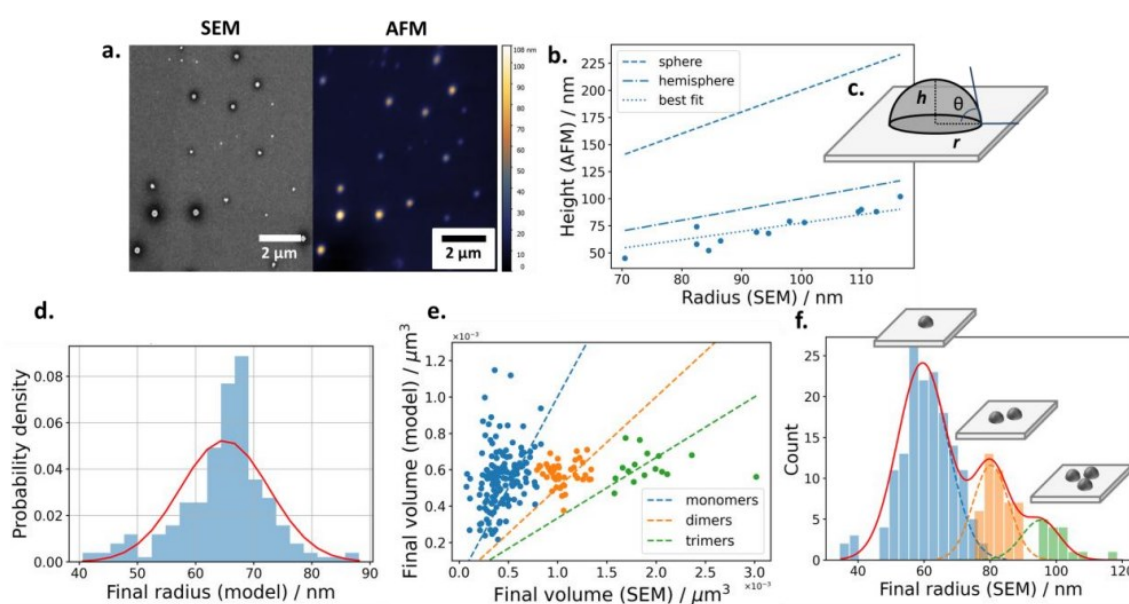


Figure 3-7. Evaluating the 3D growth dynamics of Ni NPs. (a) Correlative SEM and AFM analysis in a ROI of the droplet cell allowing to infer (b) the AFM-measured NP height and SEM-measured

projected NP radius for the same NPs, and (c) the NP contact angle by correlating both. (d) Dispersion graph of the modelled NP size obtained from the optically determined NP growth descriptors (Figure 3-2c) and a diffusion-controlled growth (Equation 3-5). (e) SEM vs modelled NP volume clustering highlighting NP growth from 1, 2 or 3 independent nuclei. (f) Size dispersion graph of the NPs optically probed but sized by SEM. The three distributions correspond to the clusters found in (e).

The structural descriptors (i.e., r , h , θ , or equivalently NP volume V , and chemical composition) obtained by SEM and AFM now complement mechanistic descriptors (growth duration Δt , onset time t_o , and number of nucleation sites) obtained by applying a growth model to the dynamic optical monitoring. They can be exploited to reconstruct the electrochemical current flowing through the droplet cell related to Ni deposition (i_d). It has been achieved by evaluating the time derivative of each Ni NP volume (V) and summing over all detected NPs, as in Equation 3-7.

$$i_d = -2 \frac{F}{V_m} \sum_{NP} n_n \frac{dV}{dt}, \quad (3-7)$$

where F is the Faraday constant, V the volume of each Ni NP derived from the growth model, and n_n the number of nuclei the NP is made of ($n_n = 1, 2$ or 3).

This optically inferred current i_d is plotted in Figure 3-8a as a function of time and is compared to the baseline-subtracted total experimental current (i_{exp}) collected by the potentiostat during the electrochemical deposition. There is a clear mismatch between both currents, the experimental one being about 3-4 times larger than the optically inferred one. This is confirmed from a coulometric analysis, without the need to rely on any model. The total charge used for the Ni NPs' formation can be precisely evaluated from the accurate NP sizing by *post-mortem* SEM and AFM analyses and Faraday's law, yielding a calculated charge of 4.8 nC. This value is again much smaller than the charge calculated by integrating the experimental current peak which is equal to 17.1 nC.

From both the optically inferred growth model and *post-mortem* SEM, the charge or current mismatch stresses another source of electron flow during Ni NP formation. One could incriminate the formation of some of the many ($N = 349$) Ni(OH)₂ NPs detected by SEM. These Ni(OH)₂ NPs act as nanoscale reporters of the electrode's catalytic activity through Equations

1, 3 and 4. Considering their sizes and number, their formation corresponds to a total catalytic charge of 0.7 nC, according to an electron/hydroxide ion ratio equal to 1. This value is negligible compared to the charge mismatch (12.3 nC) between the charge required for the growth of all Ni NPs and that estimated from the LSV. The charge mismatch is then believed to originate from the electrocatalysis of another reduction process, likely, as schematized in Figure 3-8c, water reduction operating at the Ni NPs during their formation.

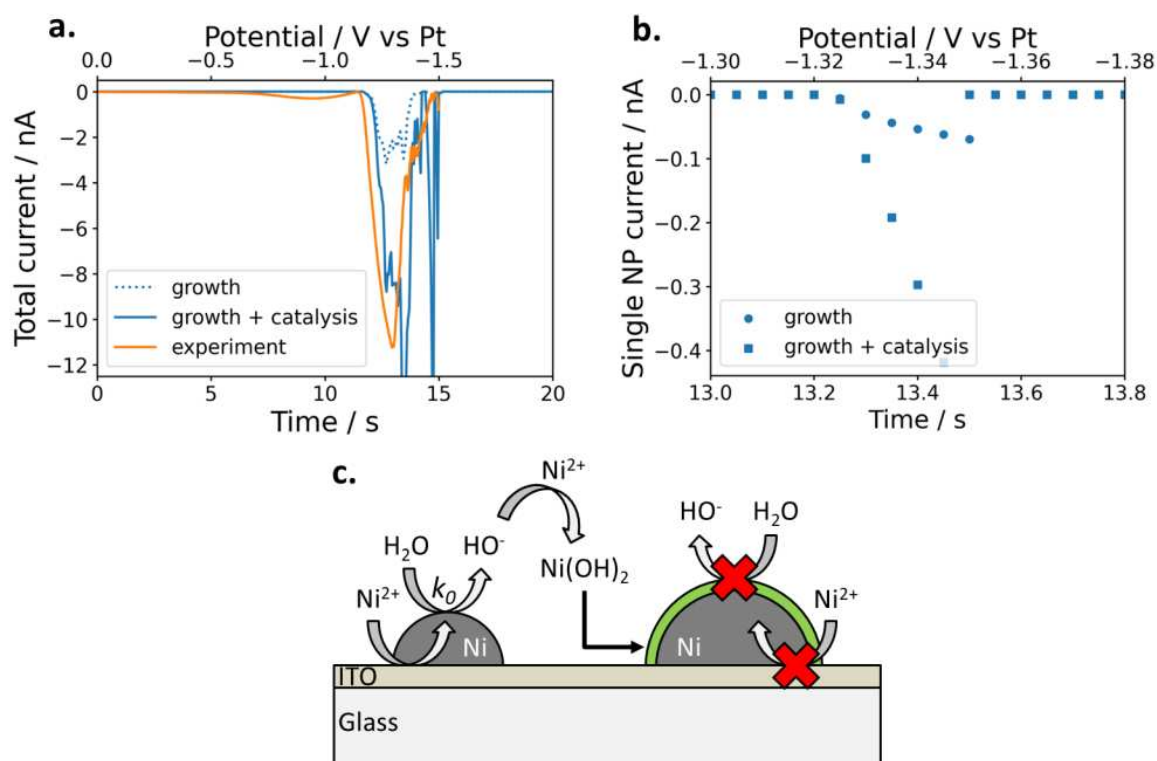


Figure 3-8. Evaluating the contribution of HER electrocatalysis in the electrochemical response from single NP growth dynamics. (a) Comparison between the electrochemical current recorded by the potentiostat (background-subtracted) and the total modelled current for Ni NP growth and electrocatalysis ($i_d + i_{cat}$) considering the growth dynamics adjusted from optical monitoring and SEM sizing (Figure 3-7e), and $k^o = 6.5 \cdot 10^{-5} \text{ cm s}^{-1}$. (b) Modelled current transients for an individual NP. (c) Mechanistic scheme used to evaluate the rate constant k_0 of water reduction at metallic Ni NPs.

Consequently, the charge mismatch should reflect the extent of the electrocatalysis of water reduction at freshly deposited Ni NPs. The charge mismatch should allow us to estimate the rate of this electrocatalytic reduction with the help of a few approximations. i) As a result of the self-terminated growth of Ni NPs, it is assumed that water reduction only occurs during

NP growth. ii) The electrocatalytic activity is similar for all NPs and does not fluctuate with NP size. It is characterized by a heterogeneous rate constant k° (in cm s^{-1}). iii) The rate-limiting step is the Volmer step as previously stated.^[278] Then, one could express the electrocatalytic current from the contributions of all NPs by Equation 3-8.

$$i_{cat} = -F \sum_{NP} k^\circ A \exp(-\alpha F(E - E^\circ) / RT) (E < E_o) \quad (3-8)$$

where A corresponds to the area of a given NP, evaluated from the growth model (see **Materials and methods**, section M.5 for its exact expression as a function of aspect ratio), α and $(E - E^\circ)$ are the charge transfer coefficient and the overpotential for water reduction at Ni, respectively. R and T stand for the molar gas constant and the temperature, respectively.

A good overlap between i_{exp} and $(i_d + i_{cat})$ is obtained for $k^\circ = 6.5 \cdot 10^{-5} \text{ cm s}^{-1}$, as shown in Figure 3-8a. This value is in fairly good agreement with the value obtained by Bard in 2017,^[278] employing SI-SECM in combination with a Tafel analysis, considering the water activity equal to 1 M. In addition, using the exact same methodology and the microscopically inferred k° , the current related to the growth and catalysis can be inferred at the single-NP level. One example is presented in Figure 3-8b for a NP with final radius of 96 nm. Note that a closer examination of Figure 3-8a tends to suggest that k° would be slightly underestimated for small NPs while it would be overestimated for large NPs. It can explain the few current spikes observed in the LSV reconstructed from the model and would indicate a catalytic efficiency fluctuating with NP size.

It should be stressed that reaching the intrinsic electrocatalytic activity of metallic Ni, besides at the single-NP level, is a difficult task as its surface gets quickly covered in Ni(OH)_2 that will mask the activity. The final proposed mechanism is schematized in Figure 3-8c. This is clearly evidenced here as the Ni NP growth is halted rapidly because of the alteration of the growth process owing to the formation of a Ni(OH)_2 shell. The Ni(OH)_2 -coated Ni NPs may still present an electrocatalytic activity which may be seen from the reduction current branch following the Ni reduction peak. However, this activity is orders of magnitude smaller than that of pristine Ni. For comparison, the k° value evaluated here, in agreement with previous estimates, is of the same order of magnitude as that of Pt.^[299]

3.3 CONCLUSION

Electrochemistry in a micro-sized droplet cell is coupled to a correlative multi-microscopy strategy assisted by machine vision concepts. In the latter strategy, optical, electron and local probe microscopies work synergistically to provide highly complementary information on a complex process, that is the electrodeposition of Ni NPs. OM monitors *operando* the NPs' nucleation and growth, while SEM and AFM image *ex situ* the deposit and provide the full 3D NP geometry. By knowing precisely, the position, size, growth dynamics and structure of all NPs, one can calculate individual growth currents based on a mathematical model and bridge the gap between these microscopic descriptors and the macroscopic electrochemical curve. The results then clearly highlight the dramatic impact of the competing reactions (water and O₂ reduction) that occur during the NPs' formation. Employing a smaller droplet cell compared to **Chapter 2** has been decisive, as it allowed downscaling the system and visualizing all the NPs that are responsible for the electrochemical response. Particularly, this local to global strategy is pertinent since it allows determining the intrinsic electrocatalytic activity of highly reactive catalysts, illustrated here in the case of metallic Ni NPs. However, while the growth current is evaluated at the single-NP level, the electrocatalytic activity is averaged over the entire NP population. We will see in **Chapter 4** how the electrocatalytic activity of Ni and Pt NPs towards water reduction can also be evaluated at the single-NP level.

Beyond demonstrating the importance of highly sensitive single-entity electrochemistry measurements, or high-spatial-resolution electrochemical imaging techniques, these results show the significance of confronting it to ensemble macroscale measurements in order to reveal new mechanistic insights.

Chapter 4 ASSESSING THE ELECTROCATALYTIC ACTIVITY OF SINGLE NANOPARTICLES BY IMAGING NANOSCALE REACTION FOOTPRINTS

In **Chapter 3**, we have closely examined the contributions of growth and HER catalysis to the reduction peak associated to the electrodeposition of Ni NPs. By adding a catalysis component to the optically inferred growth currents of all Ni NPs, it was possible to fit the overall current measured by the potentiostat and thus to estimate the charge transfer rate constant k° of HER at Ni NPs. From the shape of the calculated current in Figure 3-8a, one could sense a size dependency of k° , but this could not be verified using the methodology presented in **Chapter 3** as it only provides an average k° over hundreds of different Ni NPs. To investigate the size dependency of k° , it needs to be evaluated at the single-NP level.

This chapter was adapted with permission from ref. ^[300]. Copyright 2023 The Authors.

4.1 INTRODUCTION

As discussed in **Chapter 1**, OMs can be used to probe the catalytic activity of single NPs.^[301–303] They offer a high temporal and spatial resolution at high throughput. Moreover, they can readily be used *operando* and coupled to other microscopies as shown in **Chapter 3**.^[159] However, they are mostly limited to reactions involving the formation of gas NBs (HER,^[302–305] OER)^[301,305] and thus to very active materials (Pt, IrO_x). If gas NBs are pertinent reporters of the electro- or photocatalytic activity of catalysts, their nucleation on a surface requires local oversaturation, which is only reached at extreme current densities. With a sufficiently sensitive technique, dissolved H₂ could be detected before the nucleation of a NB,^[306] but the saturation concentration of H₂ in water at room temperature is only equal 0.8 mM. Still, the nucleation of an individual H₂ NB from the reduction of H⁺ in acidic electrolytes at a 100 nm NE requires roughly 30 nA of current,^[307] which is equivalent to a current density of 400 A cm⁻². This kind of current density is only achievable at impractical overpotentials and even so

difficult to reach from the reduction of water in neutral electrolytes. This is the reason why no H₂ NBs were detected in **Chapter 2** and **Chapter 3**.

Herein, we propose a novel approach to image and quantify *operando* the catalytic activity of single Ni (and Pt) NPs towards water reduction, as well as of bifunctional NPs made of Ni (Pt) NPs coated with a metal hydroxide nano-shell. As schematized in Figure 4-1, instead of visualizing the formation of a NB, the strategy focuses on evaluating the production of H₂ based on the rate of formation of HO⁻. Local pH changes can be imaged by fluorescence microscopy as various fluorophores are pH sensitive. Some of these strategies have been employed for monitoring *operando* electrochemical processes, particularly related to energy storage.^[308–311] Here, instead of using fluorescence microscopy, we propose a reporting strategy using the ability of metal ions, Mⁿ⁺, to precipitate hydroxides, M(OH)_n, as a nanometre-thick layer around individual NPs. This precipitation layer is again monitored *operando* by IRM and is detected as a halo expanding around the NP as the electrocatalysis of water reduction proceeds. Supported by finite element simulations, the dynamics of the halo's expansion can be used as a proxy for the electrocatalytic activity of the NP. This concept is illustrated here in the case of Ni and Pt NPs in the presence of Ni²⁺ and Mg²⁺, hence through the production of a Ni(OH)₂ and Mg(OH)₂ layer, respectively. In turn, it allows inspecting the reactivity of the bifunctional core-shell nanocatalysts Ni@Ni(OH)₂, Pt@Ni(OH)₂ and Pt@Mg(OH)₂, and to compare their performance to that of bare Ni and Pt NPs.

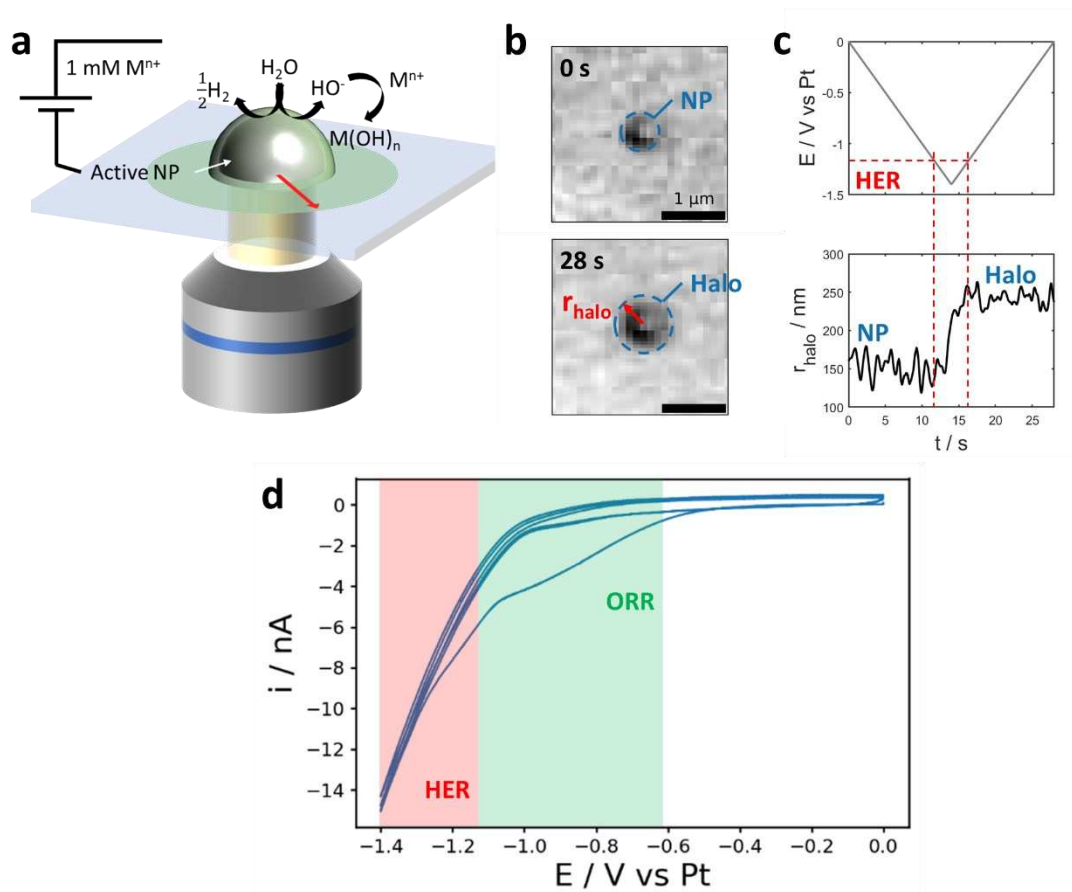


Figure 4-1. (a) Scheme of the strategy for evaluating the water reduction rate at single active NPs (grey hemisphere) immobilized on an ITO electrode from the local precipitation of a thin metal hydroxide layer (green shell and halo). (b) Optical images (blue channel) of a single Pt NP at the beginning (top) and at the end (bottom) of the potential cycle presented in (c) showing the growth of a dark halo around the NP. The experiment is performed in $1 \text{ mM NiCl}_2 + 10 \text{ mM KCl}$ solution at a scan rate of 100 mV s^{-1} . (c) Potential cycle applied at the ITO (top, current response in (d)) and corresponding evolution of halo's radius r_{halo} (defined in (b), bottom) as a function of time. The vertical red dashed lines delineate the time domain of r_{halo} evolution, highlighting the potential domain where water reduction (HER) proceeds at detectable rates for this footprinting strategy. (d) Current response measured during the potential cycle presented in (c). Even though oxygen reduction is proceeding before water reduction, the halo expands only during water reduction ($E < -1.2 \text{ V}$).

Such bifunctional nanocatalysts are promising candidates for HER in neutral or alkaline electrolytes i.e., following Equations 4-1–4-3, conditions which confer higher stability to OER catalysts.^[312–314] Classical Pt-group metals are good catalysts for the recombination of

hydrogen intermediates (Tafel step, Equations 4-2), but show poor activation for the dissociation of water (Volmer step, Equations 4-1). This kinetically limiting initial step in neutral and alkaline conditions makes the overall HER (Equations 4-3) two to three orders of magnitude slower than in acidic conditions.^[315] Inversely, metal oxides and hydroxides, due to their high oxophilicity, promote HO-H bond dissociation, but are generally poor catalysts for H* recombination (Equation 4-2). A promising strategy to both accelerate H₂O dissociation and keep a high H* recombination rate consists in engineering bifunctional materials, as proposed in 2011 by Markovic *et al.*^[316] They showed that the addition of Ni(OH)₂ clusters on Pt(111) improved the catalytic activity of Pt(111) in 0.1 M KOH by a factor of 8. The catalytic activity could be improved even further (by an overall factor of 10) with the addition of Li⁺ in the electrolyte. Ni(OH)₂-Pt edges were suggested to facilitate the water dissociation step (Equation 4-1) due to the higher oxophilicity of Ni(OH)₂ which adsorbs HO⁻ more easily than Pt(111), and Li⁺ was suggested to weaken the HO-H bond through non-covalent interactions. This discovery led to the development of numerous catalysts featuring large numbers of Ni(OH)₂-Pt edges. To further decrease the cost of these catalysts, the amount of Pt was often optimized by using carefully positioned Pt nanostructures.^[317–322]



Apart from Pt, Markovic's strategy was also successively applied to Earth-abundant metals such as Ni, Cu and Ag, making such bifunctional catalysts even more cost-effective.^[323] In each case, adding Ni(OH)₂ clusters on the metal surface enhanced the catalytic activity to the same level as the bare metal surface in acidic electrolyte. This bifunctional HER activity enhancement has since then been transposed to a wider range of materials and interfaces. Despite the effectiveness of this strategy, the mechanistic understanding of the improved catalytic activity is still under discussion. For example, the increased activity of Pt attributed to the oxophilicity of vicinal Ni(OH)₂ (or other metal hydroxides^[324,325]) could rather be attributed, based on different *operando* strategies to monitor the Pt(111)-Ni(OH)₂ interface, to the disturbance of the local electric field by Ni(OH)₂ and the reorganization of the water network.^[326]

Even if the bifunctional effect was also reported on nanocatalysts,^[327] it remains rarely studied at the single NP level. Yet studying individual NPs is crucial to understand such bifunctional nanocatalysts as their size, shape, composition and/or surface state might vary from one NP to another unlike single-crystalline surfaces.^[328] Employing the nano-impact method to study individual Ni@NiO NPs, Compton *et al.*^[329] showed that their electrochemistry is controlled by the surface oxide layer and not by a size effect. However, experiments were carried out at pH 1.95, which is not representative of the literature. Moreover, the effect of oxide coverage was not investigated. Our new approach allows to directly evaluate the effect of hydroxide coverage over several CV cycles.

To recapitulate, we will show herein how the catalytic activity of single Ni (and Pt) NPs, as well as of bifunctional NPs made of Ni (Pt) NPs coated with a metal hydroxide nano-shell, can be imaged and quantified *operando* based on the precipitation of a nanometre-thick hydroxide layer around individual NPs as they locally release HO⁻ ions during water reduction.

4.2 RESULTS AND DISCUSSION

4.2.1 DESCRIPTION OF THE PHENOMENON

The experimental configuration is schematized in Figure 4-1a (details can be found in **Materials and methods**, section M.2.1). A droplet of 1 mM MCl₂ + 0.1 M KCl (M = Ni, Mg) solution is confined between an ITO-coated glass coverslip – which serves as optical sensor – and a glass micropipette (ca. 100 μm in diameter, not shown in Figure 4-1a) filled with the electrolyte and containing a Pt wire. The whole forms a microelectrochemical cell where the ITO also plays the role of WE and the Pt wire the role of QRCE in a two-electrode configuration. The ITO is further decorated with hemispherical Ni or Pt NPs grown by electrodeposition. As already discussed in the previous chapters, electrodeposition offers several advantages compared to chemical synthesis: in addition to guaranteeing a good electrical contact between the NPs and the substrate,^[330] it can produce NPs with a wide range of sizes, allowing for the screening of size-dependent electrochemistry at the single-NP level.^[331,332] Moreover, OM allows an *in situ* monitoring of the NPs' growth.^[333–335]

The surface confined by a miniaturized electrochemical cell containing a M^{2+} solution is then subjected to HER by applying a negative potential bias cycle in a CV experiment (Figure 4-1c,d) while optical images of the surface are continuously acquired under OM observation in a reflection mode at 20 Hz by a CMOS camera.

Figure 4-1b shows the optical image corresponding to an individual 145 nm-radius hemispherical Pt NP electrodeposited on an ITO electrode. Pt NPs were electrodeposited by CA from 1 mM K_2PtCl_6 + 0.1 M KCl (Figure M-1 in **Materials and methods**) and characterized by high-resolution AFM to produce a contact angle of 103° with the ITO, which is close to a hemisphere, as shown in Figure M-2 (**Materials and methods**). The Pt NP is detected as a bright central disk surrounded by a small dark halo. Such interference pattern is common for this interferometric optical detection mode. As evidenced in the lower panels of Figure 4-1b and c, upon polarizing the ITO negatively, the dark halo grows around the NP. The halo (or NP) is characterized by its apparent outer radius r_{halo} whose dynamic growth is monitored (lower panel of Figure 4-1c; details about its determination from the optical images are given in **Materials and methods**, section M.4.3). The halo grows within a restricted negative bias range such that $E < -1.2$ V vs Pt (region denominated by HER in the upper panel of Figure 4-1c). Such potential bias suggests that the halo's formation originates from the Pt NP catalysing water reduction and producing HO^- ions (Equation 4-3), triggering the precipitation of the M^{2+} ions present in solution in the form of insoluble $M(OH)_2$.

SEM and TEM were used to perform EDX analyses and nanoscale chemical mappings (see Figure 4-2) on individual Pt NPs after the HER in the presence of Ni^{2+} . They showed that the Pt NPs are covered by a shell made mostly of an amorphous layer containing Ni and O (Figure 4-2a,b), just like the halo formed around the NPs on the electrode (Figure 4-2e,f). Still, a few crystallites were spotted at the edge of the NPs (Figure 4-2c). However, these were poorly crystallized, and their crystal structure could thus not be identified (Figure 4-2d). These results are consistent with literature suggesting that electrochemical conditions favour the electroprecipitation of amorphous $Ni(OH)_2$.^[336] It indicates that along the HER, the Pt NPs are transformed into core-shell $Pt@Ni(OH)_2$ NPs surrounded by a $Ni(OH)_2$ halo.

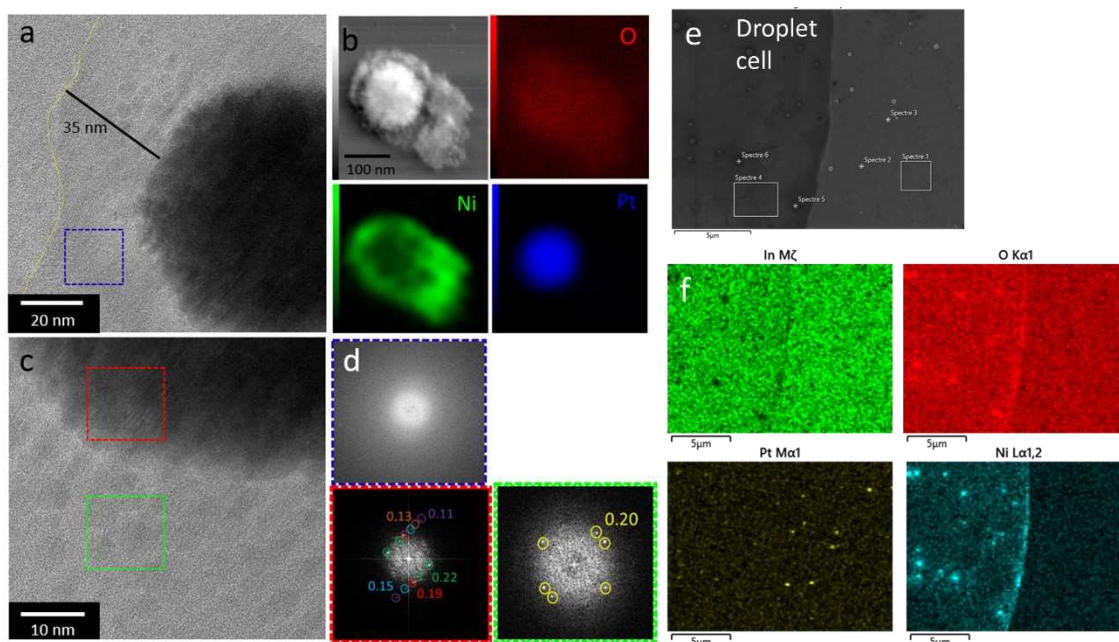


Figure 4-2. (a) Scanning transmission electron microscopy (STEM) image of a Pt NP after several CV cycles in the presence of Ni^{2+} ions showing the growth of an amorphous shell around it of approximately 35 nm with embedded crystallites (detected as lattice interference fringes). (b) STEM-EDX mappings of one of the modified Pt NPs confirming that the shell is composed of Ni and O. (c) HR-TEM image of a few crystallites spotted at the edge of the Pt core within the amorphous layer. (d) Corresponding FFT images of selected areas: blue inset in (a) – no diffraction spots, indicating that most of the layer is amorphous; red inset in (c) – diffraction pattern corresponding to lattice distances (in nm) of Pt; green inset in (c) – unidentified Ni-based crystallites. (e) SEM image of the Pt NPs probed optically after cycling in NiCl_2 (rinsed with ultrapure water at the end of the experiment). (f) EDX mappings of the same region.

4.2.2 CASE OF NI NPS

Next, the presence of this halo was tested for different NP chemistries and M^{2+} cations. It was then used as a chemical footprint of the HER to quantify the catalytic activity of single NPs. The same behaviour is also observed with Ni NPs (Figure 4-3). In this case, both the Ni NPs' electrodeposition and their HER activity are probed during the same CV experiment by sweeping the potential negatively from 0 to -1.6 V vs Pt along three successive cycles. As shown in Figures 4-3a and b, the characteristic peak of Ni electrodeposition appears at ca. -1.45 V during the first cycle, concomitantly to bright-contrasted features on the surface.^[337,338]

From the previous chapters, these optical features are related to the growth of hemispherical metallic Ni NPs from the electrode surface.^[335,339]

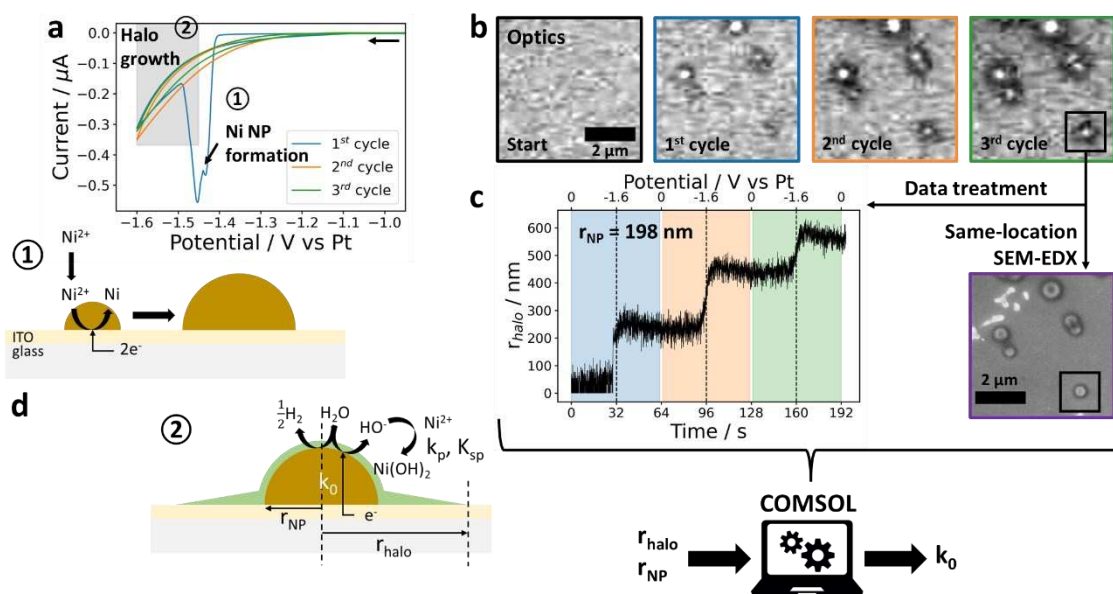


Figure 4-3. (a) CV within a ca. 100 μm droplet of 1 mM NiCl_2 + 0.1 M KCl solution on ITO (scan rate: 50 mV s^{-1}). (b) Series of optical images acquired (from left to right) at the beginning of the experiment and at the end of each CV cycle (at 0 V) showing the growth of Ni NPs (bright features) followed by the growth of a dark halo around them. (c) Evolution of r_{halo} for the NP framed in (b) during the whole experiment, correlated SEM image acquired *ex situ* at the end of the experiment, and schematic representation of the processing of r_{halo} and r_{NP} to determine k° . (d) Schemes of the proposed mechanism for the formation of Ni NPs (1) followed by the formation of $\text{Ni}(\text{OH})_2$ halos around them (2).

As for the Pt NP presented in Figure 4-1, at more negative potentials and during the subsequent backward scan (as well as during the subsequent cycles), a dark halo is detected optically, gradually growing, around all Ni NPs (Figure 4-3b). The evolution of r_{halo} over the three cycles for an average-sized and well-isolated Ni NP (black frame in Figure 4-3b) is reported in Figure 4-3c. The halo is clearly increasing in size during the subsequent cycles and in all cases for electrode potentials more negative than -1.45 V. The halo is therefore mostly produced and growing concomitantly to water reduction.

Same-location optical, SEM and AFM analyses were performed at the end of the first potential sweep on another sample (see Figure 4-4a). As already visible in Figure 4-3c, a dark halo is also

detected around the Ni NPs on the SEM images. Comparing the optical and SEM profiles of a Ni NP in Figure 4-4b shows that the dark-contrasted regions (in grey) are of the same size, ca. 370 nm in that case. At that distance, the thickness of the halo measured by AFM is ca. 5 nm, demonstrating again that it corresponds to a thin layer of deposited material and not to an imaging artifact. It also gives an estimate of the detection limit of our optical microscope (see below).

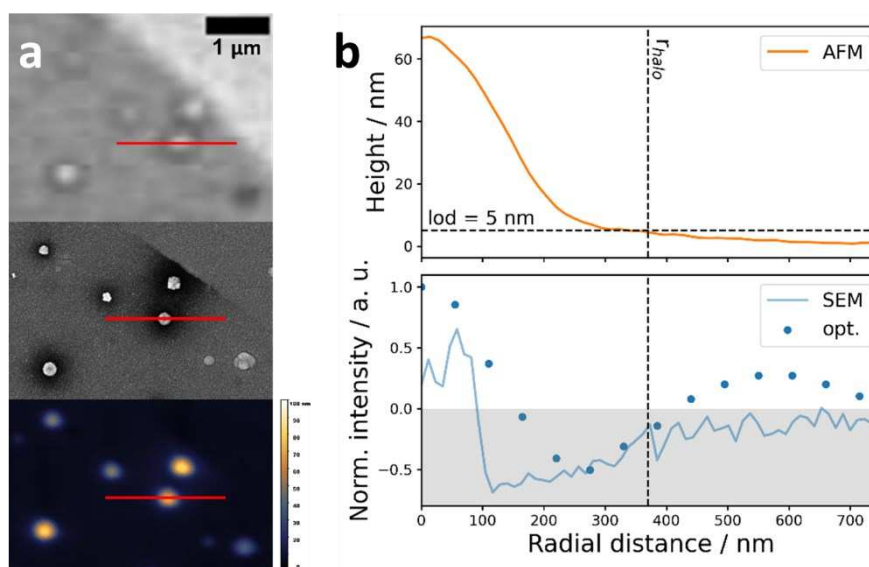


Figure 4-4. (a) Same-location optical (blue channel), SEM and AFM images of Ni NPs electrodeposited on ITO by sweeping only once between 0 and -1.5 V vs Pt (electrolyte: 1 mM NiCl₂ + 10 mM KCl, scan rate: 100 mV s⁻¹). (b) AFM profile of the NP highlighted in (a) compared to its optical and SEM intensity profiles. As the relative optical intensity starts to become positive, the thickness of the Ni(OH)₂ layer reaches approximately 5 nm, which will be used as the Ni(OH)₂ layer limit of detection, lod, in the model (see below).

The mechanism explaining the formation of the amorphous Ni(OH)₂ layer and the growth of the optically detected halo is schematized in Figure 4-3d. As for the Pt NP shown in Figure 4-1c, the halo's growth is observed while the CV shows an exponential current decrease due to water reduction on the freshly electrodeposited Ni NPs (Figure 4-3a). The HO⁻ ions produced by this reaction (Equation 4-3) likely combine with Ni²⁺ ions from the solution to form the amorphous Ni(OH)₂ shell around the NPs (Equation 4-4; Ni(OH)₂ has a very low solubility product, $K_{sp} = 5.48 \cdot 10^{-16} M^3$). Hence, the radius of the halo, r_{halo} , is indicative of the extent

of local HO⁻ liberation during the electrocatalytic reaction proceeding at the individual NP. As a chemical footprint, the halo then reveals the dynamics of local HO⁻ production by the NP and therefore provides an independent measure of its catalytic activity towards water reduction. Noteworthy, oxygen reduction is another electrochemical reaction generating HO⁻ ions. The contribution of oxygen reduction is clearly detected in the CV response of the Pt NP-decorated electrode starting from -0.8 V vs Pt (Figure 4-1d). However, the halo's growth is only detected at more negative potential, ca. -1.2 V (see Figure 4-1c), when more cathodic current assigned to water reduction is flowing. It suggests that oxygen reduction is not sufficient by itself to initiate or propagate the precipitation of Ni(OH)₂ at this scan rate. As evidenced in Figure 4-3c, r_{halo} expands inequivalently during each electrode potential cycle, hinting at changes in the HER kinetics and its dependence on the NP's structure which is evolving along the successive potential cycles.



4.2.3 COMSOL MODEL

To quantify these changes, we propose a COMSOL model which explicitly simulates the precipitation of Ni(OH)₂ on top of an electrocatalytically active NP. It was inspired by a COMSOL application note about the under-deposit corrosion of Mg in contact with mild steel.^[340] Here, the situation is much simpler as the NP's geometry does not change over time (it is a priori not corroded). The precipitation reaction is assumed to be irreversible and to initiate when the ionic product, $c_{Ni^{2+}}c_{HO^{-}}^2$, exceeds the solubility product of Ni(OH)₂, K_{sp} . The rates of reaction for the consumption of Ni²⁺ and HO⁻ ions are given by the following equations:

$$R_{s,Ni^{2+}} = k_p(c_{Ni^{2+}}c_{HO^{-}}^2 - K_{sp})H(\xi) \quad (4-5a)$$

$$R_{s,HO^{-}} = 2k_p(c_{Ni^{2+}}c_{HO^{-}}^2 - K_{sp})H(\xi) \quad (4-5b)$$

where k_p is the precipitation rate constant of Ni(OH)₂, H the Heaviside step function, and $\xi = \frac{c_{Ni^{2+}}c_{HO^{-}}^2}{K_{sp}} - 1$ the step function variable. The flux of HO⁻ ions generated by the NP is given by

the Butler-Volmer equation:

$$J_{0,HO^-} = k^\circ * 1[mol L^{-1}] * \exp\left(-\frac{\alpha F}{RT}(E_{app} - E^\circ)\right), \quad (4-6)$$

where α is the cathodic charge transfer coefficient, E_{app} the applied potential, and E° the formal potential of water reduction on Ni. r_{halo} is defined as the distance to the centre of the NP where the height of the Ni(OH)₂|electrolyte interface falls behind a chosen limit of detection, lod.

The NP is considered hemispherical (see **Materials and methods**, section M.1.6 for justification). The *Transport of Diluted Species* interface is used to treat the HO⁻ flux generated by the NP, and the *Level Set* interface is used to treat the precipitation of Ni(OH)₂. As discussed above, the rates of reaction for the consumption of Ni²⁺ and HO⁻ ions, $R_{s,Ni^{2+}}$ and R_{s,HO^-} , are given by Equations 4-5a and 4-5b, respectively. The reaction source term is defined as:

$$R_i = -R_{s,i}\delta, \quad (4-7)$$

where δ is the level set delta function used to prescribe the deposition reaction at the Ni(OH)₂|electrolyte interface. Ni(OH)₂ is allowed to precipitate on the NP as well as on the ITO, which is considered electrochemically inactive.

In summary, the model essentially depends upon four parameters: the electron transfer rate constant associated to water reduction on the NP (k°) dictating the rate of HO⁻ production from the NP, the solubility product of Ni(OH)₂ (K_{sp}), the precipitation rate constant of Ni(OH)₂ (k_p), and the optical limit of detection of the Ni(OH)₂ layer (lod). However, the results were found to depend very little on the lod (see Table A1-1 in **Appendix 1**), which was fixed at 5 nm according to same-location SEM and AFM measurements (see Figure 4-4). From a simplified version of the model (detailed in **Appendix 1**, section A1.4.2), an analytical expression of the transient evolution of the halo's radius can be proposed (Equation 4-8), showing that it depends on a single parameter: the product $k^{\circ 2}k_p$. This interdependency of k° and k_p is confirmed from the simulations discussed in Figure A1-8 in **Appendix 1**. It then suggests that to determine the absolute value of the water reduction rate constant, k° , the knowledge of the precipitation rate constant, k_p , of the metal hydroxide is required.

$$e_{Ni(OH)_2} = \frac{M_{Ni(OH)_2}}{\rho_{Ni(OH)_2}} k_p k^{\circ 2} \left(\frac{r_{NP}}{r}\right)^2 c_{Ni^{2+}} \left(\frac{c_{H_2O}}{D_{HO^-}}\right)^2 \int \exp(-2\xi) dt \quad (4-8)$$

Rather than for precipitation kinetics, databases are available for the reverse reaction i.e., crystal dissolution.^[341] These are usually obtained by titration of the solution during a dissolution reaction. Herein, the dissolution rate of the metal hydroxide thin film halo can also be evaluated optically from the slow dynamics of decrease in r_{halo} when the halo thin film is in contact with water. Since no electrochemical reaction is involved in this process, the decrease in r_{halo} during the dissolution reaction now only depends upon k_p , making it possible to determine the absolute value of this parameter. A detailed discussion of these experiments can be found in **Appendix 1**, section A1.4.4. From such analysis, the rate constant for Ni(OH)₂ precipitation is found: $k_{p,Ni(OH)_2} = 5.1 \cdot 10^{-4} \text{ m}^7 \text{ mol}^{-2} \text{ s}^{-1}$. This corresponds to a dissolution rate constant of $2.8 \cdot 10^{-14} \text{ mol cm}^{-2} \text{ s}^{-1}$, which is close to the value reported in the literature for NiO.^[341]

The knowledge of this precipitation rate constant allows the analysis of the electrochemical growth of the Ni(OH)₂ halo upon water reduction. The results of the simulation reproducing the experiment in Figure 4-3 of the electrochemical growth of a Ni(OH)₂ layer around a Ni NP upon water reduction are presented in Figure 4-5. The simulation consists in matching the transient evolution of the halo's size, r_{halo} , during the three cycles of the CV experiment, as depicted in Figure 4-5a. The simulation takes into account the electrogeneration of HO⁻ ions at the NP surface (Equation 4-3) and its later precipitation with the M²⁺ cations present in solution (Equation 4-4). This precipitation is described here, as seen in Figure 4-5b, through the formation of a new phase atop and around the NP. The concentration profiles of the species are provided in Figure 4-5c for HO⁻ and Figure 4-5d for Ni²⁺. Such experiment is first analysed along the first CV cycle. From the knowledge of $k_{p,Ni(OH)_2}$, the observed halo size matching with the simulation (Figure 4-5a, orange and black lines) yields a water reduction rate constant $k^{\circ} = 1.3 \cdot 10^{-7} \text{ cm s}^{-1}$. It is of the same order of magnitude as the value determined by microscale local electrochemical probing (considering that the activity of water is equal to 1 M),^[342] indicating no significant differences between micro- and nanoscale in agreement with Compton *et al.*^[329] At this stage, it is worth mentioning that in potential region 2 (Figure 4-3a,d), the catalytic activity of a core-shell Ni@Ni(OH)₂ is more likely probed, the Ni core being already covered with a thin layer of Ni(OH)₂ produced during the electrodeposition of Ni and naturally forming on bare Ni when exposed to water. In water, the catalytic activity of bare Ni can only be probed at the earliest stage of Ni nucleation i.e., during the

characteristic reduction peak mentioned in the previous chapters. In **Chapter 3**, we showed that during this narrow time window, the catalytic activity is two orders of magnitude higher than what is reported in the literature.^[339,342]

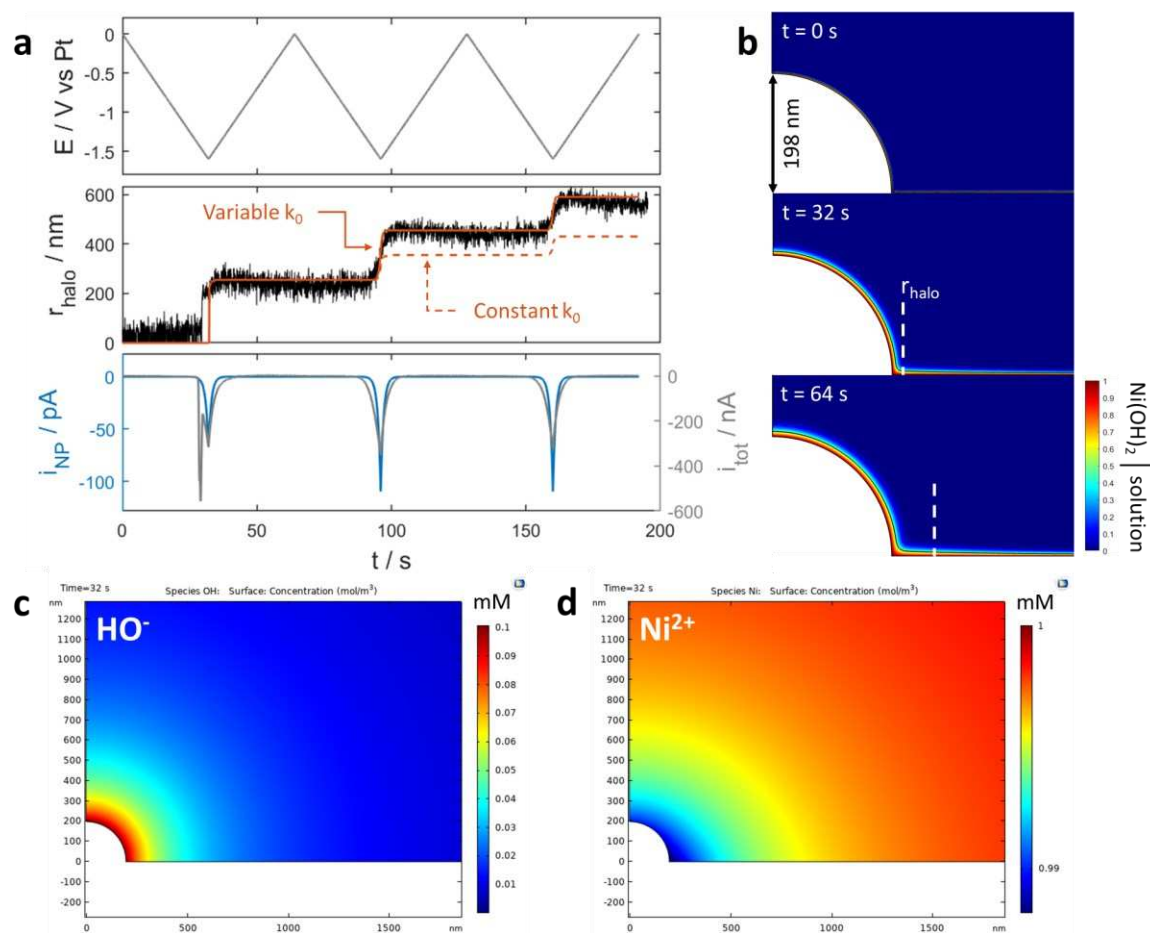


Figure 4-5. (a) Simulation of the evolution of r_{halo} for the NP framed in Figure 4-3b,c for a constant value of k^o ($1.3 \cdot 10^{-7} cm s^{-1}$, dashed orange line) and for a variable value of k^o (respectively $1.3 \cdot 10^{-7}$, $2.0 \cdot 10^{-7}$ and $2.0 \cdot 10^{-7} cm s^{-1}$, solid orange line; $k_p = 5.1 \cdot 10^{-4} m^7 mol^{-2} s^{-1}$; $lod = 5$ nm). The blue line in the lower panel represents the simulated current which flows through the NP in the case of a variable value of k^o (solid orange line) and the grey line represents the experimental current flowing through the entire electrode. (b) Screenshots of the simulated $Ni(OH)_2$ deposit at different times during the first CV cycle; the white vertical dashed line shows how r_{halo} is determined assuming a deposit of thickness 5 nm. (c, d) Concentration profiles of (c) HO^- and (d) Ni^{2+} ions obtained for the same NP at $t = 32 s$ (inversion potential).

4.2.4 ACTIVATION AND SIZE EFFECT

Next, the two subsequent cycles are simulated. When the same value of k° is used for all three cycles, the simulation does not fit the experimental transient (dashed orange line in Figure 4-5a). As mentioned above, it is not a question of l_{od} as, from the simulation, the ratio between plateaus remains approximately the same for $l_{od} = 1, 2,$ and 5 nm (Table A1-2 in **Appendix 1**). It could be due to the delay introduced by the fact that the NPs nucleate after the onset of water reduction during the first cycle, but the charge corresponding to this delay is negligible (Figure A1-10 in **Appendix 1**). This means that the rate of water reduction increases from cycle to cycle (solid orange line in Figure 4-5a). It indicates that increasing the thickness of the Ni(OH)_2 shell increases the water reduction rate at Ni NPs. This evolution of k° agrees with previous reports stating that the presence of Ni(OH)_2 enhances the catalytic activity of Ni.^[316]

The simulation further enables estimating the water reduction current at the single NP level. It is provided Figure 4-5a (lower panel, blue curve) along the three cycles. It tracks nicely (except for the Ni electrodeposition peak) the overall experimental current recorded for the whole electrode. It suggests that all electrodeposited NPs behave similarly. It also shows that the footprinting strategy provides a means to image electrocatalytic reactions at considerably low currents: for the 198 nm-radius NP considered in Figure 4-5a, a HER current of the order of 10 pA could be evaluated – indirectly – from such footprinting strategy. This corresponds to a much lower current density (about three orders of magnitude) than that required to initiate the formation of a H_2 NB. The footprinting strategy then allows expanding the scope of quantitative optical imaging to a wider range of reaction kinetics.

NPs of various sizes are then analysed in Figure 4-6 in order to discuss size effects in terms of initial activity, activation or passivation. The simulation allows to predict the evolution of the activity as a function the NP size. From Equation 4-8, a parabolic law ($r_{halo} \propto r_{NP}^2$) is expected, as illustrated by the simulated orange and blue lines in Figure 4-6a for two typical k° values. Experimentally, the halo's radius is estimated from the optical image, while the NP radius is evaluated from identical-location SEM images (an example of correlation is given in Figure 4-6c,d). The distribution of NPs sizes was clustered in five sub-groups characterized by a characteristic median NP size (NP1 to NP5). The values of k° for these five characteristic NPs were then evaluated from the fit of the experimental evolution of the halo's growth. The characteristic NPs of the smallest and the largest sub-groups, with respective size $r_{NP1} = 184 \text{ nm}$ and $r_{NP5} = 271 \text{ nm}$, are actually simulated by two different representative k°

values: the smallest, and most active, NP1 corresponds to the blue line in Figure 4-6a, while the largest, and less active, NP5 corresponds to the orange line in Figure 4-6a. The experimental halos of the whole set of NPs, with sizes spanning from ca. 145 to 380 nm, is then compared to these two representative activities in Figure 4-6a. It shows that smaller NPs ($r_{NP} < 200 \text{ nm}$) follow the trend of the most active (and smallest) NP1, whereas larger NPs ($r_{NP} > 200 \text{ nm}$) follow the trend of the less active (and largest) NP5. Over the three cycles, this analysis also shows that the largest NPs even tend to passivate after the second cycle.

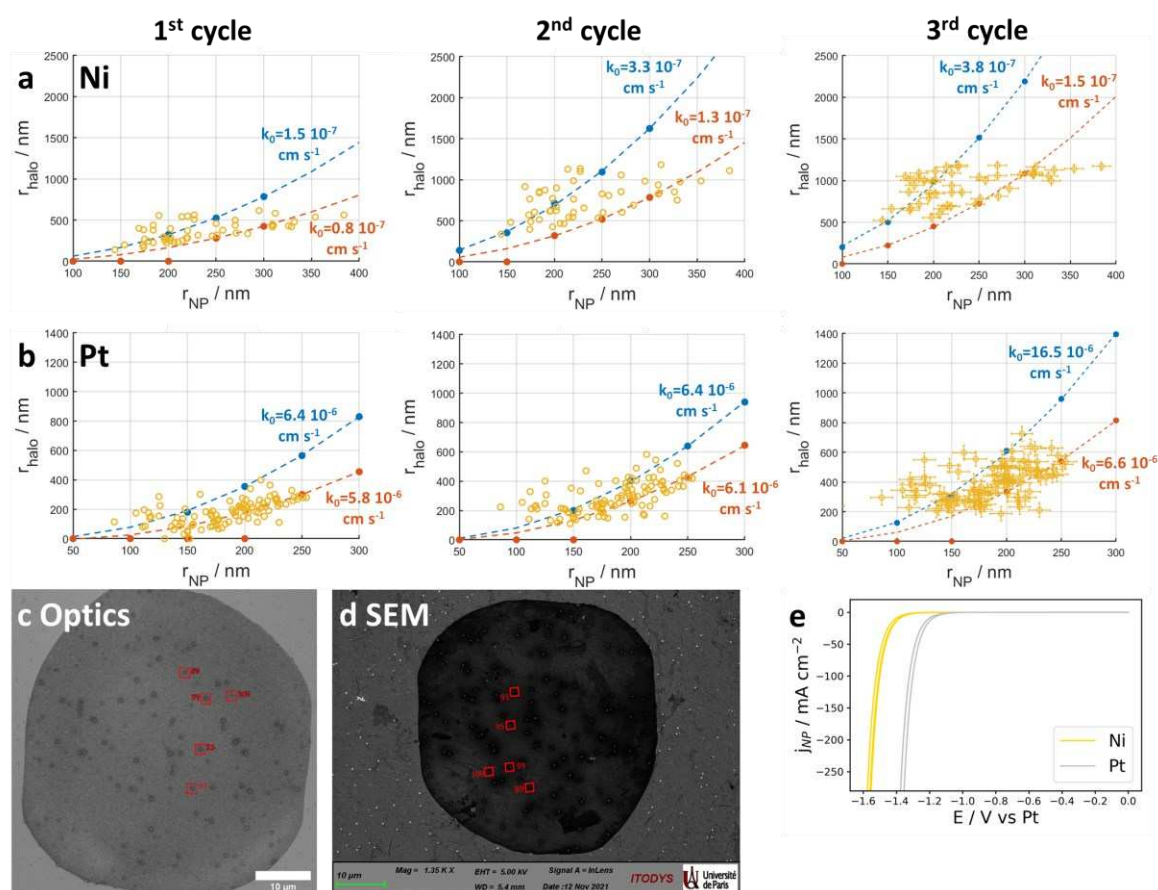


Figure 4-6. Influence of NP size and composition on water reduction activity in the presence of Ni^{2+} evaluated from the fit of the experimental r_{halo} for all NPs after each cycle. (a, b) Size effect analysed through a bimodal behaviour of low (orange) and high (blue) k° values evaluated for two characteristic NP sizes (see text); (a) for Ni NPs, the smallest (most active) population is described by NP1 ($r_{NP1} = 184 \text{ nm}$) while the largest (less active) population is described by NP5 ($r_{NP1} = 271 \text{ nm}$); (b) same for Pt NPs ($r_{NP1} = 171 \text{ nm}$ and $r_{NP5} = 243 \text{ nm}$). The error bars were omitted for clarity in the 1st and 2nd cycles, but the errors are the same for all data points. (c, d) Correlated optical and SEM images of the Pt NPs cycled in NiCl_2 (noteworthy, both images have different

orientations, ca. 180° rotation, as seen from the 5 highlighted NPs). (e) Reconstructed CVs of a Ni and a Pt NP of similar r_{NP} (respectively 206 and 203 nm).

It is interesting to note that NPs of similar r_{NP} can produce significantly different r_{halo} . Indeed, the error on the determination of r_{halo} (ca. 50 nm or 1 px) alone cannot explain the dispersity observed in Figure 4-6a (and b). This suggests that r_{NP} is not the only parameter influencing the electrocatalytic activity, but maybe also the crystal structure which cannot be probed neither by *in situ* optical microscopy nor *ex situ* identical-location SEM.^[343] This error on the determination of r_{halo} translates into a ca. 20% error on the determination of k° .

4.2.5 VERSATILITY OF THE STRATEGY

The methodology is highly versatile as proved by the first experiment (summarized in Figure 4-1) in which electrodeposited Pt NPs similarly subjected to water reduction in the presence of Ni²⁺ ions also exhibit a Ni(OH)₂ halo around them. Since water reduction occurred earlier than the nucleation potential of Ni (> -1.4 V), the Pt NPs can be considered as more active than the Ni@Ni(OH)₂ NPs. This is confirmed from the k° values determined from the simulations and visible on the simulated CVs given in Figure 4-6e. Starting from $k^\circ \approx 10^{-6} \text{ cm s}^{-1}$ for the pristine Pt NPs, in agreement with literature,^[344] an enhancement of activity is also observed along consecutive cycles, when electrocatalysis at Pt@Ni(OH)₂ is rather probed. It indicates a synergistic effect of the Ni(OH)₂ shell on water reduction electrocatalysis in neutral media. Finally, the influence of Pt NP size on activity was also studied. As seen in Figure 4-6b, the activity of Pt@Ni(OH)₂ NPs could also be clustered between two groups of more active and less active NPs depending on their size.

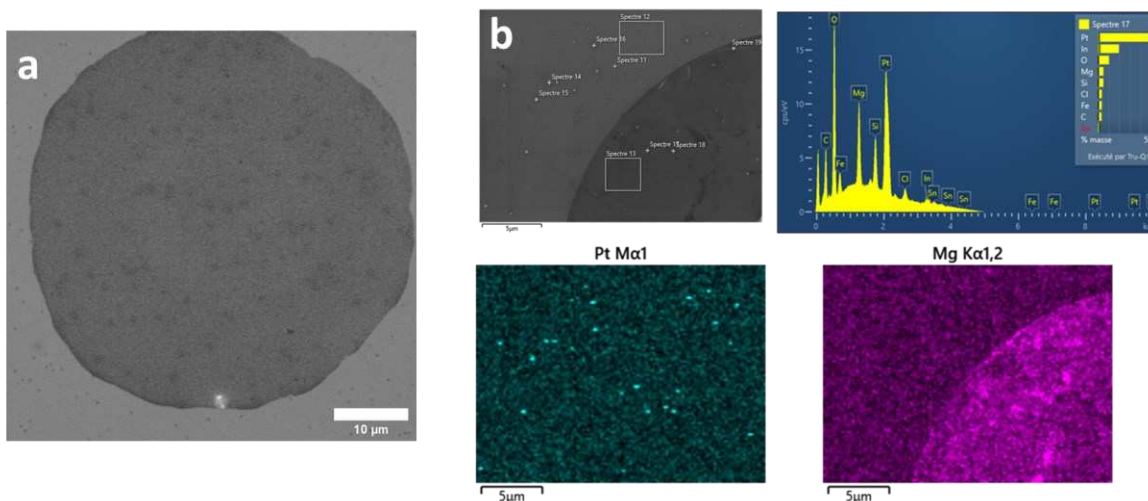


Figure 4-7. (a) Optical image of the Pt NPs cycled in MgCl_2 . (b) SEM image, corresponding Pt and Mg elemental mappings, and representative single-NP EDX spectrum of a Pt NP cycled in MgCl_2 (but not rinsed at the end of the experiment to avoid removing the $\text{Mg}(\text{OH})_2$ layer, different experiment than (a)).

To further test the versatility of our method in terms of footprint chemistry, the same Pt NPs (on another spot of the same ITO substrate) were then subjected to water reduction this time in the presence of Mg^{2+} ions. The latter have the advantage of preventing unwanted side reactions such as electrodeposition and have not been shown to have a significant effect on water reduction kinetics in dissolved form.^[345] In this case as well, a dark halo is detected around the Pt NPs on the optical images (Figure 4-7a). The halo is then very likely composed of $\text{Mg}(\text{OH})_2$ as suggested by a SEM-EDX mapping of the resulting structures (Figure 4-7b). Even though the absolute values of k° determined for Pt NPs using both Mg and Ni precipitates are different (Table A1-5 in **Appendix 1**), their evolution can be compared. The relative activity of Ni and Pt NPs (covered in both $\text{Ni}(\text{OH})_2$ and $\text{Mg}(\text{OH})_2$) along the three CV cycles is shown in Figure 4-8 in the form of a histogram. From this plot, one can conclude that $\text{Ni}(\text{OH})_2$ enhances the catalytic activity of Ni and Pt NPs, whereas $\text{Mg}(\text{OH})_2$ only blocks the activity of the Pt NPs. This clearly demonstrates the bifunctional effect of $\text{Ni}(\text{OH})_2$ and Ni/Pt.

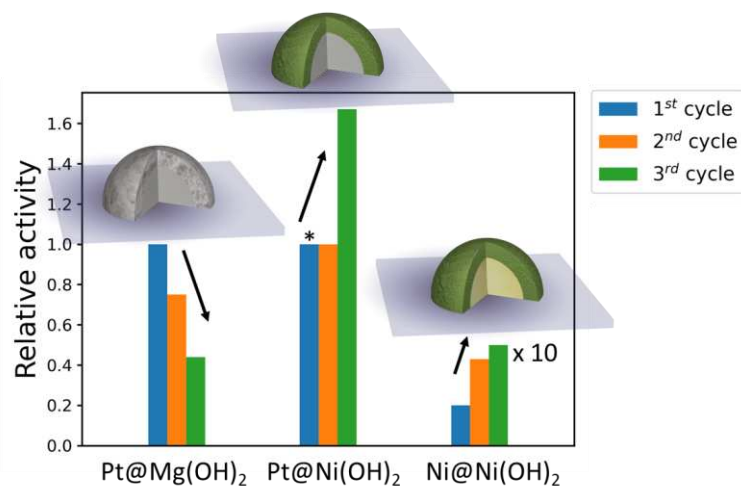


Figure 4-8. Histogram of the relative activity for water reduction electrocatalysis for NPs of comparable sizes along the three CV cycles for each composition. For the Pt NPs, the relative activity corresponds to the activity at cycle i compared to that at first cycle, $\frac{k_i^\circ}{k_1^\circ}$, evaluated for Pt NPs of $r_{NP} = 154 \text{ nm}$ and $r_{NP} = 145 \text{ nm}$, respectively. For Ni NPs, the activity along cycles is compared to that of the Pt NP cycled in NiCl_2 , $\frac{k_i^\circ}{k_1^\circ(\text{Pt@Ni(OH)}_2)}$, and is evaluated for a Ni NP of $r_{NP} = 184 \text{ nm}$. *The relative activity is assumed to be the same between the first and the second cycle because r_{halo} lies close to the detection limit during the first cycle.

4.3 CONCLUSION

In conclusion, we have demonstrated that the catalytic activity towards water reduction of single NPs can be measured by optically monitoring the growth of insoluble hydroxide halos forming around the NPs, which are used as footprints of the electrocatalytic reaction. A COMSOL model was proposed to quantify the electron transfer rate constant associated to water reduction at individual NPs from the growth dynamics of the footprint. Experiments showed that Ni and Pt NPs become more active after the first and the second cycle when Ni(OH)_2 is used as nano-shell, whereas they become less active when Mg(OH)_2 is used instead. This is consistent with previous reports stating that Ni(OH)_2 specifically enhances the catalytic activity of Ni and Pt via a bifunctional effect, while Mg(OH)_2 only blocks the NPs. The optical monitoring also revealed that larger NPs ($r_{NP} > 200 \text{ nm}$) are less active and activate less than smaller ones ($r_{NP} < 200 \text{ nm}$).

In addition to confirming the bifunctional effect of Ni/Pt and Ni(OH)₂ on water reduction activity for single NPs with ≈50 nm limit of detection (for the halo to be detected), the present study provides a powerful method for the measurement and screening of the activity of single NPs towards reactions involving the production of HO⁻ ions and not necessarily of gas NBs, like NO₃⁻ or CO₂ reduction for example. But more importantly than providing a means to image reactions which do not produce gases, this method allows to probe electrocatalysts at much lower – industrially-relevant – current densities than methods using gas NBs as proxy.

Furthermore, this strategy is not limited to OM but could also readily be applied to other types of *in situ* microscopies. For instance, we are currently working on its application to *in situ* liquid cell TEM in collaboration with the group of Damien Alloyeau (Laboratoire Matériaux et Phénomènes Quantiques, Université Paris Cité). While this technique is well-suited to probe morphological changes during electrocatalytic reactions, like most microscopy techniques it cannot quantify activity directly.

Chapter 5 DECOUPLING THE DYNAMICS OF ZINC

HYDROXIDE SULPHATE PRECIPITATION/DISSOLUTION IN AQUEOUS ZN–MnO₂ BATTERIES

This chapter was adapted with permission from ref. ^[346]. Copyright 2022 Wiley-VCH GmbH.

5.1 INTRODUCTION

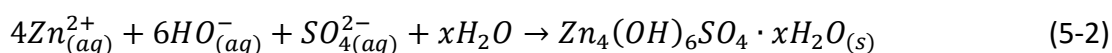
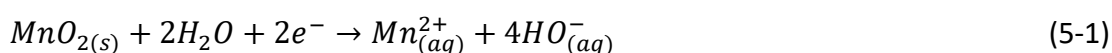
As discussed in **Chapter 1**, designing safe and sustainable batteries is paramount for the transition from fossil to renewable energy sources. For instance, by storing excess solar energy during daytime and restoring it during night-time, it could be used much more efficiently.^[347,348] However, the most wide-spread batteries, namely LIBs, are not quite suitable for grid-scale applications due to their high cost and the scarcity of their components.^[347] In this respect, aqueous Zn–MnO₂ batteries provide an interesting alternative to LIBs as Zn and Mn are more abundant in the Earth's crust than Li and Co for example. Moreover, these batteries work in aqueous electrolytes, making them safer than most LIBs which work in flammable organic electrolytes.^[349–355]

However, aqueous Zn–MnO₂ batteries have a poor cyclability, which is difficult to optimize as the charge storage mechanism of this system is still not fully understood.^[349–355] A typical galvanostatic charge-discharge cycle of an aqueous Zn–MnO₂ battery is presented in Figure 5-1a. As in most previous works, two plateaus are observed during charge and discharge. These plateaus were often attributed to Zn²⁺ insertion/extraction into/out of MnO₂,^[356–366] H⁺ insertion/extraction,^[367–370] but they could also reveal MnO₂ electrodisolution/electrodeposition,^[371–380] or combinations of the latter phenomena.^[373,381–387]

From the point of view of the electrode material, most studies discuss complex composites of carbon and chemically synthesized MnO₂ particles of a specific phase (e.g., α-MnO₂, β-MnO₂, λ-MnO₂...). However, if we admit that the electrodeposition/electrodisolution of MnO₂ is the

main pathway for charge storage, the phase control offered by chemical synthesis will be quickly lost. It thus seems relevant to propose, as in some recent examples,^[370,375,376,380,385] another approach focusing on the control and understanding of the electrodeposition of MnO₂.

From the analytical point of view, most structural and mechanistic conclusions concerning the electrochemical conversion of MnO₂ were drawn from results obtained by a single analytical technique, which might not be suitable to grasp the mechanism in all its complexity. XRD, for example, only allows to probe well-organized compounds. Therefore, it is practically blind to electrodeposited MnO₂, which exhibits only short-range order,^[388,389] as well as to potential amorphous precipitates. This is problematic as zinc hydroxides such as Zn₄(OH)₆SO₄·xH₂O (ZHS), which are expected to precipitate upon MnO₂ electrodisolution (see Equations 5-1 and 5-2) or H⁺ insertion,^[367–371,377,378,380,390] might not always appear in a crystalline form, thus hindering a comprehensive mechanistic analysis. Moreover, the temporal resolution of laboratory XRD (or spectroscopic techniques) might not be high enough to probe the competing dynamics of MnO₂ electrodisolution and ZHS precipitation.



Although not deeply inspected in the literature to the best of our knowledge, the role of ZHS is likely equally crucial during charge. The electrolyte acidification accompanying MnO₂ electrodeposition should yield ZHS dissolution. This step may then play an important role in the local buffering of the pH close to the electrode. The control of the electrolyte pH is also important during charge as recently highlighted through Pourbaix diagram analyses.^[370,391] A pH buffering may favour MnO₂ electrodeposition over the competing oxidation of water.

As discussed in **Chapter 1**, OM has emerged in the last decade as a promising tool to image and also quantify, and thus mechanistically unravel *in situ/operando* electrochemical processes related to energy storage.^[241,242,392] In Zn-ion batteries, it was mostly devoted to the imaging of the Zn anode, enabling the localization of the nucleation sites of Zn dendrites with nanometre precision.^[393–395] Regarding cathode materials, mostly Co-oxides were investigated by different OMs.^[2,396–399] They could evidence Li⁺ insertion/extraction during individual

nanoparticle cycling,^[396,397] map the Li⁺ front lines within a microparticle,^[183–185] or probe the volumetric expansion/shrinking of a microparticle associated with its charging/discharging.^[2,398]

In this study, optical reflectometry is used to monitor *operando* the preparation of the MnO₂ electrode in an aqueous Zn-MnO₂ battery environment and its further operation in subsequent charge-discharge cycles. Various *ex situ* structural and chemical analyses (ellipsometry, inductively coupled plasma-mass spectrometry (ICP-MS), X-ray diffraction (XRD), X-ray photoelectron spectroscopy (XPS), and Fourier transform-infrared reflection-absorption spectroscopy (FT-IRRAS)) of the electrode are also proposed to identify the materials formed during charge and discharge. Complemented by such *ex situ* analyses, it is shown herein how optical reflectometry enables an *in situ* quantitative evaluation of the dynamics of MnO₂ and ZHS deposition/dissolution associated with the electrochemical conversion of MnO₂. Once made quantitative, optical reflectometry is also employed as an imaging technique to resolve local electrochemical currents associated with MnO₂ electrodeposition around a ZHS microparticle, thus allowing to decipher the role of ZHS on charge.

5.2 RESULTS AND DISCUSSION

5.2.1 OPERATING PRINCIPLE

This study differs from the studies presented in the previous chapters where processes were monitored through optically transparent electrodes. Here, we inspect surface processes at reflecting (mirror) electrodes, such as metallic ones. It consists, as depicted in Figure 5-1b,c, in optically imaging the positive current collector (here a reflective Au surface) during the initial electrodeposition of MnO₂ from Mn²⁺ in the electrolyte, and subsequent charge-discharge cycles. Cycling is achieved either by CV or in galvanostatic mode, in electrolytes of compositions comparable to those used in the literature, except that the concentration of Mn²⁺ ions is 100 times lower (2 · 10⁻³ M MnSO₄ instead of 0.2 M) in order to limit the growth rate and thickness of the MnO₂ film.

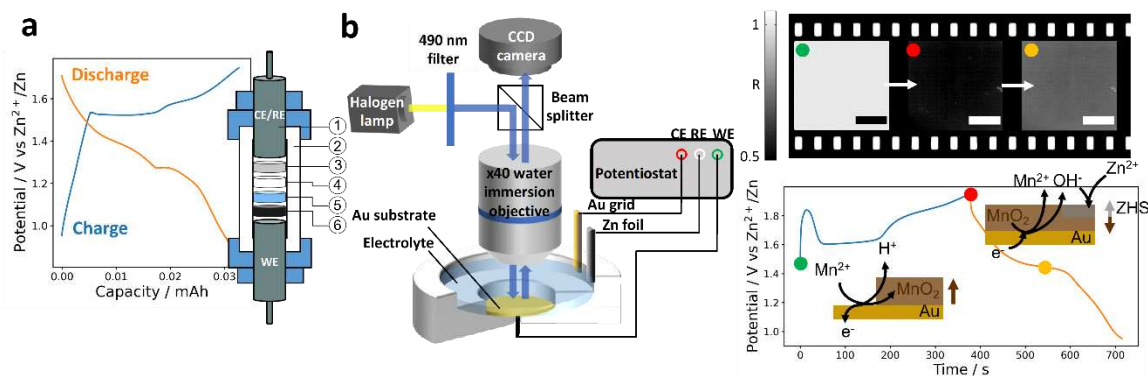


Figure 5-1. (a) Galvanostatic charge-discharge cycle (7th cycle) obtained in a two-electrode ½” Swagelok cell (scheme on the right: 1 stainless steel plunger, 2 cell body, 3 anode: Zn disk, 4 glass fibre separator, 5 electrolyte: 0.2 M MnSO₄ + 2 M ZnSO₄, 6 cathode mixture: 6 mg of carbon powder; current: 30 μA ≈ 1C). (b) Scheme of the *operando* optical reflectometry setup used to probe MnO₂ conversion on a Au current collector during CV or galvanostatic charge-discharge. Reflectivity images taken at different stages of a galvanostatic charge-discharge cycle (3rd cycle, current: 2 μA ≈ 9C, electrolyte: ZHS-saturated 2 · 10⁻³ M MnSO₄ + 2 M ZnSO₄, scale bars: 20 μm), and schematic illustration of the material deposition mechanism optically probed during the experiment.

A typical galvanostatic charge-discharge cycle performed under optical monitoring in a 2 · 10⁻³ M MnSO₄-containing electrolyte is presented in Figure 5-1b. It shows a behaviour similar to that observed at a higher Mn²⁺ concentration in a Swagelok cell (Figure 5-1a). The two characteristic plateaus with bump are detected, although at slightly different potentials in agreement with the increase of oxidation potential with decreased Mn²⁺ content and higher cycling rate.^[367,376] Optical images of the electrode surface are acquired continuously (at 0.5 frame per second) during the experiment. As explained in **Appendix 2**, they are mathematically converted into reflectivity, *R*, images, which represent the relative variation of optical contrast of the imaged surface. Typical reflectivity images, taken at different states of (dis)charge, are given in Figure 5-1b. The optical monitoring then provides a dynamic measurement of the local reflectivity, *R*, of the electrode surface during charge and discharge. During charge, the electrode darkens as a MnO₂ film grows on top of it, making it less reflective (the reflectivity, *R*, decreases) than the original Au surface. During discharge, the electrode brightens again (*R* increases), already suggesting MnO₂ electrodisolution rather than other types of conversion. By monitoring the darkening/brightening (the reflectivity, *R*) of the

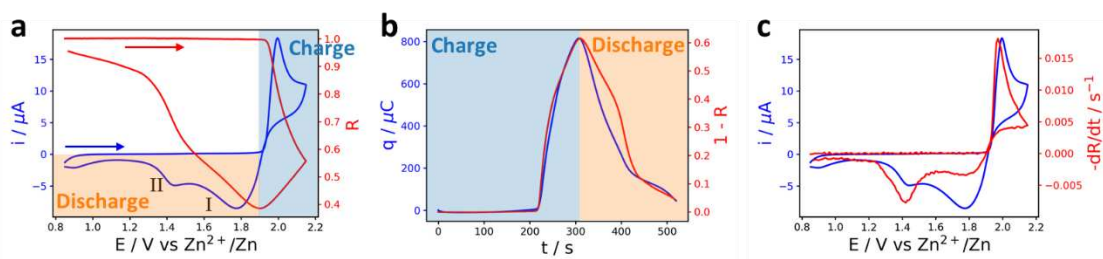
electrode surface, one can then track the accumulation/removal of material onto/from it. First, a qualitative analysis of the optical images is proposed during CV experiments.

5.2.2 CYCLIC VOLTAMMETRY – QUALITATIVE ANALYSIS

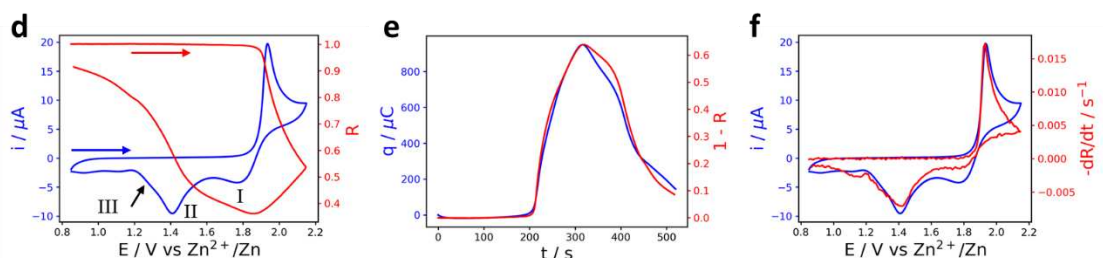
For the qualitative analysis, two different electrolytes are compared: the usual electrolyte for galvanostatic cycling in a Swagelok cell (diluted in Mn^{2+} to limit the thickness of the MnO_2 film, see above) i.e., $2 \cdot 10^{-3}$ M MnSO_4 + 2 M ZnSO_4 (pH \approx 3.8), and ZHS-saturated $2 \cdot 10^{-3}$ M MnSO_4 + 2 M ZnSO_4 (pH \approx 5.2, $[\text{Zn}^{2+}] = 2.14$ M (ICP-MS)). The latter should be more representative of the solution composition reached in a Swagelok cell. Indeed, since the electrolyte volume contained in a Swagelok cell is much smaller than in the *operando* optical reflectometry cell (300 μL vs 10 mL), a more rapid pH increase is expected upon MnO_2 electrodisolution in a Swagelok cell.

Although the electrochemical behaviour of cells is often discussed in light of repetitive (stable) charge-discharge cycles, apprehending the initial electrodeposition of MnO_2 onto the current collector is fundamental in aqueous Zn- MnO_2 batteries. Indeed, even if the battery initially contains MnO_2 particles in the cathode mixture and is started on discharge, several groups have shown that the presence of Mn^{2+} ions in the electrolyte is mandatory to achieve better cyclability. This is because a constant amount of Mn^{2+} benefits MnO_2 electrodeposition during subsequent charges.^[367,370] For this reason, we propose to observe the system's behaviour during the first cycle, starting on charge from a bare Au electrode. The first cycle of representative CVs obtained in both electrolytes is given in Figure 5-2a,d. Subsequent cycles have also been recorded and show identical to very similar behaviours (Figure 5-2g,h).

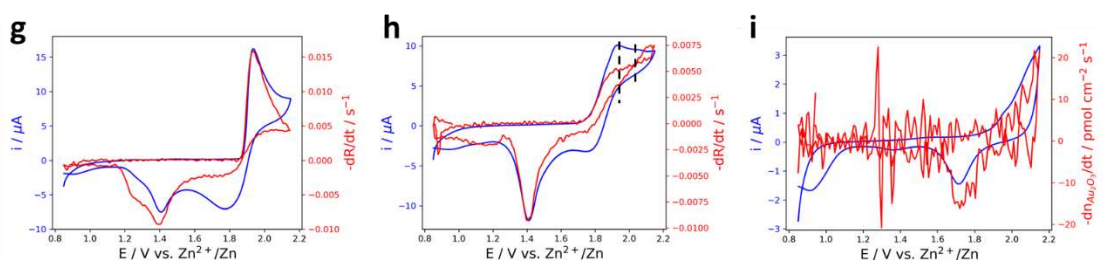
Unsaturated electrolyte



ZHS-saturated electrolyte



Second cycles



Blank

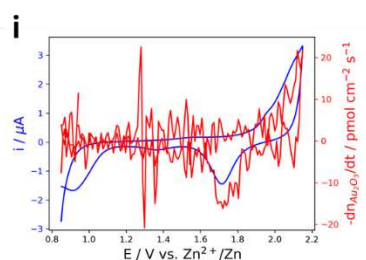


Figure 5-2. Electrochemical CV (blue line) and corresponding reflectivity, R , variation (red line) of a Au substrate (average value over $\approx 1000 \mu\text{m}^2$) obtained in (a) unsaturated and (d) ZHS-saturated $2 \cdot 10^{-3} \text{ M MnSO}_4 + 2 \text{ M ZnSO}_4$ (scan rate: 5 mV s^{-1}). (b, e) Unfolded and integrated representation of the CVs showing the charge (light blue area) then discharge (orange area) processes with corresponding electrochemical charge (q , integrated from the electrochemical current, blue line) and transmittivity ($1 - R$, red line) variations with time. (c, f) Electrochemical CVs (blue line) and corresponding optical CVs (red line). (g, h) Second cycles of the CVs presented in (a) and (d), respectively. (i) CV obtained in 2 M ZnSO_4 (blue) showing the oxidation of the Au substrate and corresponding optical CV (red), given as molar flux of Au_2O_3 according to the single-component optical model presented in **Appendix 2**, section A2.1.

Optical images of the Au current collector are recorded simultaneously and converted into reflectivity images. The changes in reflectivity, R , during the charge and discharge processes can be rationalized as changes in material deposition onto the reflective Au electrode based on Fresnel's treatment of optical reflections at multiple interfaces: a decrease/increase of the reflectivity relates to a relative accumulation/removal of material (of lower permittivity than

Au) onto/from the electrode surface. In order to monitor the cycling of MnO₂ electrodes, a first model considering the growth of a single-component layer (of MnO₂) onto a Au substrate is used (see **Appendix 2**, section A2.1). In the limit of the deposition of thin MnO₂ layers (up to ca. 20 nm, Figure A2-1 in **Appendix 2**), provided by charging from an electrolyte containing only 2 · 10⁻³ M MnSO₄, the reflectivity of the Au substrate should vary linearly with the thickness of the MnO₂ layer, δ_{MnO_2} , as:^[242,400,401]

$$1 - R = \delta_{MnO_2} n_{sol} \frac{8\pi}{\lambda} \text{Im} \left(\frac{n_{MnO_2}^2 - n_{Au}^2}{n_{sol}^2 - n_{Au}^2} \right) \quad (5-3)$$

where n_{sol} , n_{MnO_2} and n_{Au} represent the complex refractive indices of the electrolytic solution, the MnO₂ layer, and the Au surface (given in the caption of Figure A2-1 in **Appendix 2**), Im the imaginary part of the corresponding fraction, and λ the wavelength of the incident light, respectively.⁵ It is worth mentioning that coatings composed of multiple components (e.g., MnO₂ and ZHS) can also be modelled as will be discussed below.

The reflectivity images are generally homogeneous as shown in Figure 5-1b. This suggests a homogeneous transformation of the Au surface, at least within the 0.5 μm optical lateral resolution evaluated experimentally from Figure 5-8a. It means that within this 0.5 μm resolution, MnO₂ is not growing in a dendritic fashion. Hence, average values of R (over ≈1000 μm²) are considered first. The evolution of the average value of R during the CVs in both electrolytes is also presented as the red line in Figure 5-2a,d.

Noteworthy, in CV experiments, charge and discharge are performed at variable potential and current. As illustrated by the blue-coloured region in Figure 5-2a, the charge step lasts as long as the current is positive i.e., during the whole forward scan and the first part of the backward scan. The discharge step (orange region in Figure 5-2a) starts during the backward scan when the current becomes negative. For clarity, the CVs are also presented in Figure 5-2b,e in their unfolded and integrated form (charge vs time), showing more distinctly the charge and discharge steps.

During the first forward (oxidation) scan, the reflectivity of the Au substrate, R , decreases concomitantly to the appearance of an oxidation peak in the CVs. This confirms that the

⁵ The reflectivity variations for thicker MnO₂ deposits can also be evaluated from the derivations provided in **Appendix 2**, section A2.1.

oxidation of Mn^{2+} ions from the electrolyte results in the deposition of a Mn-oxide onto the Au electrode. This Mn-oxide is identified as being MnO_2 from the >95% faradaic efficiency of the process (determined by ICP-MS). According to Equation 5-3, $1 - R$ scales as the amount of deposited material, and therefore as the amount of charge, q , injected during the electrodeposition/electrodissolution. The electrochemical charge, q , exchanged during the CV is then compared to $1 - R$ in Figure 5-2b,e and both quantities match perfectly during the whole charge (up to ≈ 300 s).

During discharge, along the reverse scan, two reduction peaks are observed in the unsaturated electrolyte (Figure 5-2a), respectively at 1.8 (I) and 1.4 V (II). In the ZHS-saturated electrolyte (Figure 5-2d), peak I decreases in intensity (and amount of charge) for the benefit of peak II. In addition, a shoulder (III) appears at 1.3 V. These three features are consistent with the ones observed during galvanostatic discharge in the same conditions (Figure 5-1b). After a short discharge plateau at ca. 1.7–1.8 V (peak I), a larger discharge plateau is detected at ca. 1.4 V (peak II), followed by a last sloping discharge plateau at 1.3 V matching with shoulder III. According to the literature, peak I should correspond to the reduction of MnO_2 in an acidic environment,^[373,375,402–404] which is usually not encountered in a Swagelok cell due to its small volume, and whose contribution can be strongly attenuated by saturating the electrolyte with ZHS (see above).

The reflectivity changes during the backward scan, better visualized in the unfolded charge-time representation of the CVs (Figure 5-2b,e), do not match the evolutions of q anymore, except at the very end ($t > 400$ s) in the unsaturated electrolyte. This means that the discharge dynamics (electron injection) does not track the dynamics of MnO_2 dissolution. The better match in the unsaturated electrolyte at the end of the discharge means that overall, the discharge is consistent with the dissolution of MnO_2 into soluble Mn^{2+} . The reflectivity also almost returns to 1 and the charge to 0, indicating that nearly all the MnO_2 deposited during the forward (oxidation) scan is dissolved during the reverse (reduction) scan, which is further confirmed by *ex situ* ellipsometry (Figure 5-3a).

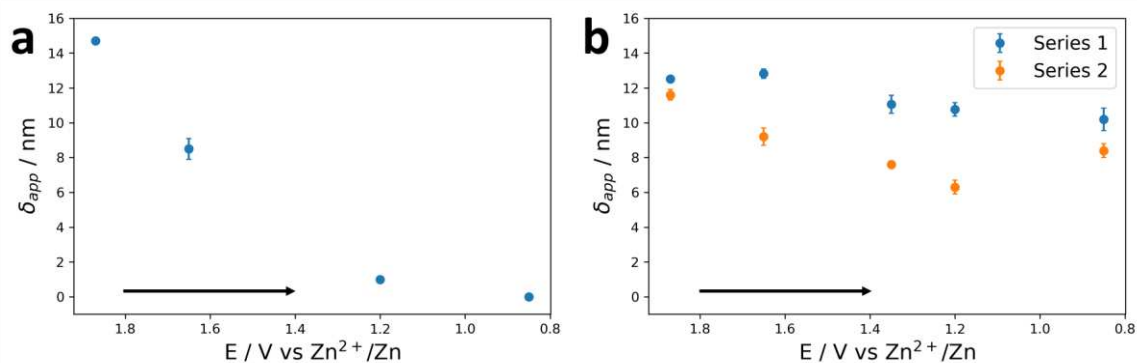


Figure 5-3. Apparent thickness of the MnO_2 film at different stages of the reverse (discharge) scan in (a) unsaturated and (b) ZHS-saturated $2 \cdot 10^{-3} \text{ M MnSO}_4 + 2 \text{ M ZnSO}_4$ (two different series of experiments).

The differences in the charge and reflectivity dynamics are also visible in differentiated variables such as the electrochemical current and equivalently for the optical signal, $-dR/dt$, hereafter denoted as optical current. If the reductive electrochemical current expresses the rate of charge injection (e.g., via Equation 5-1) for the reduction of MnO_2 , the optical current expresses the apparent rate of material deposition ($-dR/dt > 0$) or dissolution ($-dR/dt < 0$) on the electrode. For the unsaturated electrolyte, the electrochemical and optical currents are compared in Figure 5-2c. When the oxidation peak currents of both CVs are matched, significant differences during discharge are revealed. During the first reduction peak at 1.8 V (peak I), the optically inferred apparent dissolution rate is smaller than suggested by the electrochemical current, and vice versa during the second reduction peak at 1.4 V (peak II). These discharge/dissolution rate mismatches are also detected when several CV cycles are performed (Figure 5-2g).

The small dissolution rate compared to the charge transfer rate measured during peak I suggests an overall electrodedissolution of MnO_2 , but with low faradaic efficiency. It can have different explanations pointing the intervention of concurrent paths, either an electron transfer path, a chemical material deposition path, or a combination of both. The competing electron transfer path could, for example, be the reduction of MnO_2 into MnOOH . Owing to the $\approx 8\%$ decrease in refractive index when going from MnO_2 to MnOOH ,^[405] the full conversion of MnO_2 into MnOOH would yield a reflectivity variation of ≈ 0.1 . If this conversion could explain the reflectivity variations measured during peak I, it cannot explain the reflectivity

variations measured during the entire discharge, and more so as MnOOH is expected to disproportionate into soluble Mn^{2+} and MnO_2 in the investigated pH range.^[370,391] Moreover, the reductive intercalation of Zn^{2+} ions would also yield some apparent material accumulation on the electrode, but this process should be self-limited to the Au|MnO₂ interface since ZnMn₂O₄ is not electroactive.^[406] It is more likely that a chemically formed material kinetically precipitates on the electrode (at the MnO₂|electrolyte interface) during peak I. This hypothesis is supported by experiments where the potentiostat is stopped at 1.7 V in the backward scan (shortly after peak I) while images of the surface are still continuously acquired. As soon as the potentiostat is stopped, the optical current becomes positive (and stays positive for >100 s), meaning that material continuously accumulates on the substrate at open circuit although no charge is injected anymore (Figure 5-4). As the overall process occurring during peak I is an apparent dissolution, the contribution of the competing reactions is lower than (almost compensates) the overall dissolution of MnO₂. It is however difficult at this stage to evaluate the contribution of each process: 1) the electrodisolution into Mn^{2+} , 2) the reduction into MnOOH or intercalation, and 3) the chemical precipitation of another material.

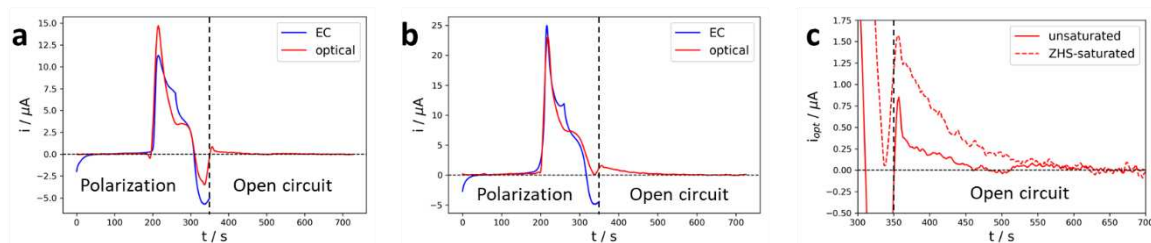


Figure 5-4. Electrochemical current (blue) and corresponding optical current (charge-normalized, red) obtained in (a) unsaturated and (b) ZHS-saturated $2 \cdot 10^{-3} \text{ MnSO}_4 + 2 \text{ M ZnSO}_4$ (scan rate: 5 mV s^{-1}). The polarization was stopped when the potential had reached 1.7 V (350 s, dashed vertical line) in the reverse scan (the system was then left unpolarized at open circuit). (c) Zoom of the optical current variation right after the polarization was stopped.

In the ZHS-saturated electrolyte, the same mismatch between the electrochemical and optical CVs is observed in the region of peak I at 1.8 V (Figure 5-2f), and the same competing paths could be invoked. However, in the ZHS-saturated electrolyte, the release of HO^- ions during MnO₂ electrodisolution should allow for a supersaturation of ZHS near the electrode surface and thus favour its precipitation. The precipitation of ZHS is widely acknowledged in this kind of systems,^[367–369,371,377,380,390] but its presence on the electrode surface has only been

revealed at the latest stages of the discharge process and particularly during the second discharge plateau. The qualitative analysis above suggests it also occurs at the beginning of the discharge (peak I). To confirm this suggestion, we propose, based on complementary chemical and structural analyses, a more quantitative analysis of the reflectivity results in the following sections.

5.2.3 CYCLIC VOLTAMMETRY – QUANTITATIVE ANALYSIS IN THE ZHS-SATURATED ELECTROLYTE

5.2.3.1 ANALYSIS OF THE CHARGE

The CV and reflectivity data from Figure 5-2d-f is now interpreted in terms of electrochemical charge and deposited/dissolved mass, providing information similar to that obtained by an optical surface plasmon resonance (SPR) sensorgram^[407] or by an electrochemical quartz crystal microbalance (EQCM). In the field of EQCM, a common analysis consists in plotting the mass change (calculated from the quartz crystal's frequency change) against the electrochemical charge.^[369,377] By virtue of Faraday's law, the slope of this plot is proportional to the molar mass of the electrodeposited/electrodissolved compound, thus enabling its identification. Similarly to the frequency change of an EQCM, the reflectivity change of the Au substrate can also be converted into a mass change. First, the experimental reflectivity change is expected to follow Equation 5-3 for a single-component film, meaning that at a constant wavelength, the complex refractive indices on the right-hand side of Equation 5-3 are constant. Then, $1 - R$ is expected to vary linearly with the MnO_2 film thickness. The experimental reflectivity is then converted into an apparent MnO_2 thickness, δ_{app} , using a calibration factor, C_f , determined by *ex situ* ellipsometry at the end of the charge, from:

$$1 - R = \delta_{\text{MnO}_2} n_{sol} \frac{8\pi}{\lambda} \text{Im} \left(\frac{n_{\text{MnO}_2}^2 - n_{\text{Au}}^2}{n_{sol}^2 - n_{\text{Au}}^2} \right) = C_f \delta_{\text{MnO}_2}. \quad (5-4)$$

Then, the optically inferred thickness, δ_{app} , is converted into an apparent mass, m_{app} , by multiplying it by ρ_{app} , the apparent density of the MnO_2 film, and S , the geometric surface area of the Au electrode in contact with the solution ($S = 0.16 \text{ cm}^2$ for the experiment shown in Figure 5-2d-f):

$$m_{app} = \delta_{app} \rho_{app} S. \quad (5-5)$$

The optically inferred mass of equivalent MnO_2 deposit, m_{app} , is then compared to the electrochemical charge, q , integrated from the CV, separated into charge and discharge as presented in Figure 5-5a,b. During charge (Figure 5-5a), the deposited mass linearly increases with the amount of injected charge, in line with the faradaic nature of the electrodeposition. Together with the overall faradaic efficiency of >95% measured by ICP-MS for MnO_2 electrodeposition, the continuous linear variation suggests the faradaic efficiency holds along the whole charge.

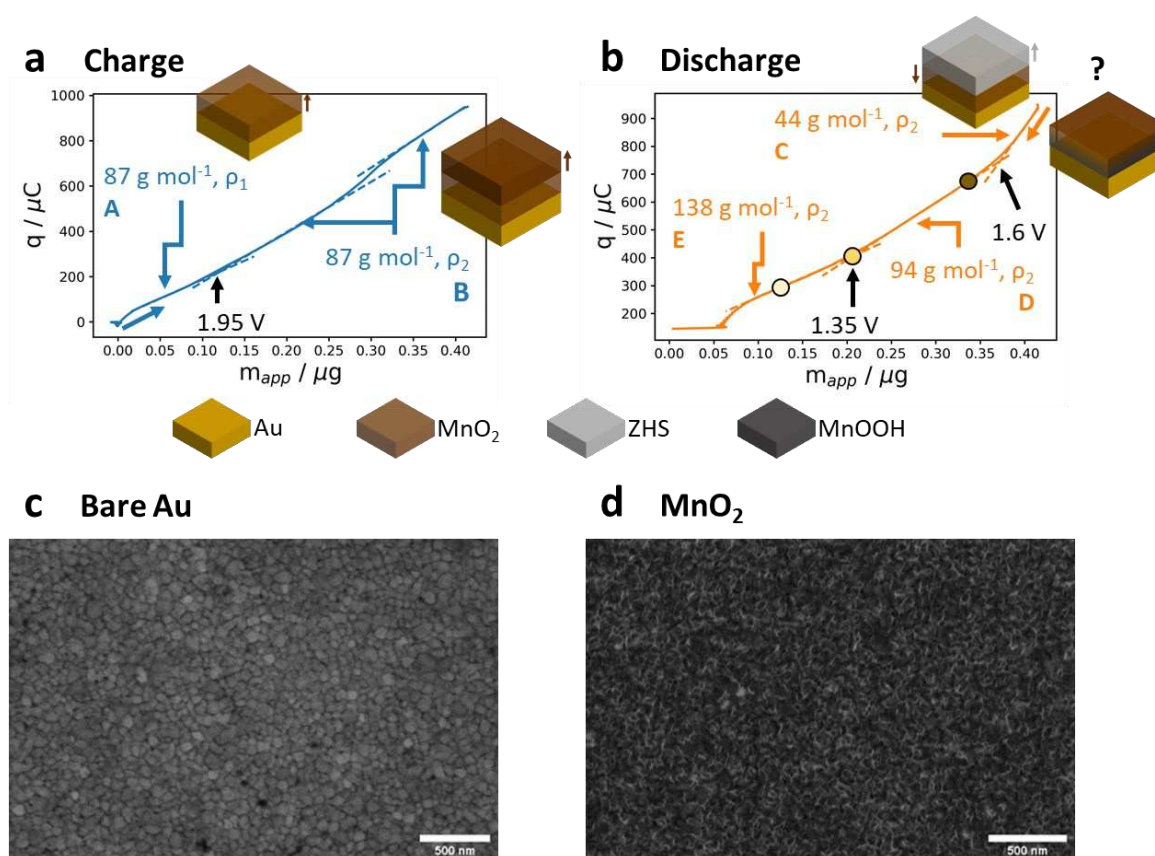


Figure 5-5. Charge versus apparent mass plot during (a) charge and (b) discharge in the ZHS-saturated electrolyte (experiment presented in Figure 5-2d-f). Dashed lines represent local slopes. The corresponding molar masses are given alongside. (c) SEM image of a bare Au substrate. (d) SEM image of an electrodeposited MnO_2 film revealing a high degree of porosity.

As explained above, the linear charge-mass relationship enables estimating the apparent molar mass, M_{app} , of the deposit according to Faraday's law:

$$q = \frac{2F}{M_{app}} m_{app} = \frac{2F \rho_{app} S}{M_{app}} \delta_{app}. \quad (5-6)$$

In order for the slope in region A (from 0.85 to 1.95 V in the forward scan) to match with the molar mass of MnO₂, a density of $\rho_{app} = \rho_1 = 1.62 \text{ g cm}^{-3}$ has to be used in the conversion. This value is approximately three times smaller than the density of bulk MnO₂ ($\rho_{bulk} = 5.03 \text{ g cm}^{-3}$), but close to the actual density of the film determined by ellipsometry and ICP-MS ($\rho_{meas} = 1.95 \pm 0.35 \text{ g cm}^{-3}$), as well as to previously reported densities of electrodeposited MnO₂.^[408] This rather low density is also supported by SEM images of the film which reveal a high degree of porosity (Figure 5-5d).^[388,389,409] If the pores are filled with electrolyte trapped inside the film during electrodeposition, it would be more difficult to determine the true molar mass of MnO₂ using an EQCM as the frequency response would be strongly influenced by these electrolyte pockets.^[369,377] Optical reflectometry, however, should not be affected by such pockets as their refractive index should be very close to that of bulk electrolyte.

Beyond 1.95 V (region B in Figure 5-5a), the apparent molar mass decreases to 66 g mol^{-1} if the same apparent density is used for the conversion. However, according to the overall faradaic efficiency, MnO₂ should be electrodeposited during the whole charge (see above). Therefore, the apparent density of the MnO₂ film likely increases in region B ($\rho_2 = 2.14 \text{ g cm}^{-3}$). This is corroborated by the fact that the actual density of the MnO₂ film measured by ellipsometry and ICP-MS at the end of the charge is very close to the mass-weighted average of ρ_1 and ρ_2 ($\rho_{mean} = 1.98 \text{ g cm}^{-3}$). The charge jump observed between 2.05 and 2.15 V likely corresponds to the formation of a small amount of gold oxide (see blank CV in Figure 5-2i). Its influence is however limited as the slope quickly gets back to its previous value. Altogether, optical reflectometry, combined with *ex situ* ellipsometric calibrations, allows to quantitatively analyse *in situ* and dynamically the electrodeposition of MnO₂ during charge.

5.2.3.2 ANALYSIS OF THE DISCHARGE

At the beginning of the discharge (Figure 5-5b), the apparent molar mass decreases to 44 g mol^{-1} (region C). Then, a first slope discontinuity is observed at approximately 1.6 V (from 44

to 94 g mol^{-1} , region D), and a second one at approximately 1.35 V (from 94 to 138 g mol^{-1} , region E).

The apparent molar mass decrease in region C again suggests that the electrodisolution of MnO_2 proceeds with a low faradaic efficiency: the amount of material removed from the surface is lower than expected considering the injected electrochemical charge. As discussed above in the qualitative analysis, this could be attributed to the occurrence of competing pathways such as the reductive conversion to Mn(III) species (discussed above) or the chemical precipitation of another material. The molar masses are however difficult to attribute, and it is therefore difficult to conclude. This is not surprising as the two steps of both proposed mechanisms probably do not track each other. In this case, the analysis based on a single-component film and Faraday's law is not valid anymore.^[369,377] To circumvent these issues, complementary structural and chemical characterizations of the MnO_2 film at different states of discharge are proposed in the following. The knowledge of the composition of the film will indeed allow to refine the optical model and analyse more precisely the reflectivity results of the discharge process.

COMPLEMENTARY CHEMICAL AND STRUCTURAL ANALYSES

Au substrates were then analysed *ex situ* by ellipsometry, XRD, FT-IRRAS, and XPS after CV experiments halted at different potentials (≈ 1.85 , 1.65, 1.35, 1.2, and 0.85 V) in the reverse scan. By *ex situ* ellipsometry, it is shown that the apparent optical thickness of the film remains almost constant below 1.65 V ($\approx 11 \pm 2 \text{ nm}$ using the refractive index of MnO_2 , Figure 5-3b), while it is admitted that MnO_2 should dissolve during this reduction step. This again suggests that the electrodisolution of MnO_2 is accompanied by the deposition of another optically probed material, likely ZHS.

No XRD signature (apart from the substrate) is detected until the end of the CV, where peaks associated with ZHS appear (Figure 5-6b). This is consistent with previous reports suggesting that crystalline ZHS is formed at the latest stages of the discharge.^[367–369,371,377,380,390] The precipitate detected during discharge, either *in situ* by optical reflectometry or *ex situ* by ellipsometry, is therefore most likely amorphous. However, when the partially discharged samples were left to dry in air (in the absence of light) for several weeks, XRD patterns could

be detected, such as at 1.2 V (Figure 5-6a). These were attributed to *sweetite* $\text{Zn}(\text{OH})_2$ as well as to residual $\text{ZnSO}_4 \cdot 7\text{H}_2\text{O}$, suggesting the presence of a precipitate composed of Zn^{2+} , HO^- , and SO_4^{2-} ions which is not only residual electrolyte.

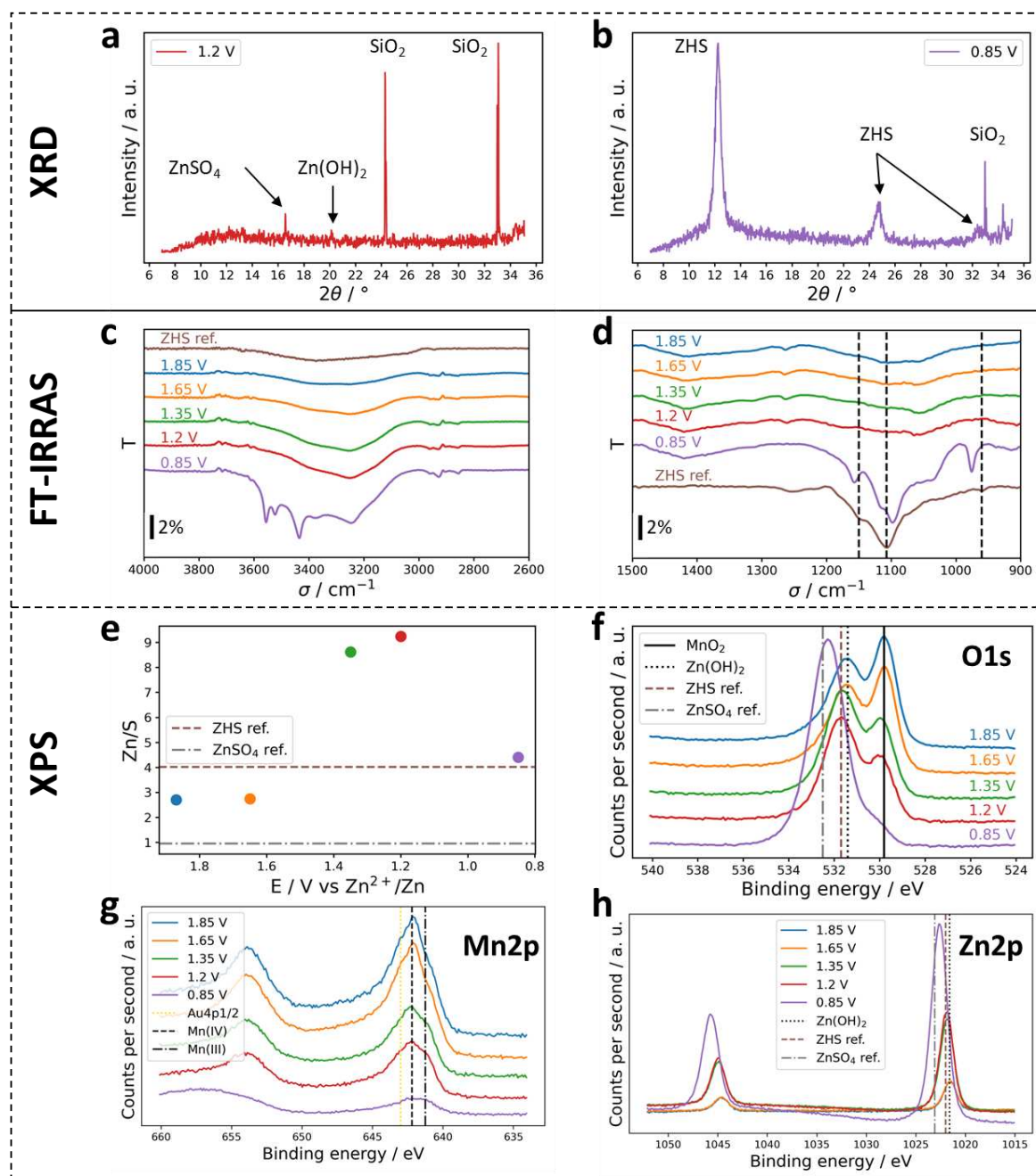


Figure 5-6. Diffractogram of the MnO_2 electrode cycled (a) until 1.2 V in the reverse scan and (b) until the end of the discharge. Attributions: ZnSO_4 ($\text{ZnSO}_4 \cdot 7\text{H}_2\text{O}$): (111), PDF 00-001-0402; $\text{Zn}(\text{OH})_2$ (*sweetite*): (110), PDF 00-001-0360; SiO_2 : (-404) and (-512), PDF 00-018-1170; ZHS (zinc hydroxide sulphate hydrate): (001), (002) and (130)-(230), PDF 00-039-0690. FT-IRRA spectra of the electrode at different states of discharge and ATR-FT-IR spectrum of synthesized ZHS powder (see **Materials**

and methods, section M.1.2) in the (c) high and (d) low wavenumber region. (e) Zn/S ratio of the electrode measured by XPS at different states of discharge by integrating the Zn2p and S2p peaks. High-resolution spectra of the electrode in (f) the O1s, (g) the Mn2p, and (h) the Zn2p region at different states of discharge. The same colour code is used for all panels.

The presence of HO^- ($3000\text{-}3600\text{ cm}^{-1}$) and SO_4^{2-} ($950\text{-}1230\text{ cm}^{-1}$) groups throughout discharge is confirmed by FT-IRRAS (Figure 5-6c,d).^[410] In agreement with the XRD results, the characteristic vibrational bands of ZHS (1150 , 1110 , and 960 cm^{-1} , brown spectrum in Figure 5-6d) are only observed at the end of the CV. The hyperfine structure in the $3000\text{-}3800\text{ cm}^{-1}$ region (Figure 5-6c) also suggests a crystallized compound is formed at the end of the discharge.

Likewise, XPS measurements on the same samples confirm the presence of Zn and S throughout discharge with a Zn/S ratio greater than 1 (which would correspond to ZnSO_4 from the electrolyte) but reaching 4 (which corresponds to crystalline ZHS) only at the end of the CV (Figure 5-6e).⁶ The crystallization of ZHS from $\text{Zn}(\text{OH})_2$ is further evidenced by the shift of the Zn2p and O1s peaks from a $\text{Zn}(\text{OH})_2$ -like to a ZnSO_4 -like environment (Figure 5-6f,h).

All these analyses confirm the presence of a Zn-based precipitate throughout discharge, likely an amorphous form of ZHS, which crystallizes only at the end of the CV for reasons not yet understood.

QUANTITATIVE IN SITU MONITORING

The detection of ZHS precipitate by different *ex situ* analyses might explain the inadequate fit of the reflectivity data with the simple optical model (Equation 5-3) considering a single-component (MnO_2) coating of the electrode. Thus, a coating consisting of a mixture of MnO_2 and ZHS was considered to refine the model. The theoretical reflectivity response of a mixed layer of ZHS and MnO_2 of varying individual composition (thickness or mass density) is then

⁶Unfortunately, the oxidation state of Mn could not be unequivocally determined by XPS as the Mn3s and Mn2p peaks, which are most commonly used for this purpose, overlap with Au and Zn peaks (Figure 5-6g). Still, the position of the Mn2p and Mn3p peaks suggests that Mn(IV) is directly converted to Mn(II) (and vice versa), but a complex fitting procedure would be necessary to confirm this hypothesis,^[457] which is out of the scope of the present study.

evaluated. It is given as a 2D reflectivity map in Figure 5-7a and used to evaluate, from the experimental reflectivity variations, the proportion of MnO_2 and ZHS during discharge (details about the model can be found in **Appendix 2**, section A2.2).

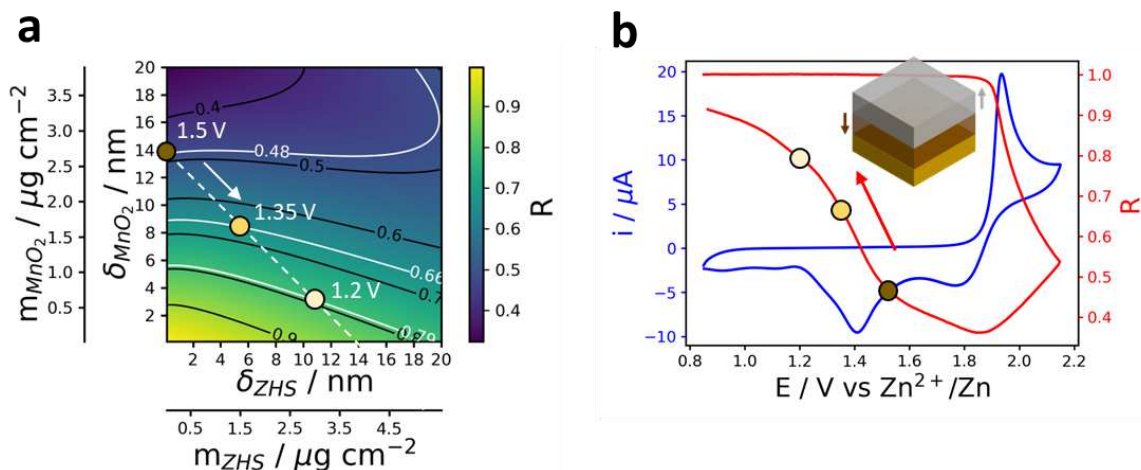


Figure 5-7. (a) Theoretical reflectivity response of a Au substrate covered by a layer of mixed MnO_2 and ZHS of varying individual composition (equivalent thickness or mass density). The white dashed line represents the path followed by the system at a constant apparent thickness. (b) Electrochemical CV (blue) and corresponding reflectivity variation (red) of a Au substrate in ZHS-saturated $2 \cdot 10^{-3} \text{ M MnSO}_4 + 2 \text{ M ZnSO}_4$ (scan rate: 5 mV s^{-1}).

Experimentally, from the slope of the measured reflectivity versus potential in Figure 5-7b, we see that the electrodisolution of MnO_2 is predominant for $E > 1.5 \text{ V}$ in the reverse scan. This is fully consistent with the qualitative analysis made before as the precipitate formed between 1.85 and 1.5 V is not stable and therefore does not accumulate on the substrate (Figure 5-4). However, it does not necessarily imply that ZHS does not precipitate in this potential region. First, it is assumed that at 1.5 V, the film is mainly composed of MnO_2 . This means, for simplicity, that the system is still on the vertical axis in Figure 5-7a. From the measured reflectivity in Figure 5-7b, $R = 0.48$, this corresponds to an apparent MnO_2 thickness of 14 nm, which is in good agreement with the ellipsometric value of 11 nm evaluated from another sample at the same potential. Based on *ex situ* ellipsometry (Figure 5-3b), when the electrode potential decreases, the discharge proceeds under roughly constant overall thickness, which means that the reflectivity should evolve following an antidiagonal line on the 2D reflectivity map in Figure 5-7a. For the experiment shown in Figure 5-7b, it should follow the 14 nm

constant thickness antidiagonal represented by the white dashed line in Figure 5-7a. When the potential decreases from 1.5 to 1.35, to 1.2 V, the reflectivity rises from 0.48 to 0.66, to 0.79, respectively (Figure 5-7b). These values are labelled in Figure 5-7a as the intersections between the dashed white antidiagonal line and the solid white iso-reflectivity curves. According to the optical model, this means that at 1.2 V, the film is composed of 3.4 nm equivalent thickness of MnO₂ and 10.7 nm equivalent thickness of ZHS, which is in good agreement with ICP-MS measurements (Table 5-1). A good match is also obtained for the sample which was cycled until 1.35 V. The larger error for ZHS than for MnO₂ can be explained by the correction which needs to be applied to the measured Zn concentration (see **Materials and methods**, section M.3.5).

Table 5-1. Comparison between the optical model and ICP-MS measurements.

Stop potential [V]	Optical model		ICP-MS	
	MnO ₂ mass [μg cm ⁻²]	ZHS mass [μg cm ⁻²]	MnO ₂ mass [μg cm ⁻²]	ZHS mass [μg cm ⁻²]
1.35	1.6 ± 0.1	1.5 ± 0.6	1.15 ± 0.20	1.35 ± 0.25
1.2	0.7 ± 0.1	3.0 ± 0.7	0.66 ± 0.15	3.00 ± 0.40

In summary, the analysis of the reflectivity variations upon the most prominent discharge peak (II) can be mostly understood from a refined optical model considering a two-component film made of MnO₂ and ZHS. It suggests that the compound which precipitates on the substrate upon electrodisolution of MnO₂, as early as at 1.5 V, is consistent with ZHS both from its refractive index and molar mass.

5.2.4 GALVANOSTATIC CYCLING

From the careful inspection of oxidation/reduction peaks during CV experiments, it is demonstrated that optical reflectometry allows monitoring *in situ* and quantitatively MnO₂ electrodeposition during charge, as well as the simultaneous electrodisolution of MnO₂ and precipitation of ZHS during discharge. This implies that ZHS is also a key player in the charge process. If so, its role must be manifested on the subsequent charge steps as ZHS accumulates on the electrode after the first and following discharge steps. Moreover, its presence on the

discharged electrode should equally play an important mechanistic role during the subsequent charges. This is confirmed experimentally since a single oxidation peak is observed during the first forward scan in CV, as opposed to two oxidation peaks (Figure 5-2h) when a second cycle is recorded. Additionally, the peak potentials are consistent with the two pseudo-plateaus observed under galvanostatic charge (Figure 5-1b). The appearance of the second oxidation peak could then be related to the presence of ZHS formed during the previous cycle.

5.2.4.1 IMAGING THE FIRST GALVANOSTATIC CHARGE ON A ZHS PARTICLE-COATED ELECTRODE

Our imaging model could here be challenged bearing in mind previous reports^[367,370,371,379,380] on the crystallization of ZHS on the positive electrode at the end of the discharge that is associated with the growth of large and stochastically distributed ZHS crystals. Nevertheless, this situation can be handled by imaging by optical reflectometry the behaviour of individual ZHS microparticles immobilized on the bare Au current collector while MnO₂ is electrodeposited and electrodisolved from a ZHS-saturated electrolyte. OM was recently used to image heterogeneous Li⁺ ion distributions and fluxes within single micrometric particles during cycling,^[399] as well as the dissolution of individual CaCO₃ biominerals induced by the electrogeneration of acid.^[411] In a similar scenario, optical reflectometry images are used here to probe *operando* local material deposition (or equivalently, through the above-proposed optical model, local charging currents) during the first three galvanostatic charge-discharge cycles of the MnO₂ electrode.

Figure 5-8a shows the optical image of the Au electrode coated with ZHS microparticles, recorded at open circuit in the ZHS-saturated electrolyte. Several micrometric ZHS crystals are clearly detected as dark-contrasted features on this optical image. The smallest optical features visualized are ca. 0.5 μm large, providing an upper limit for the spatial resolution of imaging optical reflectometry. The electrode is then submitted to three galvanostatic charge-discharge cycles while optically monitored *operando*. The optical images are again converted into reflectivity images. The quantitative single-component optical model analysis discussed earlier at the level of averaged images (such as in Figure 5-5) is applied here locally to evaluate the thickness of MnO₂ electrodeposited during charge. To highlight local electrodeposition

phenomena, a local MnO_2 thickness is evaluated, $\delta_{\text{MnO}_2} - \delta_{\text{MnO}_2, \text{bg}}$, relative to a background thickness $\delta_{\text{MnO}_2, \text{bg}}$ measured over a region remote from the particles. The map of such relative local MnO_2 thickness over the whole imaged region is provided in Figure 5-8b for $t = 287$ s, while a zoom over a specific particle is presented along different charging times in Figure 5-8c. Unlike during the CV study (performed in the absence of ZHS particles), the MnO_2 deposit is not uniform in thickness over the whole Au electrode surface. When the image of the original ZHS particles is overlaid, the regions surrounding the ZHS particles are clearly revealed as regions of higher deposition ($\delta_{\text{MnO}_2} - \delta_{\text{MnO}_2, \text{bg}} > 0$).

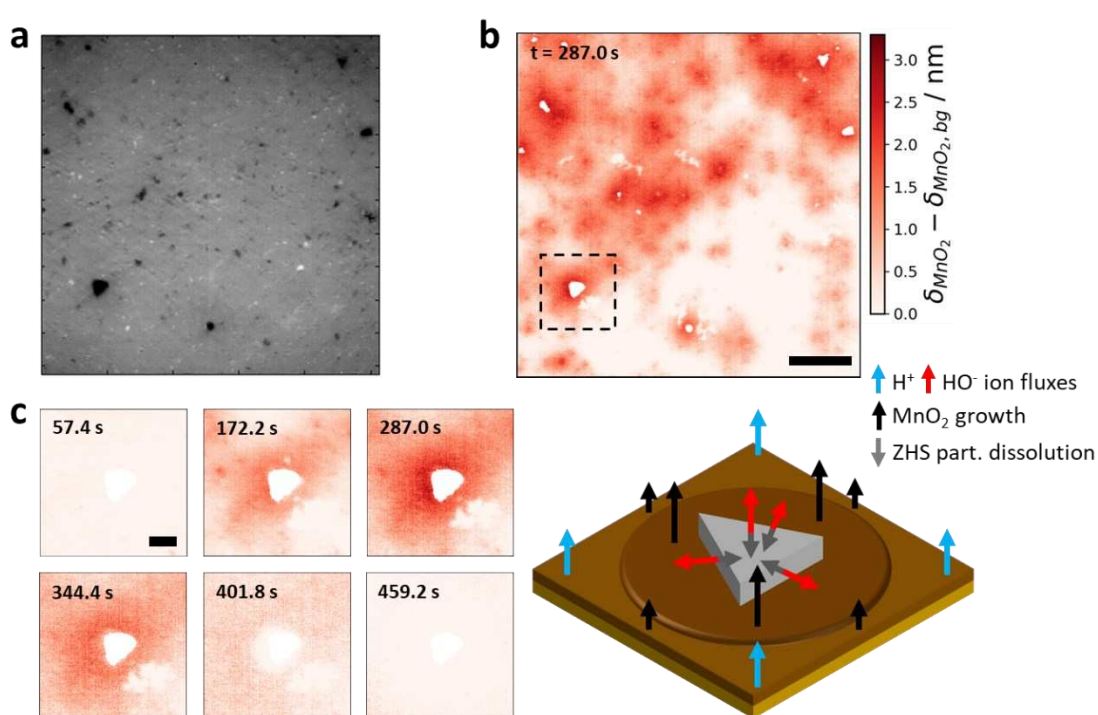


Figure 5-8. *Operando* optical imaging of the first galvanostatic charge-discharge cycle of a Zn- MnO_2 battery in ZHS-saturated $2 \cdot 10^{-3}$ M $\text{MnSO}_4 + 2$ M ZnSO_4 . (a) Background-subtracted optical reflectometry image of the Au cathode coated with ZHS particles (dark-contrasted features). (b) Reflectivity image converted into relative MnO_2 thickness, $\delta_{\text{MnO}_2} - \delta_{\text{MnO}_2, \text{bg}}$. The particles detected in (a) are masked to highlight that they are surrounded by regions of thicker MnO_2 deposits. Scale bar: $50 \mu\text{m}$. (c) Sequential relative MnO_2 thickness images showing the expansion of the excess deposition region around a ZHS particle (zoom inside the dashed region of interest in (b)) and schematic mechanistic explanation. Scale bar: $10 \mu\text{m}$.

The heterogeneity in local deposition rate is also described from the local variation in optical current ($-dR/dt$) with time. An example is provided in Figure 5-9a (dark red curve) for the

ZHS particle considered in Figure 5-8c. This local variation is compared to the average evolution of the optical current with time (red curve) over the whole imaged electrode, together with the evolution of the electrode potential. Both local and average optical currents show the same evolution at first: the optical current increases, as expected for an electrodeposition process, rapidly reaching a steady value, until it starts to decrease after about 200 s and the local behaviour starts to differ from the average behaviour. While the optical current averaged over the whole electrode surface decreases gradually, that of the ZHS particle shows a much steeper decay. Noteworthy, both local and average optical current decays start within the transition of the electrode potential from the first to the second plateau (Figure 5-9c). It is then important to decipher these local and average optical behaviours to apprehend mechanistically the origin of the two-plateau charge profile of Zn-MnO₂ batteries as done next.

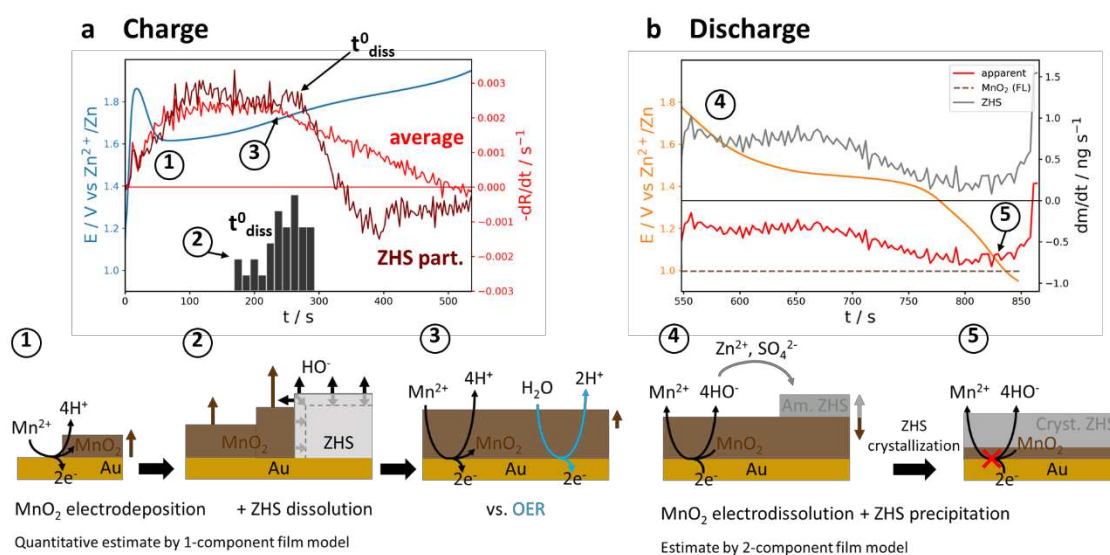


Figure 5-9. (a) Time evolution during charge of the Au electrode potential (blue curve) and of the optical currents ($-dR/dt$) averaged over the whole image (red curve) or evaluated at the centre of the ZHS particle depicted in Figure 5-8c (dark red curve); histogram of the distribution of dissolution onset times, t_{diss}^0 , for $N = 32$ particles. (b) Time evolution during discharge of the Au electrode potential (orange curve) and of the optically inferred average apparent deposition rate (red curve). Dashed brown curve: theoretical MnO₂ dissolution rate derived from Faraday's law (faradaic efficiency: 95%, see above). Gray curve: ZHS deposition rate estimated from the apparent and theoretical deposition/dissolution rates. The schemes at the bottom summarize the mechanism revealed optically at each step of the galvanostatic charge-discharge cycle.

For the ZHS particle, the steeper optical current decrease corresponds to the particle's dissolution as expected since at the end of the experiment, most particles have disappeared from the raw optical images. By analogy to previous works dealing with the optical monitoring of particle dissolution,^[411–413] a particle dissolution onset time, t_{diss}^0 , can be defined in our data from the onset of the sharp variation of the optical current. The histogram in Figure 5-9c shows the distribution of dissolution onset times, t_{diss}^0 , for the $N = 32$ largest individual particles detected in Figure 5-8a. Once these particles have dissolved (partially at least), for $t > 350$ s in Figure 5-8c, the overall surface reflectivity becomes more uniform.

The disappearance of the ZHS particles attests from the electrogeneration of H^+ . Indeed, MnO_2 electrodeposition is accompanied by a pH decrease which should thus favour ZHS dissolution (see Equations 5-1 and 5-2). The dissolution of the ZHS particles is accompanied by a local release of HO^- ions, they likely play the role of a local pH buffer. Interestingly, the reflectivity images in Figure 5-8c reveal that the ZHS particle is surrounded by a region of local excess MnO_2 deposition, which can be related to the radial steady-state diffusive release of HO^- ions from the dissolution of the ZHS particle. Also consistent with a local HO^- release from the ZHS particles, Figure 5-8b shows that i) the larger the ZHS particle and the larger the area of local MnO_2 deposition, and ii) regions of high particle density (upper right corner of Figure 5-8b) show a definite overlap of HO^- diffusion layers. To account for the local MnO_2 film thickness, one should consider that even though a constant overall current is flowing through the current collector, it imposes every part of it is polarized at the same potential. Based on the Pourbaix diagram in Figure 5-10, regions of higher local pH, as depicted schematically in Figure 5-8c, would then provide, at a constant potential, regions of higher overpotential and therefore of higher Mn^{2+} oxidation rates, or equivalently of higher local deposition rates. These observations suggest that such local variation in electrochemical current densities, related to local acidification, are probed by imaging optical reflectometry during MnO_2 electrodeposition.

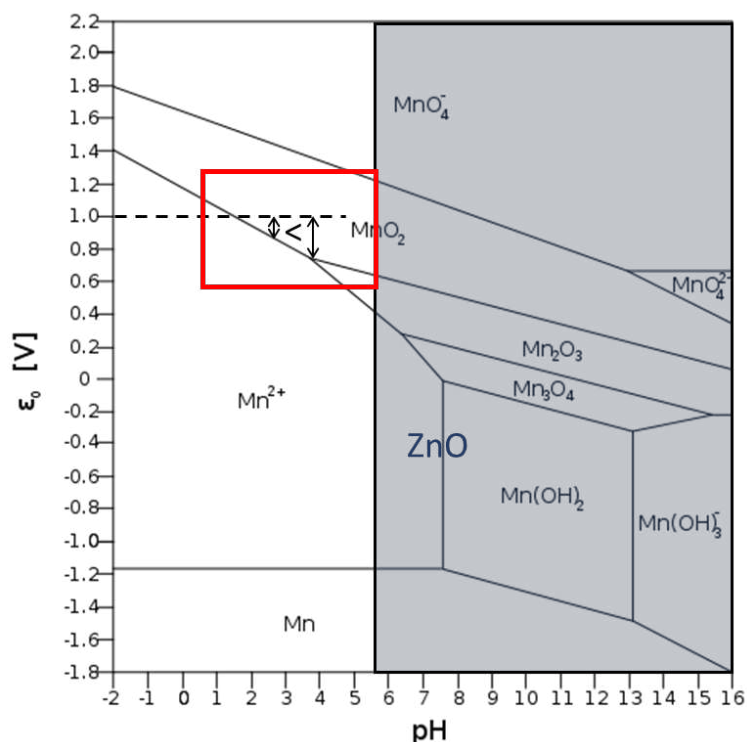


Figure 5-10. Pourbaix diagram of Mn (1 M, 25°C). The dotted line corresponds to the average potential measured during galvanostatic cycling (vs SHE, see Figure 5-9a). The arrows then show that a higher pH produces a higher overpotential for Mn^{2+} oxidation. The stability window of Zn is highlighted in blue. Adapted from https://en.wikipedia.org/wiki/Pourbaix_diagram under the terms of the CC BY-SA 2.5 licence.

Apart from particle dissolution, the average optical current shown in Figure 5-9a exhibits two distinct trends corresponding to the two potential pseudo-plateaus. MnO_2 is electrodeposited at constant (local or average) current until the second pseudo-plateau at ca. 1.75 V is reached. Using the previously determined reflectivity-mass calibration factor (Figure 5-5), the optical current can be converted into an apparent deposition rate (expressed in $ng\ s^{-1}$). The steady apparent deposition rate is very close to the theoretical MnO_2 deposition rate derived from Faraday's law, confirming the near-100% faradaic efficiency of MnO_2 electrodeposition obtained in CV. Interestingly, this is only verified until the ZHS particles start to dissolve i.e., until the electrode surface pH becomes sufficiently acidic to trigger a fast dissolution. Along with the second charge domain (for $E > 1.75\ V$ or $t > 200\ s$ in Figure 5-9a), the average optical current drops steadily. It suggests that the faradaic efficiency of MnO_2 electrodeposition steadily decreases as the electrode potential increases. This indicates that for $E > 1.75\ V$, MnO_2

electrodeposition competes with another oxidation, most likely water oxidation since at such potentials the thermodynamic stability of water is reached.^[391]



The linear evolution of the faradaic efficiency of MnO₂ electrodeposition then probes the increase of the contribution of water oxidation (either directly at the electrode or through electrocatalysis of MnO₂) with the electrode potential. From the integration of the apparent deposition rate variation with time, the faradaic efficiency of MnO₂ electrodeposition during the whole charge process is ca. 70%. Noteworthy, the shift toward a second charge plateau suggests that the buffer capacity of the electrolyte has been reached. Indeed, further charge is accompanied by the dissolution of ZHS particles acting as local solid-state suppliers of HO⁻. Once dissolved, the electrolyte pH starts increasing, enabling the competition between MnO₂ electrodeposition and water oxidation. This is in line with *in situ* pH monitoring showing that the shift to the second plateau is associated with an increase in electrolyte pH.^[370] It is shown here that this transition is also associated with the decrease of the capacity of the electrode (competition with water oxidation). Such competing reaction is a problem as it shifts, at constant current flow, from a two-proton/one-electron reaction for MnO₂ electrodeposition to a one-proton/one-electron reaction for water oxidation. This explains the gradual pH increase over cycles in the cell, as experimentally demonstrated by *in situ* pH monitoring.^[370]

The overall phenomena revealed by *operando* imaging optical reflectometry are summarized in the scheme presented at the bottom of Figure 5-9. Particularly, the heterogeneous electrodeposition rates imaged *operando* demonstrate the essential role of ZHS (particles or dissolved in solution) during the charge process: it allows a local buffering of the electrode surface during MnO₂ electrodeposition and a control of its competition with water oxidation. They also suggest that controlling the buffering capacity of the electrolyte i.e., delaying ZHS dissolution, might be an interesting solution toward increasing the capacity of Zn-MnO₂ batteries.

5.2.4.2 GALVANOSTATIC DISCHARGE

The same optical current analysis for the discharge step is provided in Figure 5-9b. It is characterized by an overall dissolution process ($-dR/dt < 0$) occurring homogeneously over the electrode surface. However, as discussed in the CV study, the apparent dissolution rate is constantly below (in absolute value) the theoretical MnO_2 dissolution rate, meaning that ZHS precipitates throughout the entire discharge. A quantitative analysis of the deposition/dissolution rates is provided. Given that the reflectivity of a Au substrate is ca. 1.45 times less sensitive to ZHS compared to MnO_2 based on the two-component optical model (from Figure 5-7a), the ZHS deposition rate (gray curve in Figure 5-9b) can be estimated by the difference between the theoretical MnO_2 electro-dissolution rate and the optically inferred dissolution rate. The apparent and approximate ZHS deposition rate obtained in this manner (ca. $0.3\text{-}0.8 \text{ ng s}^{-1}$) is comparable to that of MnO_2 dissolution (0.8 ng s^{-1}), confirming the CV discharge upon approximately constant material thickness. However, this value corresponds only to 1/5th of the stoichiometric amount of ZHS expected according to Equations 5-1 and 5-2 (for $x = 5$). Moreover, one can notice a sharp increase in the ZHS deposition rate at the end of the discharge, which could suggest the slow dynamics of ZHS crystallization. These arguments are in agreement with a kinetic control of the precipitation of ZHS: local oversaturation of the solution close to the electrode is mandatory to allow precipitation. This also explains why accurate molar masses cannot be measured by EQCM.

5.2.4.3 SUBSEQUENT CYCLES

Over the second cycle, the largest particles may show again some localized higher activity regions, but more sporadically and with lesser amplitude. The heterogeneity has completely faded out at the level of the third cycle (as suggested by the images of Figure 5-1b) as the particles have been completely removed from the electrode surface. The image-averaged optical current variation with time during the third cycle is presented in Figure 5-11. Noteworthy, for the sake of simplicity, the role of water oxidation was not considered as a first rough approximation so that the rate of MnO_2 deposition was constant. It essentially shows the same trends as for the first cycle but on a homogeneous surface. It also suggests the dissolution of the homogeneous ZHS layer already during the first plateau.

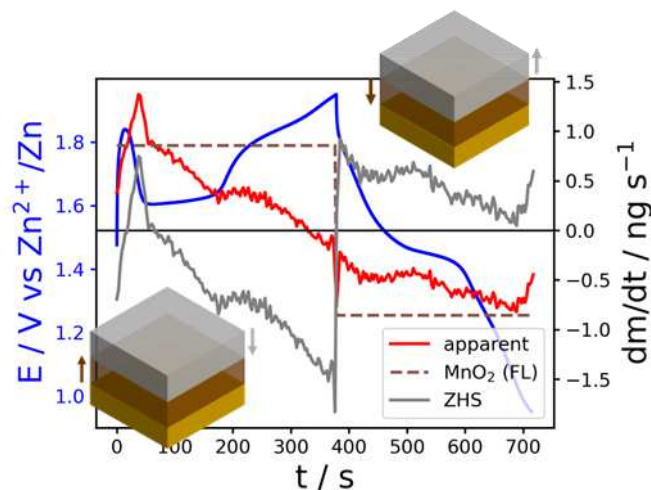


Figure 5-11. Evolution with time of the electrode potential (blue) and the optically inferred deposition rate (red) during the 3rd galvanostatic charge-discharge cycle with schematic representation of ZHS and MnO₂ deposition/dissolution. Dashed brown line is the theoretical MnO₂ deposition/dissolution rate based on 95% faradaic efficiency (corrected for the real faradaic efficiency along the second charge plateau, see Figure 5-9). Grey line: ZHS dissolution/deposition rate evaluated from the optically inferred and theoretical deposition rates. Unlike in Figure 5-9, ZHS starts dissolving before the second plateau. The other parts of the curves are similar to the behaviour observed during the first cycle.

Overall, imaging such repetitive charge-discharge cycles demonstrates that these cycles are smoothing the electrode surface activity and yielding a homogeneous ZHS layer deposition and dissolution.

5.3 CONCLUSION

Optical reflectometry is used to monitor qualitatively and quantitatively charge-transfer-induced chemical precipitation/dissolution events in aqueous Zn-MnO₂ batteries. The overall results obtained by this method are summarized in the bottom scheme of Figure 5-9. Overall, like sensorgrams in SPR microscopy, the variation of the reflectivity with the electrode potential or current during charge-discharge cycles provides a **dynamic *in situ* measurement of the amount of material deposited** onto (or removed from) the electrode. Like in a classical EQCM analysis, the exchanged charge and mass change are compared to identify the nature

of the electrodeposited/electrodissolved materials or the faradaic efficiency of the underlying processes. Even if all molar masses could not be attributed, it is shown that **along with the electrodeposition/electrodissolution of MnO₂, a precipitate is also dissolved/deposited.**

Indeed, associated charge and mass change are not perfectly correlated. In this case, unlike the mass change of an EQCM, the optical reflectivity can still be analysed, through a refined **optical model**, to **extract *in situ*** and dynamically quantitative information about **the composition of the MnO₂ electrode at a given state of discharge.** If the poor correlation between charge and mass change could also be due to a kinetic lag between MnO₂ reduction and net material removal from the electrode, combined with ***ex situ* XRD, FT-IRRAS, and XPS** analyses of the electrode's chemical composition, **optical reflectometry suggests the continuous deposition of ZHS during the entire discharge** and especially during the first discharge plateau, in an amorphous form, most likely the reason why its presence through the first discharge plateau was overlooked. Since MnO₂ electrodeposition/electrodissolution is shown to be the main pathway for charge storage, the two different ZHS precipitates (amorphous and crystalline) might be the origin of the two discharge plateaus. This would mean that by favouring or preventing crystallization, one of the two plateaus could be suppressed, thus easing the commercialization of aqueous Zn-MnO₂ batteries.

Optical reflectometry is then used in its imaging mode to probe the role of ZHS during the charge process. The **electrodeposition of MnO₂ during charge is imaged on an electrode coated with micrometric ZHS particles**, enabling to reveal the role of ZHS during charge. It is then shown that **MnO₂ electrodeposition is accompanied by the dissolution of the ZHS particles.** These particles act as a **solid-state pH buffer** or HO⁻ reservoirs which upon dissolution will locally release HO⁻ ions. This can be imaged optically as local MnO₂ deposition rates. It is then clearly demonstrated that the **two charge plateaus**, whose origin has been frequently questioned, are **due to a pH change** at the electrode surface, the second plateau also revealing the **competition between MnO₂ electrodeposition and water oxidation.** Here, retarding ZHS dissolution (increasing the buffer capacity) could be a solution toward increasing the capacity of Zn-MnO₂ batteries.^[380,414]

Altogether, this study provides a deep understanding of the ZHS precipitation/dissolution equilibrium. Since MnO₂ electrodeposition/electrodissolution is always accompanied by

dramatic pH changes, this equilibrium cannot be omitted. The different ZHS precipitates highlighted in this work underline the complexity and fragility of this equilibrium, which will hopefully guide future research towards more efficient aqueous Zn-MnO₂ batteries. Although we are well aware that this study was carried out in conditions far from practical conditions in terms of concentration, masses, and so on, it shows how OM strategies enabling an *operando* monitoring of local electrochemical processes can be applied to mechanistically understand and improve aqueous Zn-MnO₂ batteries.

Chapter 6 PROBING LOCAL CHARGE STORAGE

PATHWAYS WITHIN SINGLE POLYCRYSTALLINE

MICROPARTICLES FOR REDOX FLOW BATTERIES

This chapter presents submitted results obtained in collaboration with the group of Pekka Peljo at the University of Turku, which is specialized in redox flow batteries (RFBs). One of his PhD students, Mahdi Moghaddam, obtained a travel grant from the Institut français de Finlande, an organism promoting Finnish-French partnerships, to visit our group for two weeks in May 2022. The objective of his visit was to investigate the conversion kinetics of copper hexacyanoferrate (CuHCF) used as solid booster (SB) on our OM-SEPM platform.

6.1 INTRODUCTION

As discussed in **Chapter 1**, the rise of renewable energy sources and the concurrent decrease in fossil fuel usage necessitate reliable large-scale energy storage solutions. In addition to aqueous Zn-MnO₂ batteries (presented in **Chapter 5**), RFBs have also emerged as promising candidates thanks to their unique capability to decouple energy and power.^[415] Nonetheless, their limited energy density remains a challenge to overcome.^[416]

An innovative solution to enhance the energy density of RFBs lies in the redox targeting^[417–419] or SB concept.^[420,421] Here, redox active solid particles are added to the tank, serving as the main storage medium. The dissolved redox couple primarily serves as mediator, delivering charge from the cell to the confined solid particles. As these solid particles inherently possess a higher charge storage density than the redox electrolyte, this approach enables an overall augmentation of the battery's charge storage density, thereby improving the energy density beyond the limit set by the solubility of the dissolved redox couple.^[420]

This strategy creates a new interface between the solid particles and the electrolyte, and thus a new charge transfer reaction. The intricacies of this reaction, a coupled electron-ion transfer where dissolved cations from the electrolyte intercalate into the solid particles, mandate

thorough thermodynamic and kinetic studies, within recent theoretical frameworks,^[422] for the development and optimization of the solid-boosted configuration.

This work proposes an *operando* high-resolution optical imaging of such configuration in the case of the charge/discharge of single micrometric polycrystalline SB particles made of CuHCF, a Prussian blue analogue (PBA) commonly used in K-ion batteries.^[423,424] Our collaborators' recent research has focused on the thermodynamics of such solid-boosted flow batteries (SB-FBs) and their techno-economic design.^[425] Yet, the kinetics of such systems have been somewhat neglected, likely due to their inherent complexity.^[121,151,426–428] Unravelling the kinetics of SB-FBs, specifically the charge transfer kinetics between the solid and the electrolyte in the tank, is indeed a challenging task given the intricate nature of the reaction involving interfacial chemistry and mass transfer. Particularly, achieving the fast conversion and mass transfer rates required for high-power SB-FBs calls for porous solid phases, such as polycrystalline particles, resulting in mixed surface (capacitor-like) and bulk (battery-like) conversion behaviours^[182,429] showing up at different micro- to nanoscale observation lengths.

SECM provides a robust platform to study these complex systems. Indeed, the SECM feedback mode measures the local electrochemical activity of an interface using a redox mediator. Here, the current collected by a local probe, an UME, probes the interface's conversion at the microscale, as in the so-called “surface interrogation” mode (SI-SECM).^[430,431] This approach is particularly useful in the context of SB-FBs as it allows to track the charge/discharge of the redox solid *operando*.

Tracking these processes at the single-nanocrystal level, by using single-particle electrochemical techniques,^[42,199,432] can further our understanding of the conversion mechanisms at the nanoscale. OM techniques, for instance, provide exceptional spatial resolution, temporal resolution, and throughput, granting unique insight into the electrochemistry of materials for electrochemical energy conversion both at the micro-^[2,3,183–185] and nanoscale.^[160,177,178,180–182,192] Most notably, Wang *et al.* investigated the K⁺ diffusion dynamics within single Prussian blue (PB) NPs.^[160,177,178,192] Meanwhile, Merryweather *et al.*^[183–185] and Pandya *et al.*^[2] probed *operando* the Li⁺ insertion front lines within single lithium cobalt oxide (LCO) particles.

To explore the potential of these two techniques for SB-FBs, we propose combining SECM and OM to study the charge/discharge of single SB particles. Different optical imaging techniques, including with spectroscopic potentialities, have already been combined with SEPMs, using UMEs^[121,431,433–439] or nanopipettes^[159,195,236,440,441] as local electrochemical probes. This approach leverages the UME of the SECM to trigger and probe the electrochemical charge/discharge of a single SB particle, while its conversion is simultaneously monitored by OM with a sub-particle resolution and *operando*. This approach, depicted in Figure 6-1, is designed to probe the coupled electron transfer and K⁺ (de)intercalation into/from single micrometric polycrystalline CuHCF particles. This innovative strategy unveils the significant role of surface conversion and identifies preferential porous pathways for the redox electrolyte via nanoscale imaging. In doing so, it paves the way for a better understanding and the optimization of SB-FBs.

6.2 RESULTS AND DISCUSSION

6.2.1 PROBING THE CHARGE/DISCHARGE OF INDIVIDUAL CUHCF

MICROPARTICLES BY OPTO-ELECTROCHEMISTRY

6.2.1.1 PRINCIPLE

CuHCF particles are promising candidates as SB for the positive side of SB-FBs^[442] when associated with N,N,N-2,2,6,6-heptamethyl piperidinyloxy-4-ammonium chloride (TEMPTMA)^[443] as redox mediator. Indeed, they have close redox potentials, $E^{\circ}_{CuHCF} = +0.97 V$ vs SHE and $E^{\circ}_{TEMPTMA} = +0.91 V$ vs SHE, resulting in a favourable condition for high utilization of the solid's storage capacity.^[425]

The charge/discharge of an individual CuHCF particle is investigated by a combination of local electrochemical triggering and probing by SECM and a complementary *in situ* monitoring by OM. The operating principle of this hybrid SECM-OM setup is depicted in Figure 6-1a. Micrometric particles of CuHCF (prepared according to a procedure detailed in **Materials and methods**, section M.1.3) are drop-casted from a diluted water suspension on an optically transparent ITO substrate. The substrate decorated with particles is placed on the stage of an inverted OM and illuminated from the backside with unpolarized white light through a 63x,

1.4 numerical aperture, oil immersion objective (details in **Materials and methods**, section M.2.1). The OM enables both imaging and targeting^[195,199] individual particles for further approach of the Pt UME of the SECM just a few, ca. 10, micrometres above the selected particle. A colour optical image captured by the colour CMOS camera is presented in Figure 6-1b, left. It shows a single orange CuHCF particle in the centre of a bright disk corresponding to the Pt wire of the UME held above it.

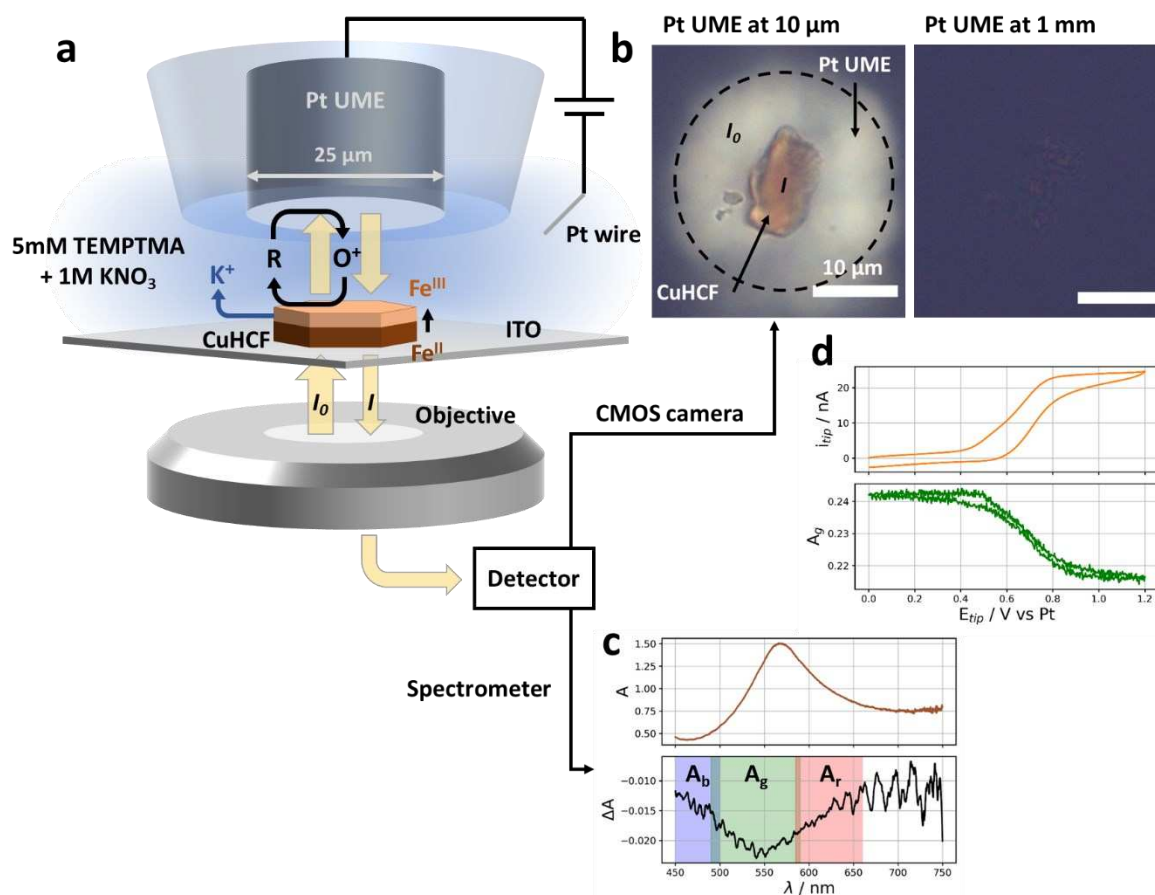


Figure 6-1. (a) Principle of the optical probing of the charge/discharge of a single CuHCF triggered by the electrogeneration of the redox mediator (O^+) at the UME of the SECM. The yellow arrows show the light path enabling, from the UME acting as a mirror, a local absorbance measurement. (b) Raw colour optical images of a pristine CuHCF particle with the UME held $10\ \mu\text{m}$ (left) and $1\ \text{mm}$ (right) above it. (c) Using a spectrometer, the absorbance spectrum of the single particle and its variation, ΔA , upon oxidation are obtained; overlaid are the spectral ranges each colour channel of the camera is sensitive to. (d) Transient evolution of the absorbance, A_g , measured from the green channel of the camera and averaged over a ROI of the particle, during a CV performed in $5\ \text{mM}$ of TEMPTMA (R) + $1\ \text{M}\ \text{KNO}_3$ at the $25\ \mu\text{m}$ -diameter Pt UME held at $10\ \mu\text{m}$ from the ITO surface (ca. $7\ \mu\text{m}$ from the top of the CuHCF particle, see Figure 6-4).

6.2.1.2 COLOUR OPTICAL ABSORBANCE IMAGING BY MIRRORED EPI-ILLUMINATION

MICROSCOPY

The UME is not only used for local electrochemical triggering and probing, but also acts as an optical mirror. Under the epi-illumination (through the objective) of the microscope, it reflects the light transmitted through the particle and redirects it (after a second transmission through the particle, see light path in Figure 6-1a) back towards the objective and the colour camera. In the present configuration, thanks to the mirror UME, the light transmitted through the particle, and therefore its absorbance, can be probed, similarly to what was done upon trans-illumination to investigate electrochromic NPs (including PB NPs).^[160,178,180–182,192] Noteworthy, due to matching refractive indices between the particle and the ITO substrate, the particles are actually almost invisible in reflection mode, as can be seen in the image of the particle in the absence of the mirror UME in Figure 6-1b, right.

From the schematic light paths presented in Figure 6-1a, the absorbance of light, A , by a ROI of the particle, can be evaluated by comparing the light intensity received in this mirror UME illumination in the absence, I_0 , or presence, I , of the particle, according to:

$$A = \log\left(\frac{I_0}{I}\right) \quad (6-1)$$

As in macroscale spectroelectrochemical or single-NP optical imaging studies, this optical configuration is used here to probe *operando* the redox transformation of individual CuHCF microparticles. According to Beer-Lambert law, A provides a measurement of the amount of absorbing material in its oxidized and reduced form,^[440] and therefore of the local 2D state-of-charge of the particle (integrated over the full particle thickness). Noteworthy, the same formalism applies to the absorbance variations of the solution layer separating the UME and the ITO surface. While this paves the way for local spectroelectrochemical studies in a SECM configuration, the low concentration of TEMPTMA (5 mM) compared to that of active centres in CuHCF (≈ 6 M, see below) makes the solution's contribution to the measured absorbance variations negligible here.

Thanks to the colour camera decomposing the image along three colour channels (red, green, and blue, respectively (RGB)), the particle's absorbance and therefore state-of-charge can be

imaged spectroscopically, within each spectral range. They are denoted A_b , A_g , and A_r , respectively. Moreover, replacing the colour camera with a fibered UV-Vis spectrometer, the light collected from the full field-of-view of the microscope provides the UV-Vis absorbance spectrum of the entire individual CuHCF particle. Since the neighbouring particles are poorly reflective (see Figure 6-1b), most of the light collected by the spectrometer comes from the region below the UME, granting the UV-Vis absorption spectrum of individual microparticles. The top panel of Figure 6-1c presents such spectrum from a single CuHCF microparticle in its fully reduced (pristine) state, with an extinction peak in the green at ca. 565 nm, consistent with literature data.^[444] The spectrum of the same particle in its fully oxidized state (after 100 s of CA) allows plotting the spectroscopic absorbance variation, ΔA , for the particle's oxidation. It is given in the bottom panel of Figure 6-1c, overlaid with the spectral ranges probed by the different colour channels of the camera. It suggests that the particle and its transformation are imaged more sensitively along the green channel (A_g).

6.2.1.3 SECM PROBING OF THE CONVERSION OF CUHCF PARTICLES

To investigate the conversion of the CuHCF particle in a SB-FB-like environment, the UME is then used to trigger its redox conversion as depicted in Figure 6-1a. At the beginning of the experiment, both CuHCF and TEMPTMA are in their reduced state, respectively denoted CuHCF^{II} and R. The Pt UME is then biased higher than E°_{TEMPTMA} (+0.91 V vs SHE), leading to the oxidation of R into O⁺ at the UME, and thus generating a concentration gradient in the gap between the UME and the particle (and substrate). The O⁺ species produced at the UME then diffuse in the electrolyte towards the particle, where they oxidize the CuHCF^{II} sites of the particle (converting them into CuHCF^{III} sites), regenerating R at the interface between the particle and the electrolyte. In battery science, this oxidation corresponds to the charging of the particle, and both terms will be used equivalently hereafter. Assuming the redox reaction results in the change of the Fe centres' oxidation state from Fe^{II} to Fe^{III}, for the sake of charge neutrality, the particle's oxidation (or charge) is accompanied by the deintercalation of K⁺ ions from tetrahedral sites and their release into the electrolyte. This charge of the CuHCF particle is depicted as the forward step of Equation 6-2:



where θ represents a vacant K^+ site. For CuHCF discharging, Equation 6-2 proceeds reversely, and the particle's reduction is concomitant to K^+ intercalation.

This conversion experiment is first performed during a CV by sweeping the UME potential, E , from 0 to 1.2 V vs Pt. The evolution of the absorbance, A_g , recorded in the green channel and integrated over a ROI of the particle, along the UME potential is provided in bottom panel of Figure 6-1d. The sigmoidal shape of the $A_g - E$ curve, named absorptiogram, nicely overlays with the sigmoidal shape of the voltammogram recorded at the UME for the oxidation of R (top panel of Figure 6-1d). It confirms that the particle's conversion coincides with the formation of the oxidized form of the redox mediator (O^+). The conversion is also completed at the time scale of the CV, when R is totally converted at the UME (plateau current). Moreover, the reverse scans of both curves also coincide, showing that the conversion is fast, reversible, and driven by the conversion of the redox mediator at the UME.

The current flowing at the UME allows charging/discharging the particle at a constant flux of O^+/R . In the context of RFBs, this flux can be compared to a convective flow of redox electrolyte. The steady-state oxidation current recorded at the UME of $i_{ss} = 20 \text{ nA}$ suggests that the particle of surface area $S \approx 85 \mu\text{m}^2$, evaluated from the optical image in Figure 6-1b, left, can be efficiently charged at a flux of $f = \frac{i_{ss}}{FS} = 2.4 \cdot 10^{-7} \text{ mol cm}^{-2} \text{ s}^{-1}$. For a redox flow system made of a 5 mM O^+ electrolyte flowing with a velocity v_f , one expects mass transfer-limited charging at a flux of $f = v_f [O^+]_{bulk}$. The experiment in Figure 6-1d is then mimicking the charging of a single particle under a flow of redox electrolyte with an equivalent velocity of $v_f = 0.48 \text{ mm s}^{-1}$.

6.2.2 CHARGE/DISCHARGE DYNAMICS AT THE SINGLE-MICROPARTICLE LEVEL

6.2.2.1 ELECTROCHEMICAL TITRATION BY SECM

Next, the dynamics of the particle's charge/discharge is investigated during CA experiments. As presented in the upper panel of Figure 6-2a, the particle is first charged by polarizing the UME at a potential for which O^+ is delivered under solution mass transfer control ($E = 1.1 \text{ V}$ corresponding to the plateau current of the CV in Figure 6-1d, top). In a second step, 100 s later, the electrode potential is reverted to 0 V to restore the initial (reduced) state-of-charge

of the particle. Meanwhile, both the transient UME current and optical images of the single particle are recorded. From the images, the global absorbance of the particle as well as the local absorbance (at the individual pixel level) are evaluated from Equation 6-1. The former global optical response is first compared to the UME current in Figure 6-2, providing a rationale for the particle's global conversion dynamics in relation to its global electrochemical response. This will be later used to analyse the local optical response in terms of local charge/discharge currents, presented in section 6.2.3, yielding charging dynamics images with sub-particle (sub-micrometre) spatial resolution.

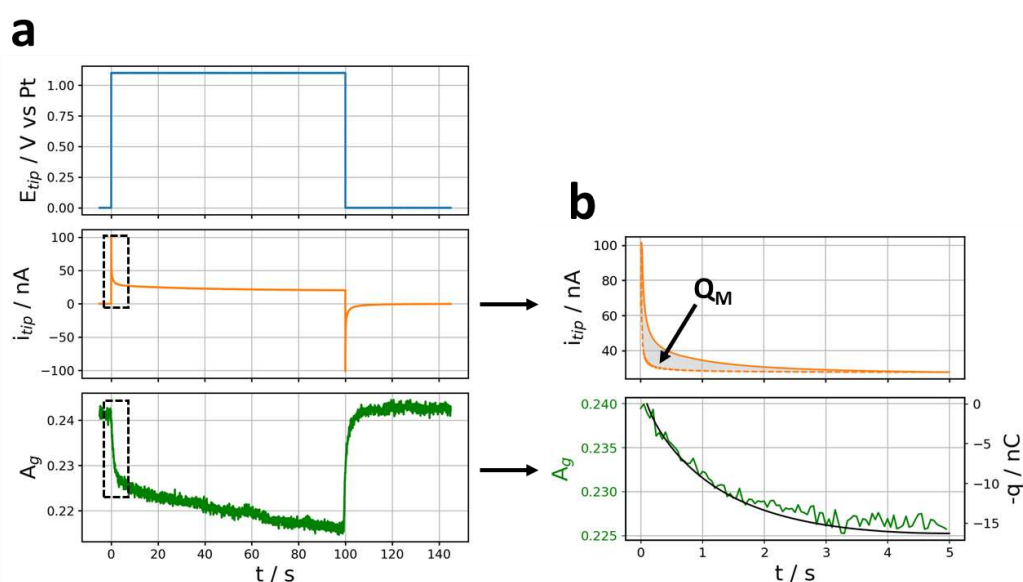


Figure 6-2. Analysis of the charge and discharge of a single CuHCF microparticle by SECM and OM. (a) Upper panel: UME polarization procedure; middle panel: experimental UME currents measured (insert: zoomed region presented in (b)) in the absence (dashed line) and presence (solid line) of the particle, allowing for an estimation of the total exchanged electrochemical charge Q_M ; lower panel: global variation of the particle's absorbance probed from the optical images (green channel) as in Figure 6-1d, bottom (insert: zoomed region presented in (b)) compared to the instantaneous electrochemical charge q , black line). Electrolyte: 5 mM TEMPTMA + 1 M KNO_3 .

CA experiments were performed in both 1 and 0.01 M KNO_3 , presented in Figure 6-2 and Figure 6-3, respectively. Figure 6-2a shows the potential program applied to the UME (upper panel) along with its current (middle panel) and the optical response of the CuHCF particle (lower panel) recorded in the green channel and averaged over a ROI of the particle. In Figure

6-2b, the UME current (solid orange line) is compared to the background UME current (dashed orange line) extrapolated from a measurement over a region devoid of particles. In the absence of particles, the background current decays rapidly towards a quasi-steady-state value. The current measured over the particle also tends at long times towards a similar quasi-steady-state limit, but a supplementary current transient is detected at short times, within the first ca. 2-3 s of the experiment. Such transient is characteristic of the regeneration of R by the particle from Equation 6-2.

The effect of K^+ concentration in the electrolyte is shown from the charge of a different particle in 0.01 M KNO_3 (see Figure 6-3a). At lower K^+ concentration, the charge is even more marked in the UME current, lasting only ca. 1 s at constant current before levelling to the background current (Figure 6-3b). The lower K^+ concentration favours a faster outflow of K^+ from the particle, and the constant current charge then indicates a limitation by the transport of the redox mediator in solution. Also owing to the low K^+ concentration, it is shown that the reverse discharge (K^+ intercalation) is disfavoured and much slower than the charge (Figure 6-3c).

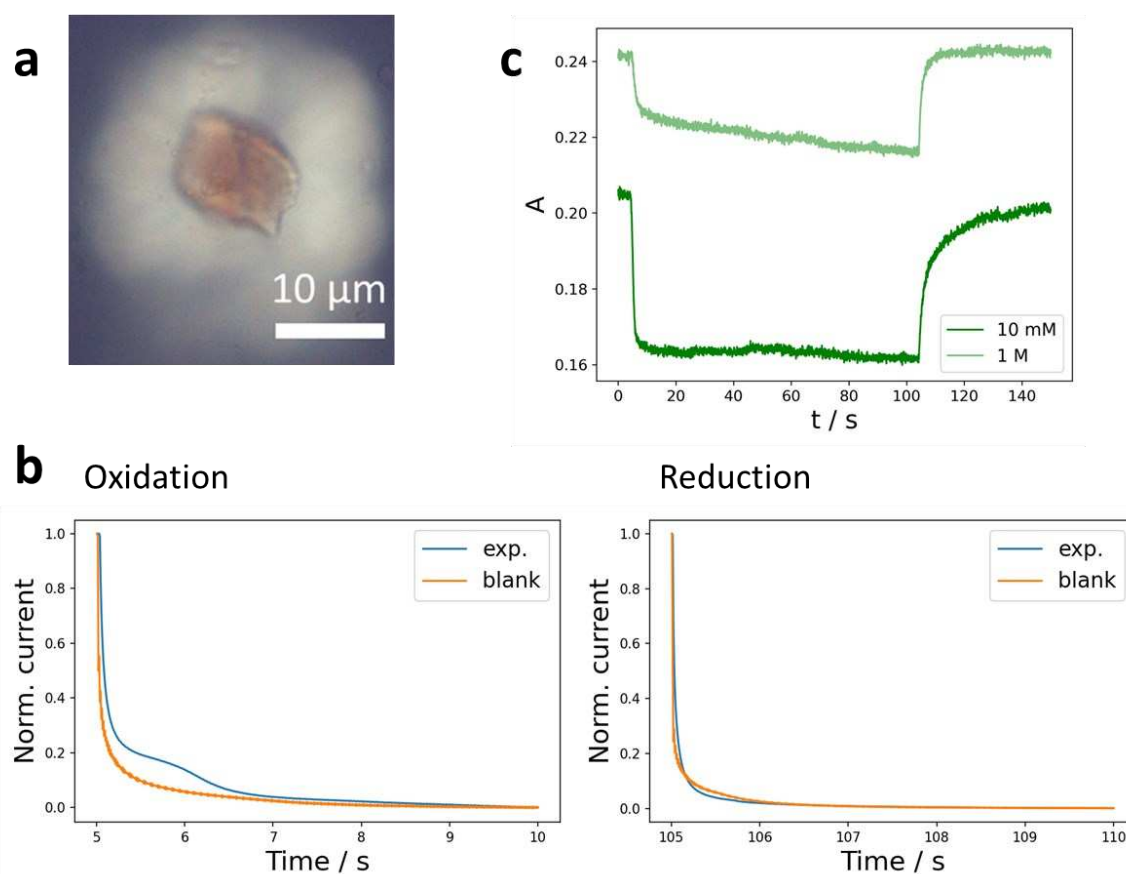


Figure 6-3. (a) Raw colour optical image of the CuHCF particle studied in 0.01 M KNO₃. (b) Normalized CAs obtained upon oxidation at 1.1 V vs Pt (left) and reduction at 0 V (right) of 5 mM TEMPTA + 0.01 M KNO₃ at the Pt UME held 10 μm above the particle. (c) Comparison between the average absorbance variations obtained in 5 mM TEMPTMA + 1 M KNO₃ (light green, experiment presented in Figure 6-2) and 5 mM TEMPTMA + 0.01 M KNO₃ (dark green) over a ROI of the same size.

The current transients measured in both cases are reminiscent of those encountered in SI-SECM, paving the way for the quantification of these processes.^[430,434] By integrating the supplemental current (greyed area between both curves in Figure 6-2b, top) over time, an estimate of the instantaneous electrochemical charge, q , exchanged during the particle's oxidation can be evaluated. A similar analysis can be done for its reduction. Over the first 5-10 s of the particle's charge/discharge, q could be fitted by an exponential function:

$$q(t) = Q_M(1 - \exp(-k_{app}t)), \quad (6-3)$$

from which Q_M , the total exchanged electrochemical charge and k_{app} , the characteristic conversion rate, could be evaluated.

From the charge dynamics given in the lower panel of Figure 6-2b, $Q_{M,ox} = 18 \text{ nC}$, while a larger electrochemical charge is obtained during discharge, $|Q_{M,red}| = 27 \text{ nC}$. This indicates that in the short-time range, the material seems more deeply discharged (reduced) than it is charged (oxidized). This discrepancy actually strongly depends on the curve subtraction method, which does not fully capture the slower long-time processes, since the conversion was found to be reversible from the optical monitoring (see Figure 6-3c). Assuming the largest exchanged electrochemical charge is 27 nC, an equivalent of 0.28 pmol of CuHCF^{II} sites is converted according to Equation 6-2. The amount of CuHCF^{II} sites initially present in the particle can be estimated from the particle's geometrical volume, $V \approx 260 \mu\text{m}^3$, evaluated from its 3D SEM image (shown in Figure 6-4a). From the structure of CuHCF, analogous to that of PB, a face-centred cubic (fcc) unit cell of 10.1 Å containing 4 $K_2Cu[Fe^{II}(CN)_6]$ units, the maximum concentration of CuHCF^{II} sites is $C_m = 6.45 \text{ M}$.^[424] The particle, composed of 1.6 pmol of CuHCF^{II} sites, is then only partly (18%) converted during the SECM experiment.

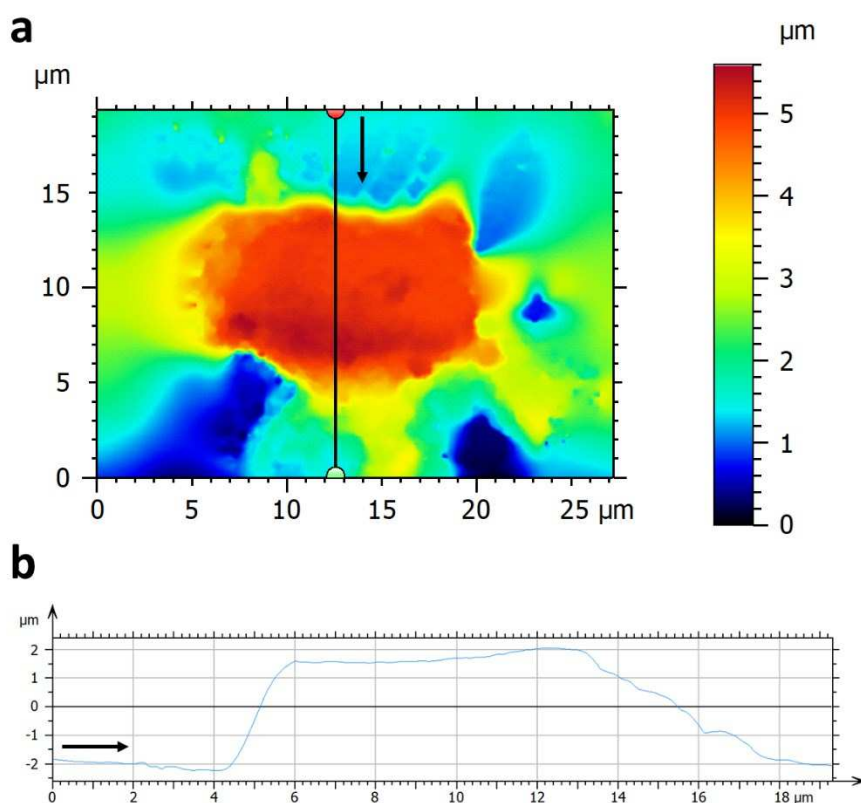


Figure 6-4. (a) Stereoscopic 3D reconstruction of the topography of the particle studied in Figures 6-1 and 6-2 based on two SEM images acquired at 0° and 16° tilt. The images were processed using the MountainsSEM software (Digital Surf). Unfortunately, the particle was flipped after rinsing the surface, but its average thickness could still be estimated using this method. (b) Height profile of the particle along the black line highlighted in (a).

6.2.2.2 MODELLING OF THE CONVERSION OF CUHCF PARTICLES

A finite element simulation, by COMSOL, of the potentiostatic charge/discharge experiment, in the SECM configuration, was performed for a cylindrical particle in order to rationalize the former approach based on UME current measurements. Figure 6-5a shows the model's geometry and the computed concentration profiles of the redox mediator R in solution and of the reduced CuHCF^{II} sites in the particle after 80 s of charge (oxidation). As seen in Figure 6-5c, the concentration profiles integrated within vertical sectors drawn over the particle in Figure 6-5a show different conversion rates along the radial coordinate: the central region is converted faster than the peripheral one. Unfortunately, such subtle local charge/discharge rate differences cannot be probed with the UME which only probes the particle's overall charge/discharge. Measuring such local charge/discharge rates would require higher spatial

resolution electrochemical probing but is likely difficult with NEs or nanopipettes given the particle's thickness. Nevertheless, the following sections will show how they can be revealed from optical images.

The overall dynamics of the charge and discharge steps are first discussed. They are presented in Figure 6-5b. As for the experiment, this figure presents the simulated background UME current (dashed orange line) along with the simulated UME current for the particle's conversion (solid orange line) evaluated under the fastest condition possible i.e., limited by solid-state mass transfer. The evolution of the electrochemical charge with time during the charge and discharge steps is presented in Figure 6-5c as the black dashed line. The simulation reproduces generally the trends observed experimentally: (i) the UME current is enhanced due to the regeneration of R upon particle oxidation from Equation 6-2, (ii) the increase of the electrochemical charge follows the exponential law in Equation 6-3, and (iii) the electrochemical charge is proportional to the average particle conversion (see Figure 6-5c). However, the total exchanged electrochemical charge corresponds to >60% of conversion, which is much more than what was observed experimentally. Moreover, the conversion's extent is reached with a much slower dynamics than that observed experimentally: >20 s based on the charge and conversion dynamics in Figure 6-6c, while experimentally it is <5 s from Figure 6-2. Noteworthy, within the condition of solid-state ion diffusion control, the electrochemical charge dynamics indeed fulfils Equation 6-3 with an apparent rate

$$k_{app} = \pi^2 D / 4L^2, \quad (6-4)$$

where D is the diffusion coefficient of K^+ in the solid CuHCF phase and L a characteristic length of diffusion. From the particle's geometry, L would be the particle's height, here 3 μm (see Figure 6-4).

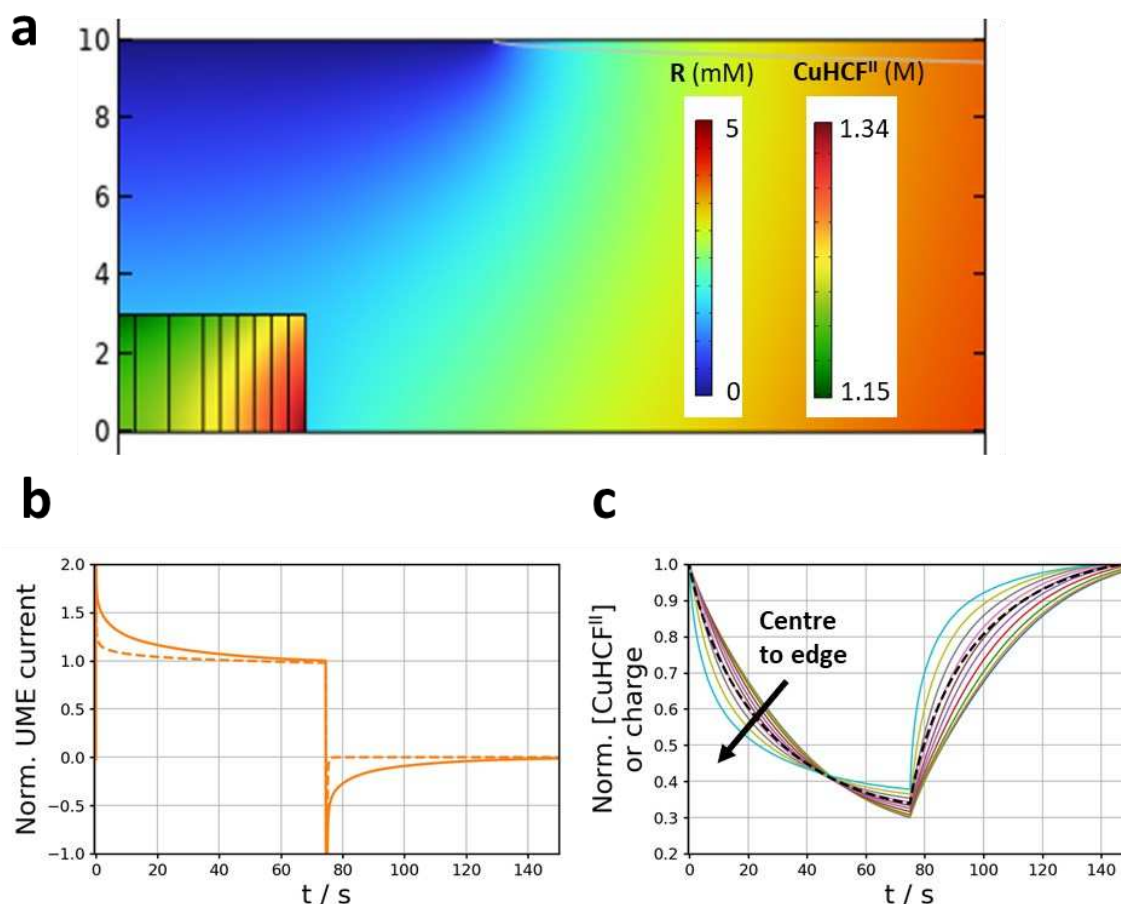


Figure 6-5. Simulated SECM potentiostatic charge then discharge of a single CuHCF microparticle. (a) Concentration profiles of R and CuHCF^{II} sites in the particle at the end of the 80 s charge (oxidation) step. (b) Evolution of the dimensionless UME current in the presence (solid line) or absence (dashed line) of the particle during charge and discharge. Currents are normalized relative to the steady-state oxidation current in the absence of particle. (c) Evolution of the dimensionless electrochemical charge during charge and discharge (black dashed line) and of the local concentration of CuHCF^{II} sites (integrated over the full particle thickness) estimated within the sectors drawn in (a) (selected sectors are at 1, 2, 3, 4, 5, 6, and 7 μm from the centre of the particle): towards the edge, a faster conversion is observed. Simulation is shown for a near-insulating substrate (charge transfer rate of $10^{-5} \text{ cm s}^{-1}$), infinite charge transfer rate at the solution-particle interface, and $D = 1.5 \cdot 10^{-9} \text{ cm}^2 \text{ s}^{-1}$.

One may argue that the faster conversion calls for higher D values. However, the situation of Figure 6-5 is close to the fastest possible conversion as for higher D values, the conversion becomes limited by the solution mass transport of R (noting its low concentration compared to that of active sites in CuHCF). Actually, the diffusion coefficients of alkali cations in CuHCF

or other PBAs are still debated in the literature and span over several orders of magnitude. It is generally admitted that ion transport in PBAs is fast, explaining their fast charging when assembled in batteries, and an upper bound of D in the 10^{-9} – 10^{-10} $\text{cm}^2 \text{s}^{-1}$ range is generally found.^[423] However, a careful consideration of the porosity and nanostructure of these material suggests more than 3 orders of magnitude lower values (from 10^{-12} down to 10^{-15} $\text{cm}^2 \text{s}^{-1}$).^[177,178,441] Nevertheless, even in the case of the highest reported value of $D = 1.5 \cdot 10^{-9} \text{ cm}^2 \text{ s}^{-1}$,^[423] Equation 6-4 gives a characteristic conversion time $\tau_{app} = 24 \text{ s}$, a value still about 8 times greater than the experimental one.

6.2.2.3 ROLE OF PARTICLE POROSITY

The two inconsistencies between experiment and simulation, namely the incomplete (18%) and overall faster conversion of the CuHCF particle, could be accounted to the porous nature of the particle. Indeed, the CuHCF materials used in electrochemical energy storage devices were shown to be assemblies of 20-50 nm NPs.^[424] Herein too, high-magnification SEM images of the studied CuHCF microparticles, in Figure 6-6a,b, confirm that they are not monocrystals but assemblies of nanocrystals: some craters, irregularities, and grains are clearly visible within the particles. This confers porosity to such assembly and should favour a surface over volume conversion, which is why porous PBAs have also been considered for supercapacitor applications.^[445] The surface-confined transformation of PBAs has been recently demonstrated by single-nanocrystal optical analysis.^[178] Inspecting individual nanocrystals allows removing the role of porosity and address more accurately ion diffusion within the crystalline structure. Such study suggested that the diffusion coefficient of K^+ within PB nanocrystals is of the order of $10^{-12} \text{ cm}^2 \text{ s}^{-1}$, leading, within the first 10 s inspected herein, to a capacitive-like conversion involving only a thin shell (about two unit cells i.e., 2 nm). Such surface process likely plays an important role in the conversion of polycrystalline and porous microparticles.

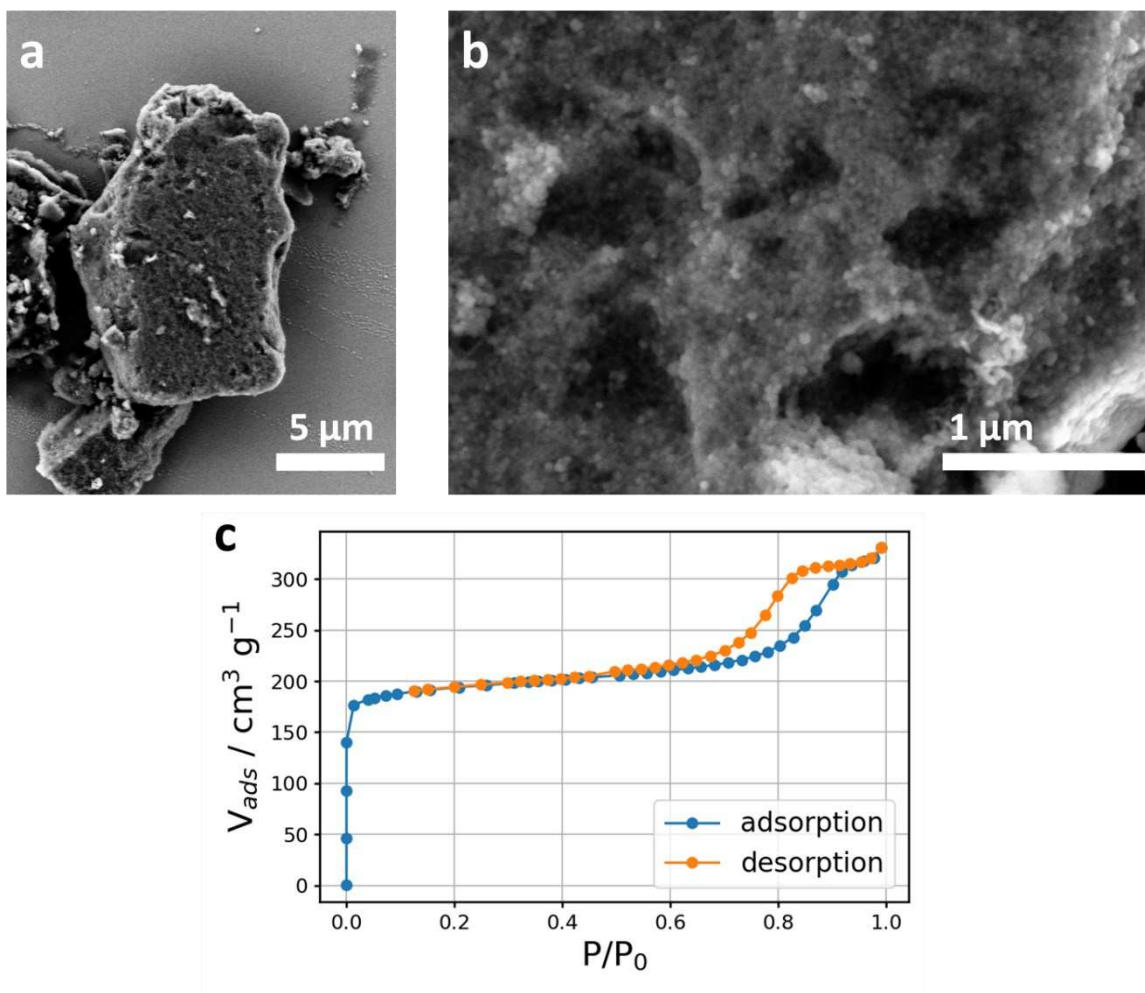


Figure 6-6. Porous nature of the CuHCF microparticles. (a, b) SEM images showing the porosity and polycrystalline structure of the particle studied in Figures 6-1 and 6-2. (c) Brunauer–Emmett–Teller (BET) adsorption and desorption isotherms measured on a 32 mg sample of CuHCF microparticles.

The porosity of a macroscopic sample of 32 mg of microsized CuHCF particles was probed by Brunauer–Emmett–Teller (BET) N_2 adsorption/desorption isotherms. The isotherms' analysis presented in Figure 6-6c suggests that the particles indeed present a micro- and mesoporosity, characterized by respective volumes of 0.31 and 0.18 $cm^3 g^{-1}$ (for a total porous volume of 0.49 $cm^3 g^{-1}$). The mesoporosity is most likely due to interparticle porosity (as supported by the aggregates observed by SEM in Figure 6-6b), with an average pore diameter of 9 nm. The analysis of the adsorption isotherm within the mesoporosity region yields a specific surface area of the order of $S_S \approx 10^2 m^2 g^{-1}$. Even if the mesoporosity could not be evaluated at the single-microparticle level, this macroscopic specific surface area allows estimating an average

ratio of surface to volume CuHCF^{II} sites, n_S/n_V , from the surface concentration Γ_m and molar mass M of the elementary site:

$$\frac{n_S}{n_V} = S_S \Gamma_m M. \quad (6-5)$$

The surface concentration is evaluated from the bulk concentration of CuHCF^{II} sites (see section 6.2.2.1 above) and the Avogadro number N_A , according to:

$$\Gamma_m = \frac{2}{N_A a^2} = \left(\frac{C_m^2}{2N_A} \right)^{1/3}, \quad (6-6)$$

This equation yields $\Gamma_m = 3.2 \cdot 10^{-10} \text{ mol cm}^{-2}$, and with $M = 352 \text{ g mol}^{-1}$, results in 13% accessible CuHCF^{II} surface sites within the porous assembly. It compares well with the amount of CuHCF^{II} sites converted electrochemically from the single-microparticle electrochemistry, and suggests that, as discussed for single PB nanocrystals,^[178] the electrochemical conversion is mostly restricted to a thin shell corresponding to approximately two unit cells.

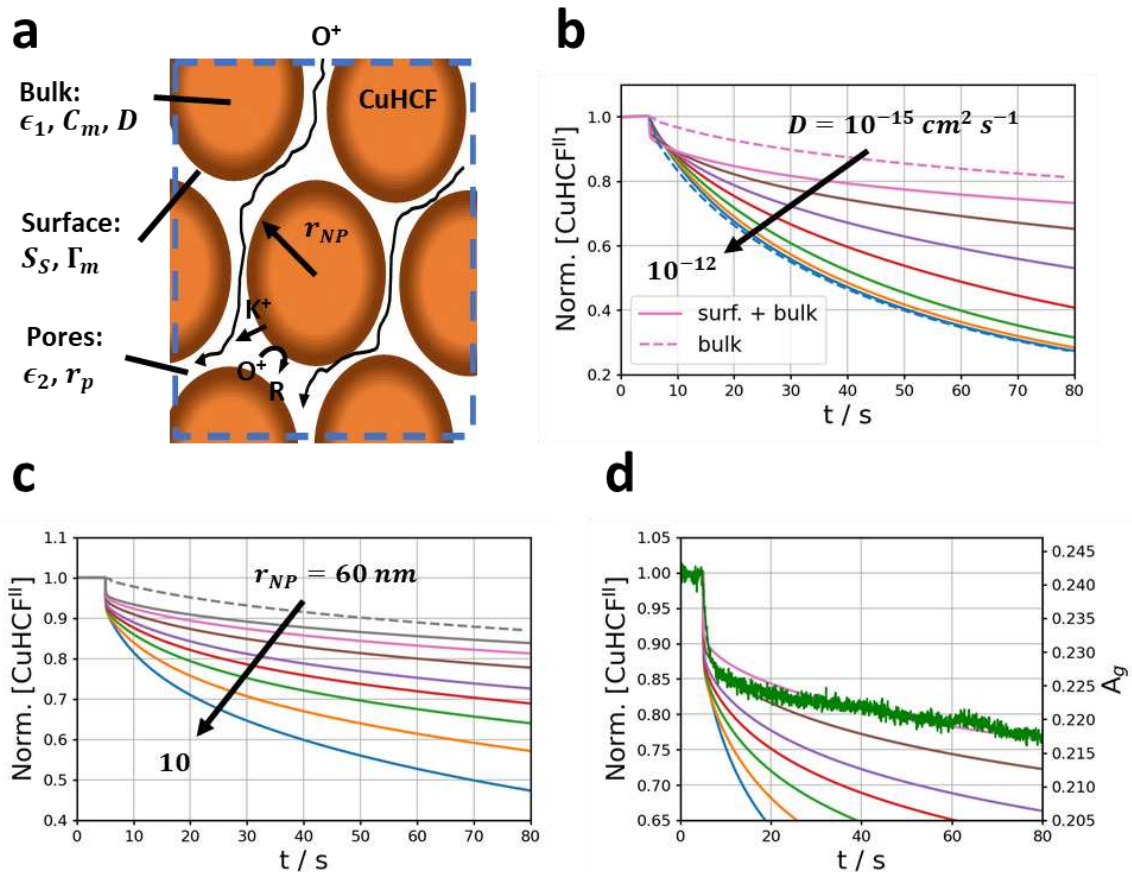


Figure 6-7. Simulating SECM potentiostatic charge of a single polycrystalline CuHCF microparticle. (a) Schematic description of the porous model employed: the microparticle is made of spherical NPs packed in a fcc network and separated by voids defining the porosity volume and dimension; the NPs' conversion takes into account surface conversion and diffusive shell-to-core conversion. (b) Example of microparticle conversion for different K^+ solid-state diffusion coefficients $D = 10^{-12}$, $3 \cdot 10^{-13}$, 10^{-13} , $3 \cdot 10^{-14}$, 10^{-14} , $3 \cdot 10^{-15}$ and $10^{-15} \text{ cm}^2 \text{ s}^{-1}$, considering either surface and bulk (plain lines) or only average bulk conversion (dotted lines). (c) Example of microparticle conversion for different NP radii $r_{NP} = 10, 15, 20, 30, 40, 50$ and 60 nm . (d) Comparison of the experimental average absorbance variation (green channel) with the simulated one for various r_{NP} values suggesting a reasonable agreement for $D = 10^{-15} \text{ cm}^2 \text{ s}^{-1}$ and $r_{NP} \approx 50 \text{ nm}$.

The conversion dynamics was further implemented in the simulation considering a porous microparticle. We do not have a priori knowledge of the size distribution of the nanocrystals composing the microparticle, and this simulation is just performed to provide a qualitative understanding of the effect of porosity on the conversion dynamics. A summary of the dynamic conversion simulation is presented in Figure 6-7 for a microparticle made of an arrangement of nanocrystals of different sizes and for different D values. As sketched in Figure 6-7a, the transport in such porous network is modelled through mean-field two-phase reaction-transport equations, assuming a regular network of nanocrystals of radii r_{NP} (with given surface and bulk CuHCF^{II} site concentrations), considering the transport of O^+/R within the porous structure, and considering a surface-to-core conversion of each NP.^[446] The simulation results are provided in Figure 6-7b and 6-7c as the evolution of the averaged CuHCF^{II} site concentration with time. Noteworthy, the simulation differentiates between surface + bulk NP conversion and bulk conversion averaged over the whole NP size. Figure 6-7b shows the effect of D on the NP conversion rate. It shows that with increasing D , the contribution of surface conversion becomes negligible. Similarly, Figure 6-7c shows that the contribution of surface conversion increases for larger NPs. Particularly for slow D and large r_{NP} , the conversion dynamics presents a faster component at short times and a slower (bulk-like) conversion at longer times like in the experiment. Actually, even if the hypothesis of a unimodal NP size distribution is unlikely to be true, the experimental electrochemical charge variation of ca. 20% and its fast dynamics could be approximately reproduced in Figure 6-7d

by considering $r_{NP} = 50 \text{ nm}$ and $D = 10^{-15} \text{ cm}^2 \text{ s}^{-1}$, which lies in the range of some reported values for PBA nanocrystals.^[177,178,441]

6.2.2.4 SPECTROSCOPIC TITRATION BY OM

The simulation in Figure 6-5c showed the good correspondence between the simulated electrochemical charge and the average conversion. Moreover, the simulation in Figure 6-8 showed that the porosity and polycrystalline nature of the CuHCF particles leads to a fast initial surface conversion followed by a slower bulk conversion of the nanocrystals composing the microparticles.

These modelled behaviours are then confronted to the potentiostatic charge/discharge experiments (lower panels of Figure 6-2). The variations of A_g , the absorbance recorded in the green channel and averaged over a ROI of the particle, during charge/discharge are given in the lower panel of Figure 6-2a. Its short-time dynamics, zoomed in the lower panel of Figure 6-2b, nicely matches the dynamics of the electrochemical charge, q . The dynamics of A_g was then also fitted by a similar exponential function, as supported by the simulation and previous observations of single PB NPs.^[177,192]

$$A(t) = A_{bg} + \Delta A \exp(-k_{app}t). \quad (6-7)$$

Noteworthy, in addition to the fast initial charge/discharge at approximately similar rates ($k_{app} = 1.1 \text{ s}^{-1}$), a slower conversion of the particle is also observed at longer time, both during charge and discharge (see e.g., the clear continuous decrease in A_g during charge in Figure 6-2a). It corroborates the simulation in Figure 6-7, suggesting a fast surface conversion followed, at longer times, by a deeper bulk conversion with slower kinetics (slower solid-state diffusion). Empirically, the slower conversion can be fitted by adding a second exponential function in Equation 6-7, typically with rates of the order of 0.02 and 0.25 s^{-1} for charge and discharge, respectively.

6.2.3 SUB-PARTICLE IMAGING OF THE CHARGE/DISCHARGE DYNAMICS

The correspondence between the short-time charge/discharge dynamics evaluated from the global optical response and the UME current points, from Equations 6-4 and 6-7, to the proportionality between Q_M and ΔA . This is now used to transform the absorbance movies recorded by OM into local electrochemical charge movies (Figures 6-8 and 6-9). From Equation 6-7, the absorbance movies are smoothed by fitting the time profile of each pixel with an exponential function, thereby revealing the spatial distribution of both the local conversion rate (k_{app}) and the local exchanged electrochemical charge ($Q_M \propto \Delta A$) over the particle. Such image analysis is shown in Figure 6-8. Figure 6-8a presents the local oxidation (charge) rate of the particle, while Figure 6-8b presents the local exchanged electrochemical charge extrapolated from the fitting procedure. These maps are also compared to the raw colour optical image of the particle given in Figure 6-8c. Finally, the discharge dynamics of the particle is also presented in Figure 6-8d. In Figures 6-8a and d, the conversion rates are evaluated by considering either the first 5 s or 15 s of the optical signal after the potential step. These images then characterize respectively the fast or slow conversion processes and therefore, from the discussion in the previous section, highlight local effects in the surface or bulk conversion dynamics.

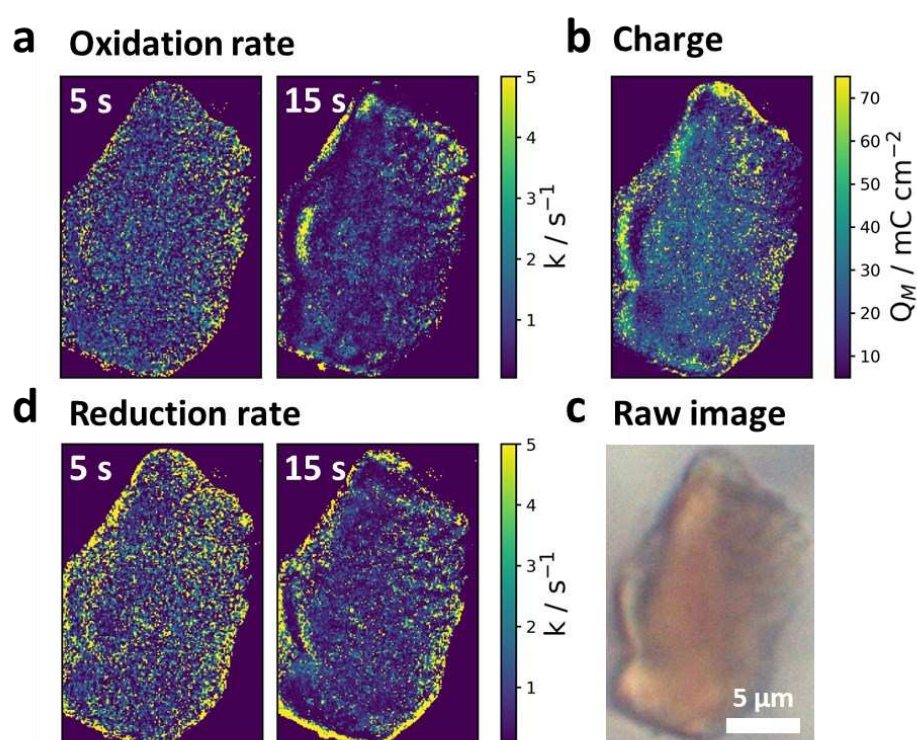


Figure 6-8. Imaging the local charge/discharge within a single CuHCF particle. From the raw optical images, the local absorbance variations are converted into local (a) oxidation or (d) reduction rates and (b) local exchanged electrochemical charges. The raw colour image in (c) presents the particle in its pristine state. The conversion rates in (a) and (d) are evaluated by fitting the optical transient corresponding to each pixel according to Equation 6-7, either over the first 5 s (fast conversion) or 15 s (slow conversion) after the potential step.

For easier visualization, a zoom in a $5 \times 7.5 \mu\text{m}^2$ region of the upper right part of the particle is also provided in Figure 6-9. Figure 6-9c shows in particular the optical contrast of the particle in the green channel, represented by the A_{bg} quantity defined in Equation 6-7. Based on Equation 6-2, this descriptor corresponds to the amount of absorbing material traversed by the light beam. Hence, the higher A_{bg} , the more absorbing the region and therefore the greater the amount of material (loading). Figure 6-9c then provides a map of local particle thickness or nanocrystal density (pore volume). While Figure 6-9c (and Figure 6-8c) shows that the particle presents regions of contrasted absorbance, the conversion rates during the first instants (5 s images of Figures 6-8a and 6-9a) of the charge and discharge steps seem rather homogeneous over the entire particle, with an average charge rate of 2 s^{-1} and a slightly faster average discharge rate of 4 s^{-1} . This is consistent with the conversion of the surface of the particle's porous network during the first instants. It then suggests that the porosity or local specific surface area is homogeneous over the entire particle. The edges of the particle seem, however, slightly more rapidly converted, but to a much lesser extent than suggested by the simulation of a microcrystal in Figure 6-5.

At longer times (15 s), the conversion rate images reveal regions with much more contrasted kinetics. At this time scale, the bulk of the nanocrystals is converted, and these images then suggest that the access to bulk CuHCF is heterogeneously distributed over the particle. A heterogeneous distribution is also found for the loading (A_{bg}) in Figure 6-9c, as well as for the local exchanged electrochemical charge Q_M in Figure 6-9b. Both descriptors are expected to be correlated: the higher A_{bg} , the higher Q_M . This is indeed confirmed from the general linear trend observed in the Q_M vs A_{bg} scatter plot presented in Figure 6-9d, considering the pixels probed in Figure 6-9a-c. As the homogeneous fast (surface) conversion rate maps, the

correlation between Q_M and A_{bg} is also consistent with a homogeneous porosity over the particle.

However, looking at the A_{bg} and Q_M maps, this correlation does not seem to hold in all regions of the particle. This is better visualized in Figure 6-9b and c, where red and white contours highlight chosen ROIs of respectively high and low loading. If on average regions of higher loading (red contours) are also regions of higher Q_M , they are sometimes less obvious to identify, or less contrasted, in the Q_M map (Figure 6-9b). This is even less clear for the regions of lower loading (white contours). For example, white-contoured region #1, near the upper border of the particle, shows areas of high Q_M (ca. 60 mC/cm²), although it exhibits an overall low loading. This could be rationalized based on the proximity of this region with the particle's edge, which is actually the region with the highest Q_M , confirming the higher (3D vs 2D) accessibility of the redox electrolyte to the solid matrix at the edge.

Similarly, white-contoured region #2 contacting the left edge of Figure 6-9b is also characterized by a local loading minimum, but it is as charged as the surrounding matrix. One could suggest that this is a region of higher porosity or smaller nanocrystals enabling a deeper (volume) conversion.

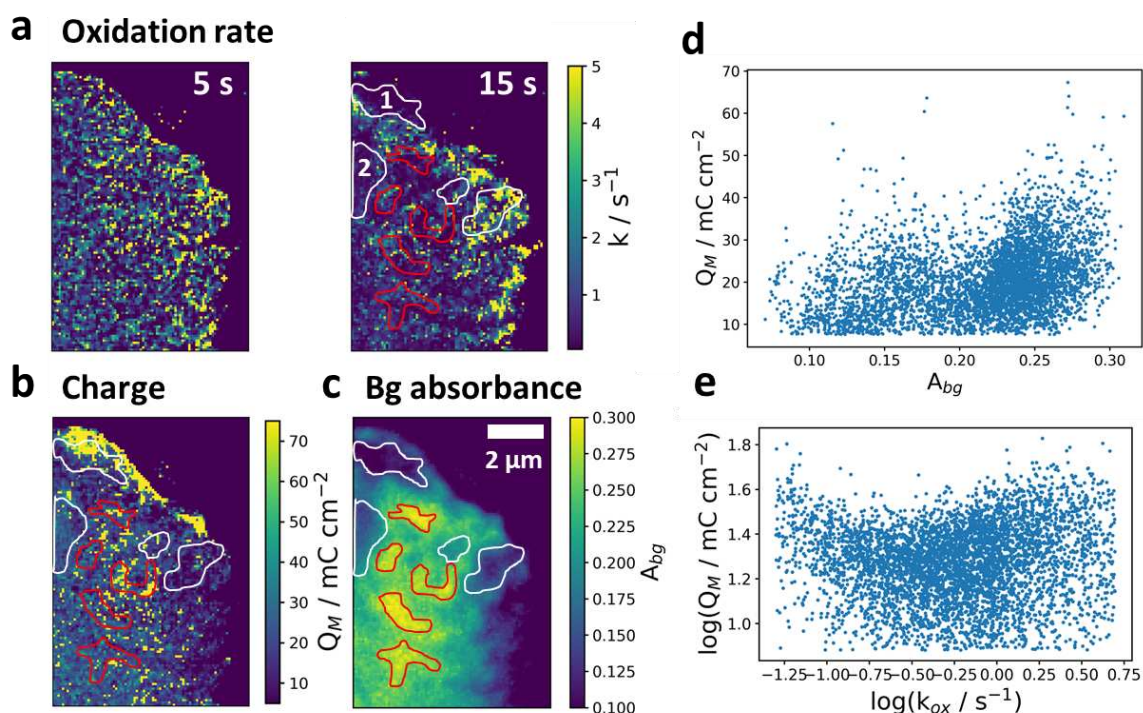


Figure 6-9. Zoom over the upper right part of the CuHCF particle presented in Figure 6-8. Same attribution of each map: (a) oxidation (discharge) rate over 5 s (left) and 15 s (right); (b) local exchanged electrochemical charge; in (c), the A_{bg} map corresponds to the local background absorbance in the green channel, which can be seen as a map of active site loading. Red and white lines are guides for the eyes, highlighting ROIs with respectively high or low loading (A_{bg}). (d, e) Scatter plots of Q_M vs A_{bg} and $\log(Q_M)$ vs $\log(k_{ox})$, respectively.

Finally, a correlation between local Q_M and local charge dynamics can be found when considering the long-time conversion rates (15 s map in Figure 6-9a). This is revealed from the scatter plot of the local Q_M as a function of the local charge dynamics given in Figure 6-9e: the larger Q_M , the slower the long-time charge. It is more specifically illustrated in the chosen ROIs discussed above. Indeed, the regions of higher loading and higher Q_M are also regions of slower conversion dynamics, suggesting that they experience a deeper volumetric charge. On the other hand, regions of lower loading also reveal some regions of faster charge. Again, white-contoured region #1 (upper edge) and #2 (left edge of the image) show contrasted and mechanistically relevant behaviours. Despite showing a low loading (low value of A_{bg} in Figure 6-9c), region #2 shows a rather large Q_M and slow charge dynamics: this region allows a deeper volumetric charge, which points again to a more nanostructured region (more porous or smaller nanocrystals). The same behaviour seems to be observed in region #1 as well: the upper part of this region is characterized by a higher Q_M and slow (deeper) charge dynamics. Interestingly too, the lower part of region #1 is associated to a low loading and low Q_M , which is also transferred at faster rates.

6.3 CONCLUSION

We have studied the SECM triggering of the charge/discharge of individual SB particles, namely polycrystalline CuHCF microparticles, in the context of SB-FBs. This new charge storage medium implies intricate charge transfer kinetics at a complex nanostructured solid-liquid interface along a micrometre-long porous network. An OM configuration enabling the local measurement of the particle's absorbance is proposed to analyse such conversion mechanism *operando*, at high throughput, and with sub-micrometre spatial resolution. Its operating

principle is first detailed, showing that the absorbance of the whole particle is correlated to the electrochemical charge expelled from the particle during charge. However, this charge is only partial (ca. 20%) and faster than expected for a monocrystalline microparticle. Based on a COMSOL simulation, this discrepancy is attributed to the surface conversion of the numerous nanocrystals composing the polycrystalline microparticle, accessible from the latter's porosity. The optical images of the particle's conversion recorded during charge/discharge are then able to reveal the dynamics of such conversion. At short times, the fast conversion of the surface is rather homogeneous over the particle. At longer times, the bulk conversion is probed and reveals a strong heterogeneity associated to the local loading or exchanged electrochemical charge: the deeper the local charge and the slower the local conversion. Eventually, such maps, obtained with sub-micrometre 2D spatial resolution, show the wealth of electrochemical behaviours which can operate during the conversion of a polycrystalline particle. Interestingly, these behaviours are revealed within neighbouring regions less than 100 nm distant from each other, suggesting that OM probes the local mass transport within locally porous or nanostructured regions. Noteworthy, the optical monitoring described herein probes the transport properties across the full particle thickness (ca. 3 μm), still with sub-micrometre 2D lateral resolution. Such information, provided *operando* and at high throughput, could not be obtained by standard nanoscale electrochemical probes (nanopipettes or NEs), whose probing depth are of the order of the probe's dimension and therefore much smaller than the particle's thickness or the conversion depth.

GENERAL CONCLUSION

At the start of my PhD, the field of single entity electrochemistry was transitioning from model systems to more complex systems such as those encountered in energy storage and conversion devices. This transition required improving data collection at single NPs as well as data analysis, which were the main objectives of my PhD. To improve data collection, we notably established a multi-microscopy methodology correlating our *in situ* OM technique to several other *ex situ* microscopy techniques such as SEM and AFM, providing additional structural and chemical information. To improve data analysis and make better use of such extensive datasets, we implemented machine vision and machine learning algorithms into our routines. These improvements were tested on various systems relevant for energy storage and conversion applications, providing crucial insights into complex (electro)chemical mechanisms.

First, we have shown how IRM can be used to distinguish between different NP populations *in situ* based on their composition (refractive index), revealing competing reaction pathways for the electrodeposition of Ni-based NPs on ITO. Complementing IRM with extensive *ex situ* SEM and AFM with the help of machine vision and machine learning algorithms, we have quantified the contribution of each pathway and estimated the average electrocatalytic activity of Ni NPs for water reduction. By visualizing the pH gradient formed around NPs upon water reduction through the precipitation of metal hydroxides, we have further demonstrated how IRM can be used to quantify the electrocatalytic activity for water reduction at the single-NP level, which had only been achieved at extreme (and therefore irrelevant for industry) current densities by monitoring the formation of gas NBs.^[124,164]

Afterwards, we have shown how OM could also reveal competing reaction pathways at the cathode of aqueous Zn-MnO₂ batteries. Based on an optical model, we evidenced the precipitation of ZHS at a much earlier state of discharge than in previous reports. This new amorphous form of ZHS is thought to be at the origin of the first discharge (and charge) plateau, which has puzzled the scientific community for decades. Monitoring the electrodeposition of MnO₂ around ZHS particles also confirmed the crucial role of ZHS as a local pH buffer on charge.

Finally, by combining IRM with SECM, we have shown that the conversion of individual polycrystalline CuHCF particles could be triggered and quantified *operando* thanks to the mirroring effect of the UME which allows visualizing the particles in transmission and not only in reflection. Comparing the electrochemical trace to the average optical response and simulations revealed the importance of transport within the pores and a mostly surface-confined conversion of the individual grains. This was also confirmed by imaging the local absorbance as regions of higher conversion were usually regions of lower density (larger pore volume).

TOWARDS MORE RELEVANT EXPERIMENTAL CONDITIONS

While these studies, and most single particle studies in the literature employing OM or other techniques, revolve around isolated particles deposited on a (mostly) inert electrode to avoid side reactions, some researchers recently engineered cells that allow to precisely investigate single particles within a complex matrix resembling a real battery electrode. Even if the former studies are very insightful from a fundamental point of view, there are only few applications where no additives are needed, and the material is self-supported on the current collector (the only exception being electrodeposited nanocatalysts like the Ni NPs discussed in **Chapters 2-4**). Therefore, re-complexifying the samples by incorporating the particles into a conductive matrix as proposed by Merryweather *et al.*^[183–185] and Pandya *et al.*^[2] is important to make single particle studies more relevant for real-life applications.

In the same vein, in collaboration with the group of Jean-Marie Tarascon, we have investigated the electrochromic behaviour of $\text{Li}_2\text{Ni}_2\text{W}_2\text{O}_9$ microparticles, prepared as a self-standing electrode, upon (de)lithiation.^[3] However, working with thin films might have been more relevant in this case as electrochromic materials are mainly used in smart windows. But this new phase could only be synthesized as microparticles for now and probing it like this was the only way to properly test their electrochromism.

Despite the numerous advantages of these cells, they have the drawback of allowing only reflectance measurements, which are difficult to make quantitative in the case of micron-thick particles as the light will only probe the outermost layers of the particles. If the particles are transparent enough, the strategy proposed in **Chapter 6** can be employed. However, this is

again not a configuration mimicking that of a real device. Following on our collaboration with the group of Pekka Peljo at the University of Turku, we then developed a flow cell that should allow probing the state-of-charge of CuHCF particles in a similar way, but under operation in an actual flow cell. Instead of approaching a mirror from the top and collecting from the bottom, a composite particle film is here directly deposited on a mirror and observed from the top. While the setup has already been validated, the actual experiment under microscope observation still needs to be performed.

Another issue we ran into concerning the experimental conditions, especially in **Chapters 2-4** concerning the electrocatalytic activity of Ni NPs, was the reactivity of the support electrode, ITO. While standard conditions for electrocatalysis are either strongly acidic or strongly alkaline, we had to perform experiments in near neutral electrolytes due to the poor stability of ITO in strongly acidic and strongly alkaline conditions. Our colleagues have indeed shown that ITO rapidly dissolves below pH 2, and that In NPs can be formed under cathodic polarization in acidic conditions.^[170] To conform to the standards, we would need to find new semi-transparent electrodes that provide a clean electrochemistry and a clean optical visualization even in these harsh conditions. Promising candidates could be thin carbon layers (as the ones deposited on TEM grids) or boron doped diamond layers.^[447] These materials are known to be very robust and much less heterogeneous than ITO.^[246,247]

TOWARDS HIGHER SENSITIVITY

While mimicking the configuration of real devices is considered critical for future developments, there are still some fundamental questions which can only be addressed by probing isolated particles, provided that some improvements in terms of sensitivity are made.

While we already claim to have a sub-25 nm limit of detection for Ni and Ni(OH)₂ NPs, which are not plasmonic and even dielectric in the case of Ni(OH)₂, using more powerful light sources such as lasers – essentially converting our IRM into an interferometric scattering (iSCAT) microscope^[448] – we could push the limit of detection even further. This is interesting as industrial catalysts usually come in the form of very small clusters of only a few nanometres, whose dynamics under operation are still poorly understood. Visualizing such clusters could also be relevant for studying electrodeposition processes in more detail as Pt group metals

are known to grow by aggregation and not by direct attachment.^[216] The diffusion of these clusters remains a challenging task to probe *operando*.

Using more powerful light sources, in combination with more sensitive cameras, could also help capturing more subtle changes in intensity as for example in the case of surface-confined processes or processes occurring within the NP's diffusion layer in the electrolyte. While we have proposed a more general way to probe the electrocatalytic activity of single NPs by visualizing pH gradients instead of gas NBs in **Chapter 4**, directly visualizing ion fluxes at the NP|electrolyte interface as proposed by Zhang *et al.*^[198] could be an even more general way to achieve this. Indeed, while most electrocatalytic reactions of interest produce pH changes (HER, OER, ORR, CO₂RR, NO₃RR...), all electrochemical reactions, without exception, produce local ionic strength changes. In this way, the rate of any electrochemical reaction could be quantified at the single-NP level and label-free, or with the reaction product/reactant itself as only label. Coupled to wide-field observation, this mode would considerably increase the interest of OMs for the screening of composition- or size-dependent activity, which is one of the major challenges the research community is facing right now.

MATERIALS AND METHODS

M.1 MATERIALS

M.1.1 CHEMICALS

All chemicals were used as received. KCl (ACS reagent) was purchased from Acros Organics. NiCl₂·6H₂O (ReagentPlus), NaH₂PO₄ (>99.0%), Na₂HPO₄ (>98.5%), MgCl₂, K₂PtCl₆, HNO₃ (Suprapur, 65%), H₂O₂ (Suprapur, 30%), H₂SO₄ (ACS reagent, 95.0-98.0%), and KOH (ACS reagent, >85%) were purchased from Sigma-Aldrich. ZnSO₄·7H₂O (98%), MnSO₄·H₂O (99%), and carbon powder (Super P, >99%) were purchased from Alfa Aesar. TEMPTMA was provided by the group of Prof. Hubert Girault at Ecole Polytechnique Fédérale de Lausanne. Solutions were prepared with ultrapure water with a resistivity higher than 18.2 MΩ.cm. ZHS-saturated solutions were prepared by adding an excess of chemically synthesized ZHS (see below) to the solution, stirring it for several hours, and gravity filtrating the supernatant.

M.1.2 ZHS SYNTHESIS

Zn₄(OH)₆SO₄·xH₂O (ZHS) was prepared by adding a 2 M KOH solution to a 2 M ZnSO₄ solution until the pH exceeded 5.2.^[449] If the pH became too alkaline, ZHS would be converted to soluble Zn(OH)₄²⁻.^[450] The white precipitate was recovered by centrifugation and dried under vacuum at ≈100 °C for a few days. It was then characterized by XRD as being *osakaite* ZHS (x = 5, PDF 00-060-0655).

M.1.3 CUHCF SYNTHESIS

Copper hexacyanoferrate (CuHCF) was synthesized by our collaborators from the group of Pekka Peljo at the University of Turku by gradual and simultaneous pumping of 120 mL of 0.1 M Cu(NO₃)₂·3H₂O and 120 mL of 0.05 M K₄Fe(CN)₆·3H₂O from two separate beakers to a third one containing 60 mL of ultrapure water under magnetic stirring. The obtained suspension was then centrifuged three times for 30 min. The suspension was allowed to rest for a couple of hours after which the sediment was collected in the form of a slurry through filtering and

washing with ultrapure water. The slurry was then dried under vacuum at room temperature overnight to obtain the pristine CuHCF agglomerates, which were characterized by XRD.

M.1.4 MICROPIPETTE FABRICATION

Micropipettes were fabricated in-house. First, borosilicate glass capillaries (outer diameter: 1.0 mm, inner diameter: 0.5 mm, Sutter Instrument) were pulled with a P-2000 laser puller (Sutter Instrument). Then, they were polished to the targeted diameter (10-100 μm) by using a BV-10 micropipette beveller (Sutter Instrument). The polishing was monitored with a long-working distance objective (10x/0.28) equipped with a motorized zoom controller (Navitar) and a digital camera, mounted on a 3-axis macro-mechanical system.

M.1.5 ITO AND AU CLEANING

ITO-coated coverslips (glass thickness #1.5) with a resistivity of 15-30 $\Omega\text{ cm}$ were purchased from SPI. They were sonicated in ethanol for 500 s and dried with an argon flux before use. Au-coated Si wafers (Au(100 nm)/Cr(5 nm)/Si(100)) were either purchased from Sigma-Aldrich or prepared in-house by physical evaporation on a bare Si wafer (Sigma-Aldrich). Prior to use, they were soaked in concentrated H_2SO_4 for 5 min, and then successively sonicated in water, acetone, and ethanol for 5 min each.

M.1.6 Pt NP ELECTRODEPOSITION ON ITO

Pt NPs were electrodeposited on ITO by chronoamperometry at -0.7 V vs Pt for 100 s in 1 mM K_2PtCl_6 + 0.1 M KCl (Figure M-1). After electrodeposition, the ITO substrate was rinsed with copious amounts of ultrapure water.

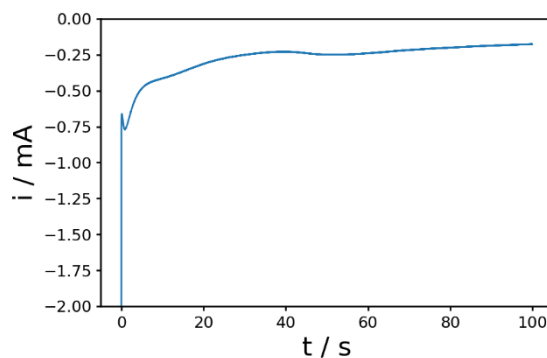


Figure M-1. Electrodeposition of Pt NPs on ITO by chronoamperometry at -0.7 V vs Pt for 100 s in 1 mM K_2PtCl_6 + 0.1 M KCl (reference electrode: Pt wire, counter electrode: stainless steel grid).

The geometry of the Pt NPs was then characterized by AFM (Figure M-2a). From the evolution of NP height vs radius, one can extract the average contact angle of the NPs, θ , using one of the following equations:

$$h = r(1 - \cos \theta) \quad \text{if } h > r, \quad (\text{M-1})$$

$$h = r \left(\frac{1 - \cos \theta}{\sin \theta} \right) = r \tan \left(\frac{\theta}{2} \right) \quad \text{if } h < r. \quad (\text{M-2})$$

If $h < r$, r represents the radius of the base of the spherical cap and not the radius of the equivalent sphere. For the Pt NPs, the radius is slightly smaller than the height on average (Figure M-2c), so Equation M-1 was used. We found $\theta = 103^\circ$, which is very close to a hemisphere (22% error on the surface area of the NP).

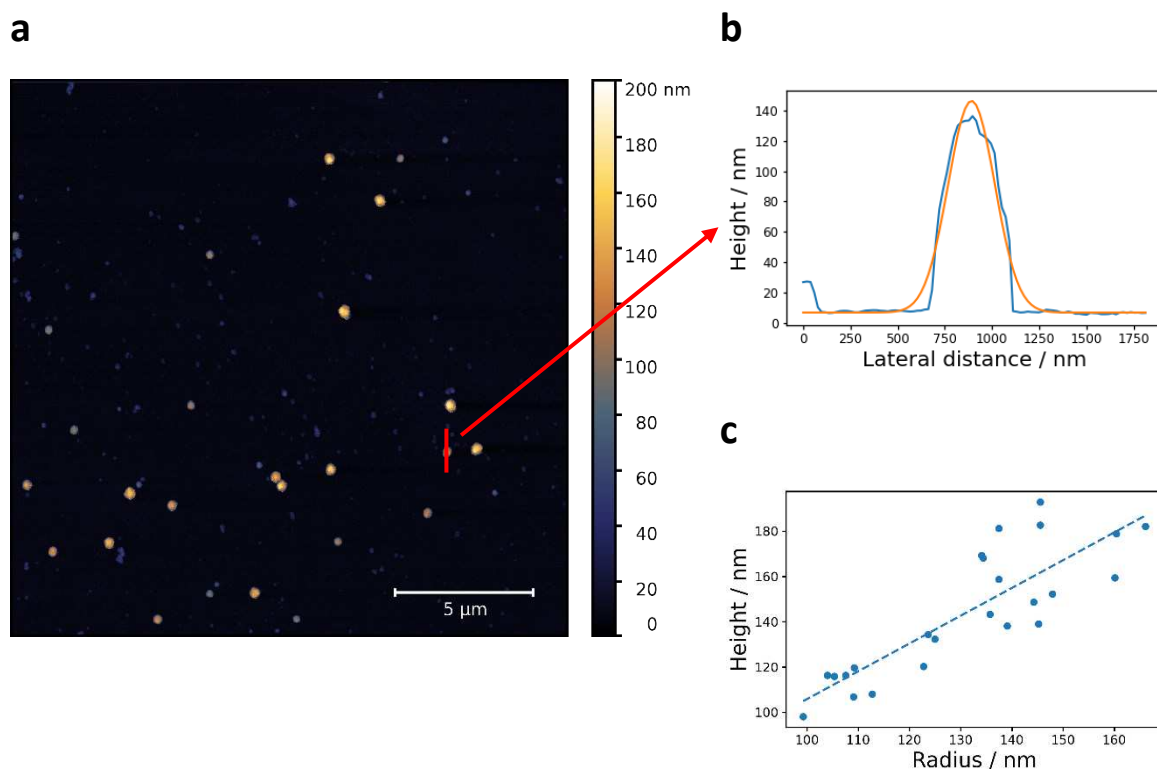


Figure M-2. (a) AFM topography image of Pt NPs electrodeposited on ITO. (b) Line profile of the Pt NP highlighted in (a) (blue) and gaussian fit (orange). (c) NP height vs radius (HWHM of the gaussian fit) for all the Pt NPs in (a) and linear regression ($r^2 = 0.711$).

M.2 OPTO-ELECTROCHEMICAL EXPERIMENTS

M.2.1 INVERTED MICROSCOPE

The ITO-coated coverslip is placed on an inverted microscope (Axio Observer 7, Zeiss) and is illuminated from the backside through a 63× oil immersion objective (Plan Apochromat, Zeiss, NA = 1.4) with a nonpolarized white light. A CMOS camera (UI-3080CP Rev. 2, IDS) operating at 20 frames per second collects the reflected light through the same objective. The opto-electrochemical experiments are performed using a CHI760e (CH Instruments) or PG 618 Ultra (Heka) potentiostat, which is triggered together with the camera by a waveform generator. The ITO is used as working electrode (WE) and a Pt wire (diameter: 100 μm, Goodfellow) as quasi-reference counter electrode (QRCE) in a two-electrode configuration. To form the microelectrochemical cell, a micropipette (diameter: 10-100 μm) – containing the electrolyte and the Pt wire – is approached close to the ITO surface owing to a 3-axis microcontroller (manual or Heka EIProScan) until a meniscus is formed. The instrument is placed in a Faraday

cage to avoid electrical noise and on a damped optical table to avoid mechanical noise. In **Chapter 6**, the microcontroller was used to approach a Pt UME 10 μm above a selected location.

M.2.2 UPRIGHT MICROSCOPE

The *operando* optical reflectometry setup was developed in-house and consists of a standard microscope (U-CMAD3, Olympus) equipped with a 40 \times water immersion objective (LUMPlanFL N 40 \times /0.80 W, Olympus) and a CCD camera (MV-D1024E-160-CL-12, Photonfocus). The light source is a halogen white lamp filtered at 490 nm (spectral bandwidth: 20 nm). As depicted in Figure 5-1b, the substrate is illuminated from the top through the objective, and the reflected light is collected through the same objective. Before each experiment, the tilt of the substrate is adjusted using a Mirau objective (CF Plan 10 \times /0.30 DI, Nikon) to achieve normal incidence.^[451] Moreover, the instrument is placed on a damped optical table to avoid mechanical noise. Such a setup allows 3D spatiotemporal imaging with sub-micrometre lateral and sub-nanometre vertical resolution.^[400] The collected images were treated using homemade MATLAB and Python routines. The relative reflectivity, R , mentioned throughout **Chapter 5** is calculated as:

$$R = \frac{Im(t)}{Im(0)}, \quad (\text{M-3})$$

where $Im(t)$ represents the raw optical image acquired at time t . Details about the theory are provided in **Appendix 2**.

Electrochemical measurements were performed using a CHI760e potentiostat (CH Instruments), which was triggered manually alongside the camera. Au-coated Si wafers were used as reflective substrate and working electrode (WE, immersed surface area: ca. 0.2 cm^2), a ca. 1 \times 1 cm^2 Au grid (Goodfellow) was used as counter electrode (CE), and a ca. 1 \times 5 cm^2 piece of Zn foil (Alfa Aesar) as a reference electrode (RE).

M.3 OTHER INSTRUMENTS

M.3.1 SCANNING ELECTRON MICROSCOPY

Scanning electron microscopy (SEM) images were recorded either on a SUPRA 40 SEM-FEG or a Gemini SEM 360 (Zeiss), with an acceleration voltage of 5 kV. Energy dispersive X-ray spectroscopy (EDX) analyses were performed on the Gemini SEM 360 microscope equipped with an Ultim Max detector (Oxford Instruments). Spectra and elemental mappings were processed using the AZtec software (Oxford Instruments).

M.3.2 ATOMIC FORCE MICROSCOPY

Atomic force microscopy (AFM) topography images were recorded in the intermittent contact mode with a NT-MDT Solver pro equipment and standard 10 nm Si tips. Image analysis was achieved with the free software Gwyddion. To investigate the geometry of the Pt NPs in Figure M-2, the scanning frequency was considerably reduced to limit the broadening effect of the tip.

M.3.3 TRANSMISSION ELECTRON MICROSCOPY

Transmission electron microscopy (TEM) images in Figure M-2 were obtained using a JEOL 2100 Plus transmission electron microscope operating at an acceleration voltage of 200 kV. The Pt NPs were electrodeposited on a carbon-coated silicon nitride window (Protochips) using the same procedure as for ITO (see section M.1.6) within a microdroplet formed by a micropipette (see section M.2.1). Again within a microdroplet, the Pt NPs were then subjected to several CV cycles in 1 mM NiCl₂ + 10 mM KCl.

M.3.4 GALVANOSTATIC CYCLING IN SWAGELOK CELL

6 mg of carbon powder were deposited on a stainless steel disk (RS), which was then adapted to a two-electrode ½" PTFE Swagelok cell. A Zn disk (Alfa Aesar) was used as anode, and a glass fiber disk (Whatman, Sigma-Aldrich) as separator. The separator was soaked with 300 µL electrolyte (0.2 M MnSO₄ + 2 M ZnSO₄). Galvanostatic cycling of the cell was performed at 30 µA between 0.85 and 1.75 V, using either a VMP3 or a VMP-300 potentiostat (BioLogic).

M.3.5 INDUCTIVELY COUPLED PLASMA-MASS SPECTROMETRY

Inductively coupled plasma-mass spectrometry (ICP-MS) measurements were performed on a NexION 2000 spectrometer (PerkinElmer) to determine the Mn and Zn content of MnO₂ films at different states of discharge. The films were dissolved in 2 mL of a mixture of 90 vol% water, 5 vol% HNO₃, and 5 vol% H₂O₂, and the resulting solutions were analysed without further dilution. The ZHS mass calculated from the measured Zn concentration (Table 5-1) was corrected for the amount of Zn contained in the MnO₂ film (Table M-1). As suggested by its low density, some electrolyte might have been trapped inside the film during the electrodeposition.

Table M-1. MnO₂ and ZHS mass measured by ICP-MS at different states of discharge (CV). The Zn concentration was corrected for the amount of Zn trapped inside the MnO₂ film (see below for details).

Stop potential (V vs Zn ²⁺ /Zn)	S (cm ²)	[Mn] (ppb)	m _{MnO₂} (µg/cm ²)	[Zn] (ppb)	[Mn]/[Zn]	
1.85 (1)	0.98 10 ⁻¹	100	3.23	209	0.48	
1.85 (2)	3.04 10 ⁻¹	230	2.39	104	2.21	
1.85 (3)	1.01 10 ⁻¹	84	2.63	24	3.50	
XPS	/	/	/	/	3.21	
					[Zn] _{corr} (ppb)	m _{ZHS} (µg/cm ²)
1.65	1.28 10 ⁻¹	94	2.32	119	87	2.86
1.35 (1)	2.79 10 ⁻¹	90	1.02	109	79	1.19
1.35 (2)	1.50 10 ⁻¹	60	1.27	74	54	1.51
1.2 (1)	1.24 10 ⁻¹	22	0.56	86	79	2.68
1.2 (2)	1.31 10 ⁻¹	68	0.77 (1.64)*	124	101	3.24
0.85	1.56 10 ⁻¹	10	0.20	124	121	3.26

Red: Samples were probably not rinsed properly because the Mn/Zn ratio lies below 1 already at a very early state of discharge ($\text{Mn/Zn} = 2.97 \pm 0.68$ on average at the end of the charge).

Green: Values used in Table 5-1.

*Value was corrected for the unusually high charge exchanged during the electrodeposition ($12.82 \cdot 10^3$ vs $(5.94 \pm 0.12) \cdot 10^3 \mu\text{C cm}^{-2}$ on average). The measured value is given in brackets.

Correction of the Zn concentration: The Mn/Zn ratio (2.97 ± 0.68 on average at the end of the charge), which is assumed to remain constant throughout discharge, is used to calculate the Zn concentration corresponding to Zn trapped inside the MnO_2 film, which is then subtracted to the measured Zn concentration.

M.3.6 FOURIER-TRANSFORM INFRARED REFLECTION-ABSORPTION

SPECTROSCOPY

Fourier-transform infrared reflection-absorption spectroscopy (FT-IRRAS) was performed on a FT/IR-6100 spectrometer (JASCO), with a resolution of 4 cm^{-1} . The substrate itself served as a reflective surface for the infrared beam. All spectra were corrected for the background and the presence of water using the Spectra Manager software (JASCO).

M.3.7 X-RAY PHOTOELECTRON SPECTROSCOPY

X-ray photoelectron spectroscopy (XPS) was performed on a K-Alpha+ spectrometer (ThermoFisher Scientific) using an Al $K\alpha$ X-ray source (1486.6 eV). These measurements were used to determine the Zn/S ratio of MnO_2 films at different states of discharge by integrating the Zn2p and S2p peaks, as well as to probe changes in the chemical environment of O and Zn atoms upon discharge. Unfortunately, as explained in **Chapter 5**, the oxidation state of Mn could not be unequivocally determined by this technique as the Mn3s and Mn2p peaks, which are most commonly used for this purpose, overlap with Au and Zn peaks.

M.3.8 X-RAY DIFFRACTION

X-ray diffraction (XRD) was performed on a D8 ADVANCE diffractometer (Bruker) using a Cu $K\alpha$ X-ray source (1.5406 \AA). Peaks were attributed using the DIFFRAC.EVA software (Bruker).

M.4 IMAGE PROCESSING (INVERTED MICROSCOPE)

Optical images are analysed using homemade Python routines. First, the raw colour images are split into their three (red, green, and blue) channels. In **Chapters 2-4**, for instance, the less sensitive green channel was selected for the analysis of the bright-contrasted features (Ni/Pt NPs) and the more sensitive blue channel for the analysis of the dimmer dark-contrasted features (Ni(OH)₂ NPs and Ni(OH)₂/Mg(OH)₂ shell).

M.4.1 NP LOCALIZATION AND OPTICAL INTENSITY EXTRACTION (**CHAPTERS 2-4**)

Then, the centroid coordinates of each feature are found using the Crocker and Grier localization algorithm, which is already pre-implemented in the *trackpy* library. Finally, the optical intensity of each feature, I_{opt} , is extracted as the average intensity of a 4×4-pixel square centred at the estimated centroid position, subtracted by the average intensity calculated on the first image (e.g., before electrodeposition is initiated). Repeating this procedure for all frames in a movie and knowing both the scan rate of the CV and the frame rate of the camera, it is possible to correlate the evolution of I_{opt} (of each feature) with the applied potential. The corresponding Python function is openly available here: <http://doi.org/10.5281/zenodo.6780029> (*Supplementary file 1_image_treatment.py*).

M.4.2 MODELLING OF NP GROWTH (**CHAPTER 3**)

The data processing associated to the NP growth model and its comparison to SEM was split into several Python sub-routines, which are all openly available along the raw datasets here: <http://doi.org/10.5281/zenodo.6780029>. A brief description of each routine is given below.

Supplementary file 1_image_treatment.py: In addition to localizing the NPs on the last frame and extracting their I_{opt} transients as described above, this routine also determines the contour of the droplet on the first frame. The contour serves as a first filter to discard spurious

features which are localized outside the droplet. As observed in Figure M-3, the contour analysis run on the first and last frame of the movie indicates there is almost no droplet expansion during the experiment.

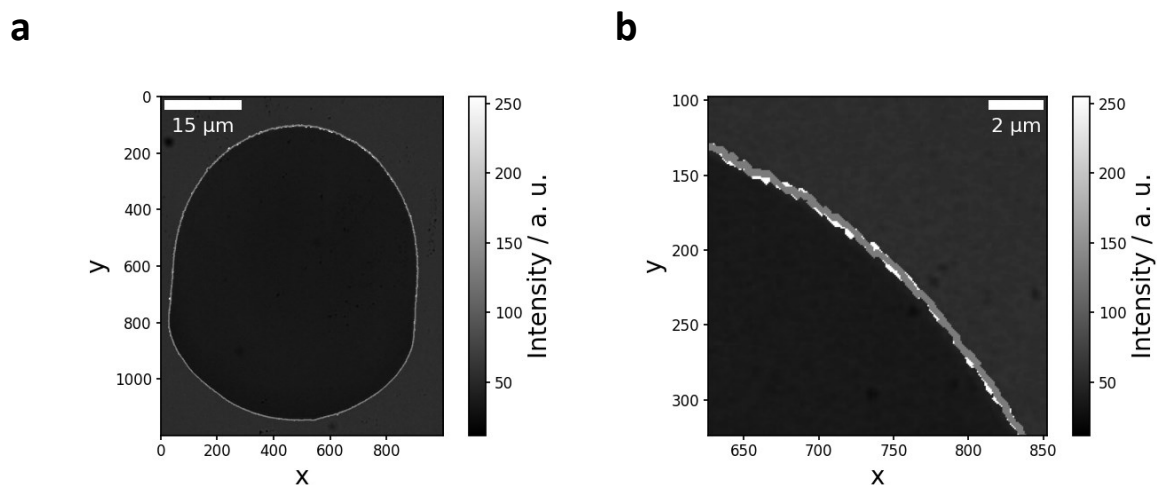


Figure M-3. (a, b) Comparison between the droplet contours determined on the first (white) and the last frame of the movie (grey) at two different scales.

Supplementary file 2_transient_analysis.py: This routine fits the transients obtained above with a logistic step function. The growth time (Δt) and onset time (t_o) of each NP are then calculated from the fitting parameters (growth rate σ , center x_c) and the frame rate (f_a).

$$\Delta t = 3\sigma/f_a \quad (\text{M-4})$$

$$t_o = \frac{x_c}{f_a} - \frac{\Delta t}{2} \quad (\text{M-5})$$

Supplementary file 3_growth_model.py: This routine first calculates the theoretical evolution of the radius of each NP (diffusion-limited growth, see Equation 3-5) considering the growth times and onset times determined above, a chosen LOD (see Figure 3-6), and the geometry of the NP. Then, the current associated to each NP is calculated as the sum of the growth current and catalytic current. Finally, the total current is calculated as the sum of all single NP currents (see Equations 3-7 and 3-8).

Supplementary file 3_growth_model_bis.py: This routine does the same as *Supplementary file 3_growth_model.py* but takes into account the multimeric nature of the NPs unveiled in *Supplementary file 6_correlation_analysis.py* (see Figure 3-7).

Supplementary file 4_comparison.py: This routine compares the experimental current to the theoretical total current determined above.

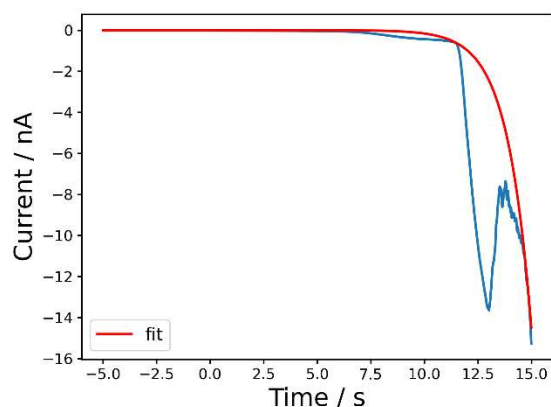


Figure M-4. Experimental current and exponential fit of the current corresponding to HER on ITO.

Supplementary file 5_crop.py: This routine crops the SEM images in order to remove the scale bar.

Supplementary file 5_resize.py: This routine resizes raw SEM images to the desired pixel size. It is exemplified with the low-magnification (LM)-SEM image, which is resized to the same pixel size as the high-magnification (HM)-SEM images. To include the intermediate-magnification (IM)-SEM images into the dataset for template matching (see *Supplementary file 5_bis_template_matching.py*), they should be resized as well using a zoom factor of 2.069 (for other magnifications, the zoom factor must be re-evaluated).

Supplementary file 5_correlation.py: This routine first correlates the position of each NP on the LM- SEM image of the whole droplet. Then, it determines the position of the NP on the closest HM-SEM image knowing the contours of all HM-SEM images inside the LM-SEM image (see *Supplementary file 5_bis_template_matching.py*). Finally, the NP is sized by fitting its profile on the HM-SEM image with a Gaussian function. The diameter of the NP is considered equal to the full width at half maximum (FWHM) of the Gaussian fit.

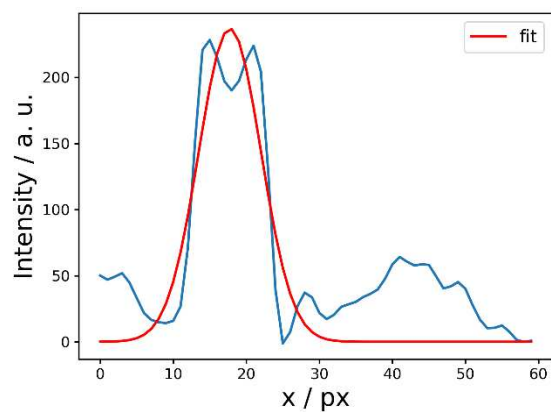
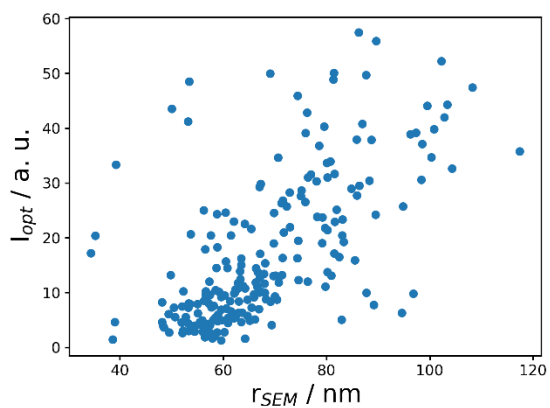


Figure M-5. Representative x-profile of a NP on a HM-SEM image and Gaussian fit.

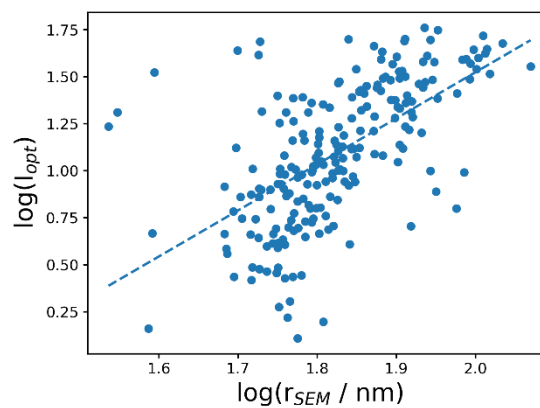
Supplementary file 5_bis_template_matching.py: This routine determines the contours of all HM-SEM images inside the LM-SEM image using the template matching algorithm implemented in the *OpenCV* library.

Supplementary file 6_correlation_analysis.py: This routine proposes several plots to confront the growth model to the actual size of the NPs measured by SEM.

a



b



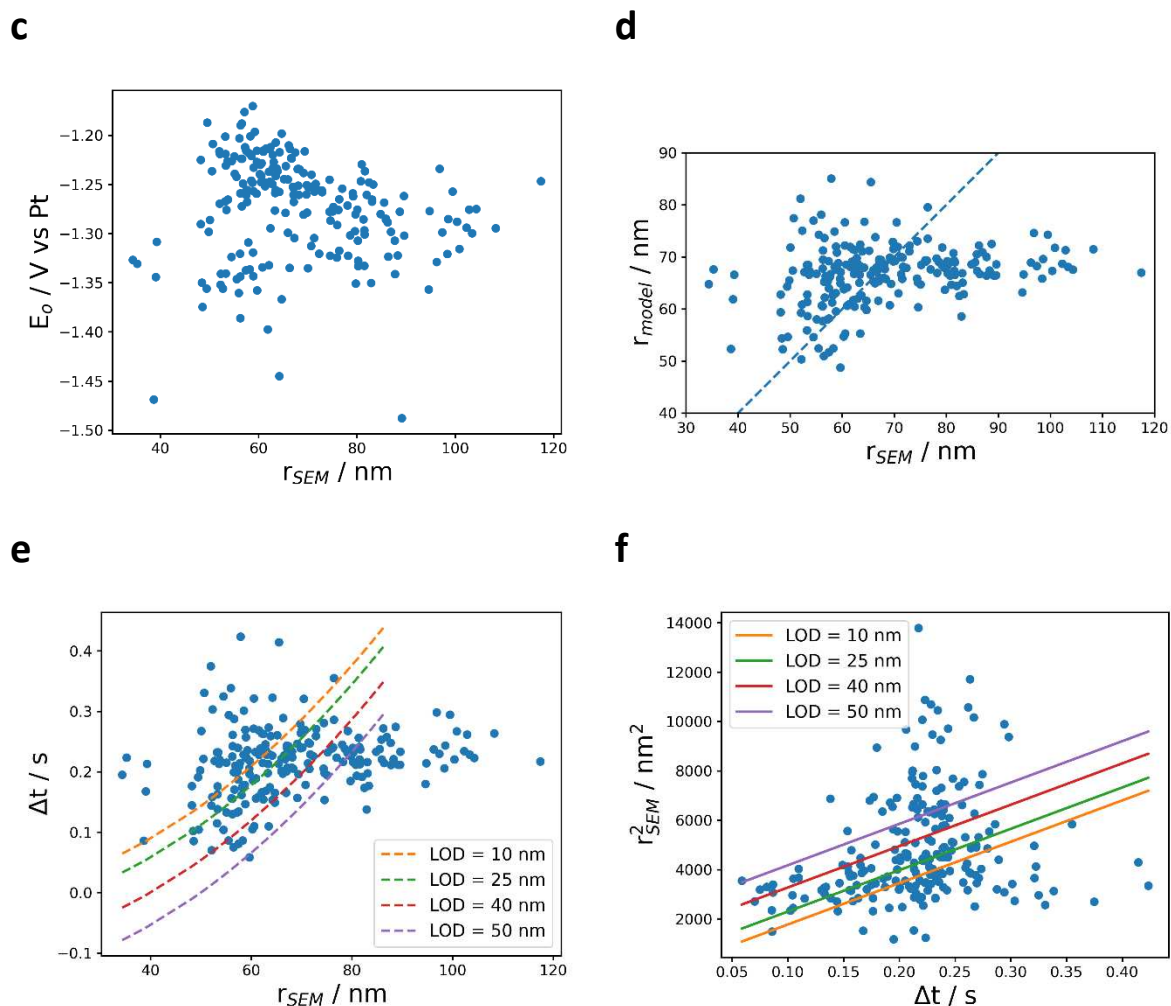
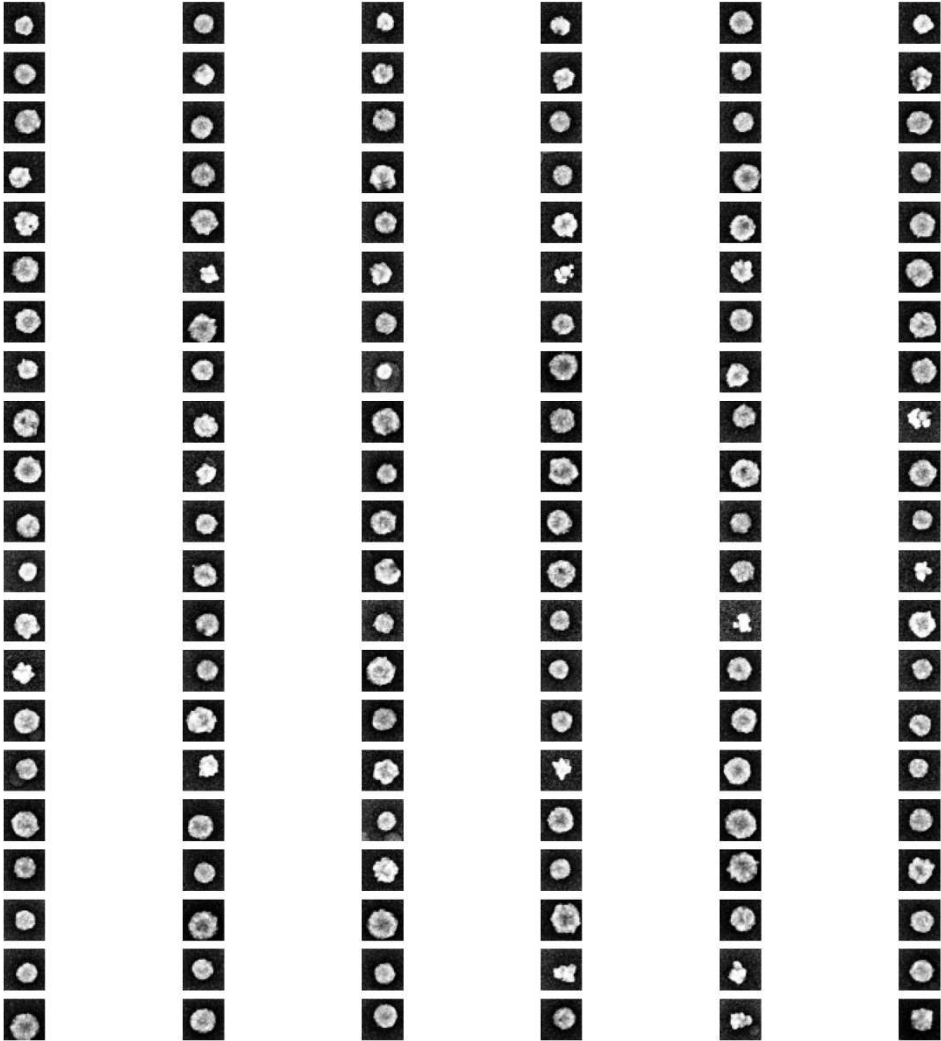


Figure M-6. Various plots confronting the growth model to the actual size of the NPs measured by SEM. (a) SEM radius as a function of the final NP optical intensity extracted from the image sequence. (b) Same as (a) in logarithmic scale. (c) SEM NP radius as a function NP onset potential. (d) SEM NP radius as a function of NP radius calculated from the growth model. (e) SEM NP radius as a function of NP growth time extracted from optical monitoring. (f) NP growth time as a function of NP radius squared. The slope of the dashed line in (b) is equal to 2.45. The slope in (d) was set to 1 (perfect correspondence between r_{model} and r_{SEM}).

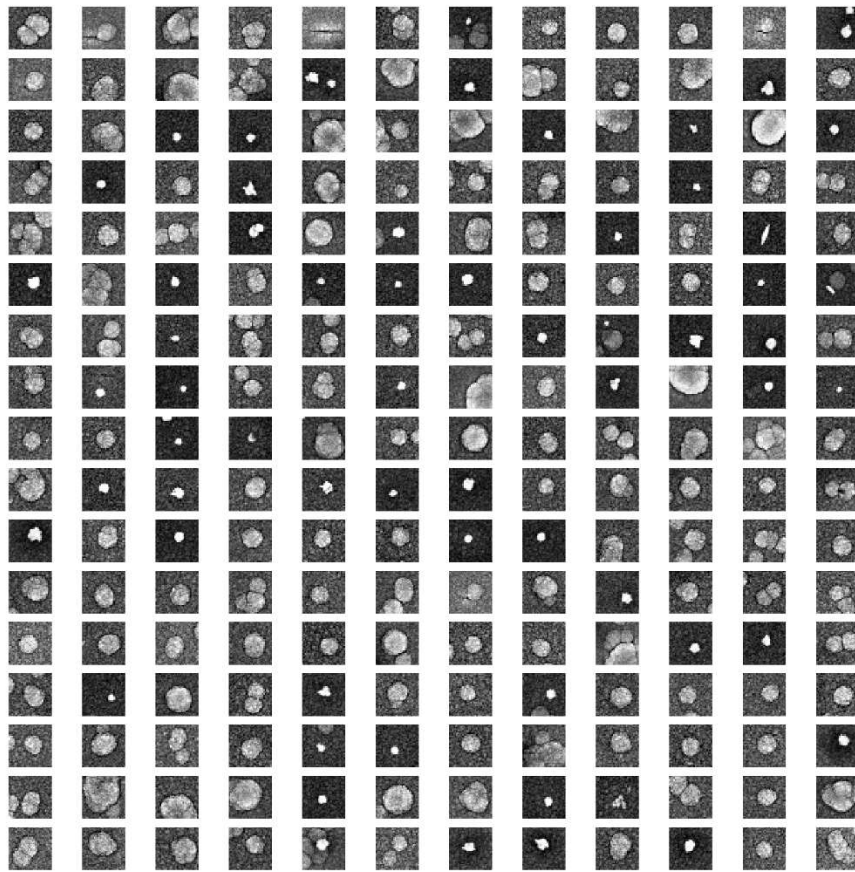
Supplementary file 7_template_matching_clustering.py: This routine first localizes the NPs on the LM-SEM image of the whole droplet. Then, it determines the position of each NP on the closest HM-SEM image and crops the image (30×30 pixels) around the determined position. Finally, the crops are flattened into a 1D array and used as data set for principal component analysis (PCA) followed by clustering. Several clustering methods were benchmarked against the classification made for a few NPs considering their Ni/O ratio determined by EDX. The best

accuracy was obtained using the following method: PCA (2 components) + agglomerative clustering (Ward, 4 clusters). Increasing the number of components for the PCA did not improve the accuracy.

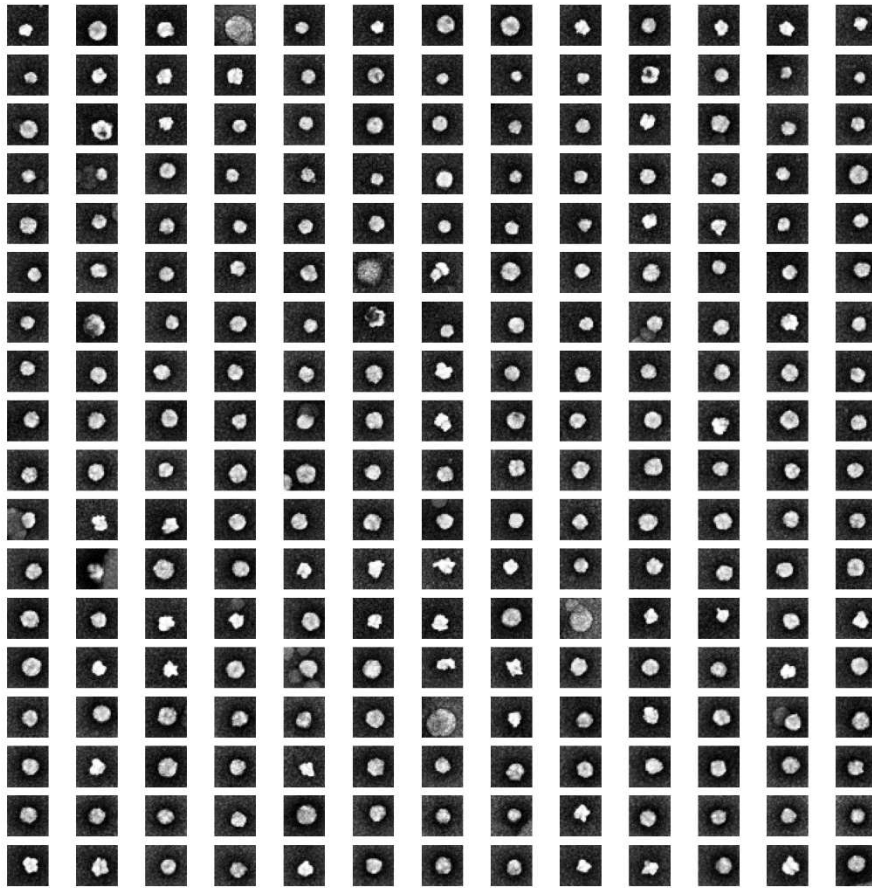
a



b



c



d

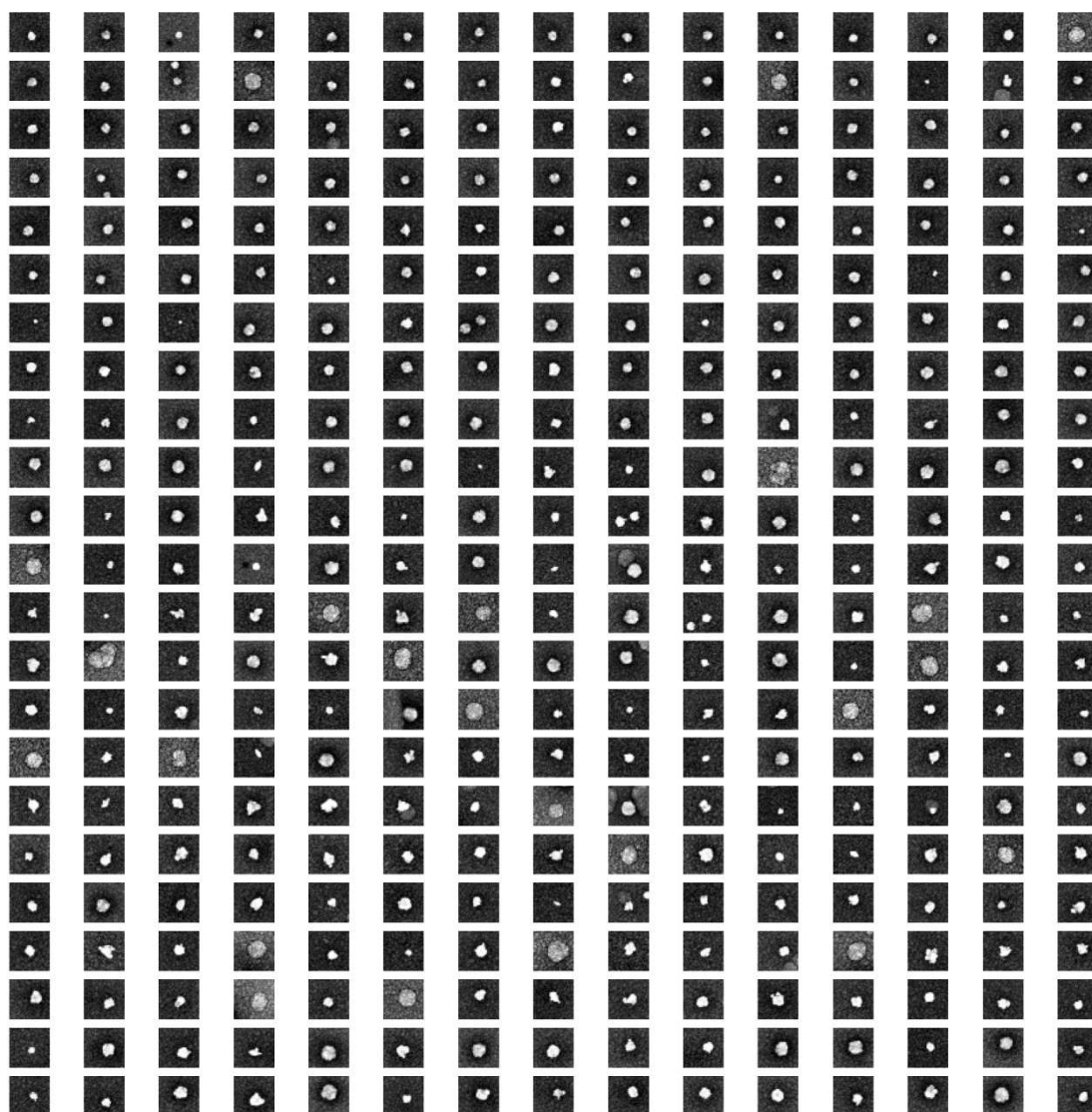


Figure M-7. Cropped SEM images of all analysed NPs divided into their respective clusters: (a) cluster 0 (large Ni NPs), (b) cluster 1 (ITO-based NPs), (c) cluster 2 (small Ni NPs), (d) cluster 3 (Ni(OH)₂ NPs).

M.4.3 EXTRACTION OF HYDROXIDE SHELL SIZE (**CHAPTER 4**)

Once the NPs are localized in the green channel, the blue channel – which is more sensitive to the hydroxide shells – the blue channel is used to monitor quantitatively their optical footprint. From the centroid coordinates obtained from the localization step, a 20×20-pixel region is selected around each NP. The first neighbour distance is evaluated to exclude NPs too close to each other in order to avoid overlaps of two or more hydroxide footprints. To count the number of pixels associated with the hydroxide footprint, a threshold masking is applied. The threshold value is selected considering a deviation from the average background

intensity of 1.5σ . The Python function used to extract the hydroxide shell's size is openly available here: <http://doi.org/10.5281/zenodo.7948233>.

M.5 INFLUENCE OF NP GEOMETRY ON THE FLUX

The aspect ratio h/r of the NP influences the steady-state current i_{ss} through the pre-factor k_{curr} .^[296]

$$i_{ss} = k_{curr} F C D r. \quad (M-6)$$

The pre-factor f for the growth rate (see Equation 3-5) is related to k_{curr} via the following equation:

$$f = \frac{k_{curr}}{3V_{cor}}, \quad (M-7)$$

where $V_{cor} = \frac{\pi h}{6r} \left(3 + \left(\frac{h}{r} \right)^2 \right)$ is the correction factor for the volume V of the NP:

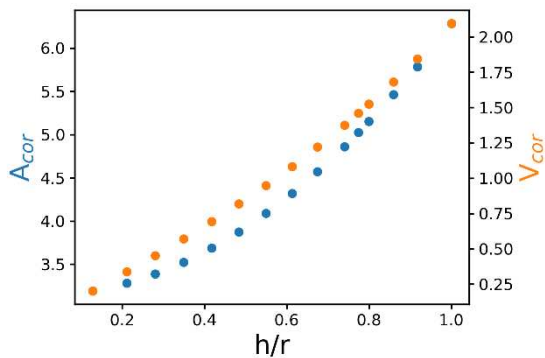
$$V = V_{cor} r^3. \quad (M-8)$$

Similarly, the surface area A of the NP can be expressed as follows:

$$A = A_{cor} r^2, \quad (M-9)$$

with $A_{cor} = \pi \left(1 + \left(\frac{h}{r} \right)^2 \right)$ the corresponding correction factor.

a



b

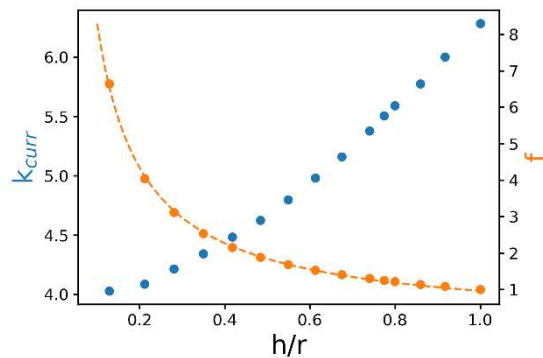


Figure M-8. (a) Surface area (left) and volume (right) correction factor as a function of the aspect ratio. (b) Steady-state current (left) and growth rate (right) pre-factor as a function of the aspect ratio. The dashed line's equation is $y = 0.96x^{-0.93}$, $r^2 = 0.9993$.

APPENDIX 1 ADDITIONAL INFORMATION ABOUT THE COMSOL SIMULATIONS

A1.1 INFLUENCE OF THE LIMIT OF DETECTION OF THE HALO

Table A1-1. Adjusted value of k° (1st cycle) for different values of lod (Ni NP, $r_{NP} = 198 \text{ nm}$, $k_p = 5.1 \cdot 10^{-4} \text{ m}^7 \text{ mol}^{-2} \text{ s}^{-1}$, $K_{sp} = 5.48 \cdot 10^{-16} \text{ M}^3$).

lod (nm)	k° (cm s^{-1})
1	$0.5 \cdot 10^{-7}$
5	$1.3 \cdot 10^{-7}$
10	$2.3 \cdot 10^{-7}$

Table A1-2. Ratios between plateaus for a variable value of k° , and a constant value of k° using different values of lod (Ni NP, $r_{NP} = 198 \text{ nm}$, $k_p = 5.1 \cdot 10^{-4} \text{ m}^7 \text{ mol}^{-2} \text{ s}^{-1}$, $K_{sp} = 5.48 \cdot 10^{-16} \text{ M}^3$).

k° (cm s^{-1})	lod (nm)	P2/P1	P3/P2	P3/P1
$k^\circ_1 = k^\circ_2 = k^\circ_3 = 1.3 \cdot 10^{-7}$	1	1.38	1.21	1.67
$k^\circ_1 = k^\circ_2 = k^\circ_3 = 1.3 \cdot 10^{-7}$	2	1.40	1.20	1.69
$k^\circ_1 = k^\circ_2 = k^\circ_3 = 1.3 \cdot 10^{-7}$	5	1.39	1.21	1.69
$k^\circ_1 = 1.3 \cdot 10^{-7}$, $k^\circ_2 = 2.0 \cdot 10^{-7}$, $k^\circ_3 = 2.0 \cdot 10^{-7}$ *	5	1.78	1.30	2.31

*Best fit of the experimental transient presented in Figure 4-3c.

A1.2 APPROXIMATE ANALYTICAL SOLUTION

To get a rough idea of the system's behaviour, the equations are solved analytically assuming that all processes operate under steady state conditions and that the consumption of HO^- and

Ni^{2+} through the precipitation of $Ni(OH)_2$ is slow compared to mass transfer. In this case, Fick's law for HO^- reduces to:

$$D_{HO^-} \left(\frac{d^2 c_{HO^-}}{dr^2} + \frac{2}{r} \frac{dc_{HO^-}}{dr} \right) = 0, \quad (A1-1)$$

where r represents the radial coordinate taking its origin at the center of the NP, and D_{HO^-} the diffusion coefficient of HO^- . This equation is equivalent to $\frac{d^2 (rc_{HO^-})}{dr^2} = 0$, which solves as:

$$c_{HO^-} = A + \frac{B}{r}, \quad (A1-2)$$

where A and B are constants to be determined from the boundary conditions. At the NP surface ($r = r_{NP}$), we have:

$$-D_{HO^-} \frac{dc_{HO^-}}{dr} \Big|_{r=r_{NP}} = k^o c_{H_2O} \exp(-\xi) = \frac{B}{r_{NP}^2}, \quad (A1-3)$$

where $c_{H_2O} = 1 \text{ mol L}^{-1}$ and $\xi = \frac{\alpha F}{RT} (E_{app}(t) - E^o)$. Hence, $B = \frac{r_{NP}^2 k^o c_{H_2O} \exp(-\xi)}{D_{HO^-}}$. Far away from the NP, $c_{HO^-} \xrightarrow{r \rightarrow \infty} 0$ so that $A = 0$. In the end,

$$c_{HO^-} = \frac{k^o c_{H_2O} \exp(-\xi) r_{NP}^2}{D_{HO^-} r}. \quad (A1-4)$$

The growth rate of the thickness of the $Ni(OH)_2$ layer, $\frac{de_{Ni(OH)_2}}{dt}$, at a given distance r then writes:

$$\begin{aligned} \frac{de_{Ni(OH)_2}}{dt} &\approx \frac{M_{Ni(OH)_2}}{\rho_{Ni(OH)_2}} k_p c_{Ni^{2+}} c_{HO^-}^2 \\ &= \frac{M_{Ni(OH)_2}}{\rho_{Ni(OH)_2}} k_p k^{o2} \left(\frac{r_{NP}^2}{r} \right)^2 c_{Ni^{2+}} \left(\frac{c_{H_2O}}{D_{HO^-}} \right)^2 \exp(-2\xi), \end{aligned} \quad (A1-5)$$

with $M_{Ni(OH)_2}$ and $\rho_{Ni(OH)_2}$ respectively the molar mass and density of the $Ni(OH)_2$ precipitate.

Hence,

$$e_{Ni(OH)_2} = \frac{M_{Ni(OH)_2}}{\rho_{Ni(OH)_2}} k_p k^{o2} \left(\frac{r_{NP}^2}{r} \right)^2 c_{Ni^{2+}} \left(\frac{c_{H_2O}}{D_{HO^-}} \right)^2 \int \exp(-2\xi) dt, \quad (A1-6)$$

which implies that for the Ni(OH)₂ layer to keep a constant thickness (equal to the optical limit of detection i.e., 5 nm based on AFM-SEM-optical correlated images, see Figure 4-4) at the edge, one condition is that $k_p k^{\circ 2}$ must remain constant. Another one is that r_{NP}^2/r must remain constant, meaning that the radius of the Ni(OH)₂ halo is proportional to the square of the NP's radius. The first condition is verified by the simulations below, the second one also experimentally in Figure 4-6.

A1.3 RELATIONSHIP BETWEEN k_p AND k°

To investigate the relationship between k_p and k° , k_p was fixed at different values and k° was adjusted so the simulation of the first CV cycle would match the experimental transient presented in Figure 4-3c. From the log-log plot presented in Figure A1-1, it appears that both parameters are interdependent and follow a power law, the exponent matching the stoichiometry of the precipitation reaction:

$$k^{\circ} = 10^{-10.5} k_p^{-0.5}. \quad (\text{A1-7})$$

This means that independently on the chosen value of k_p , the trends in k° will always be identical if $k^{\circ} k_p^{1/2}$ is kept constant, which is in agreement with the condition derived analytically (see above).

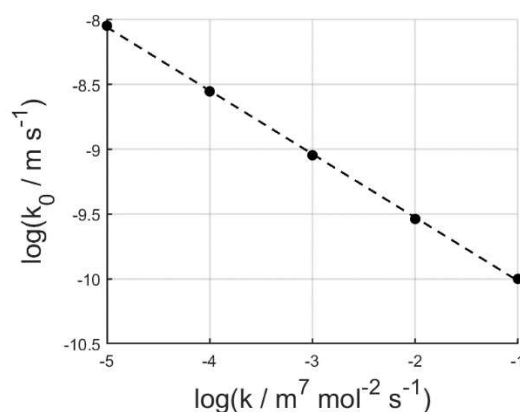


Figure A1-1. Relationship between k_p and k° for $K_{sp} = 5.48 \cdot 10^{-16} \text{ M}^3$ ($k^{\circ} = 10^{-10.5} k_p^{-0.5}$, $r^2 = 0.999$). For each value of k_p , k° is adjusted so the simulation of the first CV cycle would match the experimental transient of the Ni NP presented in Figure 4-3c ($r_{NP} = 198 \text{ nm}$).

A1.4 DISSOLUTION OF THE $\text{Mg}(\text{OH})_2$ HALOS: DETERMINATION OF k_p

To determine the true value of k_p , the dissolution of the $\text{Mg}(\text{OH})_2$ halos in the same electrolyte was also investigated. This experiment was performed on another sample (sample presented in Figure 4-7b) since rinsing the NPs for SEM analysis removed most of the $\text{Mg}(\text{OH})_2$ layer. As the electrochemical reaction is not involved in this process, the model now only depends upon k_p . This makes it possible to determine the true value of k_p . To allow for the dissolution of the precipitate, the rates of reaction were modified as follows:

$$R_{s,\text{Mg}^{2+}} = k_p(c_{\text{Mg}^{2+}}c_{\text{HO}^-}^2 - H(\xi) - K_{sp}) \quad (\text{A1-8a})$$

$$R_{s,\text{HO}^-} = 2k_p(c_{\text{Mg}^{2+}}c_{\text{HO}^-}^2 - H(\xi) - K_{sp}) \quad (\text{A1-8b})$$

Interestingly, these modifications do not affect the simulations of the CVs as the electrochemical reaction induces a rapid increase of HO^- concentration, quickly reaching the saturation of the hydroxide.

k_p was then adjusted so that r_{halo} reaches 81% of its initial value (after the three CV cycles) after 2265 s of dissolution (Table A1-4) in agreement with the average evolution of r_{halo} measured for several NPs (Figure A1-2 and Table A1-3).

An estimate of k_p for the precipitation of $\text{Ni}(\text{OH})_2$ was obtained considering that the dissolution rate constant of $\text{Ni}(\text{OH})_2$ is 2 orders of magnitude slower than that of $\text{Mg}(\text{OH})_2$.^[341]

$$k_{\text{Ni}(\text{OH})_2}K_{sp,\text{Ni}(\text{OH})_2} = 10^{-2}k_{\text{Mg}(\text{OH})_2}K_{sp,\text{Mg}(\text{OH})_2}. \quad (\text{A1-9})$$

Such time scales (several days) for studying the dissolution kinetics of $\text{Ni}(\text{OH})_2$ are hardly accessible with our current experimental setup.

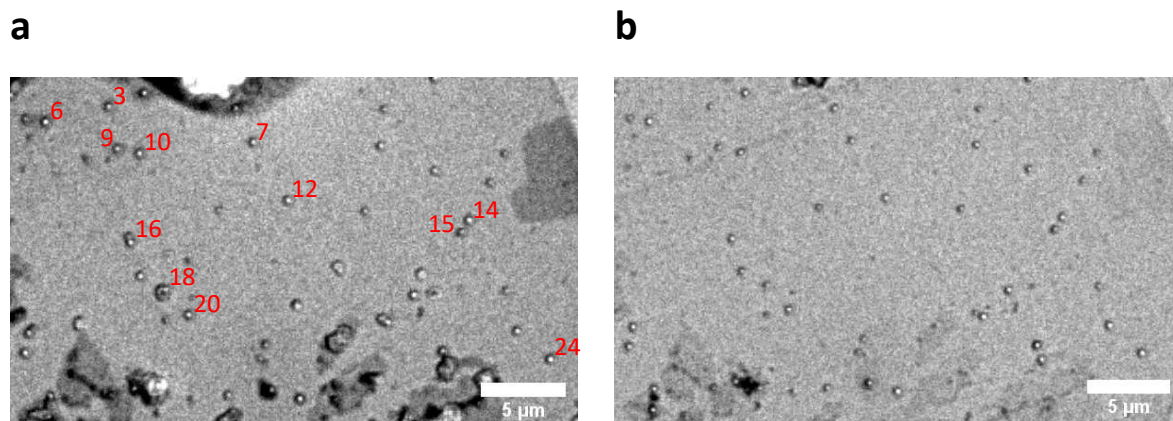


Figure A1-2. Optical images of Pt NPs cycled in MgCl_2 before (a) and after (b) dissolution in the same electrolyte (sample presented in Figure 4-7b).

Table A1-3. r_{halo} before and after dissolution of the NPs highlighted in Figure A1-2.

NP	r_{halo} before (nm)	r_{halo} after (nm)	Ratio (%)
6	370	246	67
3	272	178	65
9	271	196	73
10	263	232	88
16	315	224	71
18	372	191	51
20	258	242	94
7	217	201	93
12	217	196	90
24	276	261	95
14	250	224	89
15	263	260	99
Average			81

Table A1-4. Simulation of the $\text{Mg}(\text{OH})_2$ halo's dissolution for several Pt NPs cycled in MgCl_2 ($K_{sp} = 5.61 \cdot 10^{-12} \text{ M}^3$). The orange dot corresponds to 81% of the initial value of r_{halo} (after the three CV cycles) at 2265 s.

NP	r_{NP} (nm)	k_p ($10^{-6} \text{ m}^7 \text{ mol}^{-2} \text{ s}^{-1}$)	Result
----	---------------	---	--------

16	127	5.0	
10, 14	142	4.9	
8	154	5.1	
Average		5.0	

A1.5 INFLUENCE OF THE NUCLEATION DELAY

The delay introduced by the fact that the NPs nucleate after the onset of water reduction during the first CV cycle can be taken into account by introducing a condition in Equation 4-6:

$$J_{0,CHO^-} = k_0 * 1[mol L^{-1}] * \exp\left(-\frac{\alpha F}{RT}(E_{app} - E^\circ)\right) * (E_{app} \leq E_{nucl}). \quad (A1-10)$$

As shown in Figure A1-3, the influence of the nucleation delay is negligible.

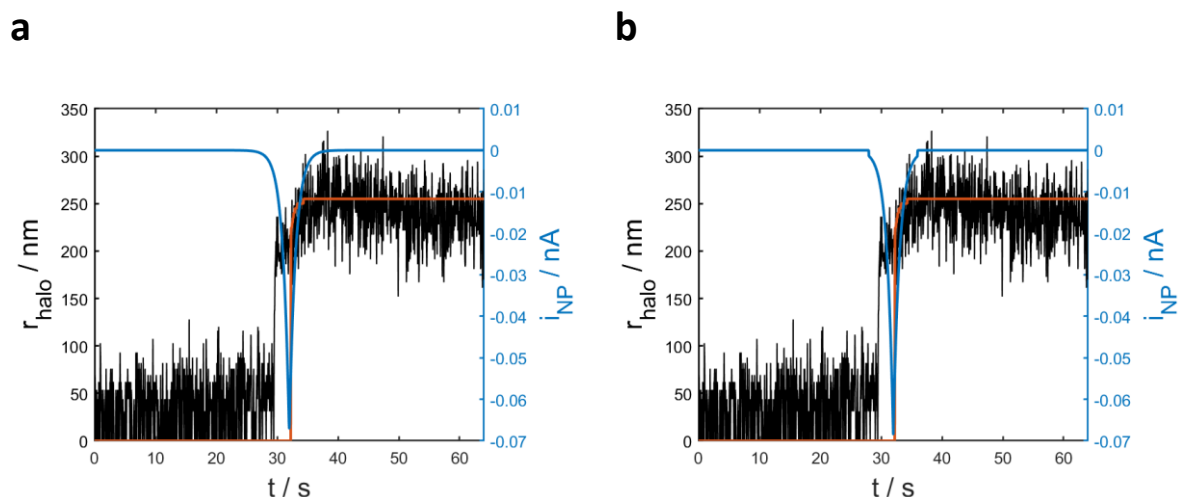
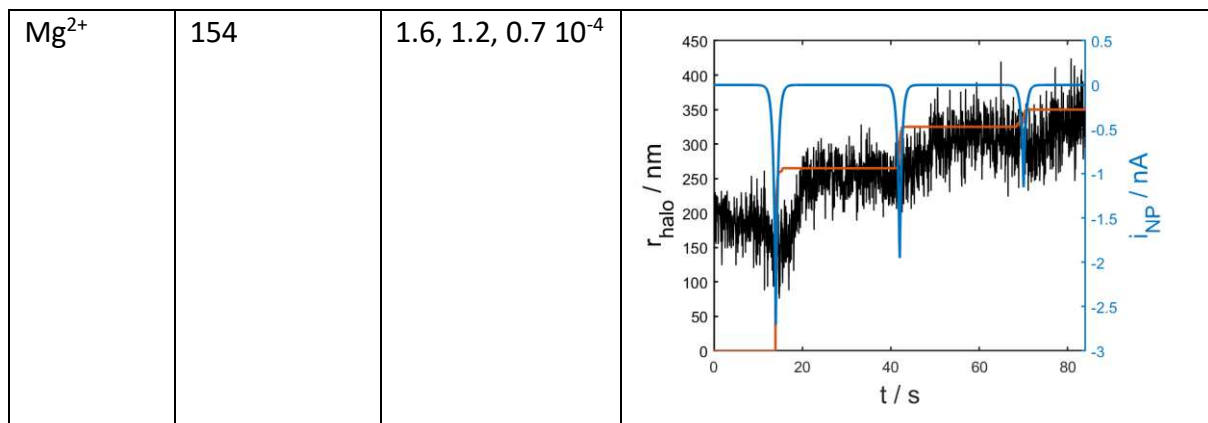


Figure A1-3. Experimental (black) and simulated evolution of r_{halo} (orange) during the first CV cycle (a) without a nucleation delay ($E_{nucl} = 0 V$) and (b) with a nucleation delay ($E_{nucl} = -1.4 V$). Ni NP, $r_{NP} = 198 nm$, $k_p = 5.1 \cdot 10^{-4} m^7 mol^{-2} s^{-1}$, $K_{sp} = 5.48 \cdot 10^{-16} M^3$, $k^\circ = 1.3 \cdot 10^{-7} cm s^{-1}$. The blue lines represent the simulated current flowing through the NP in each case.

A1.6 EXAMPLES OF PT NPs CYCLED IN Ni^{2+} AND Mg^{2+}

Table A1-5. Full simulation of Pt NPs cycled in $NiCl_2$ ($k_p = 5.1 \cdot 10^{-4} m^7 mol^{-2} s^{-1}$, $K_{sp} = 5.48 \cdot 10^{-16} mol^3 L^{-9}$) and $MgCl_2$ ($k_p = 5.1 \cdot 10^{-6} m^7 mol^{-2} s^{-1}$, $K_{sp} = 5.61 \cdot 10^{-12} mol^3 L^{-9}$).

M^{2+}	$r_{NP} (nm)$	k_1° , k_2° , $k_3^\circ (cm s^{-1})$	Result
Ni^{2+}	243	$5.8, 6.1, 6.6 \cdot 10^{-6}$	



APPENDIX 2 OPTICAL MODELS

A2.1 SINGLE-COMPONENT FILM

In the case of normal incidence, the absolute reflectivity, R_{abs} , of an electromagnetic wave propagating in an ambient medium A (of refractive index n_A) and reflecting on a substrate S (of refractive index n_S) is the square of the modulus of the reflection coefficient, r_{AS} , given by Fresnel's equation:

$$R_{abs} = |r_{AS}|^2 = \left| \frac{n_A - n_S}{n_A + n_S} \right|^2. \quad (A2-1)$$

When a homogeneous thin film of thickness δ and refractive index n_F is intercalated between the ambient and the substrate (for instance, a MnO_2 film), R_{abs} can be expressed as follows:

$$R_{abs} = \left| \frac{r_{AF} + r_{FS} \exp\left(2i\frac{2\pi}{\lambda}n_F\delta\right)}{1 + r_{AF}r_{FS} \exp\left(2i\frac{2\pi}{\lambda}n_F\delta\right)} \right|^2, \quad (A2-2)$$

where λ is the wavelength of the incident light and r_{AF} and r_{FS} the reflection coefficients of the ambient|thin film and thin film|substrate interfaces, respectively.

If the intensity of the incident light remains constant throughout the experiment, the variations of the intensity of the reflected light, I_{refl} , can be compared to its initial value. The relative reflectivity, $R = 1 + \frac{\Delta R_{abs}}{R_{abs}}$, is then linked to I_{refl} via the following equation:

$$R = \frac{I_{refl}(t)}{I_{refl}(0)}. \quad (A2-3)$$

Figure A2-1 illustrates the dependence of R with δ for the Au|MnO₂|water and Au|ZHS|water systems. The dependence is almost linear until approximately 20 nm for MnO₂ and 30 nm for ZHS. A 1% variation of R corresponds to a thickness variation of 0.3 nm and 0.9 nm for MnO₂ and ZHS, respectively, making this technique extremely sensitive.

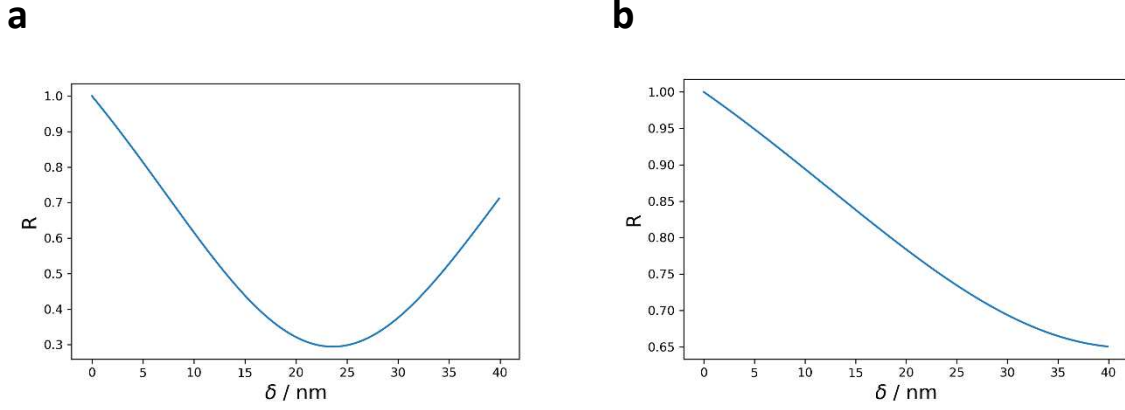


Figure A2-1. Variation of the reflectivity with the thickness of **a** MnO₂ and **b** ZHS film ($\lambda = 490 \text{ nm}$, $n_{\text{water}} = 1.33$, $n_{\text{MnO}_2} = 2.4 + 0.01j$,^[452–454] $n_{\text{ZHS}} = 1.7$, $n_{\text{Au}} = 1.10 + 1.84j$).^[254]

A2.2 TWO-COMPONENT FILM

The optical model for a mixed layer of two compounds (hereafter denoted as 1 and 2) is based on the equations presented in section A2.1 for a single-component layer. The goal here is to determine the equivalent refractive index of the mixed layer, n_{eq} , before injecting it into Equation A2-2 to calculate the reflectivity of the substrate.

The molar refractivity of the mixed layer, $R_{m,eq}$, is assumed to be an additive constitutive property of a material; it is given by the following equation:

$$R_{m,eq} = x_1 R_{m,1} + x_2 R_{m,2}, \quad (\text{A2-4})$$

where x_i and $R_{m,i}$ represent the molar fraction and the molar refractivity of compound i , respectively. Similarly, the molar volume of the mixed layer, $V_{m,eq}$, is given by the following equation:

$$V_{m,eq} = x_1 V_{m,1} + x_2 V_{m,2}. \quad (\text{A2-5})$$

$R_{m,i}$ is related to $V_{m,i}$ via the Lorentz-Lorenz equation:

$$R_{m,i} = \frac{n_i^2 - 1}{n_i^2 + 2} V_{m,i}. \quad (\text{A2-6})$$

If we pose $X_i = \frac{n_i^2 - 1}{n_i^2 + 2}$ in Equation A2-6 and inject the latter into Equation A2-4, we find:

$$X_{eq} = \frac{x_1 V_{m,1}}{V_{m,eq}} X_1 + \frac{x_2 V_{m,2}}{V_{m,eq}} X_2. \quad (\text{A2-7})$$

If we pose $Y = \frac{x_2 V_{m,2}}{x_1 V_{m,1}}$, Equation A2-7 becomes:

$$X_{eq} = \frac{X_1 + Y X_2}{1 + Y}, \quad (\text{A2-8})$$

from which we can extract n_{eq}^2 as follows:

$$n_{eq}^2 = n_1^2 \frac{1 + Y \frac{n_2^2 (n_1^2 + 2)}{n_1^2 (n_2^2 + 2)}}{1 + Y \left(\frac{n_1^2 + 2}{n_2^2 + 2} \right)}. \quad (\text{A2-9})$$

One can notice that Y is simply the ratio of the equivalent thicknesses of each component. Figure 5-7a presents the results obtained for mixed layers of MnO_2 and ZHS with the refractive indices given in the caption of Figure A2-1.

REFERENCES

- [1] L. A. Baker, *J Am Chem Soc* **2018**, *140*, 15549–15559.
- [2] R. Pandya, L. Valzania, F. Dorchies, F. Xia, J. M. Hugh, A. Mathieson, J. H. Tan, T. G. Parton, M. De Volder, J.-M. Tarascon, S. Gigan, H. B. de Aguiar, A. Grimaud, **2022**.
- [3] S. Redor, L. Godeffroy, G. Rouse, A. M. Abakumov, B. Li, F. Kanoufi, J.-M. Tarascon, *J Am Chem Soc* **2023**, *145*, 12823–12836.
- [4] Core Writing Team, in *Climate Change 2023: Synthesis Report. A Report of the Intergovernmental Panel on Climate Change. Contribution of Working Groups I, II and III to the Sixth Assessment Report of the Intergovernmental Panel on Climate Change* (Eds.: H. Lee, J. Romero), IPCC, Geneva, **n.d.**
- [5] *Council of the European Union* **2023**.
- [6] “éCO2mix - La consommation d’électricité en France,” can be found under <https://www.rte-france.com/eco2mix/la-consommation-deelectricite-en-france>, **2023**.
- [7] *Gouvernement* **2023**.
- [8] S. Read, *The World Economic Forum* **2022**.
- [9] *European Parliament* **2023**.
- [10] *McKinsey & Company* **2023**.
- [11] S. Ray, *Forbes* **2021**.
- [12] A. M. Desaulty, D. Monfort Climent, G. Lefebvre, A. Cristiano-Tassi, D. Peralta, S. Perret, A. Urban, C. Guerrot, *Nat Commun* **2022**, *13*, 1–10.
- [13] A. R. Akbashev, *ACS Catal* **2022**, *12*, 4296–4301.
- [14] E. Ventosa, *Curr Opin Electrochem* **2021**, *25*, 100635.
- [15] X. Xiao, A. J. Bard, *J Am Chem Soc* **2007**, *129*, 9610–9612.

- [16] Y. G. Zhou, N. V. Rees, R. G. Compton, *Angewandte Chemie International Edition* **2011**, *50*, 4219–4221.
- [17] Y. Y. Peng, R. C. Qian, M. E. Hafez, Y. T. Long, *ChemElectroChem* **2017**, *4*, 977–985.
- [18] K. J. Stevenson, K. Tschulik, *Curr Opin Electrochem* **2017**, *6*, 38–45.
- [19] J. E. Dick, C. Renault, A. J. Bard, *J Am Chem Soc* **2015**, *137*, 8376–8379.
- [20] Y. Xiao, F. R. F. Fan, J. Zhou, A. J. Bard, *J Am Chem Soc* **2008**, *130*, 16669–16677.
- [21] Z. Guo, S. J. Percival, B. Zhang, *J Am Chem Soc* **2014**, *136*, 8879–8882.
- [22] X. Xiao, S. Pan, J. S. Jang, F. R. F. Fan, A. J. Bard, *Journal of Physical Chemistry C* **2009**, *113*, 14978–14982.
- [23] S. J. Kwon, F. R. F. Fan, A. J. Bard, *J Am Chem Soc* **2010**, *132*, 13165–13167.
- [24] H. Zhou, F. R. F. Fan, A. J. Bard, *Journal of Physical Chemistry Letters* **2010**, *1*, 2671–2674.
- [25] R. A. Thearle, Z. Sofer, D. Bouša, M. Pumera, *ChemPhysChem* **2016**, *17*, 2096–2099.
- [26] X. Li, C. Batchelor-Mcauley, S. A. I. Whitby, K. Tschulik, L. Shao, R. G. Compton, *Angewandte Chemie International Edition* **2016**, *55*, 4296–4299.
- [27] D. A. Robinson, A. M. Kondajji, A. D. Castañeda, R. Dasari, R. M. Crooks, K. J. Stevenson, *Journal of Physical Chemistry Letters* **2016**, *7*, 2512–2517.
- [28] S. E. F. Kleijn, B. Serrano-Bou, A. I. Yanson, M. T. M. Koper, *Langmuir* **2013**, *29*, 2054–2064.
- [29] J. M. Kahk, N. V. Rees, J. Pillay, R. Tshikhudo, S. Vilakazi, R. G. Compton, *Nano Today* **2012**, *7*, 174–179.
- [30] X. Jiao, C. Lin, N. P. Young, C. Batchelor-McAuley, R. G. Compton, *Journal of Physical Chemistry C* **2016**, *120*, 13148–13158.
- [31] S. J. Percival, B. Zhang, *Journal of Physical Chemistry C* **2016**, *120*, 20536–20546.

- [32] S. E. F. Kleijn, S. C. S. Lai, T. S. Miller, A. I. Yanson, M. T. M. Koper, P. R. Unwin, *J Am Chem Soc* **2012**, *134*, 18558–18561.
- [33] A. El Arrassi, Z. Liu, M. V. Evers, N. Blanc, G. Bendt, S. Saddeler, D. Tetzlaff, D. Pohl, C. Damm, S. Schulz, K. Tschulik, *J Am Chem Soc* **2019**, *141*, 9197–9201.
- [34] Z. Liu, H. M. A. Amin, Y. Peng, M. Corva, R. Pentcheva, K. Tschulik, Z. Liu, H. M. A. Amin, M. Corva, K. Tschulik, Y. Peng, R. Pentcheva, *Adv Funct Mater* **2023**, *33*, 2210945.
- [35] Z. Liu, M. Corva, H. M. A. Amin, N. Blanc, J. Linnemann, K. Tschulik, *Int J Mol Sci* **2021**, *22*, 13137.
- [36] M. E. Hafez, H. Ma, W. Ma, Y.-T. Long, *Angewandte Chemie* **2019**, *131*, 6393–6398.
- [37] M. Chen, S. M. Lu, Y. Y. Peng, Z. Ding, Y. T. Long, *Chemistry – A European Journal* **2021**, *27*, 11799–11803.
- [38] L. J. Zhao, R. C. Qian, W. Ma, H. Tian, Y. T. Long, *Anal Chem* **2016**, *88*, 8375–8379.
- [39] F. T. Patrice, K. Qiu, L. J. Zhao, E. Kouadio Fodjo, D. W. Li, Y. T. Long, *ACS Appl Nano Mater* **2018**, *1*, 2069–2075.
- [40] Y. Y. Peng, D. Guo, W. Ma, Y. T. Long, *ChemElectroChem* **2018**, *5*, 2982–2985.
- [41] P. A. Defnet, T. J. Anderson, B. Zhang, *Curr Opin Electrochem* **2020**, *22*, 129–135.
- [42] G. Zampardi, C. Batchelor-McAuley, E. Kätelhön, R. G. Compton, *Angewandte Chemie International Edition* **2017**, *56*, 641–644.
- [43] G. Zampardi, S. V. Sokolov, C. Batchelor-McAuley, R. G. Compton, *Chemistry – A European Journal* **2017**, *23*, 14338–14344.
- [44] S. Rano, C. Laberty-Robert, K. Ngo, C. M. Sánchez-Sánchez, V. Vivier, *Physical Chemistry Chemical Physics* **2019**, *21*, 5416–5423.
- [45] W. Xu, Y. Zhou, X. Ji, *Journal of Physical Chemistry Letters* **2018**, *9*, 4976–4980.
- [46] T. Löffler, J. Clausmeyer, P. Wilde, K. Tschulik, W. Schuhmann, E. Ventosa, *Nano Energy* **2019**, *57*, 827–834.

- [47] W. Xu, X. Gao, Y. Zhou, G. Zou, H. Hou, X. Ji, *Electrochem commun* **2021**, *125*, 107000.
- [48] M. V. Evers, M. Bernal, B. Roldan Cuenya, K. Tschulik, *Angewandte Chemie International Edition* **2019**, *58*, 8221–8225.
- [49] M. W. Glasscott, A. D. Pendergast, S. Goines, A. R. Bishop, A. T. Hoang, C. Renault, J. E. Dick, *Nat Commun* **2019**, *10*, 1–8.
- [50] R. Pandya, F. Dorchies, D. Romanin, S. Gigan, A. W. Chin, H. B. de Aguiar, A. Grimaud, **2022**.
- [51] M. M. Vieira, J. F. Lemineur, J. Médard, C. Combellas, F. Kanoufi, J. M. Noël, *Journal of Physical Chemistry Letters* **2022**, *13*, 5468–5473.
- [52] X. Jiao, C. Batchelor-Mcauley, C. Lin, E. Kätelhön, E. E. L. Tanner, N. P. Young, R. G. Compton, *ACS Catal* **2018**, *8*, 6192–6202.
- [53] X. Jiao, C. Batchelor-McAuley, N. P. Young, R. G. Compton, *Physical Chemistry Chemical Physics* **2018**, *20*, 23847–23850.
- [54] W. Yu, C. Batchelor-Mcauley, X. Chang, N. P. Young, R. G. Compton, *Physical Chemistry Chemical Physics* **2019**, *21*, 20415–20421.
- [55] Xue Jiao, S. V. Sokolov, E. E. L. Tanner, N. P. Young, R. G. Compton, *Physical Chemistry Chemical Physics* **2016**, *19*, 64–68.
- [56] M. Azimzadeh Sani, N. G. Pavlopoulos, S. Pezzotti, A. Serva, P. Cignoni, J. Linnemann, M. Salanne, M. P. Gaigeot, K. Tschulik, *Angewandte Chemie International Edition* **2022**, *61*, e202112679.
- [57] N. Kostopoulos, M. M. Vieira, L. Godeffroy, J. Médard, C. Combellas, J. F. Lemineur, F. Kanoufi, J. M. Noël, *ChemElectroChem* **2022**, *9*, e202200582.
- [58] C. S. Lim, S. M. Tan, Z. Sofer, M. Pumera, *ACS Nano* **2015**, *9*, 8474–8483.
- [59] S. V. Sokolov, Shaltiel Eloul, Enno Kätelhön, Christopher Batchelor-McAuley, R. G. Compton, *Physical Chemistry Chemical Physics* **2016**, *19*, 28–43.
- [60] J. Wang, X. Sun, *Energy Environ Sci* **2015**, *8*, 1110–1138.

- [61] R. Khan, D. Andreescu, M. H. Hassan, J. Ye, S. Andreescu, *Angewandte Chemie International Edition* **2022**, *61*, e202209164.
- [62] P. A. Defnet, C. Han, B. Zhang, *Anal Chem* **2019**, *91*, 4023–4030.
- [63] L. Sun, D. Jiang, M. Li, T. Liu, L. Yuan, W. Wang, H. Y. Chen, *Anal Chem* **2017**, *89*, 6050–6055.
- [64] S. M. Lu, M. Chen, H. Wen, H. W. Wang, Z. Yu, Y. T. Long, *Chinese Journal of Catalysis* **2022**, *43*, 2815–2819.
- [65] T. Sun, D. Wang, M. V. Mirkin, H. Cheng, J. C. Zheng, R. M. Richards, F. Lin, H. L. Xin, *Proc Natl Acad Sci U S A* **2019**, *116*, 11618–11623.
- [66] J. T. Mefford, A. R. Akbashev, M. Kang, C. L. Bentley, W. E. Gent, H. D. Deng, D. H. Alsem, Y. S. Yu, N. J. Salmon, D. A. Shapiro, P. R. Unwin, W. C. Chueh, *Nature* **2021**, *593*, 67–73.
- [67] M. Kang, D. Perry, C. L. Bentley, G. West, A. Page, P. R. Unwin, *ACS Nano* **2017**, *11*, 9525–9535.
- [68] D. Momotenko, K. McKelvey, M. Kang, G. N. Meloni, P. R. Unwin, *Anal Chem* **2016**, *88*, 2838–2846.
- [69] E. Ventosa, W. Schuhmann, *Physical Chemistry Chemical Physics* **2015**, *17*, 28441–28450.
- [70] A. Kumatani, T. Matsue, *Curr Opin Electrochem* **2020**, *22*, 228–233.
- [71] S. Daboss, F. Rahmanian, H. S. Stein, C. Kranz, *Electrochemical Science Advances* **2022**, *2*, e2100122.
- [72] L. Danis, S. M. Gateman, C. Kuss, S. B. Schougaard, J. Mauzeroll, *ChemElectroChem* **2017**, *4*, 6–19.
- [73] Z. J. Barton, J. Rodríguez-López, *Anal Chem* **2014**, *86*, 10660–10667.
- [74] J. Hui, M. Burgess, J. Zhang, J. Rodríguez-López, *ACS Nano* **2016**, *10*, 4248–4257.

- [75] Y. Zeng, Z. T. Gossage, D. Sarbapalli, J. Hui, J. Rodríguez-López, *ChemElectroChem* **2022**, *9*, e202101445.
- [76] Y. Takahashi, A. Kumatani, H. Munakata, H. Inomata, K. Ito, K. Ino, H. Shiku, P. R. Unwin, Y. E. Korchev, K. Kanamura, T. Matsue, *Nat Commun* **2014**, *5*, 1–7.
- [77] B. Tao, I. J. McPherson, E. Daviddi, C. L. Bentley, P. R. Unwin, *ACS Sustain Chem Eng* **2023**, *11*, 1459–1471.
- [78] X. Shi, W. Qing, T. Marhaba, W. Zhang, *Electrochim Acta* **2020**, *332*, 135472.
- [79] K. Mahankali, N. K. Thangavel, L. M. Reddy Arava, *Nano Lett* **2019**, *19*, 5229–5236.
- [80] N. K. Thangavel, K. Mahankali, L. M. R. Arava, *J Electrochem Soc* **2022**, *169*, 060501.
- [81] Y. Takahashi, T. Yamashita, D. Takamatsu, A. Kumatani, T. Fukuma, *Chemical Communications* **2020**, *56*, 9324–9327.
- [82] M. E. Snowden, M. Dayeh, N. A. Payne, S. Gervais, J. Mauzeroll, S. B. Schougaard, *J Power Sources* **2016**, *325*, 682–689.
- [83] M. Dayeh, M. R. Z. Ghavidel, J. Mauzeroll, S. B. Schougaard, *ChemElectroChem* **2019**, *6*, 195–201.
- [84] B. Tao, L. C. Yule, E. Daviddi, C. L. Bentley, P. R. Unwin, *Angewandte Chemie International Edition* **2019**, *58*, 4606–4611.
- [85] H. Inomata, Y. Takahashi, D. Takamatsu, A. Kumatani, H. Ida, H. Shiku, T. Matsue, *Chemical Communications* **2019**, *55*, 545–548.
- [86] A. L. Lipson, R. S. Ginder, M. C. Hersam, *Advanced Materials* **2011**, *23*, 5613–5617.
- [87] A. L. Lipson, K. Puntambekar, D. J. Comstock, X. Meng, M. L. Geier, J. W. Elam, M. C. Hersam, *Chemistry of Materials* **2014**, *26*, 935–940.
- [88] C. Santana Santos, B. N. Jaato, I. Sanjuán, W. Schuhmann, C. Andronescu, *Chem Rev* **2022**, DOI 10.1021/ACS.CHEMREV.2C00766/ASSET/IMAGES/LARGE/CR2C00766_0007.JPEG.

- [89] Y. Wang, S. A. Skaanvik, X. Xiong, S. Wang, M. Dong, *Matter* **2021**, *4*, 3483–3514.
- [90] Y. Liang, J. H. K. Pfisterer, D. McLaughlin, C. Csoklich, L. Seidl, A. S. Bandarenka, O. Schneider, *Small Methods* **2019**, *3*, 1800387.
- [91] T. Sun, Y. Yu, B. J. Zacher, M. V. Mirkin, *Angewandte Chemie International Edition* **2014**, *53*, 14120–14123.
- [92] J. Kim, C. Renault, N. Nioradze, N. Arroyo-Currás, K. C. Leonard, A. J. Bard, *J Am Chem Soc* **2016**, *138*, 8560–8568.
- [93] C. L. Bentley, M. Kang, P. R. Unwin, *J Am Chem Soc* **2017**, *139*, 16813–16821.
- [94] T. Sun, H. Zhang, X. Wang, J. Liu, C. Xiao, S. U. Nanayakkara, J. L. Blackburn, M. V. Mirkin, E. M. Miller, *Nanoscale Horiz* **2019**, *4*, 619–624.
- [95] M. Ju, R. Cai, J. Ren, J. Chen, L. Qi, X. Long, S. Yang, *ACS Appl Mater Interfaces* **2021**, *13*, 37063–37070.
- [96] C. Gu, T. Sun, Z. Wang, S. Jiang, Z. Wang, *Small Methods* **2023**, *7*, 2201529.
- [97] S. Jiang, T. Sun, C. Gu, Y. Ma, Z. Wang, D. Wang, Z. Wang, *Nano Res* **2023**, 1–8.
- [98] C. L. Bentley, M. Kang, F. M. Maddar, F. Li, M. Walker, J. Zhang, P. R. Unwin, *Chem Sci* **2017**, *8*, 6583–6593.
- [99] Y. Takahashi, Y. Kobayashi, Z. Wang, Y. Ito, M. Ota, H. Ida, A. Kumatani, K. Miyazawa, T. Fujita, H. Shiku, Y. E. Korchev, Y. Miyata, T. Fukuma, M. Chen, T. Matsue, *Angewandte Chemie International Edition* **2020**, *59*, 3601–3608.
- [100] C. L. Bentley, C. Andronescu, M. Smialkowski, M. Kang, T. Tarnev, B. Marler, P. R. Unwin, U. P. Apfel, W. Schuhmann, *Angewandte Chemie International Edition* **2018**, *57*, 4093–4097.
- [101] C. L. Bentley, P. R. Unwin, *Faraday Discuss* **2018**, *210*, 365–379.
- [102] R. G. Mariano, K. McKelvey, H. S. White, M. W. Kanan, *Science (1979)* **2017**, *358*, 1187–1192.

- [103] M. Choi, N. P. Siepser, S. Jeong, Y. Wang, G. Jagdale, X. Ye, L. A. Baker, *Nano Lett* **2020**, *20*, 1233–1239.
- [104] J. C. Byers, A. G. Güell, P. R. Unwin, *J Am Chem Soc* **2014**, *136*, 11252–11255.
- [105] T. Tarnev, H. B. Aiyappa, A. Botz, T. Erichsen, A. Ernst, C. Andronescu, W. Schuhmann, *Angewandte Chemie International Edition* **2019**, *58*, 14265–14269.
- [106] S. Kolagatla, P. Subramanian, A. Schechter, *Nanoscale* **2018**, *10*, 6962–6970.
- [107] S. Kolagatla, P. Subramanian, A. Schechter, *Appl Catal B* **2019**, *256*, 117843.
- [108] S. Kolagatla, P. Subramanian, A. Schechter, *ChemSusChem* **2019**, *12*, 2708–2714.
- [109] P. Wilde, T. Quast, H. B. Aiyappa, Y. T. Chen, A. Botz, T. Tarnev, M. Marquitan, S. Feldhege, A. Lindner, C. Andronescu, W. Schuhmann, *ChemElectroChem* **2018**, *5*, 3083–3088.
- [110] Y. Li, J. T. Cox, B. Zhang, *J Am Chem Soc* **2010**, *132*, 3047–3054.
- [111] Y. Yu, Y. Gao, K. Hu, P. Y. Blanchard, J. M. Noël, T. Nareshkumar, K. L. Phani, G. Friedman, Y. Gogotsi, M. V. Mirkin, *ChemElectroChem* **2015**, *2*, 58–63.
- [112] V. Brasiliense, J. Clausmeyer, A. L. Dauphin, J. M. Noël, P. Berto, G. Tessier, W. Schuhmann, F. Kanoufi, *Angewandte Chemie International Edition* **2017**, *56*, 10598–10601.
- [113] J. Zhang, W. He, T. Quast, J. R. C. Junqueira, S. Saddeler, S. Schulz, W. Schuhmann, *Angewandte Chemie International Edition* **2023**, *62*, e202214830.
- [114] J. Clausmeyer, J. Masa, E. Ventosa, D. Öhl, W. Schuhmann, *Chemical Communications* **2016**, *52*, 2408–2411.
- [115] V. Brasiliense, J. Clausmeyer, P. Berto, G. Tessier, C. Combellas, W. Schuhmann, F. Kanoufi, *Anal Chem* **2018**, *90*, 7341–7348.
- [116] K. Huang, J. Clausmeyer, L. Luo, K. Jarvis, R. M. Crooks, *Faraday Discuss* **2018**, *210*, 267–280.

- [117] K. Huang, K. Shin, G. Henkelman, R. M. Crooks, *ACS Nano* **2021**, *15*, 17926–17937.
- [118] H. B. Aiyappa, P. Wilde, T. Quast, J. Masa, C. Andronescu, Y. T. Chen, M. Muhler, R. A. Fischer, W. Schuhmann, *Angewandte Chemie International Edition* **2019**, *58*, 8927–8931.
- [119] T. Quast, H. B. Aiyappa, S. Saddeler, P. Wilde, Y. T. Chen, S. Schulz, W. Schuhmann, *Angewandte Chemie International Edition* **2021**, *60*, 3576–3580.
- [120] T. Quast, S. Varhade, S. Saddeler, Y. T. Chen, C. Andronescu, S. Schulz, W. Schuhmann, *Angewandte Chemie International Edition* **2021**, *60*, 23444–23450.
- [121] Z. T. Gossage, N. B. Schorr, K. Hernández-Burgos, J. Hui, B. H. Simpson, E. C. Montoto, J. Rodríguez-López, *Langmuir* **2017**, *33*, 9455–9463.
- [122] T. Sun, D. Wang, M. V. Mirkin, *Angewandte Chemie International Edition* **2018**, *57*, 7463–7467.
- [123] T. Sun, D. Wang, M. V. Mirkin, *Faraday Discuss* **2018**, *210*, 173–188.
- [124] L. Luo, H. S. White, *Langmuir* **2013**, *29*, 11169–11175.
- [125] Q. Chen, L. Luo, H. S. White, *Langmuir* **2015**, *31*, 4573–4581.
- [126] Q. Chen, L. Luo, H. Faraji, S. W. Feldberg, H. S. White, *Journal of Physical Chemistry Letters* **2014**, *5*, 3539–3544.
- [127] Q. Chen, H. S. Wiedenroth, S. R. German, H. S. White, *J Am Chem Soc* **2015**, *137*, 12064–12069.
- [128] S. R. German, M. A. Edwards, Q. Chen, H. S. White, *Nano Lett* **2016**, *16*, 6691–6694.
- [129] H. Ren, S. R. German, M. A. Edwards, Q. Chen, H. S. White, *Journal of Physical Chemistry Letters* **2017**, *8*, 2450–2454.
- [130] Á. M. Soto, S. R. German, H. Ren, D. Van Der Meer, D. Lohse, M. A. Edwards, H. S. White, *Langmuir* **2018**, *34*, 7309–7318.
- [131] M. A. Edwards, H. S. White, H. Ren, *ACS Nano* **2019**, *13*, 6330–6340.

- [132] J. H. K. Pfisterer, Y. Liang, O. Schneider, A. S. Bandarenka, *Nature* **2017**, *549*, 74–77.
- [133] Y. Liang, D. McLaughlin, C. Csoklich, O. Schneider, A. S. Bandarenka, *Energy Environ Sci* **2019**, *12*, 351–357.
- [134] R. W. Haid, R. M. Kluge, Y. Liang, A. S. Bandarenka, R. W. Haid, R. M. Kluge, Y. Liang, A. S. Bandarenka, *Small Methods* **2021**, *5*, 2000710.
- [135] T. Kosmala, A. Baby, M. Lunardon, D. Perilli, H. Liu, C. Durante, C. Di Valentin, S. Agnoli, G. Granozzi, *Nat Catal* **2021**, *4*, 850–859.
- [136] T. H. Phan, K. Banjac, F. P. Cometto, F. Dattila, R. García-Muelas, S. J. Raaijman, C. Ye, M. T. M. Koper, N. López, M. Lingenfelder, *Nano Lett* **2021**, *21*, 2059–2065.
- [137] L. Seidl, S. Martens, J. Ma, U. Stimming, O. Schneider, *Nanoscale* **2016**, *8*, 14004–14014.
- [138] C. Stumm, M. Bertram, M. Kastenmeier, F. D. Speck, Z. Sun, J. Rodríguez-Fernández, J. V Lauritsen, K. J. J Mayrhofer, S. Cherevko, O. Brummel, J. Libuda, C. Stumm, M. Bertram, M. Kastenmeier, O. Brummel, J. Libuda, F. D. Speck, K. J. J Mayrhofer, S. Cherevko, Z. Sun, J. Rodríguez-Fernández, J. V Lauritsen, *Adv Funct Mater* **2021**, *31*, 2009923.
- [139] W. Zhao, W. Song, L. Z. Cheong, D. Wang, H. Li, F. Besenbacher, F. Huang, C. Shen, *Ultramicroscopy* **2019**, *204*, 34–48.
- [140] Z. Zhang, S. Said, K. Smith, R. Jervis, C. A. Howard, P. R. Shearing, D. J. L. Brett, T. S. Miller, Z. Zhang, S. Said, K. Smith, R. Jervis, P. R. Shearing, D. J. L. Brett, T. S. Miller, *Adv Energy Mater* **2021**, *11*, 2101518.
- [141] J. Deng, M. R. Nellist, M. B. Stevens, C. Dette, Y. Wang, S. W. Boettcher, *Nano Lett* **2017**, *17*, 6922–6926.
- [142] C. Dette, M. R. Hurst, J. Deng, M. R. Nellist, S. W. Boettcher, *ACS Appl Mater Interfaces* **2019**, *11*, 5590–5594.
- [143] C. R. Becker, K. E. Strawhecker, Q. P. McAllister, C. A. Lundgren, *ACS Nano* **2013**, *7*, 9173–9182.

- [144] A. V. Cresce, S. M. Russell, D. R. Baker, K. J. Gaskell, K. Xu, *Nano Lett* **2014**, *14*, 1405–1412.
- [145] J. Park, S. Kalnaus, S. Han, Y. K. Lee, G. B. Less, N. J. Dudney, C. Daniel, A. M. Sastry, *J Power Sources* **2013**, *222*, 417–425.
- [146] Q. P. McAllister, K. E. Strawhecker, C. R. Becker, C. A. Lundgren, *J Power Sources* **2014**, *257*, 380–387.
- [147] J. Wan, Y. Hao, Y. Shi, Y. X. Song, H. J. Yan, J. Zheng, R. Wen, L. J. Wan, *Nat Commun* **2019**, *10*, 1–10.
- [148] C. Shen, G. Hu, L. Z. Cheong, S. Huang, J. G. Zhang, D. Wang, *Small Methods* **2018**, *2*, 1700298.
- [149] C. Chen, T. Zhou, D. L. Danilov, L. Gao, S. Benning, N. Schön, S. Tardif, H. Simons, F. Hausen, T. U. Schüllli, R. A. Eichel, P. H. L. Notten, *Nat Commun* **2020**, *11*, 1–10.
- [150] R. R. Liu, X. Deng, X. R. Liu, H. J. Yan, A. M. Cao, D. Wang, *Chemical Communications* **2014**, *50*, 15756–15759.
- [151] T. S. Watkins, D. Sarbapalli, M. J. Coughlan, A. S. Danis, J. Zhang, L. Zhang, K. R. Zavadil, J. Rodríguez-López, *J Mater Chem A Mater* **2020**, *8*, 15734–15745.
- [152] R. Wen, M. Hong, H. R. Byon, *J Am Chem Soc* **2013**, *135*, 10870–10876.
- [153] S. Y. Lang, Y. Shi, Y. G. Guo, D. Wang, R. Wen, L. J. Wan, *Angewandte Chemie International Edition* **2016**, *55*, 15835–15839.
- [154] H. Masuda, N. Ishida, Y. Ogata, D. Ito, D. Fujita, *Nanoscale* **2017**, *9*, 893–898.
- [155] N. Hodnik, G. Dehm, K. J. J. Mayrhofer, *Acc Chem Res* **2016**, *49*, 2015–2022.
- [156] Y. Pan, X. Li, D. Su, *Curr Opin Electrochem* **2022**, *33*, 100936.
- [157] J. Kim, D. Lee, C. Nam, J. Chung, B. Koo, N. Kim, J. Lim, *J Electron Spectros Relat Phenomena* **2023**, *266*, 147337.

- [158] L. Godeffroy, P. Ciocci, J. F. Lemineur, F. Kanoufi, *Curr Opin Electrochem* **2022**, *36*, 101165.
- [159] L. Godeffroy, J. F. Lemineur, V. Shkirskiy, M. Miranda Vieira, J. M. Noël, F. Kanoufi, *Small Methods* **2022**, *6*, 2200659.
- [160] W. Jiang, W. Wei, T. Yuan, S. Liu, B. Niu, H. Wang, W. Wang, *Chem Sci* **2021**, *12*, 8556–8562.
- [161] D. Jiang, Y. Jiang, Z. Li, T. Liu, X. Wo, Y. Fang, N. Tao, W. Wang, H. Y. Chen, *J Am Chem Soc* **2017**, *139*, 186–192.
- [162] X. Shan, I. Díez-Pérez, L. Wang, P. Wiktor, Y. Gu, L. Zhang, W. Wang, J. Lu, S. Wang, Q. Gong, J. Li, N. Tao, *Nat Nanotechnol* **2012**, *7*, 668–672.
- [163] X. Shan, U. Patel, S. Wang, R. Iglesias, N. Tao, *Science (1979)* **2010**, *327*, 1363–1366.
- [164] J. F. Lemineur, P. Ciocci, J. M. Noël, H. Ge, C. Combellas, F. Kanoufi, *ACS Nano* **2021**, *15*, 2643–2653.
- [165] R. Hao, Y. Fan, M. D. Howard, J. C. Vaughan, B. Zhang, *Proc Natl Acad Sci U S A* **2018**, *115*, 5878–6588.
- [166] R. Hao, Y. Fan, T. J. Anderson, B. Zhang, *Anal Chem* **2020**, *92*, 3682–3688.
- [167] Z. Peng, B. Zhang, *Anal Chem* **2021**, *93*, 15315–15322.
- [168] D. Lohse, X. Zhang, *Rev Mod Phys* **2015**, *87*, 981.
- [169] K. Zhou, T. Yuan, H. Su, W. Wang, *Curr Opin Colloid Interface Sci* **2021**, *55*, 101465.
- [170] P. Ciocci, J. F. Lemineur, J. M. Noël, C. Combellas, F. Kanoufi, *Electrochim Acta* **2021**, *386*, 138498.
- [171] S. Chen, C. Yin, Z. Huang, J. Chen, Y. Zheng, J. Chen, S. Yang, Y. Su, Y. Fang, *Carbon N Y* **2022**, *191*, 333–339.
- [172] Y. Wang, T. Yuan, H. Su, K. Zhou, L. Yin, W. Wang, *ACS Sens* **2021**, *6*, 380–386.

- [173] S. Xu, X. Yu, Z. Chen, Y. Zeng, L. Guo, L. Li, F. Luo, J. Wang, B. Qiu, Z. Lin, *Anal Chem* **2020**, *92*, 9016–9023.
- [174] J. G. Wang, L. Zhang, J. Xie, Y. Weizmann, D. Li, J. Li, *Nano Lett* **2022**, *22*, 5495–5502.
- [175] C. Ma, H. F. Wei, M. X. Wang, S. Wu, Y. C. Chang, J. Zhang, L. P. Jiang, W. Zhu, Z. Chen, Y. Lin, *Nano Lett* **2020**, *20*, 5008–5016.
- [176] D. Jiang, L. Sun, T. Liu, W. Wang, *Anal Chem* **2017**, *89*, 11641–11647.
- [177] T. Yuan, W. Wei, W. Jiang, W. Wang, *ACS Nano* **2021**, *15*, 3522–3528.
- [178] B. Niu, W. Jiang, B. Jiang, M. Lv, S. Wang, W. Wang, *Nat Commun* **2022**, *13*, 1–9.
- [179] T. Liu, M. Li, Y. Wang, Y. Fang, W. Wang, *Chem Sci* **2018**, *9*, 4424–4429.
- [180] R. C. Evans, A. Ellingworth, C. J. Cashen, C. R. Weinberger, J. B. Sambur, *Proc Natl Acad Sci U S A* **2019**, *116*, 12666–12671.
- [181] R. C. Evans, Z. N. Nilsson, J. B. Sambur, *Anal Chem* **2019**, *91*, 14983–14991.
- [182] R. C. Evans, Z. Nilsson, B. Balch, L. Wang, J. R. Neilson, C. R. Weinberger, J. B. Sambur, *ChemElectroChem* **2020**, *7*, 753–760.
- [183] A. J. Merryweather, C. Schnedermann, Q. Jacquet, C. P. Grey, A. Rao, *Nature* **2021**, *594*, 522–528.
- [184] C. Xu, A. J. Merryweather, S. S. Pandurangi, Z. Lun, D. S. Hall, V. S. Deshpande, N. A. Fleck, C. Schnedermann, A. Rao, C. P. Grey, *Joule* **2022**, *6*, 2535–2546.
- [185] A. J. Merryweather, Q. Jacquet, S. P. Emge, C. Schnedermann, A. Rao, C. P. Grey, *Nat Mater* **2022**, *21*, 1306–1313.
- [186] X. Ye, M. Saqib, J. Mao, G. Li, R. Hao, *Cell Rep Phys Sci* **2021**, *2*, 100420.
- [187] G. Li, J. Mao, M. Saqib, R. Hao, *Chem Asian J* **2022**, *17*, e202200824.
- [188] P. Bai, J. Li, F. R. Brushett, M. Z. Bazant, *Energy Environ Sci* **2016**, *9*, 3221–3229.
- [189] B. Chen, H. Zhang, J. Xuan, G. J. Offer, H. Wang, *Adv Mater Technol* **2020**, *5*, 2000555.

- [190] J. Mao, G. Li, M. Saqib, J. Xu, R. Hao, *Chem Sci* **2022**, *13*, 12782–12790.
- [191] G. Feng, H. Jia, Y. Shi, X. Yang, Y. Liang, M. H. Engelhard, Y. Zhang, C. Yang, K. Xu, Y. Yao, W. Xu, X. Shan, *Nat Nanotechnol* **2023**, 1–10.
- [192] W. Wei, T. Yuan, W. Jiang, J. Gao, H. Y. Chen, W. Wang, *J Am Chem Soc* **2020**, *142*, 14307–14313.
- [193] M. Bernal Lopez, J. Ustarroz, *Curr Opin Electrochem* **2021**, *27*, 100688.
- [194] G. Wu, X. Zhou, W. L. Lv, C. Qian, X. W. Liu, *Nano Lett* **2022**, *22*, 4383–4391.
- [195] P. Saha, J. W. Hill, J. D. Walmsley, C. M. Hill, *Anal Chem* **2018**, *90*, 12832–12839.
- [196] L. Godeffroy, A. Makogon, S. G. Derouich, F. Kanoufi, V. Shkirskiy, *Anal Chem* **2023**, *95*, 9999–10007.
- [197] J. K. Utterback, A. J. King, L. Belman-Wells, D. M. Larson, L. M. Hamerlynck, A. Z. Weber, N. S. Ginsberg, *ACS Energy Lett* **2023**, *8*, 1785–1792.
- [198] Zhu Zhang, Sanli Faez, *Faraday Discuss* **2023**, DOI 10.1039/D3FD00040K.
- [199] E. B. Tetteh, D. Valavanis, E. Daviddi, X. Xu, C. Santana Santos, E. Ventosa, D. Martín-Yerga, W. Schuhmann, P. R. Unwin, *Angewandte Chemie International Edition* **2023**, *62*, e202214493.
- [200] L. Godeffroy, V. Shkirskiy, J.-M. Noël, J.-F. Lemineur, F. Kanoufi, *Faraday Discuss* **2023**, DOI 10.1039/D3FD00032J.
- [201] L. Godeffroy, P. Ciocci, A. Nsabimana, M. Miranda Vieira, J. M. Noël, C. Combellas, J. F. Lemineur, F. Kanoufi, *Angewandte Chemie International Edition* **2021**, *60*, 16980–16983.
- [202] M. Bernal Lopez, J. Ustarroz, *Curr Opin Electrochem* **2021**, *27*, 100688.
- [203] U. S. Mohanty, *J Appl Electrochem* **2011**, *41*, 257–270.
- [204] J. F. Lemineur, J. M. Noël, D. Ausserré, C. Combellas, F. Kanoufi, *Angewandte Chemie International Edition* **2018**, *57*, 11998–12002.

- [205] C. Yuan, H. Bin Wu, Y. Xie, X. W. Lou, *Angewandte Chemie International Edition* **2014**, *53*, 1488–1504.
- [206] W. Li, B. Song, A. Manthiram, *Chem Soc Rev* **2017**, *46*, 3006–3059.
- [207] P. Du, R. Eisenberg, *Energy Environ Sci* **2012**, *5*, 6012–6021.
- [208] V. Vij, S. Sultan, A. M. Harzandi, A. Meena, J. N. Tiwari, W. G. Lee, T. Yoon, K. S. Kim, *ACS Catal* **2017**, *7*, 7196–7225.
- [209] A. G. Oshchepkov, G. Braesch, S. Ould-Amara, G. Rostamikia, G. Maranzana, A. Bonnefont, V. Papaefthimiou, M. J. Janik, M. Chatenet, E. R. Savinova, *ACS Catal* **2019**, *9*, 8520–8528.
- [210] M. P. Zach, R. M. Penner, *Advanced Materials* **2000**, *12*, 878–883.
- [211] N. L. Ritzert, T. P. Moffat, *Journal of Physical Chemistry C* **2016**, *120*, 27478–27489.
- [212] R. Wang, U. Bertocci, H. Tan, L. A. Bendersky, T. P. Moffat, *Journal of Physical Chemistry C* **2016**, *120*, 16228–16237.
- [213] J. Clausmeyer, J. Masa, E. Ventosa, D. Öhl, W. Schuhmann, *Chemical Communications* **2016**, *52*, 2408–2411.
- [214] E. A. Mernissi Cherigui, K. Sentosun, P. Bouckennooge, H. Vanrompay, S. Bals, H. Terryn, J. Ustarroz, *Journal of Physical Chemistry C* **2017**, *121*, 9337–9347.
- [215] J. Ustarroz, *Curr Opin Electrochem* **2020**, *19*, 144–152.
- [216] J. Ustarroz, J. A. Hammons, T. Altantzis, A. Hubin, S. Bals, H. Terryn, *J Am Chem Soc* **2013**, *135*, 11550–11561.
- [217] H. E. M. Hussein, R. J. Maurer, H. Amari, J. J. P. Peters, L. Meng, R. Beanland, M. E. Newton, J. V. Macpherson, *ACS Nano* **2018**, *12*, 7388–7396.
- [218] W. Wang, *Chem Soc Rev* **2018**, *47*, 2485–2508.
- [219] B. S. Hoener, S. R. Kirchner, T. S. Heiderscheid, S. S. E. Collins, W. S. Chang, S. Link, C. F. Landes, *Chem* **2018**, *4*, 1560–1585.

- [220] A. J. Wilson, D. Devasia, P. K. Jain, *Chem Soc Rev* **2020**, *49*, 6087–6112.
- [221] C. M. Hill, S. Pan, *J Am Chem Soc* **2013**, *135*, 17250–17253.
- [222] J. G. Smith, Q. Yang, P. K. Jain, *Angewandte Chemie International Edition* **2014**, *53*, 2867–2872.
- [223] S. Hu, J. Yi, Y. J. Zhang, K. Q. Lin, B. J. Liu, L. Chen, C. Zhan, Z. C. Lei, J. J. Sun, C. Zong, J. F. Li, B. Ren, *Nature Communications* **2020** *11:1* **2020**, *11*, 1–7.
- [224] L. Godeffroy, P. Ciocci, J. F. Lemineur, F. Kanoufi, *Curr Opin Electrochem* **2022**, *36*, 101165.
- [225] R. W. Taylor, V. Sandoghdar, *Nano Lett* **2019**, *19*, 4827–4835.
- [226] C. Yurdakul, O. Avci, A. Matlock, A. J. Devaux, M. V. Quintero, E. Ozbay, R. A. Davey, J. H. Connor, W. C. Karl, L. Tian, M. S. Ünlü, *ACS Nano* **2020**, *14*, 2002–2013.
- [227] J. F. Lemineur, J. M. Noël, A. Courty, D. Ausserré, C. Combellas, F. Kanoufi, *J Am Chem Soc* **2020**, *142*, 7937–7946.
- [228] K. Namink, X. Meng, M. T. M. Koper, P. Kukura, S. Faez, *Phys Rev Appl* **2020**, *13*, 044065.
- [229] X. Shan, I. Díez-Pérez, L. Wang, P. Wiktor, Y. Gu, L. Zhang, W. Wang, J. Lu, S. Wang, Q. Gong, J. Li, N. Tao, *Nature Nanotechnology* **2012** *7:10* **2012**, *7*, 668–672.
- [230] J. F. Lemineur, P. Ciocci, J. M. Noël, H. Ge, C. Combellas, F. Kanoufi, *ACS Nano* **2021**, *15*, 2643–2653.
- [231] A. Milchev, B. Scharifker, G. Hills, *J Electroanal Chem Interfacial Electrochem* **1982**, *132*, 277–289.
- [232] N. Asi Ser ; Ben-Jacob, E. Garik, P. Matsushita, M. Sano, M. Hayakawa, Y. Honjo, H. Sawada, Y. Grier, D. Ben-Jacob, E. Clarke, R. Sander, L. M. Y. Sawada, A. Dougherty, J. P. Gollub, D. G. Grier, D. A. Kessler, L. M. ; F. Sander, A. Arneodo, G. Grasseau, H. L. Swinney, J. R. Melrose, D. B. Hibbert, R. C. ; P. Ba Li, J. Claret, F. M. Mas, F. Sagues, V. Fleury, J.-N. Chazalviel, M. Rosso, *Nature* **1994** *367:6462* **1994**, *367*, 438–441.
- [233] V. K. Laurinavichyute, S. Nizamov, V. M. Mirsky, *Electrochim Acta* **2021**, *382*, 138278.

- [234] X. Ye, M. Saqib, J. Mao, G. Li, R. Hao, *Cell Rep Phys Sci* **2021**, *2*, 100420.
- [235] L. Godeffroy, J. F. Lemineur, V. Shkirskiy, M. Miranda Vieira, J. M. Noël, F. Kanoufi, *Small Methods* **2022**, *6*, 2200659.
- [236] D. Valavanis, P. Ciocci, G. N. Meloni, P. Morris, J. F. Lemineur, I. J. McPherson, F. Kanoufi, P. R. Unwin, *Faraday Discuss* **2022**, *233*, 122–148.
- [237] P. Ciocci, D. Valavanis, G. N. Meloni, J. F. Lemineur, P. R. Unwin, F. Kanoufi, *ChemElectroChem* **2023**, *10*, e202201162.
- [238] V. Brasiliense, J. Clausmeyer, A. L. Dauphin, J. M. Noël, P. Berto, G. Tessier, W. Schuhmann, F. Kanoufi, *Angewandte Chemie International Edition* **2017**, *56*, 10598–10601.
- [239] J. M. Noël, J. F. Lemineur, *Curr Opin Electrochem* **2021**, *25*, 100647.
- [240] S. Nizamov, S. D. Sazdovska, V. M. Mirsky, *Anal Chim Acta* **2022**, *1204*, 339633.
- [241] J. F. Lemineur, H. Wang, W. Wang, F. Kanoufi, *Annual Review of Analytical Chemistry* **2022**, *15*, 57–82.
- [242] F. Kanoufi, in *Encyclopedia of Electrochemistry* (Ed.: A.J. Bard), John Wiley & Sons, Ltd, New York, **2022**, pp. 1–80.
- [243] M. Mahamdeh, S. Simmert, A. Luchniak, E. Schäffer, J. Howard, *J Microsc* **2018**, *272*, 60–66.
- [244] R. Orbach, J. Howard, *Nat Commun* **2019**, *10*, 1–11.
- [245] P. Ciocci, J. F. Lemineur, J. M. Noël, C. Combellas, F. Kanoufi, *Electrochim Acta* **2021**, *386*, 138498.
- [246] N. Y. Molina, T. Pungsrisai, Z. J. O’Dell, B. Paranzino, K. A. Willets, *ChemElectroChem* **2022**, *9*, e202200245.
- [247] O. J. Wahab, M. Kang, G. N. Meloni, E. Daviddi, P. R. Unwin, *Anal Chem* **2022**, *94*, 4729–4736.

- [248] N. Danilovic, R. Subbaraman, D. Strmcnik, K. C. Chang, A. P. Paulikas, V. R. Stamenkovic, N. M. Markovic, *Angewandte Chemie International Edition* **2012**, *51*, 12495–12498.
- [249] M. Chhetri, S. Sultan, C. N. R. Rao, *Proc Natl Acad Sci U S A* **2017**, *114*, 8986–8990.
- [250] Y. Liu, D. Gokcen, U. Bertocci, T. P. Moffat, *Science (1979)* **2012**, *338*, 1327–1330.
- [251] O. Avci, N. L. Ünlü, A. Y. Özkumur, M. S. Ünlü, *Sensors* **2015**, *15*, 17649–17665.
- [252] O. Avci, R. Adato, A. Y. Özkumur, M. S. Ünlü, *Opt Express* **2016**, *24*, 6094–6114.
- [253] D. Sevenler, O. Avci, M. S. Ünlü, *Biomed Opt Express* **2017**, *8*, 2976–2989.
- [254] M. N. Polyanskiy, “Refractive index database,” can be found under <https://refractiveindex.info>, **n.d.**
- [255] J. L. Ord, *Surf Sci* **1976**, *56*, 413–424.
- [256] F. Bagheri, S. Mosivand, *Mater Today Commun* **2021**, *26*, 101714.
- [257] N. L. Ritzert, T. P. Moffat, *Journal of Physical Chemistry C* **2016**, *120*, 27478–27489.
- [258] P. Saha, J. W. Hill, J. D. Walmsley, C. M. Hill, *Anal Chem* **2018**, *90*, 12832–12839.
- [259] D. Valavanis, P. Ciocci, G. N. Meloni, P. Morris, J. F. Lemineur, I. J. McPherson, F. Kanoufi, P. R. Unwin, *Faraday Discuss* **2022**, *233*, 122–148.
- [260] P. Ciocci, D. Valavanis, G. N. Meloni, J. F. Lemineur, P. R. Unwin, F. Kanoufi, *ChemElectroChem* **2023**, *10*, e202201162.
- [261] Y. Yang, Y. Xiong, R. Zeng, X. Lu, M. Krumov, X. Huang, W. Xu, H. Wang, F. J. Disalvo, J. D. Brock, D. A. Muller, H. D. Abrunã, *ACS Catal* **2021**, *11*, 1136–1178.
- [262] P. Unwin, *Faraday Discuss* **2022**, *233*, 374–391.
- [263] J. J. Gooding, K. Gaus, *Angewandte Chemie International Edition* **2016**, *55*, 11354–11366.
- [264] J. M. Noël, J. F. Lemineur, *Curr Opin Electrochem* **2021**, *25*, 100647.
- [265] W. Wang, *Chem Soc Rev* **2018**, *47*, 2485–2508.

- [266] N. Ebejer, A. G. Güell, S. C. S. Lai, K. McKelvey, M. E. Snowden, P. R. Unwin, *Annual Review of Analytical Chemistry* **2013**, *6*, 329–351.
- [267] L. I. Stephens, N. A. Payne, S. A. Skaanvik, D. Polcari, M. Geissler, J. Mauzeroll, *Anal Chem* **2019**, *91*, 3944–3950.
- [268] M. Tuck, L. Blanc, R. Touti, N. H. Patterson, S. Van Nuffel, S. Villette, J. C. Taveau, A. Römpp, A. Brunelle, S. Lecomte, N. Desbenoit, *Anal Chem* **2021**, *93*, 445–477.
- [269] A. Mistry, A. A. Franco, S. J. Cooper, S. A. Roberts, V. Viswanathan, *ACS Energy Lett* **2021**, *6*, 1422–1431.
- [270] L. B. Coelho, D. Zhang, Y. Van Ingelgem, D. Steckelmacher, A. Nowé, H. Terryn, *npj Materials Degradation* **2022**, *6:1*, 1–16.
- [271] L. Mill, D. Wolff, N. Gerrits, P. Philipp, L. Kling, F. Vollnhals, A. Ignatenko, C. Jaremenko, Y. Huang, O. De Castro, J. N. Audinot, I. Nelissen, T. Wirtz, A. Maier, S. Christiansen, *Small Methods* **2021**, *5*, 2100223.
- [272] X. Wang, J. Li, H. D. Ha, J. C. Dahl, J. C. Ondry, I. Moreno-Hernandez, T. Head-Gordon, A. P. Alivisatos, *JACS Au* **2021**, *1*, 316–327.
- [273] M. Ceriotti, *Journal of Chemical Physics* **2019**, *150*, 150901.
- [274] L. I. Stephens, N. A. Payne, J. Mauzeroll, *Anal Chem* **2020**, *92*, 3958–3963.
- [275] H. Chen, D. Li, E. Kätelhön, R. Miao, R. G. Compton, *Anal Chem* **2022**, *94*, 5901–5908.
- [276] P. Puthongkham, S. Wirojsaengthong, A. Suea-Ngam, *Analyst* **2021**, *146*, 6351–6364.
- [277] R. Li, A. Makogon, T. Galochkina, J.-F. Lemineur, F. Kanoufi, V. Shkirskiy, *Small Methods* **2023**, 2300214.
- [278] Z. Liang, H. S. Ahn, A. J. Bard, *J Am Chem Soc* **2017**, *139*, 4854–4858.
- [279] M. P. Zach, R. M. Penner, *Advanced Materials* **2000**, *12*, 878–883.

- [280] L. Godeffroy, P. Ciocci, A. Nsabimana, M. Miranda Vieira, J. M. Noël, C. Combellas, J. F. Lemineur, F. Kanoufi, *Angewandte Chemie International Edition* **2021**, *60*, 16980–16983.
- [281] R. Subbaraman, D. Tripkovic, D. Strmcnik, K. C. Chang, M. Uchimura, A. P. Paulikas, V. Stamenkovic, N. M. Markovic, *Science (1979)* **2011**, *334*, 1256–1260.
- [282] N. Danilovic, R. Subbaraman, D. Strmcnik, K. C. Chang, A. P. Paulikas, V. R. Stamenkovic, N. M. Markovic, *Angewandte Chemie International Edition* **2012**, *51*, 12495–12498.
- [283] J. F. Lemineur, J. M. Noël, D. Ausserré, C. Combellas, F. Kanoufi, *Angewandte Chemie International Edition* **2018**, *57*, 11998–12002.
- [284] J. F. Lemineur, P. Ciocci, J. M. Noël, H. Ge, C. Combellas, F. Kanoufi, *ACS Nano* **2021**, *15*, 2643–2653.
- [285] J. C. Crocker, D. G. Grier, *J Colloid Interface Sci* **1996**, *179*, 298–310.
- [286] S. Suzuki, K. Abe, *Comput Vis Graph Image Process* **1985**, *30*, 32–46.
- [287] P. Ciocci, J. F. Lemineur, J. M. Noël, C. Combellas, F. Kanoufi, *Electrochim Acta* **2021**, *386*, 138498.
- [288] O. J. Wahab, M. Kang, G. N. Meloni, E. Daviddi, P. R. Unwin, *Anal Chem* **2022**, *94*, 4729–4736.
- [289] N. Y. Molina, T. Pungsrilai, Z. J. O’Dell, B. Paranzino, K. A. Willets, *ChemElectroChem* **2022**, *9*, e202200245.
- [290] C. Amatore, J. M. Savéant, D. Tessier, *J Electroanal Chem Interfacial Electrochem* **1983**, *147*, 39–51.
- [291] M. E. Hyde, R. G. Compton, *Journal of Electroanalytical Chemistry* **2003**, *549*, 1–12.
- [292] N. Godino, X. Borriase, F. X. Muñoz, F. J. Del Campo, R. G. Compton, *Journal of Physical Chemistry C* **2009**, *113*, 11119–11125.
- [293] J. F. Lemineur, J. M. Noël, C. Combellas, F. Kanoufi, *Journal of Electroanalytical Chemistry* **2020**, *872*, 114043.

- [294] L. Heerman, A. Tarallo, *Journal of Electroanalytical Chemistry* **1999**, *470*, 70–76.
- [295] O. Orrick, M. Yang, C. Batchelor-McAuley, R. G. Compton, *Journal of Electroanalytical Chemistry* **2021**, *900*, 115738.
- [296] Z. Stojek, J. Osteryoung, *Anal Chem* **1989**, *61*, 1305–1308.
- [297] J. Ustarroz, J. A. Hammons, T. Altantzis, A. Hubin, S. Bals, H. Terryn, *J Am Chem Soc* **2013**, *135*, 11550–11561.
- [298] H. E. M. Hussein, R. J. Maurer, H. Amari, J. J. P. Peters, L. Meng, R. Beanland, M. E. Newton, J. V. Macpherson, *ACS Nano* **2018**, *12*, 7388–7396.
- [299] P. J. Rheinländer, J. Herranz, J. Durst, H. A. Gasteiger, *J Electrochem Soc* **2014**, *161*, F1448–F1457.
- [300] L. Godeffroy, P. Ciocci, N. Ortiz Peña, D. Alloyeau, J. M. Noël, J. F. Lemineur, F. Kanoufi, *Angewandte Chemie International Edition* **2023**, *62*, e202304950.
- [301] J. G. Wang, L. Zhang, J. Xie, Y. Weizmann, D. Li, J. Li, *Nano Lett* **2022**, *22*, 5495–5502.
- [302] X. Shan, I. Díez-Pérez, L. Wang, P. Wiktor, Y. Gu, L. Zhang, W. Wang, J. Lu, S. Wang, Q. Gong, J. Li, N. Tao, *Nature Nanotechnology* *2012 7:10* **2012**, *7*, 668–672.
- [303] J. F. Lemineur, P. Ciocci, J. M. Noël, H. Ge, C. Combellas, F. Kanoufi, *ACS Nano* **2021**, *15*, 2643–2653.
- [304] R. Hao, Y. Fan, M. D. Howard, J. C. Vaughan, B. Zhang, *Proc Natl Acad Sci U S A* **2018**, *115*, 5878–6588.
- [305] R. Hao, Y. Fan, T. J. Anderson, B. Zhang, *Anal Chem* **2020**, *92*, 3682–3688.
- [306] J. K. Utterback, A. J. King, L. Belman-Wells, D. M. Larson, L. M. Hamerlynck, A. Z. Weber, N. S. Ginsberg, *ACS Energy Lett* **2023**, *8*, 1785–1792.
- [307] Q. Chen, L. Luo, H. Faraji, S. W. Feldberg, H. S. White, *Journal of Physical Chemistry Letters* **2014**, *5*, 3539–3544.
- [308] A. Steinegger, O. S. Wolfbeis, S. M. Borisov, *Chem Rev* **2020**, *120*, 12357–12489.

- [309] M. C. O. Monteiro, M. T. M. Koper, *Curr Opin Electrochem* **2021**, *25*, 100649.
- [310] N. C. Rudd, S. Cannan, E. Bitziou, I. Ciani, A. L. Whitworth, P. R. Unwin, *Anal Chem* **2005**, *77*, 6205–6217.
- [311] M. Saqib, Y. Fan, R. Hao, B. Zhang, *Nano Energy* **2021**, *90*, 106539.
- [312] K. Sun, X. Wu, Z. Zhuang, L. Liu, J. Fang, L. Zeng, J. Ma, S. Liu, J. Li, R. Dai, X. Tan, K. Yu, D. Liu, W. C. Cheong, A. Huang, Y. Liu, Y. Pan, H. Xiao, C. Chen, *Nature Communications* **2022** *13:1* **2022**, *13*, 1–11.
- [313] W. Tong, M. Forster, F. Dionigi, S. Dresp, R. Sadeghi Erami, P. Strasser, A. J. Cowan, P. Farràs, *Nature Energy* **2020** *5:5* **2020**, *5*, 367–377.
- [314] J. Guo, Y. Zhang, A. Zavabeti, K. Chen, Y. Guo, G. Hu, X. Fan, G. K. Li, *Nature Communications* **2022** *13:1* **2022**, *13*, 1–9.
- [315] J. Durst, A. Siebel, C. Simon, F. Hasché, J. Herranz, H. A. Gasteiger, *Energy Environ Sci* **2014**, *7*, 2255–2260.
- [316] R. Subbaraman, D. Tripkovic, D. Strmcnik, K. C. Chang, M. Uchimura, A. P. Paulikas, V. Stamenkovic, N. M. Markovic, *Science (1979)* **2011**, *334*, 1256–1260.
- [317] Q. Liu, Q. Liu, Z. Yan, J. Gao, J. Gao, E. Wang, G. Sun, *ACS Appl Mater Interfaces* **2020**, *12*, 24683–24692.
- [318] L. Wang, C. Lin, D. Huang, J. Chen, L. Jiang, M. Wang, L. Chi, L. Shi, J. Jin, *ACS Catal* **2015**, *5*, 3801–3806.
- [319] R. Kavian, S. Il Choi, J. Park, T. Liu, H. C. Peng, N. Lu, J. Wang, M. J. Kim, Y. Xia, S. W. Lee, *J Mater Chem A Mater* **2016**, *4*, 12392–12397.
- [320] H. Yin, S. Zhao, K. Zhao, A. Muqsit, H. Tang, L. Chang, H. Zhao, Y. Gao, Z. Tang, *Nature Communications* **2015** *6:1* **2015**, *6*, 1–8.
- [321] L. Wang, Y. Zhu, Z. Zeng, C. Lin, M. Giroux, L. Jiang, Y. Han, J. Greeley, C. Wang, J. Jin, *Nano Energy* **2017**, *31*, 456–461.

- [322] G. Yuan, B. Wen, Y. Hu, G. Zeng, W. Zhang, L. Wang, X. Zhang, Q. Wang, *Int J Hydrogen Energy* **2019**, *44*, 14258–14265.
- [323] N. Danilovic, R. Subbaraman, D. Strmcnik, K. C. Chang, A. P. Paulikas, V. R. Stamenkovic, N. M. Markovic, *Angewandte Chemie International Edition* **2012**, *51*, 12495–12498.
- [324] R. Subbaraman, D. Tripkovic, K. C. Chang, D. Strmcnik, A. P. Paulikas, P. Hirunsit, M. Chan, J. Greeley, V. Stamenkovic, N. M. Markovic, *Nature Materials* **2012**, *11*, 550–557.
- [325] Z. Zeng, K. C. Chang, J. Kubal, N. M. Markovic, J. Greeley, *Nature Energy* **2017**, *2*, 1–9.
- [326] F. J. Sarabia, P. Sebastián-Pascual, M. T. M. Koper, V. Climent, J. M. Feliu, *ACS Appl Mater Interfaces* **2019**, *11*, 613–623.
- [327] M. Gong, W. Zhou, M. C. Tsai, J. Zhou, M. Guan, M. C. Lin, B. Zhang, Y. Hu, D. Y. Wang, J. Yang, S. J. Pennycook, B. J. Hwang, H. Dai, *Nature Communications* **2014**, *5*, 1–6.
- [328] A. R. Akbashev, *ACS Catal* **2022**, *12*, 4296–4301.
- [329] Y. G. Zhou, N. V. Rees, R. G. Compton, *Physical Chemistry Chemical Physics* **2012**, *15*, 761–763.
- [330] W. Wei, T. Yuan, W. Jiang, J. Gao, H. Y. Chen, W. Wang, *J Am Chem Soc* **2020**, *142*, 14307–14313.
- [331] J. F. Lemineur, J. M. Noël, D. Ausserré, C. Combellas, F. Kanoufi, *Angewandte Chemie International Edition* **2018**, *57*, 11998–12002.
- [332] M. Bernal Lopez, J. Ustarroz, *Curr Opin Electrochem* **2021**, *27*, 100688.
- [333] L. Godeffroy, P. Ciocci, J. F. Lemineur, F. Kanoufi, *Curr Opin Electrochem* **2022**, *36*, 101165.
- [334] P. Ciocci, D. Valavanis, G. N. Meloni, J. F. Lemineur, P. R. Unwin, F. Kanoufi, *ChemElectroChem* **2023**, *10*, e202201162.

- [335] L. Godeffroy, P. Ciocci, A. Nsabimana, M. Miranda Vieira, J. M. Noël, C. Combellas, J. F. Lemineur, F. Kanoufi, *Angewandte Chemie International Edition* **2021**, *60*, 16980–16983.
- [336] H. B. Li, M. H. Yu, F. X. Wang, P. Liu, Y. Liang, J. Xiao, C. X. Wang, Y. X. Tong, G. W. Yang, *Nature Communications* **2013**, *4*, 1–7.
- [337] N. L. Ritzert, T. P. Moffat, *Journal of Physical Chemistry C* **2016**, *120*, 27478–27489.
- [338] R. Wang, U. Bertocci, H. Tan, L. A. Bendersky, T. P. Moffat, *Journal of Physical Chemistry C* **2016**, *120*, 16228–16237.
- [339] L. Godeffroy, J.-F. Lemineur, V. Shkirskiy, M. M. Vieira, J.-M. Noël, F. Kanoufi, L. Godeffroy, J.-F. Lemineur, V. Shkirskiy, M. Miranda Vieira, J.-M. Noël, F. Kanoufi, *Small Methods* **2022**, *6*, 2200659.
- [340] W. Sun, G. Liu, L. Wang, T. Wu, Y. Liu, *Journal of Solid State Electrochemistry* **2013**, *17*, 829–840.
- [341] J. Wang, *J Mater Res* **2020**, *35*, 898–921.
- [342] Z. Liang, H. S. Ahn, A. J. Bard, *J Am Chem Soc* **2017**, *139*, 4854–4858.
- [343] Q. Wei, P. Wang, Y. Ma, K. Du, H. Yin, H. Zhu, D. Wang, *Journal of Electroanalytical Chemistry* **2022**, *923*, 116833.
- [344] P. J. Rheinländer, J. Herranz, J. Durst, H. A. Gasteiger, *J Electrochem Soc* **2014**, *161*, F1448–F1457.
- [345] M. C. O. Monteiro, F. Dattila, N. López, M. T. M. Koper, *J Am Chem Soc* **2022**, *144*, 1589–1602.
- [346] L. Godeffroy, I. Aguilar, J. Médard, D. Larcher, J. M. Tarascon, F. Kanoufi, *Adv Energy Mater* **2022**, *12*, 1–14.
- [347] B. Dunn, H. Kamath, J.-M. Tarascon, *Science (1979)* **2011**, *334*, 928–935.
- [348] J. Rugolo, M. J. Aziz, *Energy Environ Sci* **2012**, *5*, 7151–7160.

- [349] A. Konarov, N. Voronina, J. H. Jo, Z. Bakenov, Y. K. Sun, S. T. Myung, *ACS Energy Lett* **2018**, *3*, 2620–2640.
- [350] G. Fang, J. Zhou, A. Pan, S. Liang, *ACS Energy Lett* **2018**, *3*, 2480–2501.
- [351] M. Song, H. Tan, D. Chao, H. J. Fan, *Adv Funct Mater* **2018**, *28*, 1–27.
- [352] B. Tang, L. Shan, S. Liang, J. Zhou, *Energy Environ Sci* **2019**, *12*, 3288–3304.
- [353] X. Zeng, J. Hao, Z. Wang, J. Mao, Z. Guo, *Energy Storage Mater* **2019**, *20*, 410–437.
- [354] H. Li, L. Ma, C. Han, Z. Wang, Z. Liu, Z. Tang, C. Zhi, *Nano Energy* **2019**, *62*, 550–587.
- [355] D. Chen, M. Lu, D. Cai, H. Yang, W. Han, *Journal of Energy Chemistry* **2021**, *54*, 712–726.
- [356] N. Zhang, F. Cheng, Y. Liu, Q. Zhao, K. Lei, C. Chen, X. Liu, J. Chen, *J Am Chem Soc* **2016**, *138*, 12894–12901.
- [357] M. H. Alfaruqi, V. Mathew, J. Gim, S. Kim, J. Song, J. P. Baboo, S. H. Choi, J. Kim, *Chemistry of Materials* **2015**, *27*, 3609–3620.
- [358] B. Lee, C. S. Yoon, H. R. Lee, K. Y. Chung, B. W. Cho, S. H. Oh, *Sci Rep* **2014**, *4*, 1–8.
- [359] C. Xu, B. Li, H. Du, F. Kang, *Angewandte Chemie - International Edition* **2012**, *51*, 933–935.
- [360] N. Zhang, F. Cheng, J. Liu, L. Wang, X. Long, X. Liu, F. Li, J. Chen, *Nat Commun* **2017**, *8*, 1–9.
- [361] B. Lee, H. R. Lee, H. Kim, K. Y. Chung, B. W. Cho, S. H. Oh, *Chemical Communications* **2015**, *51*, 9265–9268.
- [362] K. Sada, B. Senthilkumar, P. Barpanda, *J Mater Chem A Mater* **2019**, *7*, 23981–23988.
- [363] S. Zhao, B. Han, D. Zhang, Q. Huang, L. Xiao, L. Chen, D. G. Ivey, Y. Deng, W. Wei, *J Mater Chem A Mater* **2018**, *6*, 5733–5739.
- [364] Y. Jiang, D. Ba, Y. Li, J. Liu, *Advanced Science* **2020**, *7*, DOI 10.1002/advs.201902795.

- [365] M. H. Alfaruqi, J. Gim, S. Kim, J. Song, J. Jo, S. Kim, V. Mathew, J. Kim, *J Power Sources* **2015**, *288*, 320–327.
- [366] C. Xu, S. W. Chiang, J. Ma, F. Kang, *J Electrochem Soc* **2013**, *160*, A93–A97.
- [367] H. Pan, Y. Shao, P. Yan, Y. Cheng, K. S. Han, Z. Nie, C. Wang, J. Yang, X. Li, P. Bhattacharya, K. T. Mueller, J. Liu, *Nat Energy* **2016**, *1*, 1–7.
- [368] B. Lee, H. R. Seo, H. R. Lee, C. S. Yoon, J. H. Kim, K. Y. Chung, B. W. Cho, S. H. Oh, *ChemSusChem* **2016**, *9*, 2948–2956.
- [369] L. Liu, Y. C. Wu, L. Huang, K. Liu, B. Duployer, P. Rozier, P. L. Taberna, P. Simon, *Adv Energy Mater* **2021**, 26–28.
- [370] J. Yang, J. Cao, Y. Peng, W. Yang, S. Barg, Z. Liu, I. A. Kinloch, M. A. Bissett, R. A. W. Dryfe, *ChemSusChem* **2020**, *13*, 4103–4110.
- [371] G. Li, Z. Huang, J. Chen, F. Yao, J. Liu, O. L. Li, S. Sun, Z. Shi, *J Mater Chem A Mater* **2020**, *8*, 1975–1985.
- [372] M. Mateos, N. Makivic, Y. S. Kim, B. Limoges, V. Balland, *Adv Energy Mater* **2020**, *10*, 1–12.
- [373] D. Chao, W. Zhou, C. Ye, Q. Zhang, Y. Chen, L. Gu, K. Davey, S. Z. Qiao, *Angewandte Chemie - International Edition* **2019**, *58*, 7823–7828.
- [374] T. Shoji, M. Hishinuma, T. Yamamoto, *J Appl Electrochem* **1988**, *18*, 521–526.
- [375] C. Zhong, B. Liu, J. Ding, X. Liu, Y. Zhong, Y. Li, C. Sun, X. Han, Y. Deng, N. Zhao, W. Hu, *Nature Energy* **2020**, *5*, 440–449.
- [376] H. Moon, K. H. Ha, Y. Park, J. Lee, M. S. Kwon, J. Lim, M. H. Lee, D. H. Kim, J. H. Choi, J. H. Choi, K. T. Lee, *Advanced Science* **2021**, *8*, 1–12.
- [377] I. A. Rodríguez Pérez, H.-J. Chang, M. Fayette, B. M. Sivakumar, D. Choi, X. Li, D. Reed, *J Mater Chem A Mater* **2021**, DOI 10.1039/d1ta05022b.
- [378] O. Fitz, C. Bischoff, M. Bauer, H. Gentischer, K. P. Birke, H. M. Henning, D. Biro, *ChemElectroChem* **2021**, *8*, 3553–3566.

- [379] X. Guo, J. Zhou, C. Bai, X. Li, G. Fang, S. Liang, *Mater Today Energy* **2020**, *16*, 100396.
- [380] I. Aguilar, P. Lemaire, N. Ayouni, E. Bendadesse, A. V. Morozov, O. Sel, V. Balland, B. Limoges, A. M. Abakumov, E. Raymundo-Piñero, A. Slodczyk, A. Canizarès, D. Larcher, J. M. Tarascon, *Energy Storage Mater* **2022**, *53*, 238–253.
- [381] X. Z. Zhai, J. Qu, S. M. Hao, Y. Q. Jing, W. Chang, J. Wang, W. Li, Y. Abdelkrim, H. Yuan, Z. Z. Yu, *Nanomicro Lett* **2020**, *12*, 1–15.
- [382] Q. Zhao, X. Chen, Z. Wang, L. Yang, R. Qin, J. Yang, Y. Song, S. Ding, M. Weng, W. Huang, J. Liu, W. Zhao, G. Qian, K. Yang, Y. Cui, H. Chen, F. Pan, *Small* **2019**, *15*, 1–10.
- [383] G. Liu, H. Huang, R. Bi, X. Xiao, T. Ma, L. Zhang, *J Mater Chem A Mater* **2019**, *7*, 20806–20812.
- [384] J. Huang, Z. Wang, M. Hou, X. Dong, Y. Liu, Y. Wang, Y. Xia, *Nat Commun* **2018**, *9*, 1–8.
- [385] W. Sun, F. Wang, S. Hou, C. Yang, X. Fan, Z. Ma, T. Gao, F. Han, R. Hu, M. Zhu, C. Wang, *J Am Chem Soc* **2017**, *139*, 9775–9778.
- [386] N. Qiu, H. Chen, Z. Yang, S. Sun, Y. Wang, *Electrochim Acta* **2018**, *272*, 154–160.
- [387] Y. Li, S. Wang, J. R. Salvador, J. Wu, B. Liu, W. Yang, J. Yang, W. Zhang, J. Liu, J. Yang, *Chemistry of Materials* **2019**, *31*, 2036–2047.
- [388] G. M. Jacob, I. Zhitomirsky, *Appl Surf Sci* **2008**, *254*, 6671–6676.
- [389] W. H. Ryu, J. H. Yoon, H. S. Kwon, *Mater Lett* **2012**, *79*, 184–187.
- [390] T. Shoji, T. Yamamoto, *Journal of Electroanalytical Chemistry* **1993**, *362*, 153–157.
- [391] C. F. Bischoff, O. S. Fitz, J. Burns, M. Bauer, H. Gentischer, K. P. Birke, H.-M. Henning, D. Biro, *J Electrochem Soc* **2020**, *167*, 020545.
- [392] B. Chen, H. Zhang, J. Xuan, G. J. Offer, H. Wang, *Adv Mater Technol* **2020**, *5*, 2000555.
- [393] X. Ye, M. Saqib, J. Mao, G. Li, R. Hao, *Cell Rep Phys Sci* **2021**, *2*, 100420.
- [394] J. Mao, G. Li, M. Saqib, J. Xu, R. Hao, *Chem Sci* **2022**, *13*, 12782–12790.

- [395] G. Li, J. Mao, M. Saqib, R. Hao, *Chem Asian J* **2022**, *17*, e202200824.
- [396] D. Jiang, Y. Jiang, Z. Li, T. Liu, X. Wo, Y. Fang, N. Tao, W. Wang, H. Y. Chen, *J Am Chem Soc* **2017**, *139*, 186–192.
- [397] D. Jiang, L. Sun, T. Liu, W. Wang, *Anal Chem* **2017**, *89*, 11641–11647.
- [398] V. Brasiliense, J. Clausmeyer, P. Berto, G. Tessier, C. Combellas, W. Schuhmann, F. Kanoufi, *Anal Chem* **2018**, *90*, 7341–7348.
- [399] A. J. Merryweather, C. Schnedermann, Q. Jacquet, C. P. Grey, A. Rao, *Nature* **2021**, *594*, 522–528.
- [400] S. Chakri, A. N. Patel, I. Frateur, F. Kanoufi, E. M. M. Sutter, T. T. M. Tran, B. Tribollet, V. Vivier, *Anal Chem* **2017**, *89*, 5303–5310.
- [401] G. Hass, L. Hadley, in *American Institute of Physics Handbook* (Ed.: O.F. Gray), McGraw-Hill, New York, **1972**, pp. 118–160.
- [402] S. Bodoardo, J. Brenet, M. Maja, P. Spinelli, *Electrochim Acta* **1994**, *39*, 1999–2004.
- [403] Z. Rogulski, H. Siwek, I. Paleska, A. Czerwiński, *Journal of Electroanalytical Chemistry* **2003**, *543*, 175–185.
- [404] O. G. Tsiklauri, T. A. Marsagishvili, G. S. Tsursumiya, S. A. Kirillov, D. I. Dzanashvili, *Russian Journal of Electrochemistry* **2008**, *44*, 1299–1306.
- [405] W. M. Haynes, D. R. Lide, T. J. Bruno, *CRC Handbook of Chemistry and Physics*, CRC Press, **2016**.
- [406] B. J. Hertzberg, A. Huang, A. Hsieh, M. Chamoun, G. Davies, J. K. Seo, Z. Zhong, M. Croft, C. Erdonmez, Y. S. Meng, D. Steingart, *Chemistry of Materials* **2016**, *28*, 4536–4545.
- [407] B. A. Prabowo, A. Purwidyantri, K. C. Liu, *Biosensors (Basel)* **2018**, *8*, DOI 10.3390/bios8030080.
- [408] E. Preisler, *J Appl Electrochem* **1976**, *6*, 301–310.
- [409] X. Dai, M. Zhang, J. Li, D. Yang, *RSC Adv* **2020**, *10*, 15860–15869.

- [410] G. Socrates, *Infrared and Raman Characteristic Group Frequencies. Tables and Charts*, John Wiley & Sons, Ltd, Chichester, **2001**.
- [411] M. Yang, C. Batchelor-McAuley, S. Barton, R. E. M. Rickaby, H. A. Bouman, R. G. Compton, *Angewandte Chemie - International Edition* **2021**, *60*, 20999–21006.
- [412] V. Brasiliense, A. N. Patel, A. Martinez-Marrades, J. Shi, Y. Chen, C. Combellas, G. Tessier, F. Kanoufi, *J Am Chem Soc* **2016**, *138*, 3478–3483.
- [413] A. N. Patel, A. Martinez-Marrades, V. Brasiliense, D. Koshelev, M. Besbes, R. Kuszelewicz, C. Combellas, G. Tessier, F. Kanoufi, *Nano Lett* **2015**, *15*, 6454–6463.
- [414] H. Chen, C. Dai, F. Xiao, Q. Yang, S. Cai, M. Xu, H. J. Fan, S. J. Bao, *Advanced Materials* **2022**, *34*, 2109092.
- [415] J. Winsberg, T. Hagemann, T. Janoschka, M. D. Hager, U. S. Schubert, *Angewandte Chemie International Edition* **2017**, *56*, 686–711.
- [416] Q. Huang, Q. Wang, *Chempluschem* **2015**, *80*, 312–322.
- [417] S. Gentil, D. Reynard, H. H. Girault, *Curr Opin Electrochem* **2020**, *21*, 7–13.
- [418] J. Ye, L. Xia, C. Wu, M. Ding, C. Jia, Q. Wang, *J Phys D Appl Phys* **2019**, *52*, 443001.
- [419] Y. Chen, M. Zhou, Y. Xia, X. Wang, Y. Liu, Y. Yao, H. Zhang, Y. Li, S. Lu, W. Qin, X. Wu, Q. Wang, *Joule* **2019**, *3*, 2255–2267.
- [420] E. Zanzola, C. R. Dennison, A. Battistel, P. Peljo, H. Vrubel, V. Amstutz, H. H. Girault, *Electrochim Acta* **2017**, *235*, 664–671.
- [421] M. Zhou, Y. Chen, Q. Zhang, S. Xi, J. Yu, Y. Du, Y. S. Hu, Q. Wang, *Adv Energy Mater* **2019**, *9*, 1901188.
- [422] M. Z. Bazant, *Faraday Discuss* **2023**, DOI 10.1039/D3FD00108C.
- [423] H. Kahlert, U. Retter, H. Lohse, K. Siegler, F. Scholz, *Journal of Physical Chemistry B* **1998**, *102*, 8757–8765.
- [424] C. D. Wessells, R. A. Huggins, Y. Cui, *Nature Communications* **2011**, *2*, 1–5.

- [425] M. Moghaddam, S. Sepp, C. Wiberg, A. Bertei, A. Rucci, P. Peljo, *Molecules* **2021**, *26*, 2111.
- [426] J. F. Vivo-Vilches, A. Nadeina, N. Rahbani, V. Sez nec, D. Larcher, E. Baudrin, *J Power Sources* **2021**, *488*, 229387.
- [427] R. Yan, J. Ghilane, K. C. Phuah, T. N. Pham Truong, S. Adams, H. Randriamahazaka, Q. Wang, *Journal of Physical Chemistry Letters* **2018**, *9*, 491–496.
- [428] M. Burgess, K. Hernández-Burgos, K. J. Cheng, J. S. Moore, J. Rodríguez-López, *Analyst* **2016**, *141*, 3842–3850.
- [429] N. Yang, S. Yu, W. Zhang, H. M. Cheng, P. Simon, X. Jiang, *Advanced Materials* **2022**, *34*, 2202380.
- [430] J. Rodríguez-López, A. J. Bard, *J Am Chem Soc* **2010**, *132*, 5121–5129.
- [431] N. B. Schorr, Z. T. Gossage, J. Rodríguez-López, *Curr Opin Electrochem* **2018**, *8*, 89–95.
- [432] X. Xu, D. Valavanis, P. Ciocci, S. Confederat, F. Marcuccio, J. F. Lemineur, P. Actis, F. Kanoufi, P. R. Unwin, *Anal Chem* **2023**, *95*, 319–356.
- [433] K. O. Hatfield, M. T. Gole, N. B. Schorr, C. J. Murphy, J. Rodríguez-López, *Anal Chem* **2021**, *93*, 7792–7796.
- [434] N. B. Schorr, A. G. Jiang, J. Rodríguez-López, *Anal Chem* **2018**, *90*, 7848–7854.
- [435] J. Clausmeyer, M. Nebel, S. Grützke, Y. U. Kayran, W. Schuhmann, *Chempluschem* **2018**, *83*, 414–417.
- [436] L. Wang, J. Kowalik, B. Mizaikoff, C. Kranz, *Anal Chem* **2010**, *82*, 3139–3145.
- [437] M. Etienne, M. Dossot, J. Grausem, G. Herzog, *Anal Chem* **2014**, *86*, 11203–11210.
- [438] L. Guerret-Legras, J. F. Audibert, G. V. Dubacheva, F. Miomandre, *Chem Sci* **2018**, *9*, 5897–5905.
- [439] F. M. Boldt, J. Heinze, M. Diez, J. Petersen, M. Börsch, *Anal Chem* **2004**, *76*, 3473–3481.
- [440] F. Kanoufi, *Encyclopedia of Electrochemistry* **2021**, 1–80.

- [441] A. I. Komayko, N. A. Arkharova, D. E. Presnov, E. E. Levin, V. A. Nikitina, *Journal of Physical Chemistry Letters* **2022**, *13*, 3165–3172.
- [442] E. Zanzola, S. Gentil, G. Gschwend, D. Reynard, E. Smirnov, C. R. Dennison, H. H. Girault, P. Peljo, *Electrochim Acta* **2019**, *321*, 134704.
- [443] T. Janoschka, N. Martin, M. D. Hager, U. S. Schubert, *Angewandte Chemie International Edition* **2016**, *55*, 14427–14430.
- [444] A. P. Baioni, M. Vidotti, P. A. Fiorito, E. A. Ponzio, S. I. C. De Torresi, *Langmuir* **2007**, *23*, 6796–6800.
- [445] E. S. Goda, S. Lee, M. Sohail, K. R. Yoon, *Journal of Energy Chemistry* **2020**, *50*, 206–229.
- [446] M. Guo, R. E. White, *J Power Sources* **2012**, *198*, 322–328.
- [447] H. E. M. Hussein, R. J. Maurer, H. Amari, J. J. P. Peters, L. Meng, R. Beanland, M. E. Newton, J. V. Macpherson, *ACS Nano* **2018**, *12*, 7388–7396.
- [448] G. Young, P. Kukura, *Annu Rev Phys Chem* **2019**, *70*, 301–322.
- [449] A. Moezzi, M. B. Cortie, A. M. McDonagh, *Dalton Transactions* **2013**, *42*, 14432–14437.
- [450] B. Beverskog, I. Puigdomenech, *Corros Sci* **1997**, *39*, 107–114.
- [451] S. Munteanu, J. P. Roger, Y. Fedala, F. Amiot, C. Combellas, G. Tessier, F. Kanoufi, *Faraday Discuss* **2013**, *164*, 241–258.
- [452] A. V. Soldatova, G. Balakrishnan, O. F. Oyerinde, C. A. Romano, B. M. Tebo, T. G. Spiro, *Environ Sci Technol* **2019**, *53*, 4185–4197.
- [453] J. B. Gillespie, J. D. Lindberg, *Appl Opt* **1992**, *31*, 2112.
- [454] Malvern Instruments, *Sample Dispersion and Refractive Index Guide. Mastersizer 2000 Reference Manual*, Worcestershire, **2007**.
- [455] S. Yang, P. Tsai, E. S. Kooij, A. Prosperetti, H. J. W. Zandvliet, D. Lohse, *Langmuir* **2009**, *25*, 1466–1474.

[456] L. Trotochaud, S. L. Young, J. K. Ranney, S. W. Boettcher, *J Am Chem Soc* **2014**, *136*, 6744–6753.

[457] E. S. Ilton, J. E. Post, P. J. Heaney, F. T. Ling, S. N. Kerisit, *Appl Surf Sci* **2016**, *366*, 475–485.